Electron Microscopy Studies of Precipitation in Nuclear Reactor Pressure Vessel Steels under Neutron Irradiation & Thermally Ageing



Joven Jun Hua Lim

Linacre College

University of Oxford

A thesis submitted for the degree of

Doctor of Philosophy

Michaelmas 2014

"If it's not part of the solution, it must be part of the precipitate"

For My Family

"Ever since the creation of the world His eternal power and divine nature, invisible though they are, have been understood and seen through the things He has made. So they are without excuse."

Romans 1:20

Electron Microscopy Studies of Precipitation in Nuclear Reactor Pressure Vessel Steels under Neutron Irradiation & Thermally Ageing

Thesis submitted for the degree of
Doctor of Philosophy
in the Michaelmas term of 2014

Joven Jun Hua Lim
Linacre College

ABSTRACT

Maintaining the safe operation of nuclear power plants (NPPs) is crucial. This requires fully understanding the mechanism of long term irradiation and thermal ageing, as well as their effects, on components including the reactor pressure vessel (RPV). The research community is collecting data that will be required to support the case for extending the operation of western-type NPPs beyond that of 60 years. One of the current dilemmas faced by the long-term operation of RPVs is the formation of nanometre scale precipitates. These precipitates are known to cause embrittlement where it increases the ductile-to-brittle transition temperature of the RPV steels. The chemistry of these precipitates is strongly dependent on the chemistry of the RPV steels. In general, these precipitates can be categorised into two types, copper-rich precipitates (CRPs) and manganese-nickel (-enriched) precipitates (MNPs) [1, 2]. The concentration of copper in the precipitates depends on the bulk content of the steel [3]. The formation mechanism of the precipitates under neutron irradiation and thermal ageing, and their influence on material degradation at high neutron fluence (ϕt), is still unclear.

To understand the long term precipitation under irradiation and thermal ageing, high nickel and copper containing RPV steels with a similar microstructure an chemical composition as those currently in service were subjected to either neutron irradiation (to high neutron fluences, $\phi t \geq 5 \times 10^{23}$ neutrons.m^{-2}) or thermal ageing (for as long as $\approx$ 50,000 hours).

CRPs and MNPs were both detected. The co-precipitation of the CRPs and MNPs were observed in thermally aged steels. The development of crystal structures in the CRPs is believed to be dependent on the size of the precipitates and the ambient temperature. When the CRPs reached a critical size, they underwent the martensitic transformation from $BCC \rightarrow 9R \rightarrow 3R \rightarrow FCC\ or\ FCT$. The CRPs preferentially nucleate heterogeneously at the dislocation lines. Chemical analysis suggests that most of the CRPs are iron free. Under thermal ageing, the MNPs were found to precipitate at the interface of the CRPs and the matrix. These MNPs are found to be iron free too. Larger MNPs were often found to be at CPRs that were associated with dislocation lines. Also, based on the volume fraction observed, it is possible to suggest that the kinetics of nucleation and growth of the MNPs are relatively slow compared to the CRPs. This is in good agreement with the simulations reported in Refs. [4, 5].

It is the first time the MNPs are directly imaged from neutron irradiation low copper steels using electron microscopy. These irradiation-induced MNPs are densely populated in the neutron irradiated samples. It was found that the irradiation-induced MNPs are more sensitive to electron beams. It was thought that this was due to a relatively large amount of point defects present in the irradiation-induced MNPs.

PREFACE

This doctoral thesis reports the research carried out by the author in the Department of Materials, University of Oxford from January 2011 to July 2014, under the supervision of Professor Christopher R. M. Grovenor and Professor Sergio Lozano-Perez. All of the research carried out for this thesis is original and where the work of others has been included, it has been clearly referenced and acknowledged. All figures reproduced from journal articles and books have been used with permission from the respective copyright owner. No part of this thesis has been submitted for a degree at this, or any other university. Some of the work has been published in peer reviewed journals and deliverable reports, as well as presented at conferences and workshops as detailed below:

LONGLIFE Deliverable Reports:

J J H Lim, S R Ortner, C R M Grovenor, S Lozano-Perez, K B Wilford, F Bergner, E Alstadt, H Hein, B Radiguet, M Hernandez-Mayoral, and M Serrano, "*LONGLIFE Deliverable D3.5: Chemical Effects on Neutron Induced Microstructure*," December 2013.

F Bergner, M Hernandez-Mayoral, M Serrano, V Slugen, S R Ortner, K B Wilford, J Barthelmess, H Hein, **J J H Lim**, A Ulbricht and A Wagner, "*LONGLIFE Deliverable D3.4: Effects of neutron flux on the neutron-induced microstructure of RPV materials*," December 2013.

B Radiguet, S Cammelli, P Pareige, F Bergner, A Ulbricht, A Wagner, M Hernandez-Mayoral, M Serrano, S R Ortner, K B Wilford, **J J H Lim**, C R M Grovenor, E Meslin, J Michalicka and J Kocik, "*LONGLIFE Deliverable D3.3: Effects of Neutron Dose on the Neutron-induced Microstructure of RPV materials*," January 2014.

Journal Articles:

J J H Lim, J M Hyde, S Lozano-Perez, and C R M Grovenor, "Microstrutural Characterization of Irradiation-Induced MnNi-Rich Solute Cluster in Highly Neutron-Irradiated MnNiMo Alloyed Weld Metals," Effects of Radiation on Nuclear MaterialsL 26th volume, STP 1572, Mark Kirk and Enrico Lucon, Eds., pp. 57-73, DOI: 10.1520/STP157220130120, ASTM International, West Conshohocken, PA 2014.

M Serrano, F Bergner, B Radiguet, **J J H Lim**, C R M Grovenor, M Hernandez-Mayoral, E Meslin, K B Wilford, W Van Renterghem, J Kocik, S Ortner, H W Viehrig, R Chaouadi, M Brumovsky, H Hein, F Gillemot, P Todeschini, T Planman, J Ruoden,

and E Altstadt, "Correlation Between Microstructural Features and Mechanical Properties of Irradiated LONGLIGE RPV Steels," *Submitted to: Proceedings of the Fontevraud 8 - Contribution of Materials Investigations and Operating Experience to LWRs' Safety, Performance and Reliability*, Avignon, France, 2014

Conferences:

J J H Lim, J M Hyde, P D Styman, S Lozano-Perez, K B Wilford, and C R M Grovenor, "*High Resolution Analytical Characterisation of 'Slow-Blooming Phases' in Irradiated Reactor Pressure Vessel Steels*," Oral presentation, March 2013, TMS 2013, San Antonio, Texas, USA.

J J H Lim, J M Hyde, S Lozano-Perez, and C R M Grovenor, "*Finding Nano-clusters in Neutron Irradiated Nuclear Steels with Advanced Analytical Electron Microscopy*," Poster presentation. June 2013, Oxford University, Oxford, UK

J J H Lim, J M Hyde, K B Wilford, S Lozano-Perez, and C R M Grovenor, "*Finding Ni-Mn-Si Clusters in Neutron Irradiated RPV Steels with Advanced Electron Microscopy Techniques*," Oral presentation, 17th International Group on Radiation Damage Mechanisms (IGRDM-17), May 2013, Embiez island, France

J J H Lim, J M Hyde, S Lozano-Perez, K B Wilford and C R M Grovenor, "*High Resolution Microstructural Characterisation on Irradiation-induced Defect in Reactor Pressure Vessel Steels and its Effect on Long Term Operation*," Oral presentation, at 26th Symposium on the Effects of Radiation on Nuclear Materials, June 2013, Indianapolis, Indiana, USA

J J H Lim, G M Burke, S Lozano-Perez, J M Hyde, P D Styman, I MacLaren, M L Jenkins, G D W Smith, K B Wilford and C R M Grovenor, "The Evolution of Cu-rich Precipitate in High Cu and High Ni Weld Metal Under Thermal Annealing", Oral Presentation, 18th International Group on Radiation Damage Mechanisms (IGRDM-18), Nov 2014, Miyazaki, Japan

J J H Lim, G M Burke, S Lozano-Perez and C R M Grovenor, "When Irradiation-induced Solute Clusters & Thermally Aged Precipitates Exposed to The Electron Beam", Oral Presentation, 18th International Group on Radiation Damage Mechanisms (IGRDM-18), Nov 2014, Miyazaki, Japan

Workshops:

J J H Lim, P D Styman, S Lozano-Perez, and C R M Grovenor, "*High Resolution Analytical Characterisation of Reactor Pressure Vessel Steels*," Poster presentation, F-BRIDGE, July 2011, Cambridge University, Cambridge, UK

J J H Lim, S Lozano-Perez, and C R M Grovenor, "*Chemical Effects on Irradiation-induced Solute Clusters & How to Study them with TEM based Techniques,*" Oral presentation, LONGLIFE Final Workshop, 15-16 January 2014, HZDR, Dresden, Germany

ACKNOWLEDGEMENTS

Without the advice and assistance from a number of people the work presented in this thesis would not have been possible. Firstly, I would like to express my deepest gratitude to my supervisors Prof. Christopher R M Grovenor and Prof. Sergio Lozano-Perez. I thank you both for passing on some of your encyclopaedic knowledge of materials, literature and electron microscopy. Your fruitful discussions, scientific guidance, and motivation throughout my time here have been invaluable. I am also grateful for the free time both of you have given up to read through and improve the quality of this thesis. I would also like to thank you both for giving me the opportunity back in early 2011 to pursue this DPhil.

I would also like to offer my special thanks to Dr. Mike L Jenkins, Prof. John M Titchmarsh, and Prof. Collin A English. I thank you all for the extensive knowledge of radiation damages and electron microscopy. Your valuable advice, priceless experiences and continuous support has been the source of inspiration for me throughout this work. I am particularly grateful for the advice provided by Prof. Angus Kirkland and Prof. Peter Nellist on electron microscopy.

I would like to thank all members of the Nanoanalysis group, Oxford Electron Image Analysis group, Dr. Peter Nellist's Research group, MFFP group and FIM groups, both past and present for helpful discussions over the years. Particular thanks goes to Dr. Benjamin Britton, Dr. Jicheng Gong, Dr. Chris Hardie, Dr. Lewys Jones, Dr. Judy Kim, Dr. Hiroto Kitaguchi, Dr. Karen Kruska, Dr. Katie Moore, Dr. Ceri Williams, and Dr. Xiaoou Yi for helpful discussions on my work over the years. Also, I would like to acknowledge my colleagues in the Department of Materials. I thank Mr. Bob Lloyd and Mr. Laurie Walton for maintaining the workshop facilities. Also thanks to all members of the support group from the David Cockayne centre for electron microscopy, particularly to Mr. Ron Doole, Dr. Neil Young, Dr. Gareth Hughes, Mrs. Gabriella Chapman, and Ms. Fay Chicken for help and training on the FIB machines and electron microscopes. I would also like to thank Dr. Ian MacLaren and Ms. Joanna Cholewa for the helpful discussion and helps while I was in Glasgow.

I am also grateful for the financial support received from the European Commission who has also supported the LONGLIFE project (grant agreement number 249360), without whom I would not have been able to undertake my doctoral studies. I would also like to acknowledge the partners of the LONGLIFE project, particularly to Dr. Susan R Ortner, Dr. Keith Wilford, Dr. Mercedes M. Hernandez Mayoral, Dr. Marta Serrano García, Dr. Hieronymus Hein, Dr. Frank Bergner and Dr. Bertrand Radiguet for their contribution to this work and for fruitful discussions. I would also like to thank The Worshipful Company of Founders, the Institute of Physics and the Institute of Materials, Minerals and Mining for financial support to attend conferences and seminars.

Finally, I would like to thank Yi Guo, Jing Hu, Chen Huang, Haibo Jiang, Stella Pedrazzini, Alan Xu and Jennifer Zelenty for their endless supply of food, fun times and banter! Lastly, I would like to thank and dedicate this thesis to my dear grandfather, parents, godparents and my beloved fiancée for their love, encouragement and support throughout my time in the United Kingdom.

ACRONYMS & NOMENCLATURES

3DAP	3 Dimensional Atom Probe
ADF	Annular Dark Field
AKMC	Atomistic Kinetic Monte-Carlo
ANP-G	AREVA NP GmbH
APT	Atom Probe Tomography
BF	Bright Field
BM	Base Metal
DBTT	Ductile-Brittle Transition Temperature
DC	Direct Current
DF	Dark Field
EDX	Energy Dispersive X-ray
EELS	Electron Energy Loss Spectroscopy
EFTEM	Energy Filtered Transmission Electron Microscopy
EHT	Extra High Tension
EOL	End of Life
FIB	Focussed Ion Beam
FZD	Forschungszentrum Dresden-Rossendorf e. V
HAADF	High Angle Annular Dark Field
HRTEM	High Resolution Transmission Electron Microscopy
HT	Heat Treatment
HZDR	Helmholtz-Zentrum Dresden-Rossendorf
KMC	Kinetic Monte-Carlo
LONGLIFE	Treatment of long term irradiation embrittlement effects in RPV safety assessment
MC	Monte-Carlo
PAS	Positron Annihilation Spectroscopy
PWR	Pressurised Water Reactor

RPV	Reactor Pressure Vessel
SANS	Small-angle Neutron Scattering
SAW	Submerged Arc Welding
SEM	Scanning Electron Microscopy
SIA	Self Interstitial Atoms
SRIM	Stopping and Range of Ions in Matter
STEM	Scanning Transmission Electron Microscopy
TEM	Transmission Electron Microscope/Microscopy
TRIM	Transport of Ions in Matter
TTS	Transition Temperature Shift
WM	Weld Metal
at.%	Atomic percentage
T_{41}˚C	Charpy 41-J transition temperature shift
ΔT_{41}˚C	Change of Charpy 41-J transition temperature shift
S_g	Deviation parameter
g	Diffraction vector
ξ_g	Extinction Distance
ϕt	Fluence
φ	Flux
T_{irra}	Irradiated temperature
wt.%	Weight percentage

CONTENT

1 INTRODUCTION 12

1.1 RESEARCH AIMS 14

1.2 OXFORD CONTRIBUTIONS TO THE LONGLIFE PROJECT 15

1.3 LAYOUT OF THE THESIS 17

2 MECHANISMS CONTROLLING THE FORMATION OF NEUTRON IRRADIATION-INDUCED DEFECTS 18

2.1 PRIMARY DAMAGE 18

2.1.1 Displacement cascades 19

2.1.2 Current vision of primary damage 19

2.2 FORMATION OF IRRADIATION-INDUCED DEFECTS 22

2.2.1 Hardening defects 22

2.2.2 Structure of the hardening defects 23

2.2.2.1 Self-interstitial atom clusters: 23

2.2.2.2 Vacancy clusters: 24

2.2.2.3 Solute precipitates: 24

3 PRECIPITATION IN RPV STEELS 25

3.1 PRECIPITATION IN MEDIUM OR HIGH COPPER STEELS 26

3.1.1 Formation of copper-rich precipitates 26

3.1.1.1 Solubility 26

3.1.1.2 Irradiation enhanced diffusion 27

3.1.1.3 Alloying element effects 27

3.1.2 Phase of copper-rich precipitates 28

3.1.2.1 9R structure 29

3.1.2.2 3R structure 33

3.1.2.3 FCC or FCT structures 34

3.1.2.4 Intermediate structure between 3R and FCC/FCT structure 35

3.1.3 Triggers for the martensitic transformations 35

3.1.3.1 Ambient temperature 36
3.1.3.2 Dislocation interactions 37
3.1.3.3 Irradiation 37
3.1.4 The chemical composition of copper-rich precipitates 38
3.1.4.1 The segregation of alloying elements and impurities to copper-rich precipitate interfaces 40
3.1.5 Differences between neutron irradiation-induced and thermally aged copper-rich precipitates 41
3.1.5.1 Structural results 41
3.1.5.2 Size and number density 42
3.1.5.3 Chemical composition 43
3.2 PRECIPITATION IN LOW COPPER OR COPPER-FREE STEELS 44

4 EXPERIMENTAL MATERIALS & METHODS 47
4.1 MATERIALS BACKGROUND 47
4.1.1 Neutron implantation 49
4.1.1.1 ANP-type weld metals 50
4.1.2 Thermally annealing or ageing 51
4.1.2.1 WV weld metal 52
4.2 TEM SAMPLE PREPARATION 53
4.2.1 Mechanical polishing 54
4.2.2 Jet electropolishing 54
4.2.3 Focused ion beam milling for TEM specimen preparation 57
4.2.3.1 In-situ lift-out FIB TEM specimen with specific zone axis 61
4.3 EXPERIMENTAL TECHNIQUES 63
4.3.1 Transmission electron microscopy imaging 64
4.3.1.1 Diffraction contrast analysis 64
4.3.1.2 Phase contrast analysis 65
4.3.2 Scanning transmission electron microscopy imaging 65
4.3.3 Electron energy filtered imaging 66
4.3.3.1 Foil thickness measurement 67
4.3.4 Energy dispersive x-ray analysis 68

5 FEATURES OF IDENTIFICATION 70

5.1 INTRODUCTION 70

5.2 ARTEFACTS 71

5.2.1 Nature-of-the-material induced artefacts 71

5.2.1.1 Magnetic field 72

5.2.1.2 Surface oxides 72

5.2.2 Sample preparation induced artefacts 82

5.2.2.1 Electro-chemical polishing induced artefacts 82

5.2.2.2 FIB-induced defects/ artefacts 87

5.2.3 Electron beam induced defects/ artefacts 96

5.2.3.1 Knock-on effects 97

5.2.3.2 Surface sputtering effects 98

5.3 RADIATION DAMAGE 102

5.3.1 Identifying dislocation loops 103

5.3.2 Identifying voids 104

5.4 PRECIPITATES & SOLUTE CLUSTERS 104

5.4.1 Diffraction (Strain) contrast imaging 105

5.4.3 Phase contrast imaging 107

5.4.4 High resolution electron microscopy (HRTEM) 108

5.4.5 Scanning transmission electron microscopy (STEM) 109

5.4.6 Elemental mapping 110

6 THERMALLY AGED PRECIPITATE 112

6.1 INTRODUCTIONS 112

6.2 CONVENTIONAL TRANSMISSION ELECTRON MICROSCOPY 113

6.2.1 Banded precipitate structure 119

6.2.1.1 Banded structure orientation 121

6.3 HIGH RESOLUTION TRANSMISSION ELECTRON MICROSCOPY 122

6.3.1 Un-twinned 9R precipitates 123

6.3.2 Twinned 9R precipitates 125

6.3.3 Intermediate structure between 3R and FCC or 3R and FCT 127

6.4 EELS AND EDS SPECTRUM IMAGING 128

6.4.1 WV weld steel after thermal ageing for 18,620 hours 129

6.4.1.1 Low magnification elemental mapping 129

6.4.1.2 High magnification elemental mapping 132

6.4.2 WV weld steel after thermal ageing for 49,800 hours 134

6.4.2.1 Low magnification elemental mapping 134

6.4.2.2 Medium magnification elemental mapping 137

6.4.2.3 High magnification elemental mapping 139

6.5 DISCUSSION 144

6.5.1 Structure of precipitates 145

6.5.2 Chemical composition of precipitates 147

6.5.2.1 Iron concentration in precipitates 147

6.5.2.2 Silicon concentration of precipitates 150

6.5.3 Size of precipitates and number density 151

6.5.3.1 WV weld steel after being thermally aged for 49,800 hours 152

6.5.4 Precipitation under long term thermal ageing 156

6.5.4.1 Potential phase for the MnNi-rich shell of the copper precipitates 158

6.6 SUMMARY 160

7 IRRADIATION-INDUCED SOLUTE CLUSTERS 162

7.1 INTRODUCTION 162

7.2 NEUTRON IRRADIATED ANP-2 WELD STEEL 163

7.2.1 Diffraction contrast imaging 163

7.2.2 Phase contrast imaging 164

7.2.3 High angle annular dark field imaging 166

7.3 NEUTRON IRRADIATED ANP-6 WELD STEEL 167

7.3.1 High angle annular dark field imaging 167

7.3.2 Electron energy loss spectroscopy 169

7.4 DISCUSSION 171

7.4.1 Analytical methods 171

7.4.2 Chemical composition of solute cluster 173

7.5 SUMMARY 174

8 ELECTRON BEAM INDUCED DAMAGE TO PRECIPITATES &/OR SOLUTE CLUSTERS 176

8.1 INTRODUCTION 176

8.1.1 Experimental procedures for EDX-line scans 176

8.2 OBSERVATIONS 177

8.2.1 Neutron irradiation-induced precipitates 177

8.2.2 Thermally aged precipitates 179

8.3 DISCUSSION 179

8.3.1 Irradiation-induced solute clusters & thermally aged precipitates 179

8.3.1.1 Chemical composition 180

8.3.1.2 Structure of the precipitates/solute clusters 180

8.3.1.3 Formation of precipitates/solute clusters 181

8.3.2 Plausible explanation for the electron beam damage on irradiation-induced solute clusters 182

9 FUTURE WORK 183

9.1 CHEMICAL ANALYSIS 183

9.2 THERMALLY AGED PRECIPITATION 184

9.3 NEUTRON IRRADIATION-INDUCED SOLUTE CLUSTERING 185

10 REFERENCES 186

11 APPENDICES 197

11.1 APPENDIX A: LONGLIFE DELIVERABLE REPORT 3.6 - CHEMICAL EFFECTS ON IRRADIATION-INDUCED PRECIPITATION 197

1 INTRODUCTION

All types of power plants have a finite lifetime. This is due to the components and materials deteriorating during the service of the power plant. Once beyond this, it is no longer economically feasible to operate a power plant. For nuclear fission power plants (NPPs), the design end-of-life[1] (EOL) for a newer plant, i.e. 3rd generation reactor, is 40 years to 60 years, though some have proved capable of continuing well beyond this. This is because the design life of a NPP does not necessarily equate to the physical or technological EOL in terms of its ability to operate safely to produce electricity [7].

It is important to address the issue of licensing NPPs for long term operation as there are an increasing number of ageing NPPs that are close to their licensed lifetime but have the potential to be able to operate well beyond this. Moreover, the owners of these ageing NPPs would like to keep them in service if they can be operated safely and economically. This involves the consideration of a number of factors, one of which is the condition of the materials of the key components of the plant.

Neutron irradiation and temperature can both cause significant changes in the microstructure and mechanical properties of the structural components of a NPP. Hence it is essential to make sure that the life defining component – the reactor pressure vessel (RPV) which is generally constructed from low-alloy steel – is physically safe for operation after being subjected to neutron irradiation for many years. One of the most critical forms of irradiation induced embrittlement of low-alloy steels is the elevation of the ductile-brittle transition temperature (DBTT) that is often characterised by Charpy V-notch impact test 41J temperature shifts (T_{41J}) [8]. As a result of the increase in DBTT, the embrittled material requires very little energy to break and can fail quickly and unexpectedly. This poses an unacceptable risk and is an

[1] End-of-life can also be referred as end-of-license [[6] M.G. Burke, The origin of the term 'End-of-life' of a nuclear power plant, in: J.J.H. Lim (Ed.)IGRDM-18, Miyazaki, Japan, 2014.

important concern if an NPP is to allow extending its lifetime up to 80 years and/or beyond.

Even though there have been tremendous advances in understanding this embrittlement mechanism in the past 25 years, the current knowledge of the effect of long term neutron irradiation embrittlement on reactor pressure vessel steels is still limited [9, 10]. Little data, i.e. about 1% of the data from the largest data base, the PREDB[2], is available at a neutron fluence[3] (ϕt) that is equivalent and/or greater than that experiences in 60 years of service (i.e. > 5 x 10^{23} neutron/m^{-2}). This is because it involves a significant amount of effort, time and funds to obtain sufficient information on the changes in microstructure and mechanical properties from low-alloy steels neutron irradiated up to neutron fluences of 5 x 10^{23} neutron.m^{-2} or beyond under the conditions seen in an NPP. For these reasons, predictive irradiation embrittlement models have been developed for low alloy steels to anticipate the mechanical property changes in these steels after long term neutron irradiation. To help obtain more data, low-alloy steels of similar microstructure and chemical composition as those used to construct reactor pressure vessels are sometimes subjected to neutron irradiation at a higher neutron flux[4] (φ) under conditions similar to surveillance samples in NPPs, i.e. similar temperature and same irradiation environment. This reduces the time required to achieve the neutron fluence of interest, but raises questions on the reliability of the results obtained since flux effects may be important [9].

The predictive embrittlement models are developed based on an understanding of the effect of both external and internal parameters on changes in the ductile-brittle transition temperature (ΔT) of low-alloy steels during neutron irradiation. The external parameters are neutron fluence, flux and irradiation temperature, whereas the internal

[2] PREDB is a U.S. power reactor (surveillance) embrittlement database.
[3] Neutron fluence, ϕt, is the number of neutrons irradiated per surface area of a material. It is often used to compare with the neutron dose.
[4] Neutron flux, ϕ is the number of neutrons irradiated per surface area of a material per unit time, $n.m^{-2}.s^{-1}$. It is often used to compare with dose rate.

parameters are the initial microstructure and chemical composition of low-alloy steels. ΔT depends on the synergistic effects of both external and internal parameters [1, 2].

The selection of parameters to be used in a predictive embrittlement model are based on the current mechanistic understanding and broadly observed trends from the data that is already available [11]. Therefore, our confidence in the reliability of these embrittlement models to predict the ΔT values for low-alloy steels is strongly dependent on our understanding of the neutron irradiation embrittlement mechanisms in these low-alloy steels; i.e. a predictive embrittlement model is only as good as the data collected and our understanding of the key atomistic and microstructural mechanisms. Since the data at high neutron fluence is lacking, i.e. neutron fluence $\phi t > 5 \times 10^{23}$ neutron.m^{-2}, the current predictive embrittlement model, e.g. Ref. [11], is unable to include all potentially important variables at a very high neutron fluence [9, 10].

1.1 RESEARCH AIMS

This project was part of the EU Framework 7 LONGLIFE[5] project to contribute the understanding of high fluence embrittlement mechanisms in neutron irradiated low-alloy steels. The aim of this thesis was to investigate the effect of long term neutron irradiation and thermal annealing on the microstructure of a series of low-alloy steels. The primary focus was on understanding the effects of alloying elements and impurities present in low-alloy steels on the nanometre scale precipitates that are nucleated after long term neutron irradiation and thermal annealing. Conventional and advanced transmission electron microscopy techniques have been used to characterise these precipitates, and also other defects induced in neutron irradiated and thermally annealed low-alloy steels.

[5] LONGLIFE is the project acronym for “Treatment of long term irradiation embrittlement effect in RPV safety assessment” (Grant agreement number 249360).

1.2 OXFORD CONTRIBUTIONS TO THE LONGLIFE PROJECT

The University of Oxford is one of the 16 organisations that took part in the LONGLIFE project (contract No. 249360). It is one of the many EURATOM FP7 projects that was supported by the European Commission. This project was designed to examine the effects of long term neutron irradiation on the embrittlement of RPV steels. A complex matrix of 12 surveillance samples with different chemical compositions was chosen to be analysed in the LONGLIFE project. Table 1 shows the chemical composition, irradiated conditions and type of analysis performed on each sample.

The University of Oxford was involved in the work package of microstructural characterisation and was responsible for TEM characterisation of two of the RPV surveillance samples listed in Table 1, where the information of these samples, ANP-2 and ANP-6, is listed in a bold font. Some of the results obtained have been summarised and written as a part of this thesis (Chapter 7). Apart from that, the University has taken the responsibility in performing a detailed analysis on all the information collected in the LONGLIFE project on the chemical effects of the neutron irradiation-induced microstructure, focussing on the irradiation-induced precipitation. A summary of this analysis had been written and peer-reviewed by other partners as well as published as the scientific deliverable report 3.5 for the LONGLIFE project. A copy of this report is attached as Section 11.1 (Appendix A).

Summaries of the effects of neutron fluence and flux on the neutron irradiation-induced microstructure as well as the comparison of microstructural data and macro-physical material properties of neutron irradiated materials can also be found on the LONGLIFE website: http://projects.tecnatom.es/webaccess/LONGLIFE/.

Table 1: Summary of the RPV surveillance samples that have been selected for the LONGLIFE project.

Code	Steel Ref. Code/Name	Cu (Wt.%)	Mn (Wt.%)	Ni (Wt.%)	Si (Wt.%)	P (Wt.%)	T_{irra} (°C)	Highest ϕt 10^{23} n.m^{-2} (E>1MeV)	ϕ 10^{16} n.m^{-2}s^{-1} (E>1MeV)	ΔYS	ΔT_{41J}	APT	SANS	TEM
ANP-2	**WM S3NiMo1**	**0.03**	**1.08**	**1.01**	**0.12**	**0.019**	**285**	**4.97**	**2-3**	**X**	**X**	**X**	**X**	**X**
ANP-6	**WM S3NiMo**	**0.08**	**1.41**	**1.69**	**0.15**	**0.012**	**280**	**5.22**	**1-2**	**X**	**X**	**X**	**-**	**X**
ANP-4	BM 22NiMoCr3-7	0.05	0.85	0.84	0.22	0.006	285	4.22	1.2-1.9	X	X	-	X	-
ANP-5	WM 22NiMoCr3-7	0.22	1.14	1.11	0.15	0.015	285	2.22	0.06	X	X	-	X	-
							285	2.25	2.00	X	X	-	X	-
EDF-2	BM 16MND5	0.06	1.32	0.69	0.22	0.006	286	6.95	0.1-0.2	X	X	X	X	X
EDF-3	WM 16MND5	0.03	1.41	0.64	0.35	0.009	286	5.13	0.1-0.2	X	X	X	X	X
FZD-1a	high P JPB	0.03	1.30	0.74	0.24	0.020	255	8.90	0.1-3.5	X	X	X	X	X
							290	15.00	6-83	X	-	-	X	X
FZD-1b	low P JPC	0.03	1.32	0.73	0.24	0.005	255	8.90	0.1-3.5	X	-	-	X	X
							290	11.70	14-65	X	-	-	X	X
AEK-1	BM 15Kh2MFA	0.09	0.54	0.07	0.29	0.018	275	90.60	2.1-3.2	X	X	X	X	X
NRI-1	WM 5Kh2NMFAA	0.04	0.74	1.67	0.37	0.006	288	8.50	37-42	X	X	X	-	X
VTT-1	WM 10KhMFT	0.20	1.06	0.13	0.60	0.020	275	4.00	0.1-1.6	X	X	-	X	X
FZD-2	WM 10KhMFT	0.11	1.13	0.14	0.44	0.043	265	3.10	0.07	X	X	-	X	-

WM = Weld metal
BM = Base metal
ϕt = Neutron fluence
ϕ = Flux

T_{irra} = Irradiation Temperature
ΔYS = Change of Yield Stress
ΔT_{41J} = Change of Charpy 41-J Transition Temperature Shift

APT = Atom Probe Tomography
SANS = Small-angle Neutron Scattering
TEM = Transmission Electron Microscopy

1.3 LAYOUT OF THE THESIS

The work presented in this thesis is laid out in 9 chapters beginning with a review on the current understanding of the mechanisms controlling the formation of neutron irradiation-induced defects in Chapter 2 and an overview of the current knowledge of precipitation in reactor pressure vessel (RPV) steels, also known as low alloy steels, in Chapter 3. Chapter 4 details the materials, sample preparation techniques and associated electron microscopy analysis methods used. Chapter 5 describes the features identification of artefacts and 'real' features of interest as well as challenges encountered in obtaining good quality electron microscopy data.

The results and discussions of the electron microscopy investigation of thermally aged material and neutron irradiated materials are presented in Chapter 6 and Chapter 7, respectively. These compare the work on the same materials analysed using atom probe tomography (APT). In addition, the so called "Late Blooming Phases" (LBPs), manganese-nickel precipitates, was observed in the neutron irradiated and thermally aged materials using electron microscopy techniques for the first time. A brief summary of the main results of the investigation performed on the thermally aged and neutron irradiated materials are detailed at the end of its respective chapter. Observation of the electron beam damages on the irradiation-induced precipitates is presented in Chapter 8. The observation shows the irradiation-induced precipitates are more vulnerable to the electron beam, and this provides a good indication for the differences between the thermally aged and irradiation-induced precipitates. Finally, important directions for future research are outlined in Chapter 9.

2 MECHANISMS CONTROLLING THE FORMATION OF NEUTRON IRRADIATION-INDUCED DEFECTS

2.1 PRIMARY DAMAGE

Primary damage, as the name suggests, is lattice atoms being displaced and rearranging after direct impact from neutrons during irradiation. It has a direct relationship with the energy required for primary knock-on of atoms (PKAs). Table 2 shows data on PKA energy relative to the neutron energy.

It is noteworthy that the migration of surviving point defects, i.e. Frenkel pairs, generated in primary damage is the main contribution to the evolution of microstructure and the mechanical properties of irradiated RPV steels [12]. Due to the formation of these defects, the diffusion rates increase and other phenomena are made possible such as clustering and intergranular segregation of impurities which are of concern for the long-term operation of low-alloy steels.

Table 2: Kinetic energy of and damage energy of primary knock-on atoms versus neutron energy [12]

Neutron Energy *(keV)*	Average PKA kinetic energy (recoil) *(keV)*	Corresponding PKA damage energy *(keV)*
3.4	0.116	0.1
5.8	0.236	0.2
14.0	0.605	0.5
36.0	1.240	1.0
74.0	2.540	2.0
190.0	6.600	5.0
400.0	13.700	10.0
830.0	28.800	20.0
1800.0	61.300	40.0

2.1.1 Displacement cascades

PKA depends strongly on the energy transferred from the neutron to the atom it collides with in the irradiated material. If the transferred energy is greater than the displacement threshold energy of iron, $E_{d(Fe)}$, i.e. 40 eV [13], the PKA will leave its lattice site and move through the lattice with the rest of the transferred energy, also known as recoil energy. The PKA recoil energy will be dissipated by interaction with electrons and collisions with other lattice atoms. At last, it will come to rest as an interstitial atom or by filling up a vacancy created by other local damage events during irradiation.

As the consequence of the movement of PKAs, secondary knock-on atoms (SKAs) are produced and undergo the same mechanism to produce ternary knock-on atoms (TKAs). This whole process will then proceed until the final knock-on atom has a kinetic energy smaller than the displacement threshold energy. This whole process created a damaged volume called a displacement cascade.

2.1.2 Current vision of primary damage

It is important to understand the process of primary damage as it is the mechanism that produces the initial point defects which, later, lead to other irradiation-induced microstructural evolution mechanisms in RPV steels. Due to the short lifetime of each displacement cascade, i.e. picoseconds, and small volumes, on the scale of nanometres, it is very difficult to do direct experimental studies on primary damage. Hence the only way to study this phenomenon is to do modelling and simulation to provide explanations for the microstructural evolution in damaged materials. Details on the techniques developed for modelling and simulation of a displacement cascade can be found in [12], and an example of this kind of simulation is shown in Figure 1 using molecular dynamic codes MOLDY, MDCASK and DYMOKA. In the same simulation, it is shown that when the displacement transferred energy is high enough, one original cascade will split into multiple smaller cascades as shown in Figure 2.

Figure 1 has been removed due to Copyright restrictions.
The original image can be found in the following reference:

Ref. [12] Figure 51. Displacement cascade as simulated by MD in pure iron at 100 K. Cascade damage energy: 15 keV (recoil energy: 21 keV)

Figure 1: Snapshots of a displacement cascade as simulated by molecular dynamics in pure iron at -173 °C. Cascade damage energy of 15 keV; recoil energy of 21 keV [12].

Figure 2 has been removed due to Copyright restrictions.
The original image can be found in the following reference:

Ref: [12] Figure 52. Splitting of a displacement cascade into sub-cascades as simulated by MD in pure Fe at 100 K. Cascade damage energy: 40 keV (recoil energy: 61 keV)

Figure 2: A snapshot of displacement cascade spliting into sub-cascades by using molecular dynamics in pure iron at -173 °C. Cascade damage energy of 40 keV; recoil energy of 61 keV [12].

After the success in simulating displacement cascades, a series of qualitative simulations based on different recoil energies was performed to provide quantitative information on Frenkel pair formation. Figure 3 shows the ratio of surviving Frenkel pairs to the number of generated Frenkel pairs for different PKA recoil energies. The ratio has decreased from 1 to 1.5 for near zero recoil energies and to approximately 0.3 for recoil energies greater than 10 keV. Figure 4 shows the size of the surviving clusters, i.e. vacancy clusters and interstitial clusters formed by fusing multiple Frenkel pairs, in pure iron at different PKA recoil energies.

Figure 3 has been removed due to Copyright restrictions.
The original image can be found in the following reference:

Ref. [12] Figure 54. Energy dependence of the number of surviving point defects relative to the NRT model versus the PKA damage energy.

Figure 3: Energy dependence of the number of surviving point defects to the Norgett Robinson and Torrens model versus the PKA recoil energy [12].

Figure 4 has been removed due to Copyright restrictions.
The original image can be found in the following reference:

Ref. [12] Figure 53. Molecular dynamics simulation - size of surviving point defect clusters in pure iron versus the PKA damage energy at 600 K.

Figure 4: Molecular dynamics simulation on the size of surviving point defect clusters in pure iron versus the PKA damage energy at 527 °C [12].

2.2 FORMATION OF IRRADIATION-INDUCED DEFECTS

As previously stated, the mobility of surviving defects, i.e. Frenkel pairs, produced by displacement cascades remains unknown, but the previous studies show a clear relationship of this mobility to the formation of a series of hardening defects in low-alloy steels [12]. Understanding the mechanisms governing this formation is carried out by comparing modelling with the experimental results presented in Section 2.2.1. It is noteworthy that these mechanisms do not only form hardening defects but also the non-hardening defects presented in Section 2.2.2.

2.2.1 Hardening defects

Mechanisms which control the formation of irradiation-induced defects from displacement cascades are difficult to understand when they involve different phenomena, irradiation parameters and different types of atoms [12, 14-21]. Hence model alloy steels and different types of irradiations were used in previous studies to isolate these parameters and make the analysis simpler. The conclusions of these studies are summarised below [22]:

- 20 HV hardening was observed in neutron irradiated pure iron (neutron fluence of 5.5 x 10^{23} neutrons.m^{-2}, E > 1 MeV) and no hardening effect was observed in electron irradiated specimens (2.5 MeV electrons, electron fluence of 2 x 10^{23} electrons.m^{-2}). This experiment indicates that displacement cascades assist in the nucleation of point defects clusters as electron irradiation only produces isolated Frenkel pairs [12, 22].
- Mechanisms governing solute precipitation were studied after neutron and electron irradiations of binary Fe-Cu alloys steels. This precipitation process is further discussed in section 3:
    i. For copper content ≤ 0.1 wt%, no copper-rich precipitates were found in electron irradiated steels. On the other hand, copper-rich precipitates were

found in neutron irradiated steels. This affirms that the nucleation mechanism of hardening defects in dilute alloys requires the presence of displacement cascade and not just Frenkel pairs [23].

ii. For copper contents > 0.1 wt%, copper-rich precipitates were found in both electron irradiated and neutron irradiated steels at 290˚C. This suggests that isolated Frenkel pairs enhanced the diffusion of copper atoms and encouraged the formation of copper-rich precipitates in high supersaturated alloys.

However, when it comes to actual RPV steels with multiple alloying elements and irradiation parameters, experimental difficulties arise especially in high fluence neutron irradiated low-alloy steels. This is because of a large variety of phenomena and participating types of atoms involved in the data analysis [24].

2.2.2 Structure of the hardening defects

Up until now, three types of neutron irradiation-induced defects and precipitates have been recognised by the nuclear safety authorities and other nuclear related agencies such as the International Atomic Energy Agency (IAEA). These defects have a direct influence on changes in mechanical properties of RPV steels during service and can be summarised as follows:

2.2.2.1 Self-interstitial atom clusters:

Self-interstitial atom (SIA) clusters were observed in previous experimental studies. However the structure of these SIA clusters and SIA dislocation loops are yet to be elucidated [12]. By using numerical simulation, Puigvi et al. [25, 26] and Kuramoto [27, 28] suggested that if SIA clusters are to behave like a SIA dislocation loop, it will require about 160 to 200 SIAs. SIA clusters often nucleate on (110} planes and will transform to a faulted loop nucleus. According to Eyre, Bullough and Perrin [29], SIA clusters moved to their stable configuration through shear reactions.

2.2.2.2 Vacancy clusters:

Simulations showed that in Body Centred Cubic (BCC) crystal structures, small vacancy clusters are more stable in three dimensional configurations. When these small clusters grow to more than 30 vacancies, they will transform to vacancy loops [12]. During this transformation, small vacancy clusters will exhibit fragments of {110} vacancy platelets [30, 31]. Further growth of vacancies clusters, i.e. to about 100 vacancies, will lead to the nucleation of stable {110} vacancy loops ($b = \frac{1}{2} < 110 >$) [12].

2.2.2.3 Solute precipitates:

Figure 5 has been removed due to Copyright restrictions. The original image can be found in the following reference:

Ref. [12] Figure 56 (b) Precipitate of solute atoms obtained by LKMC simulations

Figure 5: Simulated copper-rich precipitate [12]

Nanometre size copper-rich precipitates are the dominant solute cluster in neutron irradiated copper-containing (≥ 0.1 wt.%) low-alloy steels [32]. Figure 5 shows a copper-rich precipitate simulated by using Lattice Kinetic Monte Carlo simulations. Manganese-nickel-rich precipitates with little copper are the dominant precipitates in neutron irradiated low copper containing (< 0.1 wt.%) steels. The formation of these precipitates is discussed further in section 3.

3 PRECIPITATION IN RPV STEELS

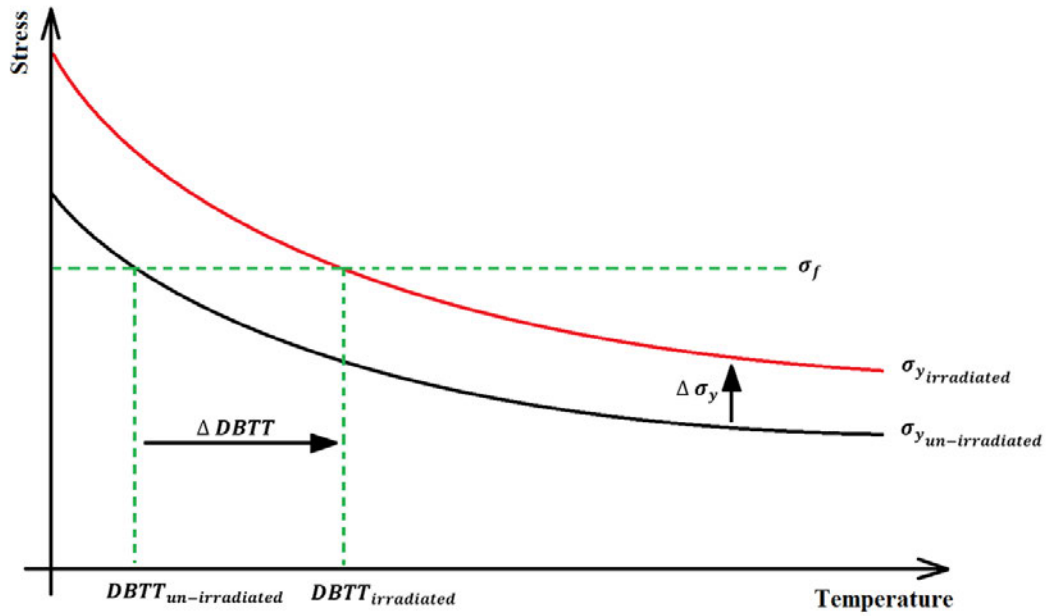


Figure 6: Schematic plot showing the effect of irradiation and/or thermal annealing on the Ductile-Brittle Transition Temperature of low alloy steels. The temperature dependence of yield stress (σ_y) and fracture stress (σ_f) in Body-Centred Cubic metals is also shown.

Precipitation of second phase particles in an alloy is an important hardening mechanism that has been widely studied since the report by Alfred Wilm in 1901 [33]. Many industries, especially aerospace and automotive, have been taking advantage of this hardening mechanism in alloys to achieve the required strength/mechanical properties for different components. However in the nuclear industry, precipitation hardening is a major disadvantage, especially for the lifetime-governing component – the reactor pressure vessel (RPV) of a nuclear power plant (NPP), since as well as increasing the strength of an alloy precipitation hardening generally also increases the ductile-brittle transition temperature (DBTT), as shown in Figure 6. As a result, if the increase of DBTT is severe, the low-alloy steels used to construct RPVs can become brittle even at elevated RPV operating temperatures of 280 ˚C to 360 ˚C. The change of yield strength and DBTT due to precipitation depends principally upon the strength,

structure, spacing, size, shape and distribution of precipitates, as well as on the degree of coherency of the precipitate with the matrix [34]. Hence significant efforts have been focussed on the characterisation of the precipitates formed in low-alloy steels after neutron irradiation and/or thermally annealing.

3.1 PRECIPITATION IN MEDIUM OR HIGH COPPER STEELS

Previous studies have shown that copper in low-alloy steels (with copper concentration of > 0.1 at.%) precipitates from the matrix solid solution as nanometre scale particles after both neutron irradiation at elevated temperatures and simple thermal ageing [35] [36]. These particles are known as either copper-rich precipitates (CRPs) or copper-enriched clusters (CECs). The copper in these low-alloy steels is an impurity introduced to the weld regions from the use of copper coated welding rods/wires in the construction of older reactor pressure vessels. These copper coated welding rods are no longer used for the construction of reactor pressure vessels as a results of the substantial literature on the effects of copper on irradiation sensitivity of low-alloy steels [12, 37-39].

3.1.1 Formation of copper-rich precipitates

3.1.1.1 Solubility

At typical reactor operating temperatures, the concentration of copper, particularly at weld regions of an old reactor pressure vessel, is often well above the solubility limit of copper in iron. The reported solid solubility of copper in iron is 1.6×10^{-4} at.% (1.8×10^{-4} wt.%) at 290˚C [40]. Miller et al. [41] used APT to study the concentration of copper that remained in solid solution in the matrix of a submerged arc beltline weld (where the concentration of copper ranged from 0.18 to 0.28 at.%) after neutron irradiation. This study shows that ≈ 0.05 ± 0.01 at.% of copper remained in solid solution after neutron irradiation to a neutron fluence of 1.1×10^{23} neutron.m^{-2} (E > 1 MeV) at an irradiation temperature of 288˚C [42]. Miller reported that at lower neutron fluences, i.e. ≤ 1×10^{23}

neutrons.m^{-2}, the amount of copper that remained in the matrix was reasonably constant at about 0.1 at.%. The low solid solubility of copper strongly indicates that the formation of CRPs is driven primarily by the large thermodynamic driving force which originated from the super-saturation of copper in iron.

3.1.1.2 Irradiation enhanced diffusion

Precipitates often form more quickly in neutron irradiated materials compared to thermally aged materials. This is because the irradiation increases the diffusivity of solutes by introducing more vacancies and point defects in the matrix. Odette terms this as 'radiation enhanced diffusion', and it is further discussed in Ref. [40]. Odette also suggested that copper precipitation under irradiation is accelerated by the increased diffusivity of copper caused by the radiation induced defects. Odette calculated that the radiation-enhanced diffusion coefficient can be several orders of magnitude higher than that of thermal diffusion.

3.1.1.3 Alloying element effects

Both simulations and experimental results have indicated that nickel and manganese have a strong influence on the formation of copper-rich precipitates in low alloy steels [5, 43]. A higher number density of precipitates is often found in steels that contain higher nickel and manganese concentrations [44]. Cerezo et al. [45, 46] studied the effects of nickel and manganese on copper precipitation using Atom Probe Tomography and simulations. They have shown that nickel and manganese are non-randomly distributed after the initial stress relief heat treatments. Due to this non-randomness, the copper-rich precipitates are then heterogeneously nucleated and grow, as indicated in their simulations. Seko et al. [47] confirmed that nickel and manganese act as catalysts that can lower the activation energy for the nucleation of critical copper-rich precipitates by segregating to the precipitate-matrix interface. The same conclusion is made by Al-Motasem et al. [48] on the effects of nickel on the formation of copper-rich precipitates. They suggested that the effect of nickel is greater

when the precipitate is small due to the surface area effects, i.e. a larger precipitate will require more nickel atoms to cover the surface of the precipitate. Kolli et al. [49] studied the effects of nickel, manganese and aluminium on the interfacial energy of copper-rich precipitation by calculating the energy using the Gibbs adsorption isotherm. The results showed that all of these chemical elements reduce the interfacial energy of a copper-rich precipitate.

Glade et al [44] studied the effect of manganese by comparing neutron irradiated Fe-Cu and Fe-Cu-Mn alloys. They reported that the presence of manganese delays the formation of a high volume fraction of precipitates, but found a higher number density of smaller precipitates in the manganese-containing alloy. Based on their observations, they hypothesised that the inclusion of manganese in the precipitates reduced the matrix-precipitate interface energy and thereby reduced the driving force for the coarsening of precipitates. This was in agreement with the observations reported in Ref. [50]. They also suggested that manganese has a strong interaction with point defects induced during irradiation. As a result, it reduces the overall rate of vacancy diffusion, vacancy clustering and diffusion of copper.

3.1.2 Phase of copper-rich precipitates

The crystal structure of the CRPs and their orientation relationship with the surrounding ferritic matrix has been the subject of many studies to characterise the nature of the nanometre scale precipitates formed in model alloys like binary Fe-Cu [51-53] and more complicated Fe-Cu-Ni/Mn/Si materials [54-58]. As a consequence, these precipitation reactions are relatively well understood. However, it is worth noting that strong synergistic effects have been identified between copper and other alloying elements, particularly nickel and manganese, have been found in real engineering steels, i.e. low-alloy steels with similar chemical composition to those that are currently used as reactor pressure vessels. These synergistic alloying effects arise from the kinetic and thermodynamic interactions of the constituent chemical elements, resulting

in the thermal stability of copper precipitation [59]. These synergistic effects are less well understood, and can have a serious influence on the precipitation mechanisms, and can lead to a significant increase in the measured ductile-brittle transition temperatures [9].

High resolution electron microscopy on both neutron irradiated [60] and thermally aged [56] model alloys have shown that the CRPs undergo a series of crystal structure transformations owing the nucleation and coarsening processes. Studies have suggested that at the nucleation stage the very small metastable copper-rich embryos are Body Centred Cubic (BCC), and are fully coherent with the matrix [61, 62]. As these copper-rich embryos continue to grow and once they reach a critical size, they will transform into Face Centred Cubic (FCC) or Face Centred Tetragonal (FCT) precipitates through 9R and then 3R structures by martensitic transformation [53, 54, 60, 63, 64]. The $BCC \rightarrow 9R$ transformation is preferred for CRPs because these is a better fit between the atomic planes of the 9R structure and the BCC ferritic matrix. Othen, P. J. [65] suggested that the martensitic transformation of $BCC \rightarrow 9R$ is driven by the coherent strain energy induced by the lattice misfit between the BCC CRP and the BCC ferritic matrix. Most of these studies were done on binary or ternary model alloys. Limited evidence is available for the existence of 9R structures in copper-rich precipitates found in real engineering alloys.

3.1.2.1 9R structure

CRPs with the 9R structure were first identified in thermally aged Fe-Cu and Fe-Cu-Ni model alloys by Othen et al. [54]. The 9R structure is a closed-packed layer structure that differs from FCC (or FCT) through the stacking sequence of the closed-packed planes of hexagonal symmetry [56, 64]. It is a structure that is commonly observed following bulk martensitic transformation from the BCC phase in binary copper based alloys that show the shape memory effect [66-68]. 9R describes the symmetry of the

Figure 7 has been removed due to Copyright restrictions.
The original image can be found in the following reference:

Ref. [60] A. C. Nicol, Aspects of copper precipitation and irradiation hardening in Fe-Cu alloys, University of Oxford, Faculty of Physical, Department of Materials, Thesis (D.Phil), 2000.

Figure 7: Schematic diagram showing the lattice deformation of BCC to 9R [60]. A) Atom positions on the close-packed $(009)_{9R}$ *basal planes, A, B, C for the 9R structure. B) BCC lattice from* $[0\bar{1}0]_{BCC}$ *direction. C) 9R lattice (solid lines) viewed from* $[010]_{9R}$ *direction. Dotted lines show corresponding positions in the 9R crystal after the BCC lattice (b) has been transformed into the 9R lattice (reprinted from Ref. [60]).*

unit cell as recorded in Ramsdell's notation [69]. Different notations for describing the close-packed lattices are reported in Ref. [70]. The stacking sequence for a 9R structure is 'ABC/BCA/CAB', as shown schematically in Figure 7. The ideal 9R lattice is orthorhombic with a β_0 angle of 90˚. As a result of this martensitic transformation from BCC to 9R, the lattice vectors $[\bar{1}0\bar{1}]_{BCC}$, $[0\bar{1}0]_{BCC}$ and $[\bar{5}04]_{BCC}$ become $[100]_{9R}$, $[010]_{9R}$ and $[001]_{9R}$, respectively, in 9R co-ordinates [56, 60].

3.1.2.1.1 Stacking fault

Figure 8 has been removed due to Copyright restrictions.
The orginal image can be found in the following reference:

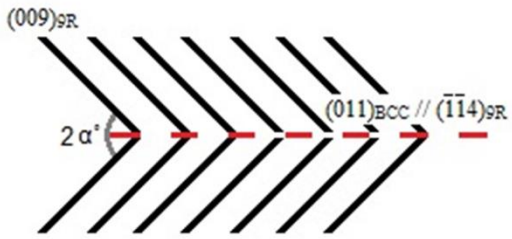
Ref. [71] Figure 1. Stacking faults introduced by single violations of the (+ + -) sequence in the 18R structure.

Figure 8: Schematic representation of the three possible types of stacking faults in a 9R structure. The stacking sequence along the $(009)_{9R}$ basal planes is given for each case (reprinted from Ref. [71]).

Othen [56] has shown that the 9R structure consists of a periodic array of hexagonal stacking faults, one on every third close-packed plane in the perfect FCC stacking sequence. Other studies also showed that additional stacking faults can occur randomly on the $(009)_{9R}$ close-packed/basal planes [56, 60, 72]. Previous studies have shown that these stacking faults in the 9R structure are only visible when viewed in the TEM along $<111>_{Fe}$, and shown a characteristic herring-bone fringe contrast, as shown in Figure 9 (b). It has been reported that cubic, hexagonal and twinning types of stacking faults are theoretically possible in the long period stacking order of 9R structures [71]. These stacking faults are shown schematically in Figure 8. Evidence for the existence of the cubic and hexagonal types of stacking faults have been observed

in the 9R structure of CRP in Fe-Cu [56, 73], Fe-Cu-Ni [56], Fe-Cu-Si [57] and Fe-Cu-Mn-Ni-Al [74] multi-component ferritic alloys. The cubic or hexagonal stacking faults in the 9R structure produce a fringe spacing of four or two layers respectively at the position of the stacking fault [56]. No evidence has yet been found for the existence of twin type stacking faults.

a)



b)

Figure 9 (b) has been removed due to Copyright restrictions.
The original image can be found in the following reference:

Ref. [73] Figure 1.HRTEM image of a twinned 9R copper precipitate in an Fe-Cu specimen aged at 550°C. The angle a between the $(009)_{9R}$ basal and the $(-1-14)_{9R}$ twin planes is 61˚.

Figure 9: (a) Schematic diagram showing a 9R structure in the BCC matrix along $< 111 >_{Fe}$ (b) High resolution micrograph of a twinned 9R CRP in an Fe- 1.5 wt.% Cu alloy thermally aged at 550˚C for 8-350 hours imaged along $< 111 >_{Fe}$ (reprinted from Ref. [73]). The angle α between the $(009)_{9R}$ basal and the $(1\bar{1}4)_{9R}$ twin planes is 61˚.

3.1.2.1.2 Twinning

The 9R structure is often found to be twinned. It is believed that this twinning minimises the shape deformation caused by the martensitic transformation [54, 60, 75]. The banded appearance of a 9R precipitate under an electron microscope, as shown in Figure 9 (b), is due to the twin-related variants, and this is confirmed by molecular dynamics simulations [76]. A model developed by Kajiwara, S. [77] has allowed us to predict the observed orientation relationship between the 9R structure and the BCC matrix should be $(011)_{BCC}//(\bar{1}\bar{1}4)_{9R}$ and $[1\bar{1}1]_{BCC}//[\bar{1}10]_{9R}$, as shown in Figure 9 (a). The angle α between the herring-bone fringes in adjacent twin bands, i.e. between the $(009)_{9R}$ basal planes and $(\bar{1}\bar{1}4)_{9R}$ twin planes, is predicted to be approximately 64.5˚.

The number of twin segments in the 9R copper precipitates is dependent on the size of the precipitate [53].

3.1.2.1.3 Relaxation of the 9R structure

Previous studies by Monzen et al. [53] and Nicol et al. [60] have shown that the angle α will decrease with the increase of precipitate size during thermal annealing and electron irradiation. One of the many examples available is shown in Figure 9 (b); in this case the angle α is 61˚. Monzen et al. [53] also showed that the average change of angle α is temperature dependent. For example at an annealing temperature of ≈ 230˚C, the average change of α is ≈ 3˚. This rotation of the $(009)_{9R}$ basal planes toward the $\{110\}_{Fe}$ matrix planes is believed to correspond to a relaxation of the twinned 9R structures and is associated with a relief of elastic stresses produced by the $BCC \rightarrow 9R$ martensitic transformation [60]. By considering the driving force for these rotations, Monzen et al. [53] concluded that the elastic strains relax by atomic diffusion along the interfaces between the iron matrix and copper precipitates.

Slight differences were observed between the rotation of $(009)_{9R}$ planes induced by thermal annealing and electron irradiation. Monzen et al. [53] reported that the $(009)_{9R}$ plane rotation induced by thermal annealing took place without the 9R precipitate first un-twinning and before the removal of the regular stacking faults. For electron irradiation, Nicol et al. [60] reported that the $(009)_{9R}$ planes rotated and de-twinning occurred simultaneously. This difference might be a result of the atomic displacement and/or Frenkel pairs induced by the electron irradiation [78, 79].

3.1.2.2 3R structure

Othen et al. [56] provided indications that copper precipitates larger than 15 nm undergo a second transformation to an FCC structure possibly via a more stable 3R structure. A partially transformed 3R copper-rich precipitate is shown in Figure 10. Direct evidence was shown by Monzen et al. [73] that 3R is a non-cubic structure

obtained when the regular stacking faults on the $(009)_{9R}$ basal planes are removed and resulting in $(003)_{3R}$ basal planes that retain the spacing characteristic of $(009)_{9R}$ basal planes. The angle α between $(003)_{3R}$ and $(011)_{Fe}$ (or $(\bar{1}\bar{1}4)_{9R}$) is the same as the α for a relaxed 9R structure, i.e. 61˚. It is important to note that little is known about when the transformation of the $9R \rightarrow 3R$ structure occurs.

Figure 10 has been removed due to Copyright restrictions.
The original image can be found in the following reference:

Ref. [73] Figure 2. HRTEM image of a partially transformed precipitate. The structure of the upper region is 9R, while the lower region is 3R.

Figure 10: HRTEM image of a partially transformed precipitate. The structure of the upper region is 9R and the lower region is 3R (reprinted from Ref. [73])

3.1.2.3 FCC or FCT structures

Monzen et al. [73] showed that the transformation to FCC or FCT can occur without complete de-twinning of the copper-rich precipitates. Large over-aged copper precipitates are FCC or FCT with a Kurdjumov-Sachs (K-S) orientation relationship to the BCC iron matrix. Othen et al. [56] speculated, and this was agreed by Monzen et al. [73], that the heavily distorted 3R structure is responsible for the FCT copper-rich precipitates. The FCT structure has larger lattice parameter values than bulk FCC copper. The FCT structure has a lattice constant a = b = 0.369 nm and c = 0.366 nm and the bulk FCC copper lattice constant is a = 0.361 nm [73]. At this stage, the FCC

or FCT copper-rich precipitates with an overall diameter $\geq \approx 30$ nm are rod-like or elliptical in shape, having a direction of growth along <110>$_{Cu}$ [73, 80].

3.1.2.4 Intermediate structure between 3R and FCC/FCT structure

a)

Figure 11 (a) has been removed due to Copyright restrictions.
The original image can be found in the following reference:

Ref. [73] Figure 4(a) HRTEM image of a precipitate which consists of two variants with fcc and fct structures.

b)

Figure 11 (b) has been removed due to Copyright restrictions.
The original image can be found in the following reference:

Ref. [60] A. C. Nicol, Aspects of copper precipitation and irradiation hardening in Fe-Cu alloys, University of Oxford, Faculty of Physical, Department of Materials, Thesis (D.Phil), 2000.

Figure 11: Intermediate structure between 3R and FCC/FCT. (a) twinned structure (reprinted from Ref. [73]) and (b) un-twinned structure (reprinted from [60]).

The martensitic transformation of copper-rich precipitates from 3R to FCC is rather complicated. Intermediate structures were observed from 3R copper-rich precipitates during/after thermal aging [81] and electron irradiation [60, 72]. These intermediate structures, either twinned or un-twinned, showed W shaped fringes, as shown in Figure 11. Monzen et al. [73] showed that the segments of C and T, as labelled in Figure 11 (b), show W-shaped diffuse fringes formed by interference between the $10\bar{1}_{Fe}$ and $\bar{1}\bar{1}1_{Cu}$ reflections and the 110_{Fe} and $11\bar{1}_{Cu}$ reflections respectively. The angle α between the C and T diffuse fringes is ≈ 68˚. They suggest that these lattice fringes correspond to (111)$_{Cu}$ planes that originated from the $(\bar{1}\bar{1}4)_{9R}$ twin plane and the $(009)_{9R}$ basal plane [73].

3.1.3 Triggers for the martensitic transformations

Extensive studies have been performed to understand the cause of the martensitic transformation of copper-rich precipitates from $BCC \rightarrow 9R \rightarrow 3R \rightarrow FCC/FCT$. Previous studies have shown that the martensitic transformation from BCC to 9R structure

depends on the ambient temperature [73]. Also, modelling and simulation and further experiments show that apart from thermal annealing that allows the copper-rich precipitates to grow to a critical size for the martensitic transformation to the 9R structure, this transformation can also be triggered by interactions with dislocations [82-85] and by irradiation [60, 72].

3.1.3.1 Ambient temperature

Figure 12 has been removed due to Copyright restrictions.
The original image can be found in the following reference:

Ref. [64] Figure 3. Diagram representing the structure of Cu precipitates as a function of temperature and size. The light colored regions next to the phase transition line delineate the extend of the hysteresis. The hysterectic critical point is located along the dashed line between 200 and 300 K. The experimental data points are from Ref. [21].

Figure 12: Diagram representing the structure of copper-rich precipitates as a function of temperature and size (reprinted from Ref. [64]). The experimental data points are from Ref. [53].

Monzen et al. [53] have shown experimentally that the critical precipitate size at which the $BBC \rightarrow 9R$ martensitic transformation occurs depends on the ambient temperature, and can be identified by measuring the angle α between the $(009)_{9R}$ basal plane and $(\bar{1}\bar{1}4)_{9R}$ twin plane. Erhart and Sadigh [64] have used a combination of molecular dynamics and Monte Carlo simulations as well as empirical interatomic potentials to understand the correlation between the copper-rich precipitate structure and size as a function of temperature for the martensitic transformation from BCC to 9R. They have

suggested that the martensitic transformation is reversible, i.e. $BCC \leftrightarrow 9R$. The results of their study are shown as Figure 12, and show a reasonably good agreement with the experimental results obtained by Monzen et al. [53].

3.1.3.2 Dislocation interactions

Molecular dynamics (MD) simulations suggest that the martensitic transformation to an FCC-based structure can be triggered by dislocation passing through the BCC copper-rich precipitates [82-85]. MD simulations also suggested that the mechanism of dislocation-precipitate interactions in iron depends on the size of the precipitate. Bacon and Osetsky [85] suggested that precipitates with a diameter of less than 3 nm will simply be sheared by a dislocation. Lozano-Perez et al. [86] performed both in-situ and ex-situ straining experiments on a Fe-1.3 wt.% Cu alloy that had been thermally aged at 550˚C for 3 hours. They have shown that 9R structures were observed on copper-rich precipitates that were as small as 3nm in the strained/deformed sample compared to copper-rich precipitates that are above 5nm in the unstrained/deformed sample. This observation shows a good agreement with the results from MD simulations.

3.1.3.3 Irradiation

Previous studies have shown that the irradiation can increase the kinetics of the formation of copper precipitates and trigger the martensitic transformation from $BCC \rightarrow 9R \rightarrow 3R \rightarrow FCC\ or\ FCT$. This is because Frenkel pairs that are created in the lattice during irradiation enhance the diffusion rate of copper in the ferritic matrix. Nicol et al. [60] reported that those martensitically transformed copper-rich precipitates found in irradiated Fe-1.3 wt.% Cu are much smaller than those observed in the same alloy but thermally aged at the same temperature, i.e. smaller than the critical size for temperature dependent martensitic transformation at a respective temperature [60, 62]. Similar phenomena have been seen in other alloys. Sato et al. [78] showed using HRTEM that irradiation-induced defects migrate to a spherical coherent γ-iron precipitate in a copper matrix to reduce the elastic strain. These observations may be

due to the incorporation of vacancies in the precipitates and/or to the nucleation of small dislocation loops at the precipitate matrix interface, as suggested by the authors of Refs. [60, 62]. As a result, copper-rich precipitates may transform to 9R more readily under irradiation.

3.1.4 The chemical composition of copper-rich precipitates

Previous Atom Probe Tomography studies on thermally aged and neutron irradiated samples have shown that the chemical composition of the precipitates are directly associated with the alloying elements and impurities present in the low alloy steel. A core-shell like structure is often observed in multicomponent steels that contain copper at a concentration of greater than 0.1 at. % [10, 46, 87, 88]. Both the composition of the core and shell is affected by the environmental condition that the material is subjected to, i.e. the conditions of thermal ageing [89] and/or irradiation [90].

It is important to note that an accurate determination of iron concentration in copper-rich precipitates has been a long running issue for Fe-Cu based alloys. This is because of the widely different concentrations of iron detected using different techniques such as Small Angle Neutron Scattering (SANS) [91], Atom Probe Tomography (APT) and Energy Filtered Transmission Electron Microscopy (EFTEM) [92]. Note that the concentration of iron obtained by APT is controlled by artefacts induced by the preferential evaporation, 3D reconstruction errors and cluster analysis [35, 89]. This issue is further discussed in Refs. [35, 93].

Based on these APT studies, the precipitate core is copper-rich with some iron content, particularly for those precipitates that are formed under irradiation, as discussed in section 3.1.5.3.

An EFTEM study on multicomponent low-alloy steel weld materials by Lozano-Perez et al. [92] reported that two groups of copper-rich precipitates were detected, one which is virtually iron-free and one which contains around 25 -40 at.% of iron. Based on this

observation, they hypothesised that the iron concentration in each copper-rich precipitate is influenced by its crystal structure, i.e. the BCC, 9R, 3R, FCC or FCT structures that these precipitates can have. They suggested that the differing crystal structures of these copper-rich precipitates can accommodate different amounts of iron, but they made no comment regarding the size of the precipitate and the respective concentration of iron. This hypothesis is supported by a thermodynamic modelling study predicting the composition of copper-rich precipitates in binary Fe-Cu alloys by Kozeschnik [94]. The model predicts that the smaller copper-rich precipitates contain a large proportion of iron, especially in alloys that contain a higher concentration of copper. As these precipitates continue to grow, the iron concentration reduces, so that the larger precipitates (2 – 4 nm in diameter) contain very little iron. In addition, the model implies that the copper concentration of the critical nucleus will be higher in a less saturated condition and at a higher temperature of thermal annealing.

The same type of low-alloy steel weld as studied by Lozano-Perez et al. [92] has also been studied by Morley [89] using APT. He also reported that the concentration of iron in the copper-rich precipitates are 17 at.% and 7 at.% after thermal ageing at 330 °C and 405 °C respectively. These temperature effects on the concentration of iron in the precipitates is in agreement with the modelling results by Kozeschnik [94], and similar a study on different thermally aged Fe-Cu alloys by Pareige et al. [95]

In multicomponent Fe-Cu based steels, the chemical elements found in the shell of the copper-rich precipitates is strongly dependent on the concentration of alloying elements and impurities. So far, the reported elements that segregate are nickel, manganese, silicon, aluminium and phosphorus. Many studies have suggested that the shell is formed due to the segregation of solutes during the nucleation process, as further discussed in Section 3.1.4.1 and Section 3.1.1.3.

3.1.4.1 The segregation of alloying elements and impurities to copper-rich precipitate interfaces

In multicomponent Fe-Cu based steels, the segregation of alloying elements and impurities at the matrix-precipitate interfaces is shown both in experiments and through modelling. Simulations of the precipitation of copper in Fe-Cu-Ni, Fe-Cu-Mn and Fe-Cu-Ni-Mn alloys have all shown that nickel and manganese segregate at the precipitate-matrix interface [96, 97]. These simulations suggest that nickel segregation to the interface occurs at a faster rate than manganese segregation. Koyama et al. [97] used the phase-field simulation method to include the structural phase transformation of copper precipitates into their simulation. The results are in good agreement with other simulations, but also show that the manganese appears to segregate to the precipitate-matrix interface after the copper-rich precipitate is martensitically transformed from the BCC to FCC structure. It is useful to note that these authors made the assumption that the copper-rich precipitates transformed from BCC to FCC, whereas the consensus is that it occurs from the BCC structure through to 9R, 3R and then to the FCC structure.

Experimental studies of Fe-Cu based alloys found nickel and manganese at the precipitate-matrix interface of copper precipitates in agreement with simulation results [35, 46, 89, 98, 99]. A study of a Fe-Cu-Ni steel after both thermal ageing and neutron irradiation conducted by Pareige et al. [95] showed that nickel was present at the matrix-precipitate interfaces in both materials. They suggested that nickel was involved in the early stages of the copper precipitation process. It is during growth and coarsening that the nickel is then rejected from the copper-rich precipitate. Isheim et al. [100] studied a thermally aged copper-containing low carbon steel. They also found that nickel and manganese segregated around the copper-rich precipitates, and also observed sharpening of the interface and as increase in nickel and manganese concentration with thermal ageing time.

Apart from nickel and manganese, the segregation of aluminium at the copper-rich precipitate-matrix interface is also reported in Refs. [101, 102]. Similarly, in an observation by Isheim et al. [100], the segregation of aluminium also increases with ageing time. The segregation of tin, present as a trace impurity, is reported to be segregated at the copper-rich precipitate-matrix interface [103]. The authors only observed this interfacial segregation at large copper-rich precipitates. They suggested that the segregation of tin is driven by the high number of sites for large solute atoms available at the precipitate-matrix interface.

3.1.5 Differences between neutron irradiation-induced and thermally aged copper-rich precipitates

3.1.5.1 Structural results

Observations have shown that the copper-rich precipitates found in neutron-irradiated materials (i.e. in Fe-Cu based model alloys) are different to those found in thermally-aged or electron-irradiated samples [60, 62, 72, 104]. As previously mentioned in section 3.1.3.3, neutron irradiation induces martensitically transformed 9R copper-rich precipitates in Fe-Cu alloys that are much smaller than those found in the thermally-aged and even electron-irradiated samples at the same temperature, e.g. 280°C [60]. The precipitates observed are generally below 4nm even at relatively high neutron fluence [60, 62]. This lack of coarsening is a result of the high energy cascades produced by fast neutrons. High energy cascades can cause partial disintegration/dissolution of larger precipitates as suggested by Calder and Bacon [105] using molecular dynamic (MD) modelling. These MD simulations have shown that the extent of damage inflicted on the precipitates appear to be a function of the degree of overlap of the cascade core at the end of the ballistic event of the displacement cascade, i.e. time of peak atom displacements. The following are significant events that were observed from the simulations when a considerable overlap between a cascade induced by a fast neutron and a copper-rich precipitate.

- Size of the copper-rich cluster is reduced due to the loss of copper atoms.
- The rearrangement of copper and iron atoms at the matrix-precipitate interface changes the shape of the precipitate
- Vacancies accumulate in the copper-rich precipitates and at the matrix-precipitate interface.
- Interstitials are sometimes trapped in the copper-rich precipitates.

Experimental results indicate that an increase in neutron fluence increases the number of un-twinned copper-rich precipitates in a sample [60]. This may be caused by de-twinning induced by irradiation, as similar observations have been reported from an in-situ electron irradiation experiment performed by Nicol et al. [60]. Most of these precipitates have a relaxed 9R structure, i.e. the angle α is less than 64.5°; with an average α of about 62.5°. Buswell et al. [62] suggested this may be due to the interaction of neutron irradiation-induced matrix defects with copper-rich precipitates by decreasing the critical size at which the 9R transformation take place. As a result, angle α of these precipitates is reduced, and so is the strain within the precipitates. It is important to note that very little evidence from electron microscopy work is available on the irradiation-induced precipitates in real engineering steels, i.e. multicomponent steels. This has been suggested to be an extremely difficult task due to the nature of these precipitates, i.e. very low strain field and nanometre scale (diameter of < 4 nm) [106].

3.1.5.2 Size and number density

Experimental results have shown that copper-rich precipitates formed under neutron irradiation and those formed thermally have a different size and number density for the same material. The precipitation process under thermal annealing occurs in following stages, nucleation, growth and coarsening [49]. Smaller precipitates with a higher number density are first observed in the nucleation stage. Bigger precipitates with a lower number density are then observed in the growth and coarsening stages. These

precipitates grow by consuming those that are less stable, i.e. smaller precipitates by Ostwald ripening, and eventually this leads to over-ageing [107]. Under neutron irradiation, the number density of these precipitates is significantly higher and smaller in size. Even though the size of the precipitate increases with neutron fluence, there is a little or no evidence found for the coarsening and over-ageing of precipitates in neutron irradiated multicomponent Fe - (low) Cu based steels even at high neutron fluence, i.e. $\phi t \geq 1 \times 10^{23}$ neutrons.m^{-2}; $\phi t < 1 \times 10^{25}$ neutrons.m^{-2} [108-110].

3.1.5.3 Chemical composition

Atom Probe Tomography (APT) is able to characterise nanometre scale precipitates that have a much wider range of chemical compositions in irradiation-induced copper-rich precipitates than those formed thermally [87, 111]. The common chemical elements that have been detected in both thermally aged and irradiated low-alloy steels are copper, manganese, nickel and silicon. In irradiated steels, phosphorous is often detected in/at the precipitates using APT [112, 113]. The copper concentration of irradiated precipitates is found to be generally lower than those found in thermally aged materials. Also, a higher concentration of iron is detected in precipitates formed under irradiation [35]. This observation could be related to the irradiation-induced precipitation as discussed in Refs. [114, 115].

A comparison between the composition of precipitates in irradiated and thermally aged samples was made by Hyde et al. [90] from a high nickel and a low nickel weld containing about 0.4 at. % copper. They have not found evidence for any differences in the solute distribution within the precipitates formed under irradiation or thermal ageing, i.e. precipitates of copper enriched cores with nickel, manganese and silicon around the edges of these cores were found in both cases. In term of overall chemical composition, they found lower copper and higher manganese concentrations in precipitates formed under irradiation than those formed by thermally ageing in the low nickel weld.

3.2 PRECIPITATION IN LOW COPPER OR COPPER-FREE STEELS

Manganese and nickel-rich precipitates (MNPs) were detected in low copper concentration (< 0.1 at. %) and/or copper-free low-alloy steels. This phase was first predicted by Odette [116] using computational simulations [1, 4, 114] and was later confirmed by experimental results, as reported in Refs. [111, 117, 118]. Note that the prediction of the formation of MNPs was based on the operating conditions of the reactor pressure vessel in a pressurised water nuclear fission reactor, i.e. low neutron flux irradiation at a typical RPV operating temperature (≈ 285 °C).

Lattice Monte Carlo modelling [5] indicates that these MNPs will be formed in a steel with a low copper and a high nickel content at a lower irradiation temperatures at high neutron fluences after a long incubation time. It is important to note that the author does not explain or provide any definition of 'low' temperature or the threshold for 'high' fluence. Thermodynamic-kinetic models also suggest that the precipitation of this manganese and nickel-rich phase has a lower nucleation rate compared to copper-rich precipitates [9]. Odette categorises this MNP as an irradiation-enhanced phase due to slow formation kinetics under thermal ageing conditions. Moreover, the simulations indicate that it is thermodynamically favourable for MNP to nucleate heterogeneously at the copper-rich precipitate-matrix interface.

Experimental studies have reported the existence of MNPs in neutron irradiated low copper welds and plate types of low-alloy steels. These MNPs are often enriched with high concentrations of manganese, nickel and silicon, with a relatively low concentration of copper. This type of MNP is also known as MnNiSi(Cu)-rich precipitates. APT studies also reported that these MNPs formed under irradiation also contain a significant amount of iron (> 50 at.%) [119], some of this iron could be the artefact induced by APT analysis. Pareige et al. [120, 121] reported that the APT analysis of concentration profiles of MnNiSi(Cu)-rich precipitates in neutron irradiated low copper steels is unable to provide clear evidence for the existence of a core-shell

structure, i.e. a copper-rich core with a manganese and nickel-rich shell. However, this APT analysis shows that the copper-rich region does not coincide precisely with the regions that are manganese and nickel-rich. Similarly, Miller et al. [10] performed a similar analysis on neutron irradiated high nickel, low copper steels. They reported that, by using a different set of APT-clusters identification analysis parameters, copper-rich cores and manganese and nickel shells could be identified. They also claimed that the core-shell type of MnNiSi(Cu)-rich precipitates were present in the low-alloy steel with a copper concentration greater than 0.05 at. %. This value was obtained by measuring the copper concentration in the remaining in the matrix after neutron irradiation up to 1.1×10^{23} neutrons.m^{-2} (E > 1MeV). It is important to note that it is possible for these MnNiSi(Cu)-rich precipitates to form in low-alloy steels under thermal annealing alone. Styman [35] reported that a MnNiSi(Cu)-rich precipitate was detected along a grain boundary in a high copper, high nickel weld steel thermally aged for 50, 000 hrs at 365 °C. This MnNiSi(Cu)-rich precipitate has a copper core and manganese, nickel and silicon-rich shell.

MNPs were also observed in copper-free steels after neutron irradiation. Meslin et al. [122] studied Fe-1.1 at.% Mn-0.7 at.% Ni alloys that had been neutron irradiated up to 1.8×10^{23} neutron.m^{-2} and 1.3×10^{24} neutron.m^{-2} at an irradiation temperature of 300 °C. They reported a high number density of MNPs in both materials. In addition, they showed that the average manganese concentration of these MNPs increased with an increase of neutron fluence, but the average concentration of nickel remained rather constant.

Malerba et al. [114, 123] studied the kinetics of nucleation of MNPs using first principles-based Atomistic Kinetic Monte Carlo (AKMC) simulation. The simulations suggested that MNPs formation is often associated with self-interstitial atoms (SIAs). Apart from copper being the catalyst for the formation of MNPs in low-alloy steels [2, 124], these simulations also indicate that SIAs can act as the nucleating site for MNP.

The thermodynamic model suggests that the presence of SIA clusters stabilises the formation of MNP. As a result lower saturations of manganese and nickel are required for the precipitation of MNP. Furthermore their simulation suggests that the kinetic mechanism for the formation of MNP is self-interstitial migration leading to a local accumulation of manganese, while the formation of copper-rich precipitates was by substitutional diffusion.

It is important to note that even though these MNPs have been shown to exist in a variety of different alloys, our understanding on the effect of these precipitates on the hardening and embrittlement of low-alloy steels at high neutron fluences, $\phi t \geq 5 \times 10^{23}$ neutron.m^{-2} is still limited. Additionally, the detailed conditions leading to the precipitation of MNPs is still lacking. In order to understand the hardening effect of these MNPs, it is important to obtain information on the structure and shape of these precipitates to understand the degree of coherency of these precipitates with the matrix, and their precipitation behaviour, i.e. growth and coarsening.

4 EXPERIMENTAL MATERIALS & METHODS

This chapter gives details on the materials analysed in this project. It also includes details of how the transmission electron microscopy (TEM) specimens were prepared and their storage requirements so that they were suitable for analysis under an electron microscope. This chapter also provides information on the electron microscopy techniques used for the analysis of irradiation-induced defects and nanometre scale solute clusters.

4.1 MATERIALS BACKGROUND

Low alloyed ferritic steels, also known as reactor pressure vessel (RPV) steels, that have been analysed in this project are commercial grade ferritic steels. These steels are the same as and/or similar to those used to build reactor pressure vessels (RPV) for pressurised water reactors (PWRs) and light water reactors (LWRs) types of nuclear fission power plants (NPPs).

These steels have been subjected to neutron irradiation to study the effects of irradiation-induced embrittlement at high neutron fluence. Also, a similar steel have been subjected to a long term thermal annealing to study the nanometre scale precipitates that have nucleated and grown during the process. Previous studies have proposed that these thermally aged precipitates are to be similar of those nucleated in neutron irradiated steels [2, 56, 125]. The RPV steels that have been investigated in this project are summarised in Table 3. The chemical composition of all 3 RPV steels is detailed in Table 4.

These RPV steels investigated are weld metals. The manufacturing processes of these RPV steels are identical to that used in the industry that casts and welds RPVs. The full detail of the manufacturing processes of these RPV steels are not fully presented in the LONGLIFE project nor is it well documented in any of the reports available.

The weld metals, ANP-2 and ANP-6, investigated in this project are produced from original wires and flux used for 'real' RPV steels and prepared via submerged arc welding, as per procedures used for the RPV. The WV weld metal is also prepared via submerged arc welding. The wire and flux used to fabricate WV weld metal are not reported. The temper and stress relief treatments for RPV steels investigated are presented and recorded in Table 5.

Table 3: List of RPV steels that have been investigated in this project

Reference Code	Organisation	Description	Type of Mat.
ANP-2	ANP-G	Weld Metal; S3NiMo1	Neutron Irradiated
ANP-6	ANP-G	Weld Metal; S3NiMo	Neutron Irradiated
WV	RRs	Weld Metal; A533B/ A302B	Thermally annealed

Table 4: Chemical compositions of RPV steels that have been investigated

Ref. Code	Chemical composition (at.%)											
	Cu	Ni	Mn	Si	P	S	Cr	Mo	V	C	Oth.[1]	Fe
ANP-2	0.026	0.961	1.097	0.239	0.034	0.016	0.107	0.361	0.011	0.239	0.037	Bal.
ANP-6	0.070	1.606	1.432	0.298	0.022	0.012	0.075	0.267	0.004	0.298	0.066	Bal.
WV	0.440	1.660	1.380	0.750	0.018	0.054	0.054	0.240	0.006	0.190	0.027	Bal.

Table 5: Manufacturing and heat treatment data of RPV steels that have been investigated

Reference Code	Welding Process	Wire	Powder	Manufacturer	Heat Treatment
ANP-2 (WM)	SAW	S3NiMo1	OP41TT	MAN GHH Sterkrade AG	Stress relief heat treated 550˚C/10hrs – 600˚C/20hrs/air cooling
ANP-6 (WM)	SAW	S3NiMo	OP41TT/ A 2	Uddcomb Sweden AB	Stress relief heat treated 550˚C/10hrs – 600˚C/10hrs/air cooling
WV (WM)	SAW	-	-	Rolls Royce	Post weld heat treatment: Annealed at 920˚C/6hrs – water quenched – tempered 600˚C/42hrs; Stress relief heat treated 650˚C/6hrs – ≤50˚C/hr slow cooling

Table 6: Irradiation conditions and heat treatments of RPV steels that have been investigated

Ref. Code	Condition	ϕ (n.m^{-2}.s^{-1}; E>1MeV)	ϕt (n.m^{-2}; E>1MeV)	$T_{irr.}$ (˚C)	Duration of Irra./ HT (hrs)
ANP-2	As-received	-	-	-	-
	Neu. Irradiated	2.33 x 10^{16}	4.97 x 10^{23}	285 ± 5	5,925
ANP-6	Neu. Irradiated	2.41 x 10^{16}	5.22 x 10^{23}	290 ± 10	5,918
WV	Heat treated	-	-	365 ± 5	18,620
	Heat treated	-	-	365 ± 5	49,800

4.1.1 Neutron implantation

The investigated RPV steels that have been neutron irradiated are provided by AREVA NP GmbH (ANP-G) for the LONGLIFE project. These steels have been neutron irradiated to high neutron fluences (ϕts), specially, for the study of irradiation-induced embrittlement of RPV steels. The range of neutron fluences that LONGLIFE was interested in is similar to or above the neutron fluence of RPV steels from NPP with operating lifetime of 60 or 80 years, i.e. $1x10^{23}$n.m^{-2} < ϕt < $1 x10^{24}$n.m^{-2}, depending on the region measured in a RPV of a NPP.

4.1.1.1 ANP-type weld metals

The ANP-type weld metals were neutron irradiated in the 1980 s at a German experimental NPP in Khal (VAK), with a neutron spectrum comparable to that found in commercial PWRs manufactured by Siemens/KWU in Europe, albeit at a higher flux.

Our primary interest in these materials are the relative differences in their chemical composition, especially the nickel content, and mechanical property changes at high neutron fluence. It is good to note that ANP-6 weld metal has a nickel content comparable to the highest reported nickel content of Westinghouse PWR weld metals (i.e. ≈ 1.60 at%) [10]. It's nickel content is greater than the highest reported nickel content in the U. S. Nuclear Regulatory Commission Regulatory Guide 1.99, Rev. 2 (i.e. 1.20 wt% or ≈ 1.10 at% of nickel) [126].

The changes in the mechanical properties of the ANP-6 weld metal after irradiation were consistent with those seen in Ringhals RPV weld metals of similar nickel content, as reported in Ref. [127]. The Charpy 41-J transition temperature shift (TTS) in surveillance testing for ANP-6 weld metal, as reported in Ref. [128], showed a temperature shift ΔT_{41J} ≈ 180˚C at neutron fluence, $\phi t \approx 5 \times 10^{23}$ n.m^{-2}. This temperature shift is considered very high and is indicating that this steel has very high radiation sensitivity despite its low copper content (> 0.1 wt% of copper content).

The Charpy 41-J transition temperature shift in surveillance testing for ANP-2 weld metal, as reported in Ref. [128], showed a temperature shift ΔT_{41J} ≈ 40˚C at neutron fluence, $\phi t \approx 5 \times 10^{23}$ n.m^{-2}. This temperature shift is comparatively lower than others reported for RPV weld metals with similar chemistry that have been neutron irradiated to comparable neutron fluence [127-129]. It should also be noted that the data from ANP-2 weld metal reported in Ref. [128] show that no significant transition temperature shift was observed at a neutron fluence of ≈ 1 x 10^{23} n.m^{-2}. This observation could be

interpreted as an evidence of the 'late-blooming effect' or 'slow-growing effect' [1, 129]. However, the uncertainties in mechanical property measurements must be considered.

Both neutron irradiated weld metals, ANP-2 and ANP-6, are of great interest in the LONGLIFE project. This is because the mechanical properties of the weld metals change as a result of neutron irradiation, particularly for ANP-2. Also, their differences in chemical composition could help explain the role of Ni, Mn and Si in the formation of irradiation-induced solutes clusters. Note that in the later chapters, much effort has been focused on the irradiated microstructural analysis of the ANP-2 and ANP-6 RPV steels.

Table 7: Charpy data of neutron irradiated ferritic steels that have been investigated. The data is taken from Ref. [128].

Ref. Code	ϕ ($n.m^{-2}.s^{-1}$; E>1MeV)	ϕt ($n.m^{-2}$; E>1MeV)	T_{41} °C (Best-fit average curves)	ΔT_{41} °C
ANP-2	0	0	-7	0
	3.53×10^{16}	1.36×10^{23}	-7	0
	2.33×10^{16}	4.97×10^{23}	31	38
ANP-6	0	0	-55	0
	1.07×10^{16}	4.14×10^{22}	-15	40
	3.01×10^{16}	1.16×10^{23}	12	67
	2.45×10^{16}	5.22×10^{23}	123	178

4.1.2 Thermally annealing or ageing

The WV weld metal is thermally aged in an in-house small-scaled furnace separately for a long period of time, at a temperature that is comparable with the NPP operation temperature experienced by RPV. This long period of thermally aging, i.e. > 18,000 hours, allows solutes and/or impurities to decompose from the ferrite matrix of these steels and allows nanometre scale precipitates to nucleate homogeneously throughout the sample. The chemical composition and details of the manufacturing process and stress-relief heat treatment for the weld metal are presented and shown in Table 4 and Table 5 respectively.

4.1.2.1 WV weld metal

The WV weld metal is supplied by Roll Royce and Associates Limited (RRs) with heat treatments initiated by Dr. S. Hirosawa and further thermally aged by Dr. A. Morley. This weld metal has been thermally aged up to a duration of 49,800 hours followed by quenching with water. The thermal ageing of this weld metal was carried out in sealed quartz tubes under an argon gas atmosphere at 365˚C. Note that the thermally ageing temperature used for this sample is higher than the typical in-service operating temperature, i.e. ≈ 290˚C, experienced by RPV steels. The reason a temperature of 365˚C was chosen for thermally ageing of this weld metal is to promote and increase the kinetic processes of the precipitation of alloying elements while maintaining the underlying thermodynamic regime of precipitation of alloying elements that are similar or comparable to that experienced by an in-service reactor.

The solid solubility of nickel [130, 131] and manganese [132] is reasonably consistent over a temperature range from 290˚C and 405˚C. Note that both the solubility of nickel and manganese in iron is taken into the consideration in this experiment because both these chemical elements are thought to affect the kinetic process of the precipitation in RPV steels [133]. Hence thermally ageing WV weld metal at 365˚C allows us to compare the literature, microstructural data available for in-service operating temperature with reasonable confidence. It is worth noting that the precipitation mechanism in thermally aged RPV steel is significantly different compared to the neutron irradiated RPV steel.

The thermally aged WV weld metal is chosen for transmission electron microscopy (TEM) study on nanometre-scaled precipitates because of the precipitates nucleated and grown in this metal. The precipitates are large enough to be detected by conventional transmission electron microscope. Apart from the size of the precipitates, this weld metal can also be handled and prepared TEM specimens using in-house focused ion beam machines, unlike the radioactive (neutron irradiated) weld metals.

Furthermore, the precipitates in this weld metal has been analysed in detail with atom probe tomography (APT) by Hirosawa [133], Morley [133] and Styman [125]. However, the limited sampling size of APT does not provide an overall view and representation of this weld metal. Also, APT is unable to provide much of the crystallography information of these precipitates in this weld metal. Some of the APT data is reported again here for comparison between the electron microscopy data obtained for this thesis. It is worth noting that APT results presented in Ref. [133] and [125] showed that precipitates detected in this weld metal contain similar chemical composition to those nucleated in neutron irradiated RPV steels that was studied in this work. Furthermore, previous studies on high copper steels have proposed that the nanometre scaled precipitates found in thermal annealed steels could well be of the same type of precipitates as those in neutron irradiated steels [51].

4.2 TEM Sample Preparation

Ferritic steel is a rather difficult material to be analysed using transmission electron microscopes. This is because the material is ferromagnetic and has a high oxidation rate. These properties are one of the main factors that constraint us from imaging nanometre sized features of interest using electron microscopes. All electron microscopy (EM) analyses were performed on either electropolished 3 millimetre diameter thin foils or in-situ lift-out specimens using focused ion beam (FIB) machine.

The type of specimen used is dependent on the TEM analysis performed and the information needed. For example, diffraction contrast analysis is used to identify the presence of irradiation-induced dislocation loops. In this work, only the electropolished 3 millimetres diameter thin foils were used for this analysis. This is due to the FIB induced matrix damages on a sample that could lead to misinterpretation of results. It is difficult to differentiate between neutron irradiation-induced damage and gallium-ion irradiation-induced damage from in-situ lift-out FIB specimen. This will be further

discussed in Section 5.2.2. It is worth noting that all EM images of neutron irradiated RPV steels presented in this thesis were taken from 3 millimetre diameter electropolished thin foils.

4.2.1 Mechanical polishing

3 millimetre diameter thin foils were punched from thin sheets with a thickness of 250 μm. The thin sheets were first cut from the bulk materials then subjected to mechanical grinding to less than 150 μm using silicon carbide abrasive paper that has a particles size of 6.5 μm (median diameter). Further mechanical polishing was performed on these thin foils to less than 100 μm. The ideal thickness of a thin foil is between 60 and 80 μm. At this range, the specimen induced magnetic effect of a thin foil in a transmission electron microscope is minimized. At the same time a good surface finished electropolished thin foil can still be obtained for TEM analysis [56]. It is worth noting that the magnetic field from the thin foil distorts the magnetic fields used in the electromagnetic lens system of the transmission electron microscope. The strength of magnetic field from a thin foil with a thickness of less than 100 μm will not limit the physical tilting range available of a transmission electron microscope, nor will it limit the adjustability of the stigmatism of the electromagnetic lens in a transmission electron microscope.

4.2.2 Jet electropolishing

The electron transparent region of a thin foil is produced by jet electropolishing with a commercially available STRUERS Tenupol-5 twin-jet electro-polisher. The specimen quality of an electropolished thin foil is strongly dependent on the competing process of chemical and electrolytic polishing. This competing process needs to be balanced carefully in order to obtain an ideal TEM specimen, i.e. a TEM specimen with a large area of thin region that has a slow change in the thickness from an edge of the hole to a thicker region. As illustrated in Figure 13, two scenario for a non-ideal TEM specimen could be produced by electropolishing [56, 134, 135]

1) If applied direct current (DC) voltage is lower than the ideal voltage for sample polishing and/or the temperature of the electrolyte is too high, chemical etching is preferable in the electropolishing process. This will produce a specimen with multiple small holes formed and decorated all around and surrounded by thick regions of foils.
2) If applied DC voltage is higher than the ideal voltage for sample polishing and/or the temperature of the electrolyte is too low, electrolytic etching will dominate the electropolishing process. This results in a specimen with a single large hole with very little thin region around the perimeter. It will also produce an oxidized surface on both sides of the thin foils.

Thin foils that have been mechanically polished to less than 100 μm were then electropolished using a solution of 5% perchloric acid in methanol at approximately –60 ˚C. Once an electron transparent region has been produced via electropolishing, the thin foils were immediately washed with fresh methanol and ethanol. “Fresh” electropolished thin foils are vulnerable to the open environment because they are prone to oxidation. Therefore, these thin foils were kept in fresh anhydrous isopropanol before being analysed using transmission electron microscope.

This extra process does not make the thin foils immune to oxidation, but it significantly delays the process. Furthermore, it can reduce the growth of surface oxides if immediate loading of the thin foil into the transmission electron microscope is not possible. Thin foils that are kept under the anhydrous isopropanol, generally, have a shelf life of at least three weeks or are available for about five transmission electron microscope sessions before the surface oxides grows and becomes too thick resulting in the TEM images of the foil being obscured. A disadvantage of storing the specimen in an anhydrous isopropanol is that the thin foil will have a significant amount of carbon contamination. The carbon contamination on a thin foil can be reduced by plasma

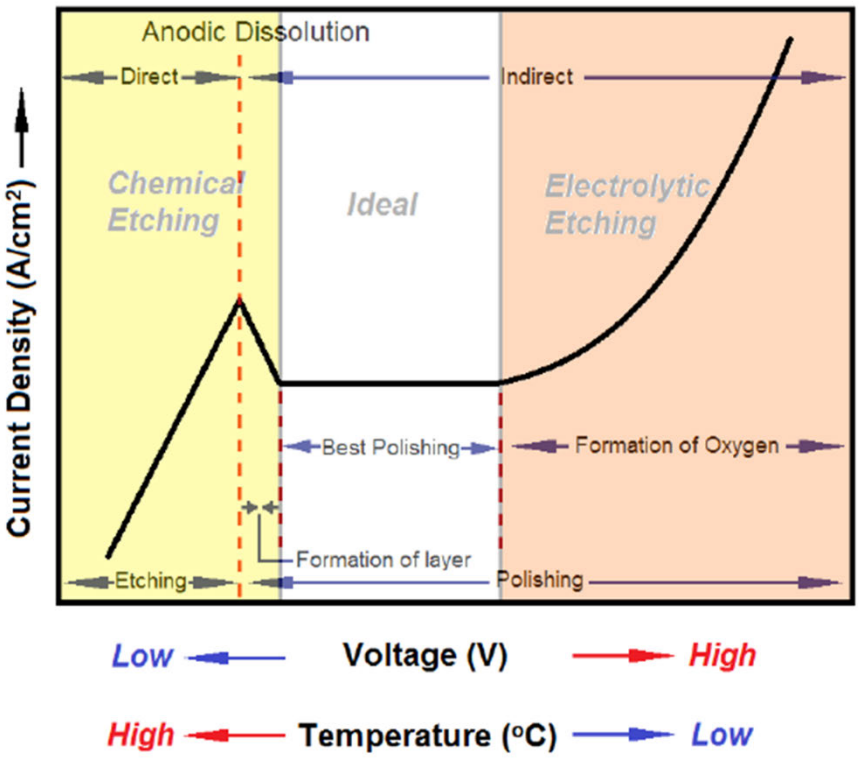


Figure 13: Schematic diagram to illustrate the optimum condition for getting a ideal TEM specimen using jet electropolishing

cleaning under low vacuum (< 10^{-5} Torr) in any commercial plasma cleaner. The duration of plasma cleaning is strongly dependent on the severity of the carbon contamination. The standard procedure for plasma cleaning a thin foil for 5 minutes before screening it under transmission electron microscope for high resolution imaging and/or chemical analysis.

A thin region of less than 40nm of an electropolished thin foil which is suitable for high resolution transmission electron microscopy (HRTEM) imaging is not often found. It was found in practice that if a thin region was available, it was either

1. bent or
2. full of re-deposited of precipitates, or
3. precipitates leached out of the foil by falling out during the electropolishing process as the iron matrix is preferentially etched, or
4. all that mentioned above.

This TEM sample preparation problem could be solved by preparing a TEM specimen using focused ion beam (FIB), instead of dip recovery polishing [56]. The main advantage of using FIB over dip recovery polishing is that the FIB allows full control during the specimen preparation and has almost 100% success rate in obtaining a thin region of less than 40nm. Besides these, the TEM specimens after dip recovery polishing will have chromium contamination that was induced by the chemical solution used on the surfaces of the TEM specimens. This contamination is due to the chromic/acetic acid solution used for dip recovery polishing.

4.2.3 Focused ion beam milling for TEM specimen preparation

An increase in the use of focused ion beam (FIB) system with ion beam assisted chemical vapour deposition as tools for TEM specimen preparation was testified by the increase number of publications in this area. This is because of the FIB's capability of sample positioning and making a specific area of interest as electron transparent membrane for microstructural analysis. The detail of FIB instrumentation and theory is well reported in Ref. [136]. In this work, all of the electron transparent specimens or membranes have been prepared using FIB milling and are based on an in-situ lift-out technique that was similar to those as reported in the literatures [137-141]. The ex-situ lift-out approach is not used in this work. This is because of the need of

1. Further thinning a lift-out specimen for HRTEM imaging, and
2. Removing oxides on the surface of a specimen using low energy ion beam.

Two different instruments were used to prepare FIB TEM specimens that were analysed in this work – FEI FIB 200 and Zeiss Nvision 40. Both instruments are operated using a gallium ions source. The range of operating voltages available for FEI FIB 200 is from 5 keV to 30 keV with beam currents between 10 pA and 20 nA. As for Zeiss Nvision 40, it is a dual beam instrument, having both an ion column with a gallium ion source and an electron column with an electron gun. Its operating voltages

available for FIB component of this instrument are between 2keV and 30keV with beam currents available at 0.1 pA to 45 nA.

Three millimetre diameter electropolished TEM discs were used for producing electron transparent membranes. This is because of the limited material available to make 3 millimetre diameter TEM discs for microstructural characterization. Apart from that, there are advantages for using 3 millimetre diameter electropolished TEM discs for preparing in-situ lift-out FIB electron transparent membranes. These advantages are as follow:

1. No or negligible damages induced during mechanical grinding and polishing remained on the surfaces of the 3 millimetre diameter TEM discs.
2. Re-deposition of material from milling is minimised
3. Reduce sample preparation time required to produce an in-situ lift-out TEM specimen since no under-cut is needed.
4. Larger electron transparent membranes could be produced in lesser time.

The FIB in-situ lift-out and FIB milling procedures adopted for this work are formed of two parts. The first part is choosing site of interest for in-situ lift-out using FEI FIB 200. The second part is thinning and polishing of lifted-out membranes to achieve electron transparency using low energy gallium ion beam on Zeiss Nvision 40. Using a dual beam FIB system for thinning and polishing could provide better control in obtaining a thin region needed for HRTEM imaging and/or chemical mapping.

The procedure for the first part is illustrated in Figure 14. An area of interest is first identified (see Figure 14(a)). A platinum layer is then deposited on the area of interest of the sample (see Figure 14(b)). To ensure an easy thinning and polishing at the second part, a thick platinum layer of 1 – 2 μm is used. Next, trenches around the platinum ‘strap’ are milled by using a 30 keV gallium ion beam operating at ≈ 20 nA to excavate materials at the trenches (see Figure 14(c)). Note that the sample membrane

that to be lifted-out is thick and is not electron transparent. This is to allow the membrane to have sufficient thickness to mill away the oxides that have grown on the membrane surfaces while it is kept in a non-vacuumed sample storage box.

A micromanipulator is inserted to the working chamber and is carefully attached and welded on to the membrane using platinum deposition mode available in the machine (see Figure 14 (d) – 2(f)). The connection between the membrane and the sample is cut (see Figure 14 (g)). The membrane is then moved next to a TEM grid and welded on to the grid using platinum deposition (see Figure 14 (h)-(j)). The micromanipulator is cut away from the membrane (see Figure 14 (k)). The sample is further welded at the side to increase the conductivity of the membrane with the TEM grid (see Figure 14 (L)).

The second part, i.e. thinning and polishing of lifted-out membrane, is performed using lower gallium ion beam energies with various current available. We have noticed in practice that a different current at a same beam energy does not induce any significant different of ion beam induced damages on to the lifted-out membrane, i.e. the depth of the ion beam induced damages and thickness of the beam induced amourphised surface layer are very similar [142]. A 30 keV and 10 keV gallium ion beams with a current of 150 pA are used to thin the membrane to ≈ 500 nm and to ≈ 300 nm, respectively. The specimen is further thinned to 100 – 150 nm using a 5 keV gallium ion beam with a current of 250 pA. A 2 keV gallium ion beam with a current of 40 pA is used for final polishing. It is important to note that the 2 keV beam energy for polishing can produce membranes with a very thin amorphous layer, i.e. less than 2 nm of amorphous layer formed in silicon sample [143]. The final thickness of the lift-out membrane depends on the experiments and analyses to be performed. For HRTEM imaging and chemical analysis such as EELs mapping and EDX mapping, the ideal final thickness of a membrane should less than 50 nm or transparent under the secondary electron imaging in a SEM at extra high tension (EHT) of 3 keV.

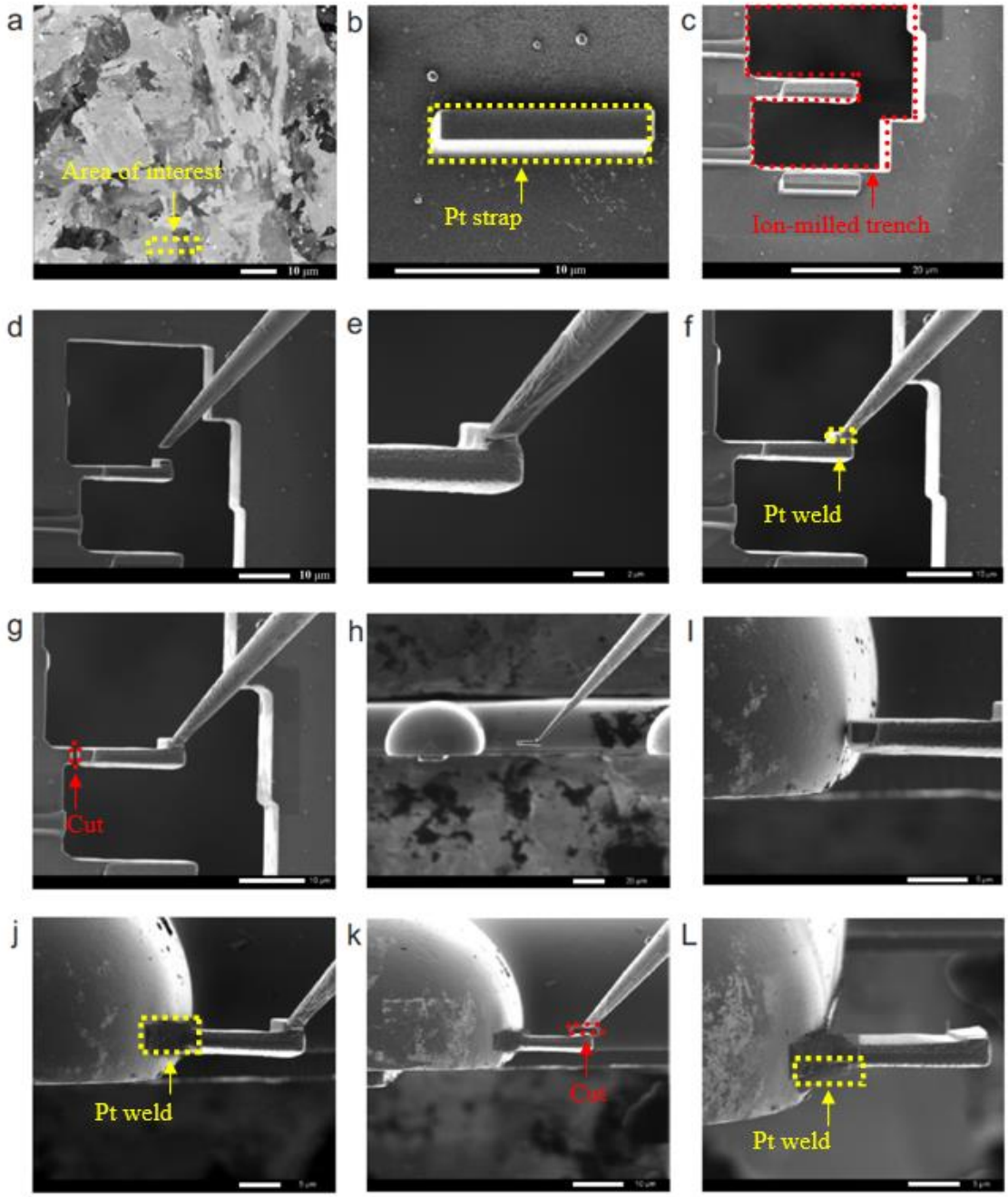


Figure 14: Ion-induced secondary electron images that show the procedure adopted for in-situ lift-out at separate stages using FIB and metal vapour deposition system available on the FEI FIB 200.

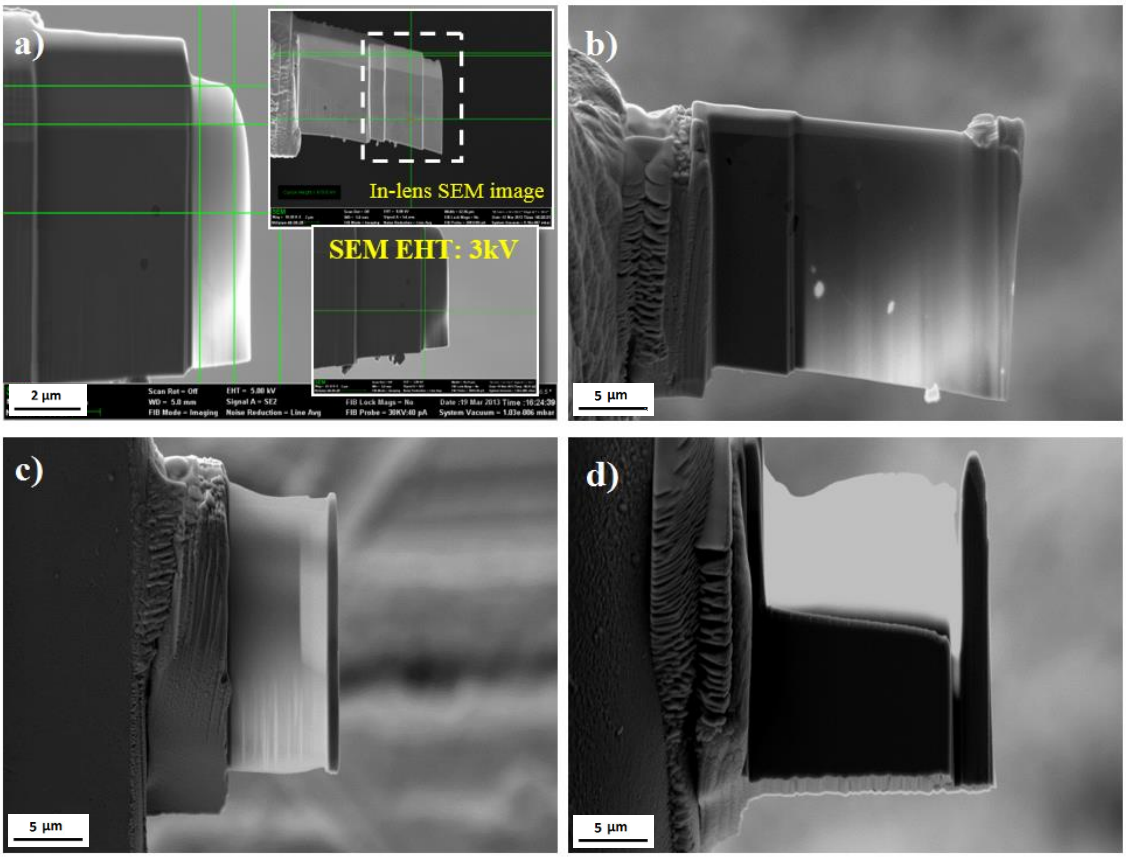


Figure 15: Secondary electron images that show electron transparent membranes after using lowest energy gallium ion beam available, i.e. 2keV, for polishing. These images were taken at SEM EHT of 5keV, unless mention otherwise.

It is worth noting that the gallium ion beam induces damages on to a membrane during milling and polishing. This damage is complicated and is strongly dependent on the beam energy. At 30 keV, the top 25 nm of a silicon substrate will be amourphised [138]. The depth of amorphous layer formed due to the gallium ion beam is related to the ion/solid interactions. The theory of ion/solid interaction has been discussed in detail in Ref. [142]. In Section 5.2.2, the gallium ion beam induced damage to ferritic steel will be discussed.

4.2.3.1 In-situ lift-out FIB TEM specimen with specific zone axis

As previously mentioned, it is important to prepare TEM specimen using focused ion beam (FIB) milling for high resolution transmission electron microscopy imaging on nanometre scaled precipitates. Previous studies on copper-rich precipitates in Fe-Cu

model alloys have reported that, due to the semi-coherent nature of the precipitates, a characteristic 'herring-bone' contrast can only be observed at zone axis of $< 111 >_{matrix}$ [54, 56, 75, 81]. Hence, it is important to have zone axis of $< 111 >_{matrix}$ parallel to the electron beam of a transmission electron microscope. It is difficult to ensure an electron transparent membrane that prepared by using FIB has a grain that could be tilted to a zone axis of $< 111 >_{matrix}$ that is parallel to the electron beam. This is especially difficult for a modern transmission electron microscope that is dedicated for high resolution imaging as the tilting range available for this type of microscopes are very limited, i.e. a tilting range of ± 25˚.

To ensure an in-situ lift-out FIB membrane contains a grain that are close to a zone axis of $< 111 >_{matrix}$ that parallel to the electron beam of a transmission electron microscope, a sample is first examined using an electron backscatter diffraction (EBSD) mapping on a region of interest. The EBSD mapping was performed on a JEOL-6500 FEG SEM with TSL OIM DC version–4 software at 20 keV with a probe current of approximately 1 nA. The sample used for EBSD mapping is an electropolished three millimetre diameter TEM specimen, as shown in Figure 16 (a). The advantage of using an electropolished TEM specimen for EBSD mapping is a series of high quality images of electron backscattered Kikuchi pattern can be recorded, owing to the surface that is free from defects induced during mechanical grinding and polishing.

The Kikuchi patterns of each single points collected by a EBSD detector is cross correlated to a build-in database of Body Centre Cubic (BCC) crystal structures that have Kikuchi patterns of all orientations of this crystal structure. The results of this provide us a grains orientation map of the area that have been analysed, as shows in Figure 16 (b). As noticed during practice, only grains with zone axes of $< 111 >$ and $< 110 >$ that are parallel to the incident gallium ion beam of a FIB machine are suitable for FIB in-situ lift-out as a membrane, as shown in Figure 16 (c), (d) and (e).

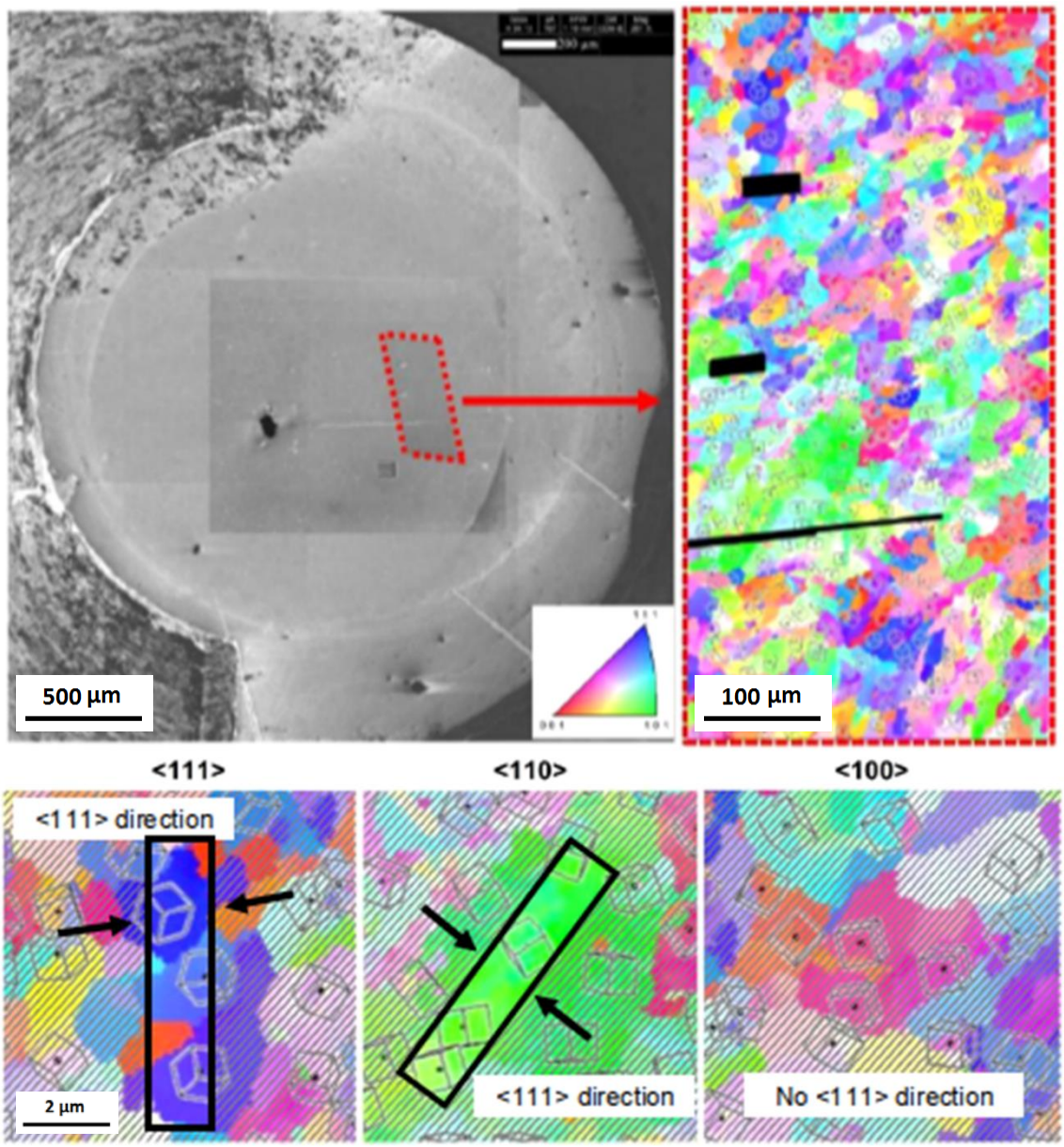


Figure 16: Schematic diagram that shows the choosing of a specific grain to make them into a TEM specimens with grains with <111> direction parallel to the electron beam.

4.3 Experimental Techniques

The experimental techniques used in this work are various types of electron microscopy techniques. The focus of the research is to characterize the irradiation-induced microstructural defects, particularly the irradiation-induced nanometre scale solute precipitates. The results obtained are compared with work performed by other collaborating partners from LONGLIFE using different experimental techniques such as

APT and SANS. Also, the results on thermally aged weld metals are compared with precious works performed.

The TEM specimens were analysed in various transmission electron microscopes. The electron microscope used is depending on the type of analysis to be performed. The list of transmission electron microscopes and operating conditions used in this work can be found in Table 8.

Table 8: Analytical instrumentation

Manufacturer	Model	Techniques	Beam	Voltage
Philips	CM20	TEM, EDS	e^-	200 kV
JEOL	2100	TEM, STEM, EDX	e^-	200 kV
JEOL	3000 FEG TEM	(HR)TEM, (HR)STEM, EFTEM, EDS	e^-	300 kV
JEOL	ARM 200	(HR)STEM, Dual EELS, EDS	e^-	200 kV
JEOL	2200 MCO	HRTEM, EFTEM	e^-	200 kV
JEOL	6500 FEG SEM	SEM	e^-	20 kV
FEI	FIB 200	FIB	Ga^+	30 kV
Zeiss	Nvision	SEM, FIB	e^- & Ga^+	3 kV, 5 kV, 8kV; & 30 kV, 10 kV, 5 kV, 2 kV/ (40pA – 300pA)

4.3.1 Transmission electron microscopy imaging

In the TEM analysis, systematic diffraction contrast analysis and phase contrast analysis was performed.

4.3.1.1 Diffraction contrast analysis

The TEM specimens were imaged in two-beam dynamical conditions with the deviation parameter (S_g) at or near zero. This imaging technique enhances the contrast of small

defects with little strain located within or near the extinction distance (ξ_g) from the surface of TEM specimens [144]. This is a common imaging technique used to analyse small dislocation loops, also known as un-resolvable dislocation loops that are less than ≈ 5 nm in diameter. However, the contrast shown in this imaging mode is diffraction-condition and orientation dependent. This imaging technique can provide different contrast from small dislocation loops (black and white lobe contrast) and other defects with small dislocation strain fields. Thus it is possible to identify the presence of nanometre scale coherent precipitates such as those formed in RPV steels. These can manifest as two dark lobes with a line of no contrast [145]. More details of this technique can be found in Ref. [144].

In some cases, two-beam kinematic conditions with the deviation parameter (S_g) greater than zero are used to image dislocation loops as well. The dark field images from these beam conditions, also known as weak beam dark field (WBDF) images, give a good contrast for small dislocation loops to be identified from a region of complicated microstructure [144].

4.3.1.2 Phase contrast analysis

The TEM specimens are also imaged at different focus values (between – 1000 nm and + 1000 nm) to form a stack of through-focus images. It is known that this technique is capable of making small coherent precipitates visible using the structure factor contrast [146]. Based on previous studies, nanometre scale solute clusters have an average diameter of around 2 nm. with these cluster sizes, it is not necessary to use high spatial frequency to visualize the solute clusters, and the lens aberrations can be ignored (more information can be found in Ref. [147].

4.3.2 Scanning transmission electron microscopy imaging

High angle annular dark field (HAADF) scanning transmission electron microscopy (STEM) imaging with an inner collection semi-angle of > 70 mrad and a probe size of

0.1 nm were used for imaging in this microscope mode. With such a setup, the image contrast will be dominated by the average local Z-contrast and will reflect changes in material density [148]. Note that the image contrast can be affected by the local strain field and is sensitive to the local specimen thickness. Descriptions of this imaging technique can be found in Refs. [149-151].

4.3.3 Electron energy filtered imaging

Figure 17 has been removed due to Copyright restrictions.
The original image can be found in the following reference:

Ref. [152] Website: http:// www7430.nrlssc.navy.mil/facilities/emf/gif.htm.

Figure 17: A schematic diagram that shows a typical electron energy loss spectrum [152].

A typical EELS spectrum is shown in Figure 17. The zero loss peak represents electrons that suffered no energy loss, i.e. inelastic scattering. The low loss spectrum, region corresponds to energy losses below 50 eV apart from the zero loss peak, contains information of Plasmon excitations. The remaining of the spectrum is the core loss regime. The main feature of the core loss regime is the characteristic absorption edges that are unique for each chemical element. The intensity of an absorption edge is proportional to the number of atoms present which absorb energy from transmitted electrons. The quantification of chemical elemental abundances is by integrating the

intensity of characteristic absorption edges and taking into account of the adsorption cross sections of corresponding chemical element. The information of local bonding around an atom and valence state can also be determined from the fine shape of the characteristic absorption edges present at the core loss regime.

Electron Energy Loss Spectroscopy (EELS) imaging was used to identify and quantify chemical distributions with high spatial resolution in the areas of interest. The spatial resolution and chemical elemental sensitivity optimization of this EELS imaging are discussed in Refs. [153] and [154]. Multivariate statistical analysis (MSA) was applied to an EELS chemical map series containing the relevant element edges. An explanation of the mathematical procedures of MSA and MSA processing in microscopy and spectroscopy can be found in Refs. [155] and [156].

Previous studies on copper-rich clusters in thermally aged model alloys using the same technique have shown that it is easier to visualize the nanometre scale solute clusters from the iron-L_{23} elemental map [92, 157]. Thus an experimental setup that could provide a good iron-L_{23} elemental maps and images recorded using a 10-eV energy slit and a 20 mrad half angle collection (objective) aperture. The acquisition time for each image is 15 s. The energy range covered for the series of EFTEM images range is between 450 eV and 900 eV (yielding a total of 46 images). This energy range is wide enough for background extrapolation and for constructing elemental maps.

4.3.3.1 Foil thickness measurement

The local foil thickness can be measured using either EELS or convergent beam electron diffraction (CBED). The thickness measurements using EELS or CBED have been well documented in Ref. [158] and Ref. [159], respectively. Both techniques could provide a reasonable accuracy from the thickness measurements made, i.e. EELS achieves an accuracy of 10 % and CBED gives about 5 % [158].

In this study, local foil thicknesses were measured to calculate the volume number density of features of interest observed under the electron microscopes, using EELS. The volume number density could then be compared with those measured and calculated by other experimental techniques, such as atom probe tomography (APT) and small angle neutron scattering (SANS). Thickness measuring using EELS is preferred in this study than using CBED. This is because of EELS thickness measurement is more suitable at thin regions, i.e. less than 40 nm. Also, it is a direct method that does not require further tilting to a two beam condition with specific g-vector for measurement.

The local foil thickness, t, is measured using Equation 1, where λ is mean free path of steel that can be calculated based on the method describe in Ref. [158], I_t is the integrated intensity of the whole spectrum, and I_0 is the integrated intensity of the zero-loss peak. Note that the error of the thickness measured using EELS is affected by the ratio of signal to noise during the image acquisition and the electrons collection angle used. The effect of the collection angle on the measurements made is corrected based on the calculations reported in Ref. [160].

Equation 1:

$$t = \lambda ln(\frac{I_t}{I_0})$$

4.3.4 Energy dispersive x-ray analysis

EDX chemical analysis was also applied to the characterisation of some samples. EDX make use of the X-ray spectrum emitted by a region in a TEM specimen that is bombarded with an electron beam. Determination of the concentrations of the elements using EDX is rather straight forward. A quantitative analysis of EDX spectrum involves the measuring of the characteristic x-ray peaks intensities for each elements in the sample and for the same elements in calibration standards of known composition. Each

EDX spectrum is acquired with the spectrum energy range from 0.1 keV to 20 keV until sufficient counts are received. It is worth mentioned that below energy range of 3 keV, the separation of the members of the K, L or M families of the characteristic x-ray peaks becomes small. As a result, the peaks are difficult to resolve with an EDX system. Further information about EDX analysis is presented in details in Refs. [161] and [162].

5 FEATURES OF IDENTIFICATION

5.1 INTRODUCTION

In general, neutron irradiation induced both structural and compositional changes in a low alloyed steel. The resulting radiation damage to the microstructures is among the most complex known. Depending upon the irradiation conditions and materials, various defects and clusters of different natures, sizes and types are present in the material after irradiation. For neutron irradiated low alloyed steels at pressurized water reactor operating condition, i.e. 280 – 300°C operating/irradiation temperature, dislocation loops with mostly interstitial nature, voids, precipitates that may be induced, enhanced, suppressed or impeded, and segregation of alloying elements to or away from grain boundaries or dislocations have been observed in the LONGLIFE project. These irradiation-induced defects and precipitates have also been reported in previous studies.

The major part of the work presented in this thesis is concerned with the results from TEM investigations into the development of microstructural defects and/or precipitates with neutron fluence and the development of precipitates with thermal ageing time. Such investigations were carried out using various types of electron microscopy (EM) technique. Details of the EM techniques and electron microscopes used are reported previously in Chapter 4. The majority of these techniques, especially the diffraction contrast and phase contrast imaging, have been extensively employed in the characterization of irradiation-induced microstructural defects in structural materials and have been well described in the book by Jenkins and Kirk [144].

It has become clear in previous studies that it is a challenge to study irradiation-induced defects in a low alloyed steel using transmission electron microscope. This is because of the irradiation-induced defects are generally very small and are only visible

under certain diffraction condition/s. Apart from that, artefacts with similar contrast as irradiation-induced defects may be induced during the sample preparation and, even during, imaging under the transmission electron microscope. To complicate the problem even more, low alloy steel are prone to oxidize, especially on electropolished TEM specimen. This thin layer of surface oxide will strongly affect the visibility of the irradiation-induced defects, especially at two-beam diffraction condition.

Hence, detailed studies with specific diffraction conditions are necessary/required in order to provide strong indications and evidences of the presence of neutron irradiation-induced defects. The following sections demonstrate the identification of irradiation-induced defects and thermally aged precipitates with various techniques that have been previously mentioned. It also establishes the importance of identifying irradiation-induced defects and precipitates with a combination of EM techniques.

5.2 ARTEFACTS

As mentioned earlier in the introduction of this chapter, existent or induced artefacts can affect the quality of the TEM micrographs. This will significantly influence the interpretation of micrographs. Hence it is important to understand the contrast caused by an artefact on a micrograph. These artefacts can be grouped into 3 categories according to its origin and are as follows:

1. Nature-of-the-material induced artefacts
2. Sample preparation induced artefacts
3. Electron beam induced defects

5.2.1 Nature-of-the-material induced artefacts

Low-alloyed steels that have been analysed are ferritic-type steels. They are highly magnetic and easily oxidized in air.

5.2.1.1 Magnetic field

The magnetic field from the ferritic TEM specimen will significantly affect the imaging resolution of a transmission electron microscopy by interfering with the electro-magnetic lenses in a transmission electron microscope. Also, the magnetic field, if significant, will restrict and limit the physical-tilting range available in a transmission electron microscope by deviating the electron beam away from the specimen. The magnetic disturbance introduced by the TEM specimen can be diminished by reducing the magnetic field strength. This is achieved by using as small a volume of the ferritic sample as possible [163].

Apart from interfering with the magnetic field of the electromagnetic lenses, the magnetic field of the TEM specimen will also interact with the electrons passing through the TEM specimen. A series of interference fringes, also known as magnetic-domain walls, will form and affect the interpretation of a micrograph [164]. These magnetic-domain walls could be misinterpreted as second phase precipitates that present in a sample. Note that the magnetic-domain walls will only be visible under parallel illumination [163]. This phenomenon is well described in Ref. [165].

5.2.1.2 Surface oxides

It is a well-known fact that on ferritic steels oxidation starts rapidly and then almost ceases. Teddington et al. show that a layer of oxides with a thickness of about 20 Å forms in just 1 minute and 50 Å in one year from pure iron at room temperature [166]. The oxide film was examined by electron diffraction and the results were compared with those from steel. Both diffraction patterns matched with each other, except that the film from steel contained inclusions [167]. Note that the surface oxide can be confused with radiation damage and/or irradiation-induced solute cluster under some imaging conditions.

Four types of oxides can form on ferritic steel depending on different conditions. In fact, under some circumstances, it is possible for all types of the oxides to be present on a ferritic steel [167]. These four types of oxides are Wüstite (FeO), Magnetite (Fe_3O_4), Hematite (α-Fe_2O_3), and Maghemite (γ-Fe_2O_3). The crystal structure information of these oxides is summarized in Table 9. Previous studies have shown that the oxide formed on ferritic steel is strongly dependent on the, surface condition, temperature and local chemical composition of the sample surface [167, 168].

At room temperature, a thin sheet of Fe_3O_4 with nucleation of thicker clumps of cubic oxides of γ-Fe_2O_3 will quickly form on the surface of a ferritic steel when it is in air [167, 169]. A secondary oxide of α-Fe_2O_3 can be nucleated on the thin oxide sheet of γ-Fe_2O_3 if the steel is gently warmed and results in a complicated oxides structure on the ferritic steel [167].

Table 9: Summary of the type of oxides develop on iron [167, 169, 170]

Name	***Chemical Formula***	***Crystal system/structure***
Wüstite; Iron (II) oxide	FeO	Cubic structure
Magnetite; Iron (II, III) oxide	Fe_3O_4	Cubic structure
Hematite; Iron (III) oxide	α-Fe_2O_3	Rhombohedral lattice system
Maghemite; Iron (III) oxide	γ-Fe_2O_3	Cubic structure

Figure 18 is a series of micrographs taken at various two-beam diffraction conditions from a low alloyed steel to show the influence of surface oxides on the image quality. The ANP-2 TEM specimen analysed has been electropolished. It was then immediately transferred to a transmission electron microscope, for this instance, a Philip CM20 that operates at 200kV. The total amount of time this specimen in contact with air was less than 5 minutes. A thin layer of surface oxide was formed on the TEM specimen. This thin sheet of oxides will interact with the incident electron beam, especially at a two-beam condition, and affect significantly the diffraction contrast of two dimensional microstructural defects, like dislocation lines and loops. It was found that the influence

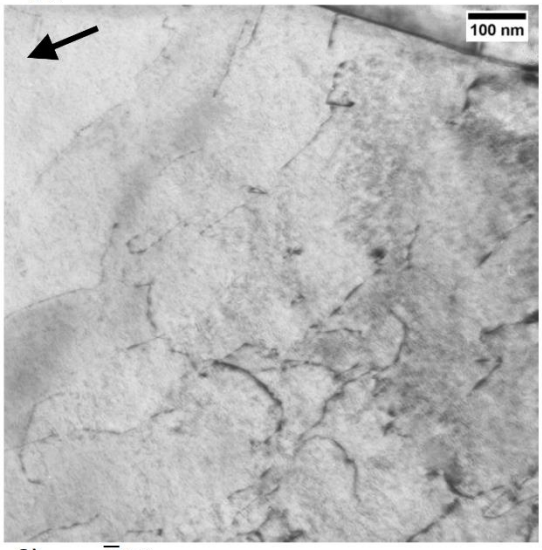
of these oxides during diffraction contrast imaging is stronger at certain crystal orientation and diffraction condition. This observation is directly related to the crystals orientation relationship between the oxide and the sample.

Table 10: Summary of the observation of Moiré fringes under either a dynamical &/or kinematical two-beam diffraction condition from various g-vectors obtained from ANP-2 weld metal

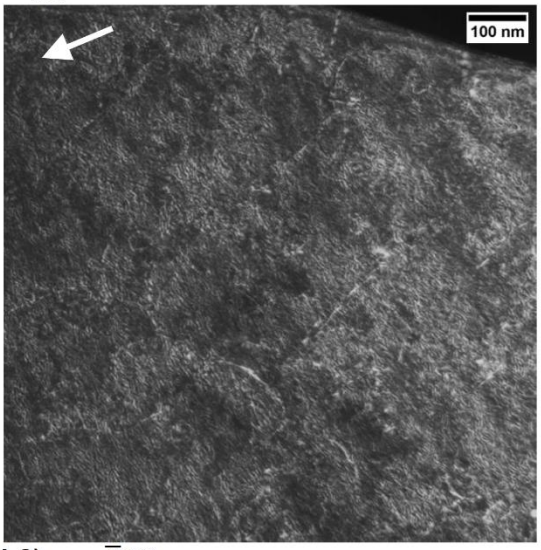
Zone Axis	g-vector	Unirradiated	Irradiated
001	$020; 0\bar{2}0$	Strong islands of Moiré (oxide) fringes	Strong Islands of Moiré (oxide) fringes
001; 011	$200; \bar{2}00$	Islands of Moiré (oxide) fringes	Islands of Moiré (oxide) fringes
001; 013	$1\bar{1}0; \bar{1}10$	Strong Moiré (oxide) fringes	Strong Moiré (oxide) fringes
001	$110; \bar{1}\bar{1}0$	No obvious Moiré (oxide) fringes	No obvious Moiré (oxide) fringes
011	$01\bar{1}; 0\bar{1}1$	No obvious Moiré (oxide) fringes	No obvious Moiré (oxide) fringes
011	$21\bar{1}; \bar{2}\bar{1}1$	No obvious Moiré (oxide) fringes	No obvious Moiré (oxide) fringes
011	$2\bar{1}1; \bar{2}1\bar{1}$	No obvious Moiré (oxide) fringes	No obvious Moiré (oxide) fringes
013	$21\bar{1}; \bar{2}\bar{1}1$	No obvious Moiré (oxide) fringes	No obvious Moiré (oxide) fringes
013	$12\bar{1}; \bar{1}\bar{2}1$	No obvious Moiré (oxide) fringes	No obvious Moiré (oxide) fringes

Table 10 is a summary of the observation of Moiré fringes, which is most probably due to the surface oxides, under either a dynamical &/or kinematical two-beam diffraction condition from different g-vector used. Magnified micrographs that show where these Moiré fringes at $g = \pm(020)$, $g = \pm(200)$ and $g = \pm(1\bar{1}0)$ are shown as Figure 19 (a-b), (c-d) and (e-f) respectively. Apart from affecting the contrast of two-dimensional microstructural defects, the Moiré fringes shown could be mis-interpreted as second phase precipitates, as shown in dark field micrographs of Figure 19 (b & d).

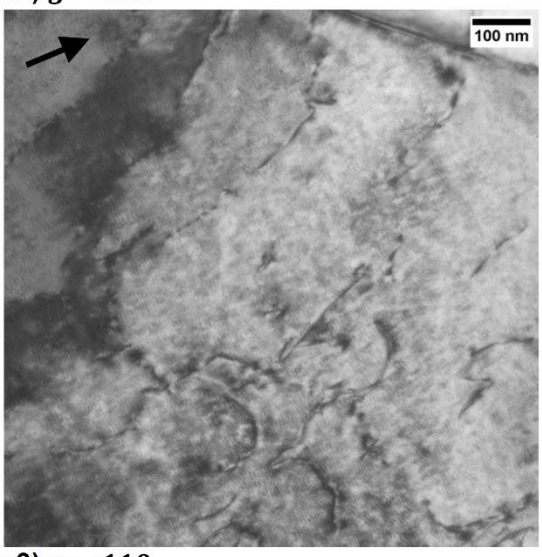
a1) $g = 1\bar{1}0$



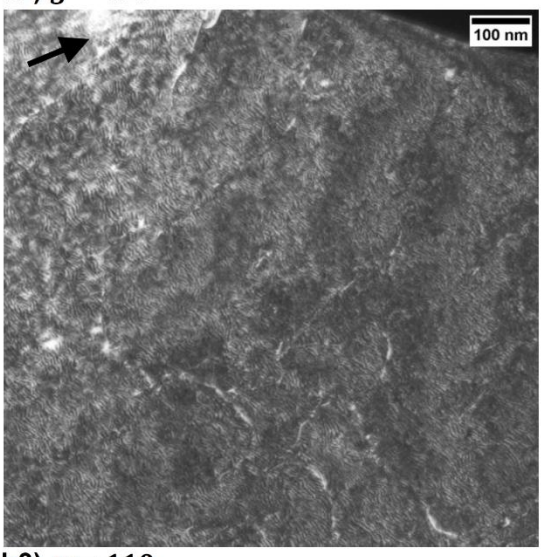
b1) $g = 1\bar{1}0$



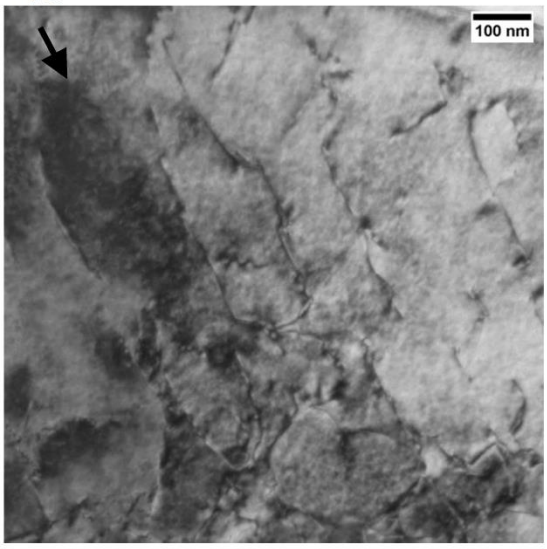
a2) $g = \bar{1}10$



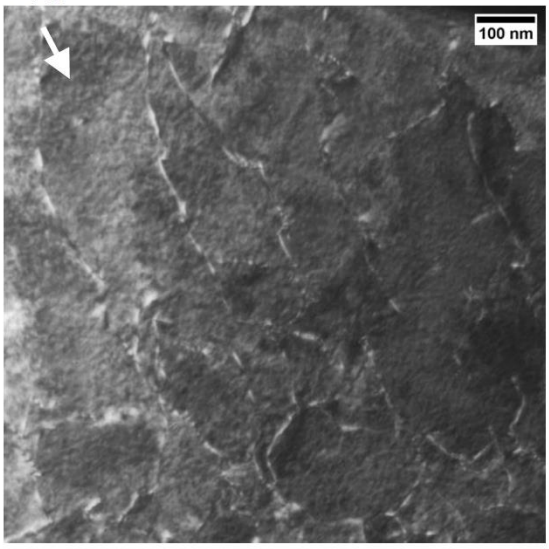
b2) $g = \bar{1}10$



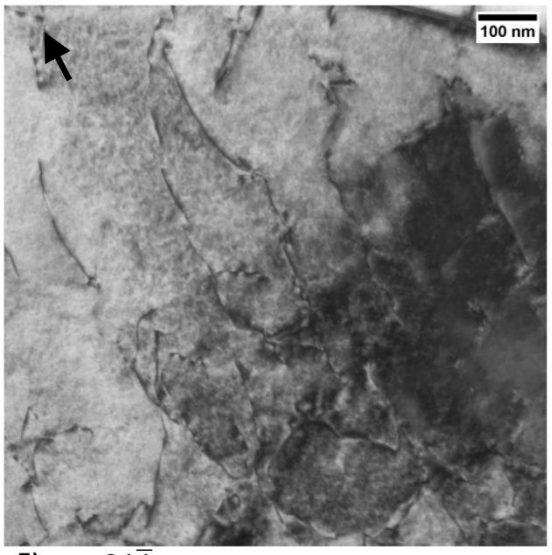
a3) $g = 110$



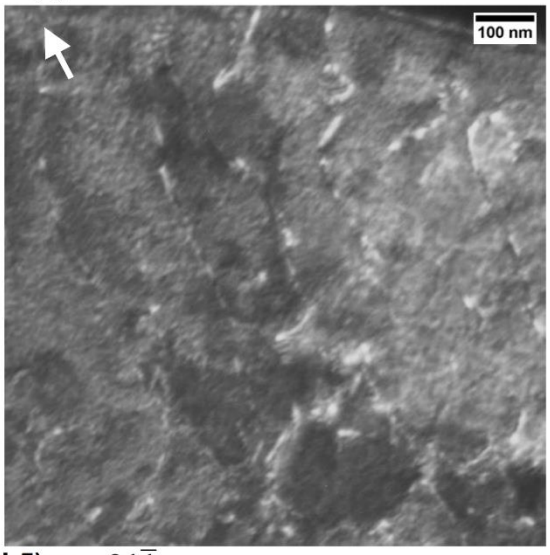
b3) $g = 110$



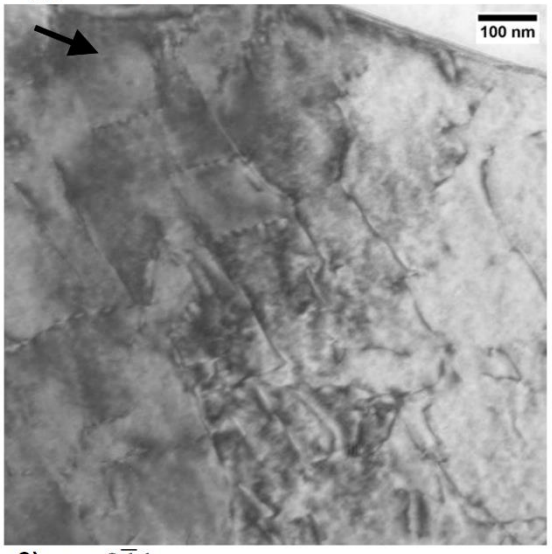
a4) $g = \bar{1}\bar{1}0$



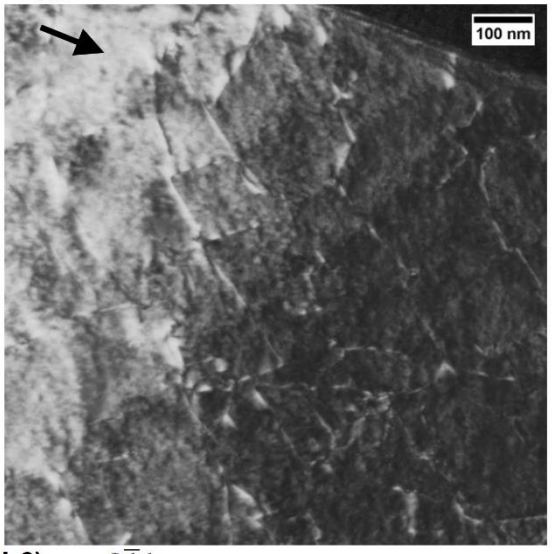
b4) $g = \bar{1}\bar{1}0$



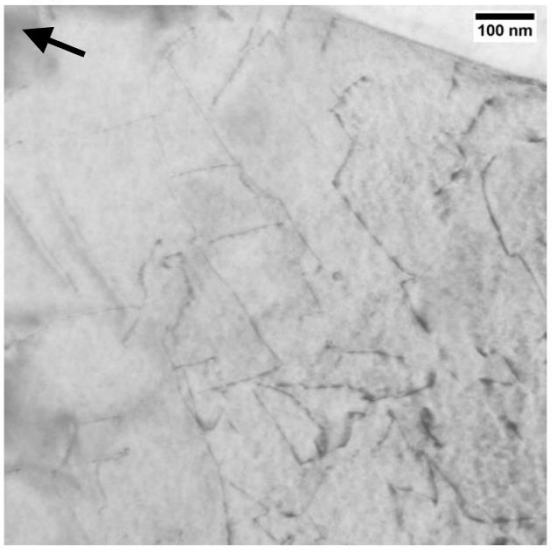
a5) $g = 01\bar{1}$



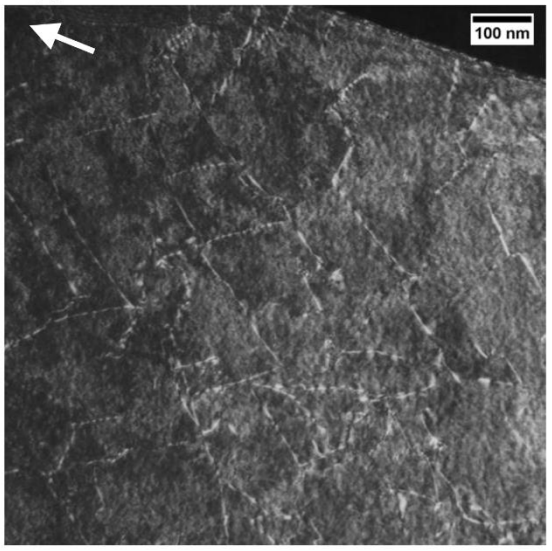
b5) $g = 01\bar{1}$



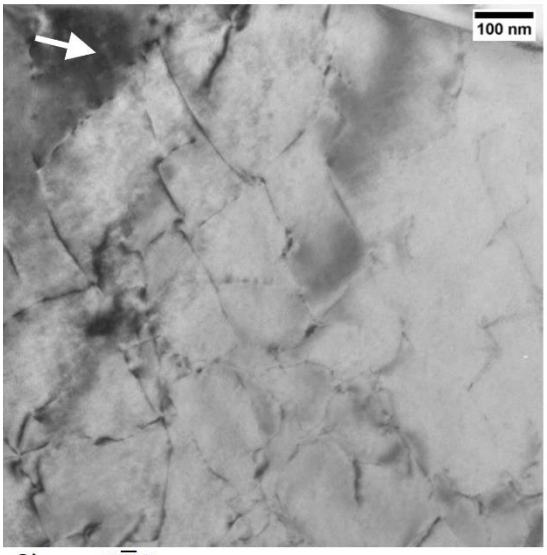
a6) $g = 0\bar{1}1$



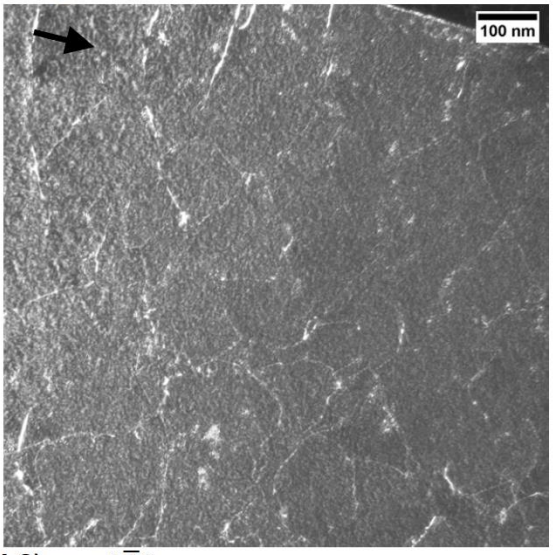
b6) $g = 0\bar{1}1$



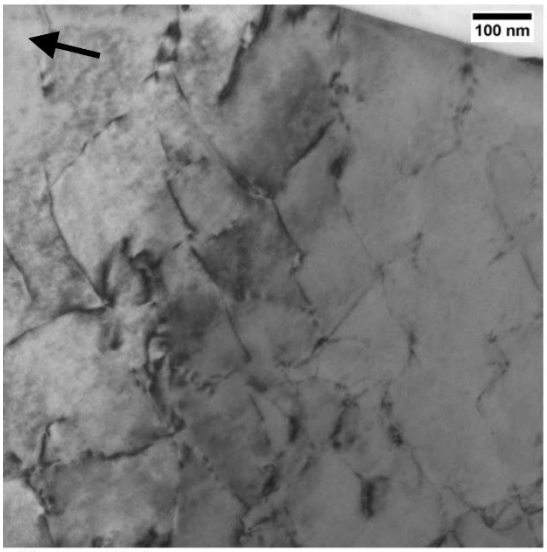
a7) $g = 020$



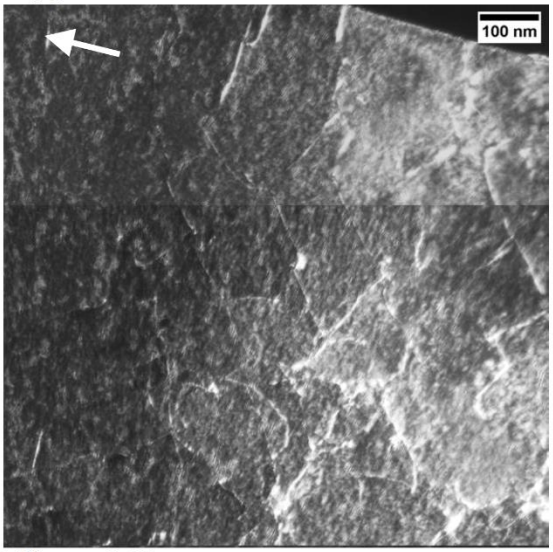
b7) $g = 020$



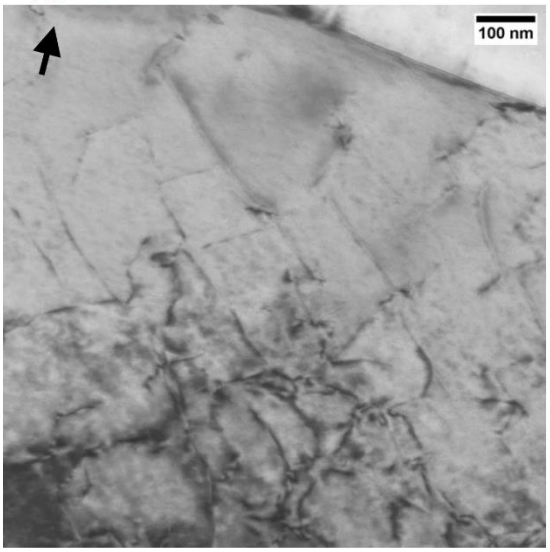
a8) $g = 0\bar{2}0$



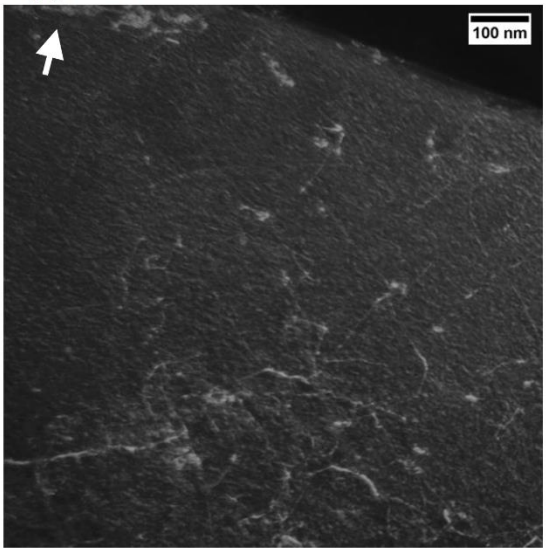
b8) $g = 0\bar{2}0$



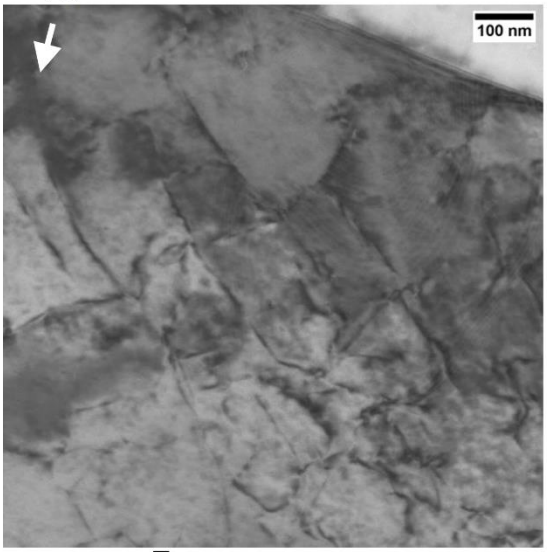
a9) $g = 200$



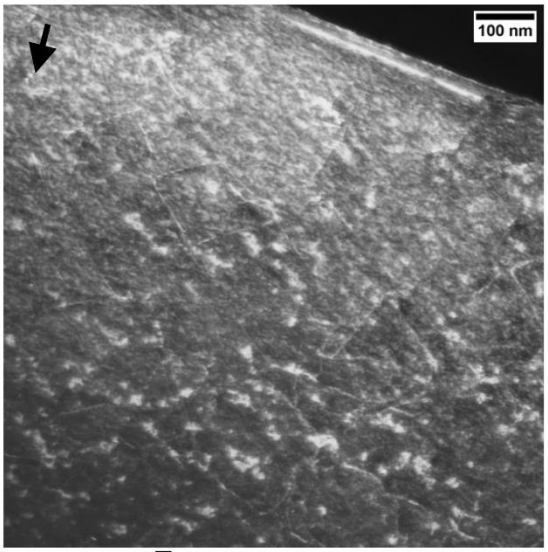
b9) $g = 200$



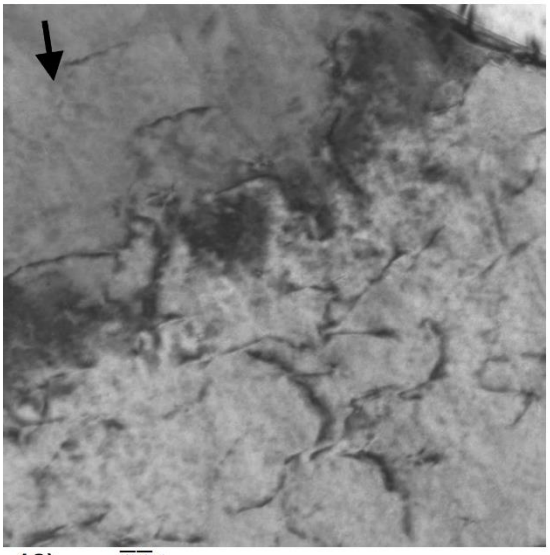
a10) $g = \bar{2}00$



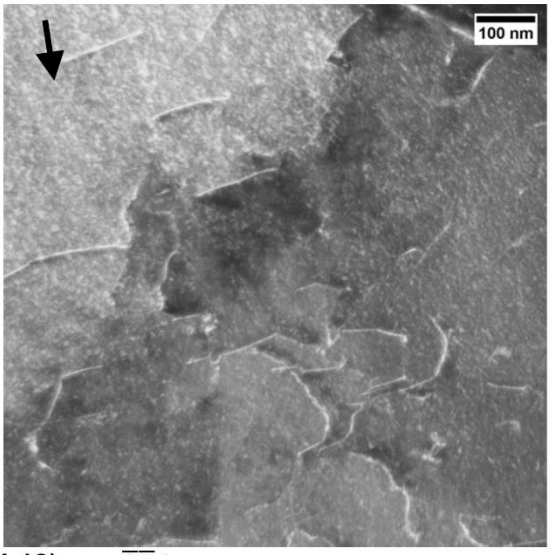
b10) $g = \bar{2}00$



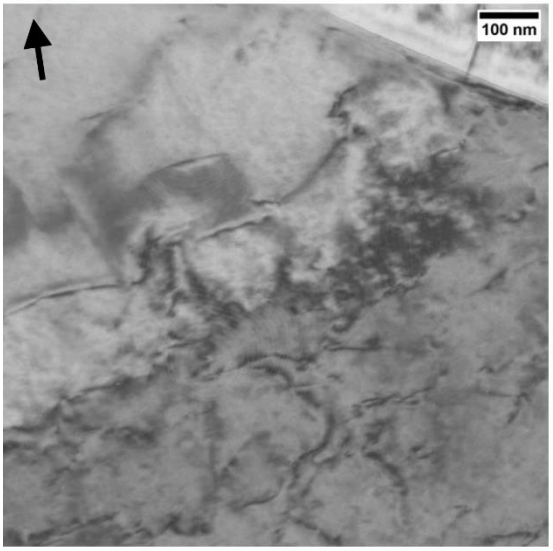
a11) $g = 21\bar{1}$



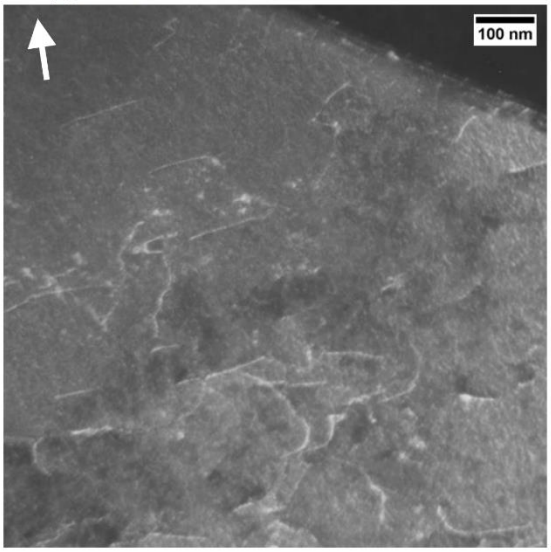
b11) $g = 21\bar{1}$



a12) $g = \bar{2}\bar{1}1$



b12) $g = \bar{2}\bar{1}1$



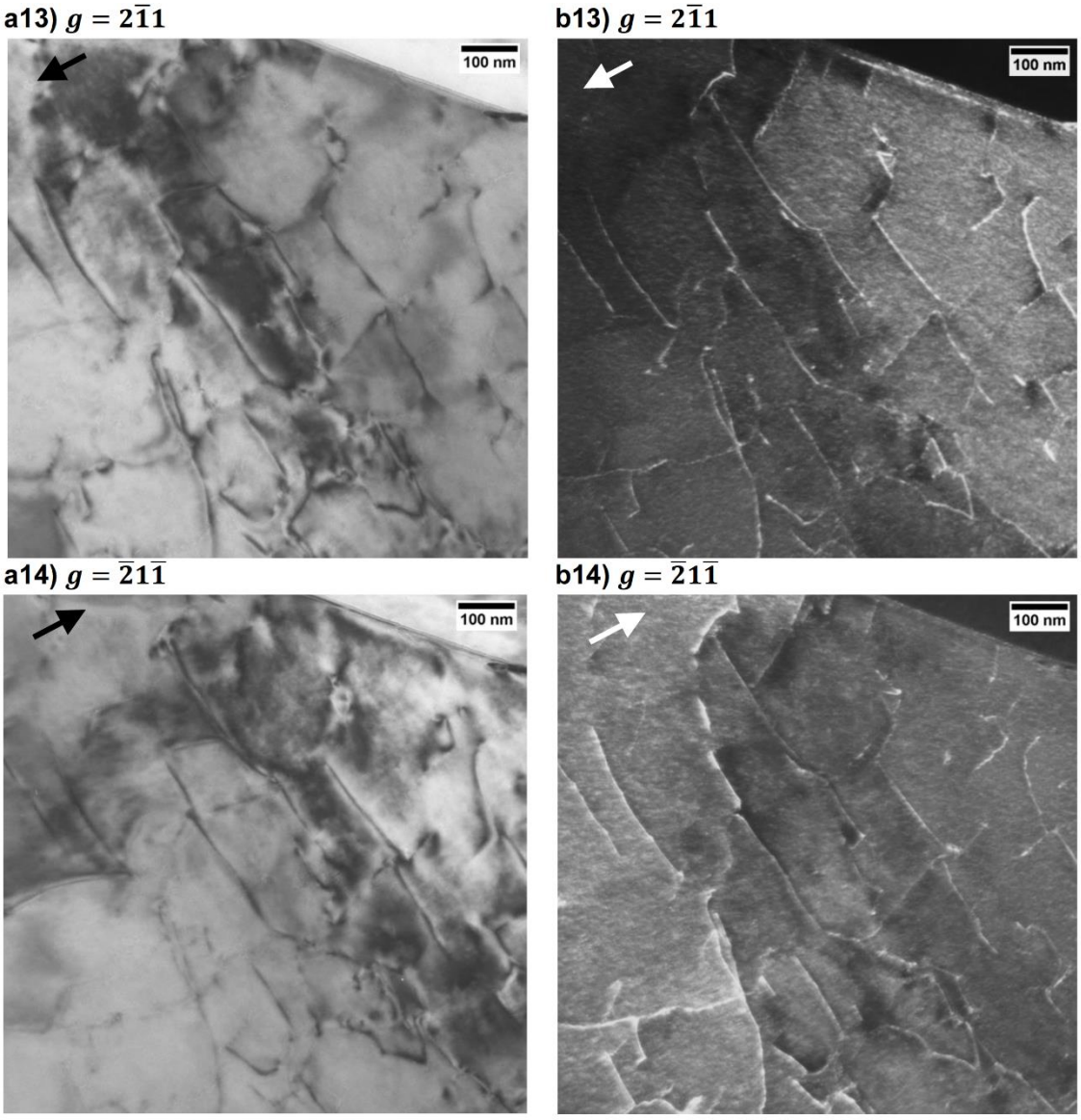


Figure 18: A series of diffraction contrast micrographs were taken from neutron irradiated ANP-2 TEM specimen that covered all g-vectors available at matrix crystal orientations of zone axis <001> and <011>, apart from g = ± (200) at zone axis <001>. The micrographs imaged using g = ± (200) at zone axis <001> are not included in here. This is due to the same g-vector is included at zone axis <011>. (a1 & b1) Bright field (BF) and dark field (DF) micrographs of $g = 1\bar{1}0$ *at zone axis (ZA) =* $[001]$*, (a2 & b2) BF and DF micrographs of* $g = \bar{1}10$ *at* $ZA = [001]$*, (a3 & b3) BF and DF micrographs of* $g = 110$ *at* $ZA = [001]$*, (a4 & b4) BF and DF micrographs of* $g = \bar{1}\bar{1}0$ *at* $ZA = [001]$*, (a5 & b5) BF and DF micrographs of* $g = 01\bar{1}$ *at* $ZA = [011]$*, (a6 & b6) BF and DF micrographs of* $g = 0\bar{1}1$ *at* $ZA = [011]$*, (a7 & b7) BF and DF micrographs of* $g = 020$ *at* $ZA = [001]$*, (a8 & b8) BF and DF micrographs of* $g = 0\bar{2}0$ *at* $ZA = [001]$*, (a9 & b9) BF and DF micrographs of* $g = \bar{2}00$ *at* $ZA = [011]$*, (a10 & b10) BF and DF micrographs of* $g = 200$ *at* $ZA = [011]$*, (a11 & b11) BF and DF micrographs of* $g = 21\bar{1}$ *at* $ZA = [011]$*, (a12 & b12) BF and DF micrographs of* $g = \bar{2}\bar{1}1$ *at* $ZA = [011]$*, (a13 & b13) BF and DF micrographs of* $g = 2\bar{1}1$ *at* $ZA = [011]$ *and (a14 & b14) BF and DF micrographs of* $g = \bar{2}1\bar{1}$ *at* $ZA = [011]$.

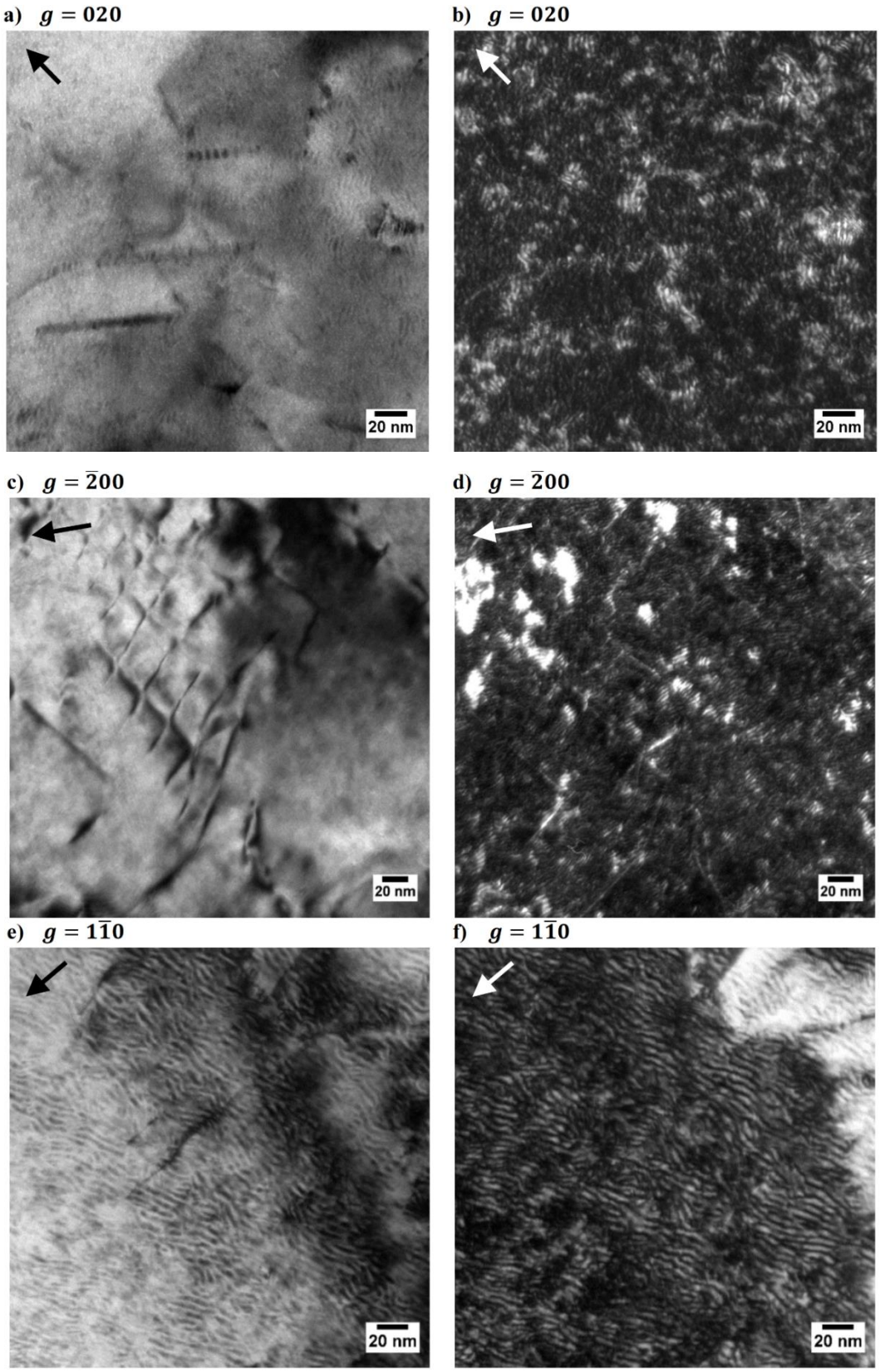


Figure 19: Bright field and dark field micrographs imaged at (a & b) $g = \pm(020)$, (c & d) $g = \pm(200)$ and (e & g) $g = \pm(1\bar{1}0)$ that show contrast of Moiré fringes.

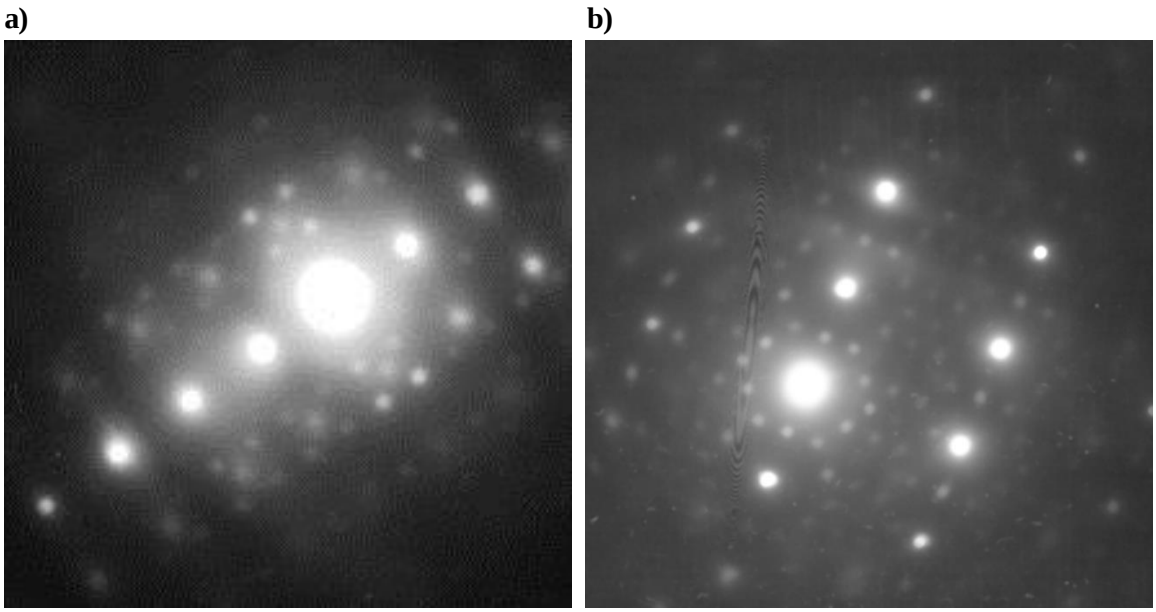


Figure 20: Diffraction patterns obtained closed to (a) zone axis of <001>$_{matrix}$ and (b) zone axis of <011>$_{matrix}$ from a low alloyed steel.

Diffraction spots other than the matrix were observed during the g. b – tilting experiments. Figure 20 shows the extra diffraction spots appearing at zone axis <001>$_{matrix}$ and <011>$_{matrix}$. The lattice parameters were calculated using the extra diffraction spots other than those from the matrix crystals. The calculated lattice parameters, i.e. 8.3 ± 0.1 Å, are reasonably close to those reported for Fe_3O_4 or γ-Fe_2O_3 in Refs. [169, 171, 172]. Hence it is reasonable to assume that the surface oxides formed on low alloyed steel are similar to those reported in previous studies, i.e. Fe_3O_4 or γ-Fe_2O_3 formed as a surface oxide on low alloyed steel. Note that both the Fe_3O_4 and γ-Fe_2O_3 have unit cells that are identical in size. Therefore, it is difficult to distinguish the type of oxides formed on low alloyed steel by using the diffraction method. Based on previous studies, the orientation relationships between iron matrix and Fe_3O_4 observed under the transmission electron microscope are matched with those reported in Ref. [169], as described by Relationship 1 and Relationship 2.

Relationship 1:

$$[111]_{oxide}(0\bar{1}1)_{Fe_3O_4} //[110]_{BCC\ Fe}(001)_{BCC\ Fe}$$

Relationship 2:

$$[211]_{oxide}\,(0\bar{1}1)_{oxide}\;||\;[011]_{BCC\,Fe}\,(001)_{BCC\,Fe}$$

5.2.2 Sample preparation induced artefacts

The TEM specimens were prepared through electro-chemical polishing and focused ion beam (FIB) milling method. The details of these methods and its procedures are documented in Section 4. Various types of defects, mainly surface-type or subsurface-type of defects, were observed from the specimens prepared from the methods mentioned above. The following sections show the defects observed in TEM specimens prepared during the duration of this study. Section 5.2.2.1 will focus on the artefacts induced in the TEM specimens prepared through the electro-chemical polishing process. Artefacts induced by FIB will be discussed in Section 5.2.2.2.

5.2.2.1 Electro-chemical polishing induced artefacts

The quality of an electro-chemical polished thin foil is directly controlled by the competition between the chemical-etching and electrolytic polishing process. Any overpowering of either one of these processes will result in a thin foil with a poor quality surface that could potentially make the interpretations of the micrographs difficult. To obtain a good electro-chemically polished thin foil, the applied DC voltage and temperature for the polishing process is crucial. Figure 21 and Figure 22 show the condition of the surface of a thin foil that was electro-chemically polished at a higher DC voltage than the ideal voltage and/or an electrolyte with a temperature that was lower than the ideal temperature. In the TEM bright-field micrographs, as shown in Figure 21, needle-shaped like surface features are clearly observed decorating the specimen. Preferential electrolytically polished regions were also observed, as marked on Figure 21. Under HAADF imaging, these surface features appear to have a brighter contrast compared to its surrounding, as shown in Figure 22. This is because of the mass-thickness effects. In the reversed condition, when the applied DC voltage was

lower and/or the temperature of the electrolyte was higher than the ideal condition, secondary precipitates that were close to the surface will be preferentially etched out from the thin foil and small surface 'craters' are seen on the thin foil, as shown in Figure 23 and Figure 24. This was observed even if the electropolishing conditions are optimal. Note that the nanometre scale surface craters are often misinterpreted as either irradiation-induced vacancy clusters or void or precipitates. The identification of these features is discussed in Section 5.3.

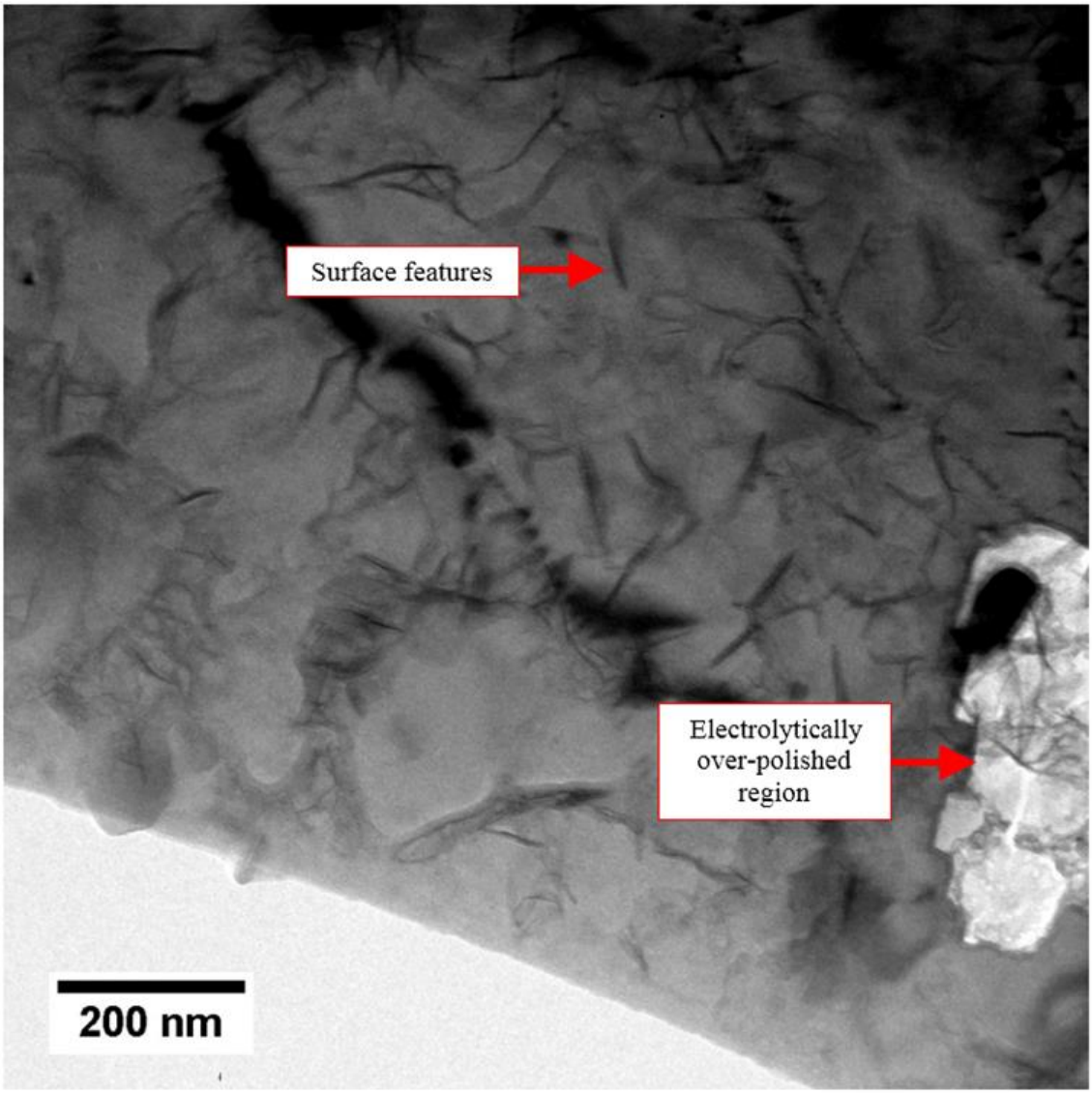


Figure 21: TEM Bright-field micrograph showing a ANP-2 thin foil with surfaces that has been preferentially electrolytically polished. Needle-shape like surface features with a darker contrast are fully decorated on the specimen.

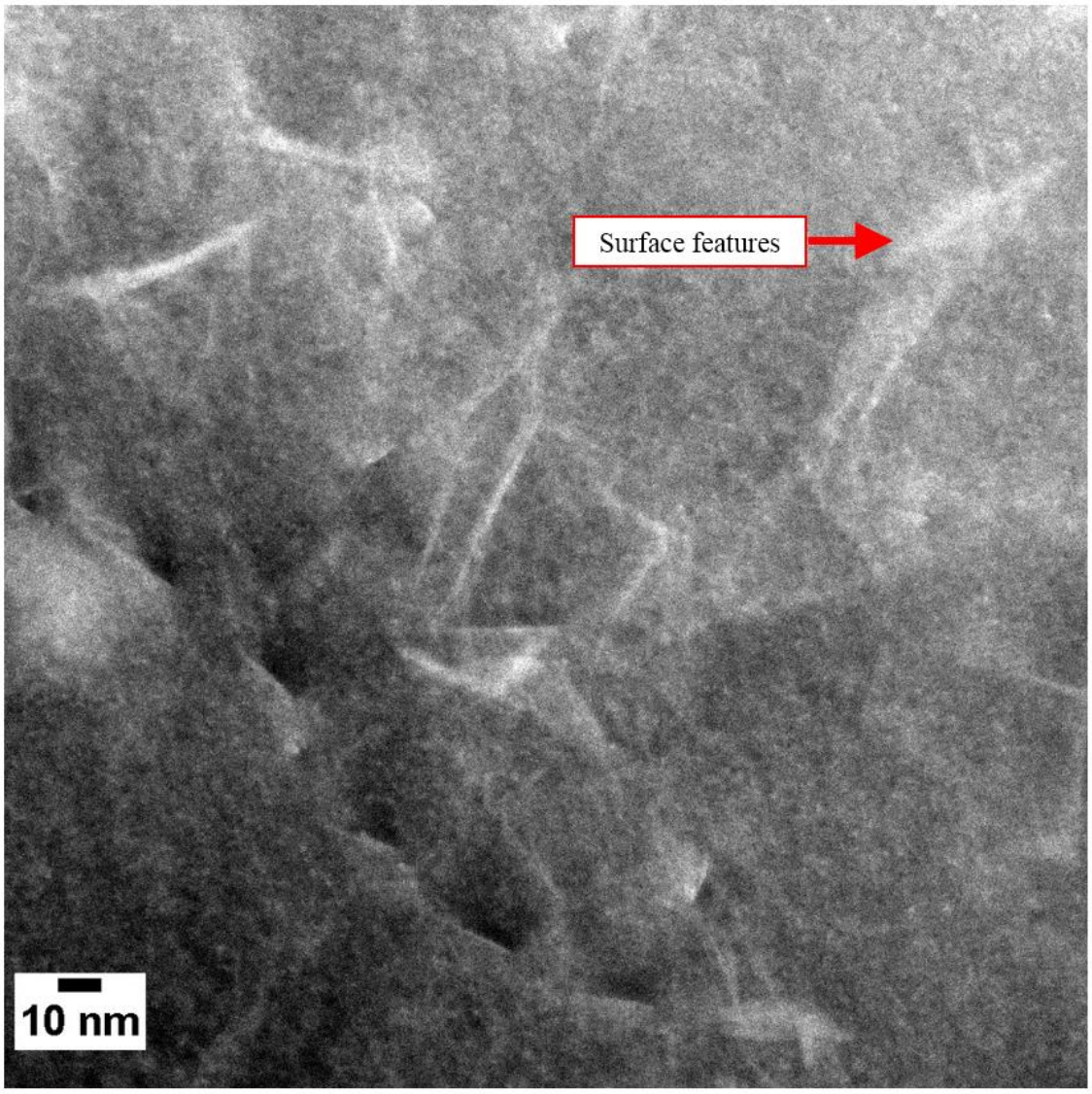


Figure 22: HAADF micrograph showing needle-shape like surface features of the same region that was shown in Figure 21. The brighter contrast of these surface features is due to thickness effects.

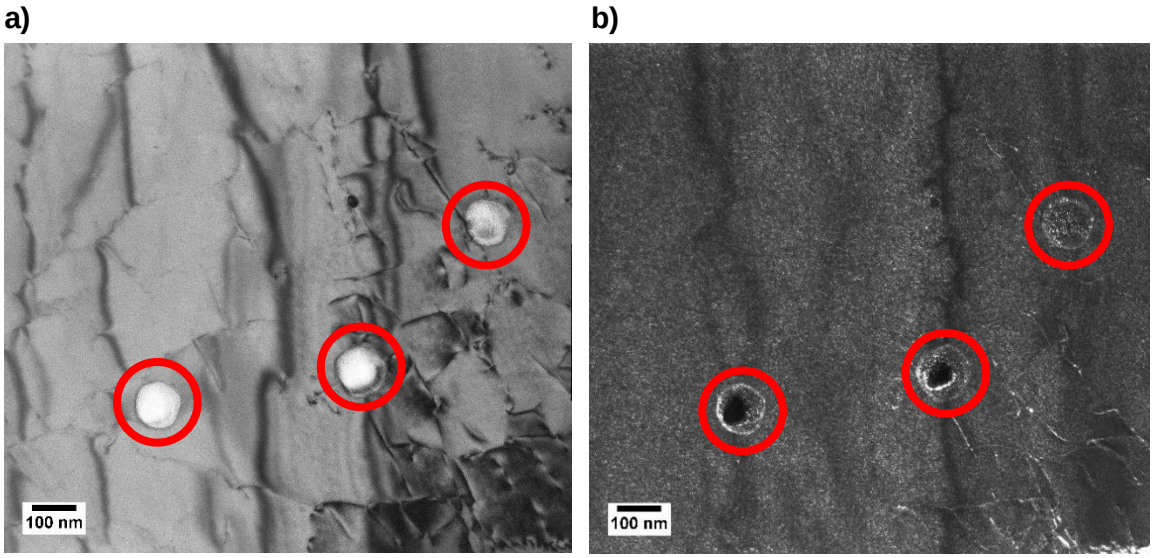


Figure 23: (a) bright-field and (b) dark-field micrographs of the same region showing large craters on the surface of a thin foil. These craters, as marked by red circles, have a brighter contrast in the bright field micrograph due to the effects of mass and thickness. In the corresponding dark-field micrograph, these craters have little contrast different compared to the surrounding matrix.

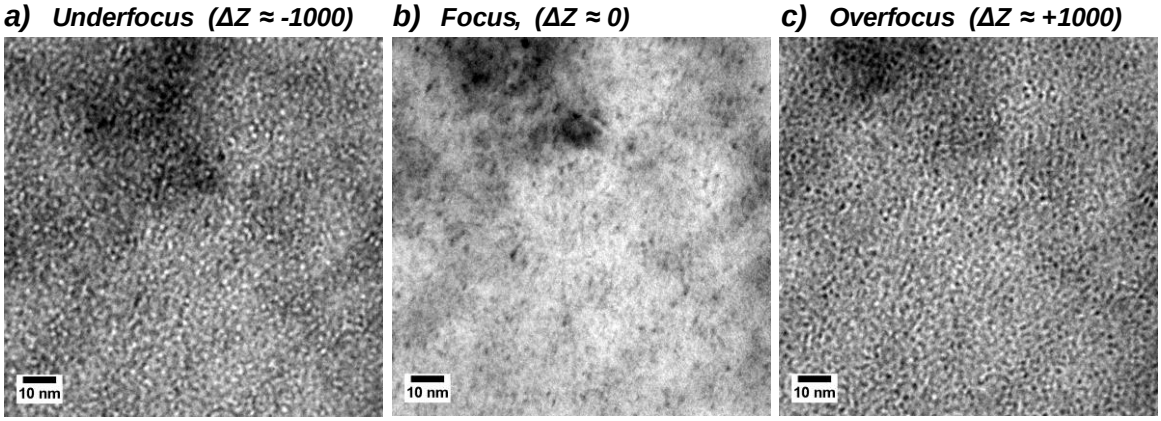


Figure 24: Focal series showing the nanometre-scale surface craters induced onto the surface of a thin foil during electro-chemical polishing. (a) an underfocus bright-field micrograph imaged at ΔZ ≈ - 1000 nm, (b) a focus bright-field micrograph imaged at ΔZ ≈ 0 nm and (c) an overfocus bright-field micrograph imaged at ΔZ ≈ + 1000 nm.

5.2.2.1.1 Re-deposition of precipitates

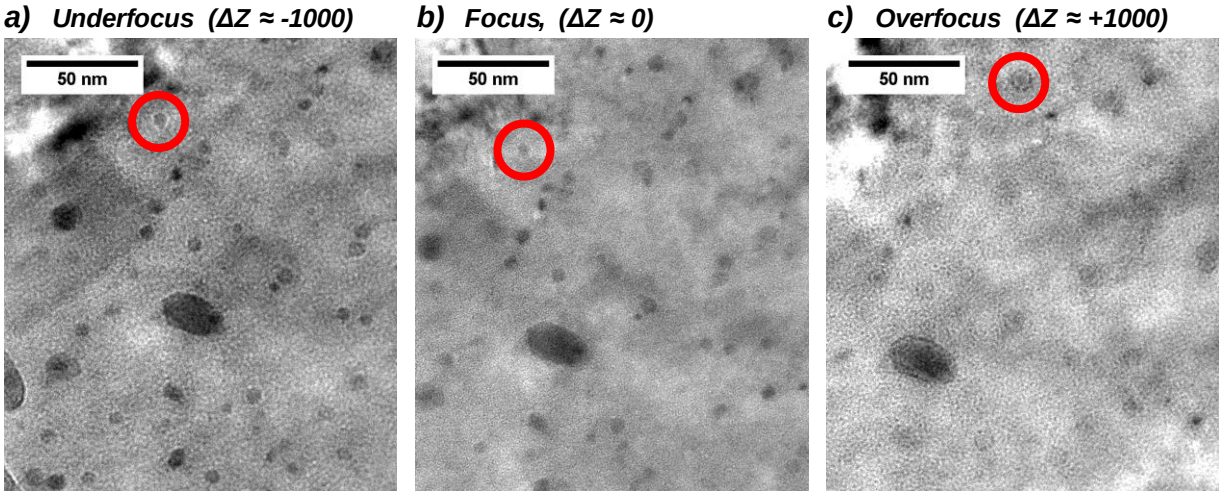


Figure 25: Focal series showing precipitates that are in the sample and re-deposited on a thin foil. (a) an underfocus bright-field micrograph imaged at ΔZ ≈ - 1000 nm, (b) a focus bright-field micrograph imaged at ΔZ ≈ 0 nm and (c) an overfocus bright-field micrograph imaged at ΔZ ≈ + 1000 nm.

Even though the sample was electro-chemical polished, re-deposition of precipitates on the surface of the thin foils is often observed. It is difficult to differentiate precipitates that have been re-deposited onto a thin foil. Figure 25 shows an electro-chemical polished thin foil with various sizes of precipitates decorated around the material. Based on just a bright-field micrograph, it is impossible to identify the precipitates that are re-deposited onto the surface of the thin foil, as shown in Figure 25 (b). A through-focal series would enable us to distinguish between the re-deposited precipitates from those in the sample, as shown in Figure 25. A re-deposited precipitate was identified from the region shown in Figure 25, as marked by the red circle. The fringes around the re-deposited precipitate are thicker compared to those that are in the sample. Other techniques such as chemical elemental mapping can be used to differentiate a re-deposited precipitate from those already found in the sample are discussed in Section 6.4.1.1.

5.2.2.2 FIB-induced defects/ artefacts

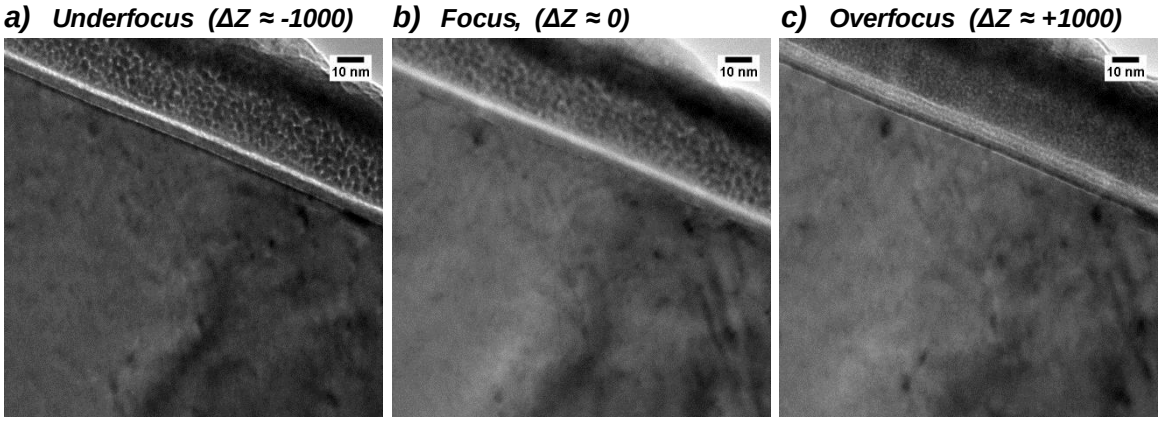


Figure 26: Focal series showing a section of the surface condition of a FIB lift-out TEM specimen. (a) an underfocus bright-field micrograph imaged at ΔZ ≈ -1000 nm, (b) a focus bright-field micrograph imaged at ΔZ ≈ 0 nm and (c) an overfocus bright-field micrograph imaged at ΔZ ≈ + 1000 nm.

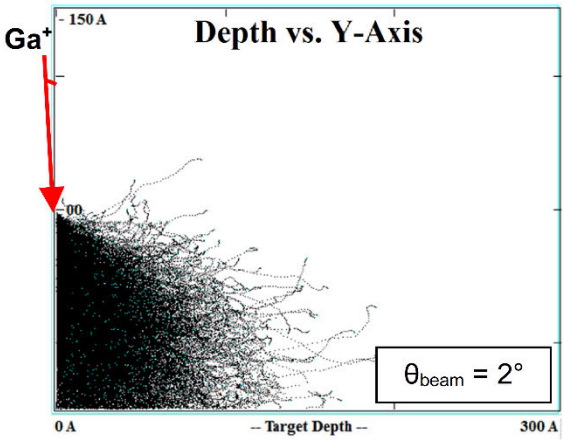
Surface defects or re-deposition of precipitates can be prevented by using the focused ion beam (FIB) milling technique. This technique has been successfully used as a means to prepare ultrathin TEM specimens with a specific grain orientation of interest for high resolution imaging. Figure 26 shows the quality of the surface of the sample membrane that was produced using FIB milling. No obvious surface craters were found in under-focused and over-focused images, as shown in Figure 26 (a) and Figure 26 (b).

There are some drawbacks with FIB milling despite it being a robust technique that is capable of producing an ultrathin specimen. The TEM specimens that were prepared using the FIB milling were often found to have ion beam irradiation-induced defects at the sub-surface of the specimens [143, 173]. The accelerated ions that have sufficient energy will result in some degree of microstructural disruption at the sub-surface of a material. It is important to note that these FIB induced damages are very similar to those produced by neutron irradiation. This is because both ion and neutron irradiation produced the similar type of displacement cascade events in the materials. A basic difference between ion and neutron irradiation is that the depth of penetration of neutron irradiation is far greater than ions. One of the reasons for this is due to the

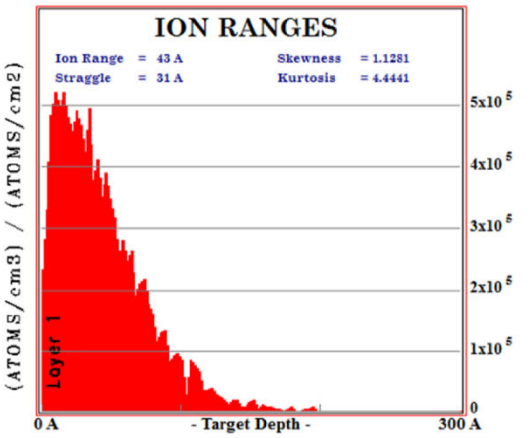
interaction between the charged ion and the interacting atoms in the materials. The differences between neutron and ion irradiation will not be further discussed in this study as this topic is not the focus of this study. More detailed scientific explanations regarding the ions and solid interactions or the neutrons and solid interactions are documented in Ref. [174].

An amorphous layer is often observed from FIB lift-out TEM specimen. For many crystalline materials, there exists a critical implantation dose, above which the lattice disruption caused by the irradiation-induced damages is so extensive that the material is amourphised [142]. Previous studies have shown that these irradiation-induced damages can be reduced and minimized by using a lower beam energy, lower incident beam angle and mill at low temperature by using a liquid-nitrogen cold stage [143, 144]. In order to reduce the irradiation-induced damage onto the FIB lift out TEM specimens used in this study, beam damage simulation was used to optimise the quality of the specimens. Computer-aided calculations of ion-solid interaction, such as the 'Transport of Ions in Matter' (TRIM), that was based on the understanding of random statistical nature of linear collision cascade dynamics was used to estimate the ions beam irradiation induced damages and the depth of the damage on iron. Figure 27 shows the TRIM Monte Carlo (MC) simulated irradiation-induced damage into the sub-surfaces of the iron. These simulations were calculated based on the FIB milling condition used to prepare TEM specimens. The corresponding maximum penetration depth of gallium ions and the maximum depth of vacancies produced is summarised in Table 11. Note that the TRIM MC simulation treats all targets as amorphous [175]. Hence, any contributions due to the crystallographically dependent phenomena that will affect the irradiation-induced damage will somehow underestimate or overestimate the damage induced by the gallium ion beam.

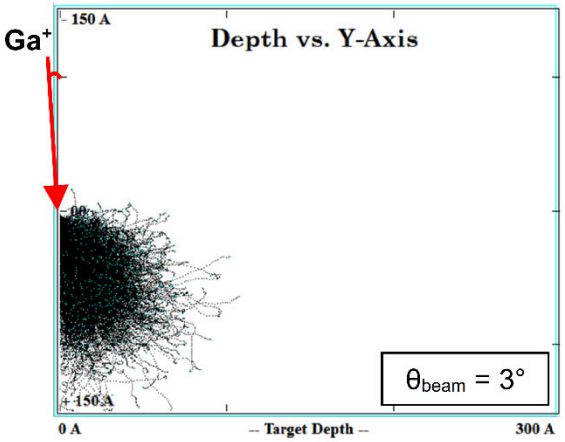
a) 30 keV Ga^+ beam at 2°



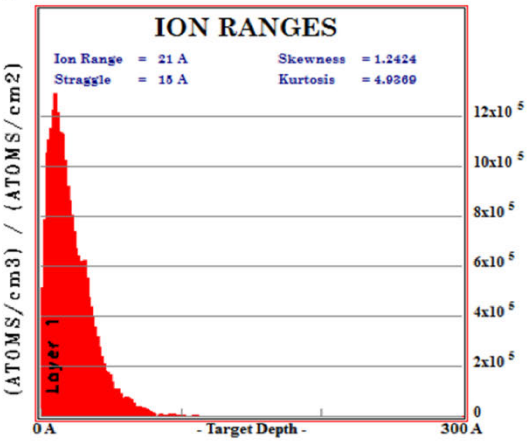
b)



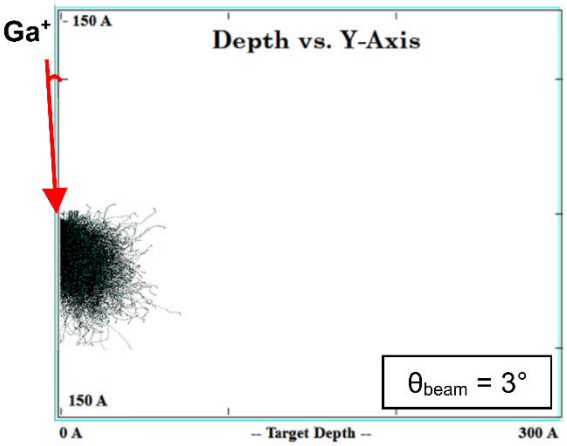
c) 10 keV Ga^+ beam at 3°



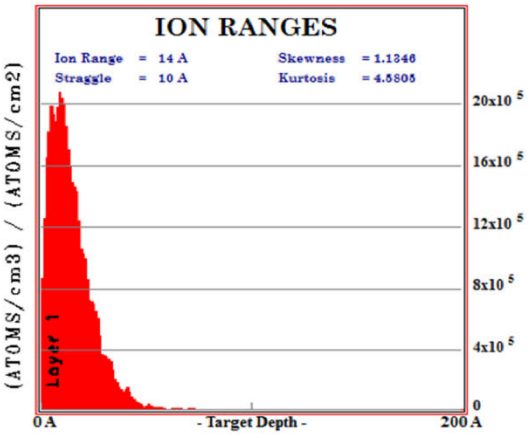
d)



e) 5 keV Ga^+ beam at 3°



f)



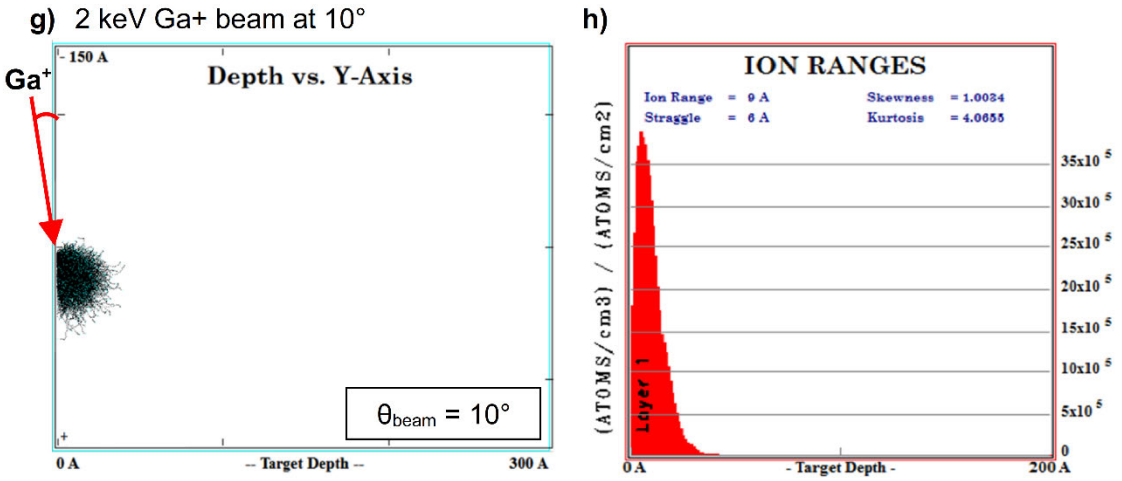


Figure 27: TRIM Monte Carlo simulations of the damage cascades for gallium ion beam energy used for FIB lift-out into iron. (a) 30 keV at an incident angle, θ = 2°, (c) 10 keV at an incident angle, θ = 3°, (e) 5 keV at an incident angle, θ = 3°, (g) 2 keV at an incident angle, θ = 10°, and (b, d, f & h) are the corresponding gallium ion penetrated ranges into iron was that calculated by the 'Stopping and Range of Ions in Matter' (SRIM) simulations.

Table 11: Summary of TRIM Monte Carlo simulations regarding the beam energy of gallium ions and its respective maximum depth of penetration and maximum depth of vacancies produced.

Beam energy (kV)	**Beam incident angle** (°)	**Penetration depth** (Å)	**Depth of vacancies produced** (Å)
30	2	200	100
10	3	100	54
5	3	75	34
2	10	45	21

Figure 28 shows that the FIB-induced damage observed at $< 111 >_{BCC}$ zone axis was significantly reduced after low keV Ga cleaning. Minimum irradiation-induced damage was observed from the specimen that was finished with 2keV gallium ions beam energy. This observation is in good agreement with the TRIM MC simulations and also previous studies documented in Refs. [143, 173, 176]. However, even with the lowest beam energy in the FIB milling machine available, i.e. 2 keV, a significant amount of

matrix damage were still observed in the FIB-lift out specimens. A $g.b$ analysis were performed in order to learn about the nature of these matrix damages induced into the sample with a 2 keV gallium ions beam. The series of diffraction contrast micrographs used for the $g.b$ analysis are shown in Figure 29.

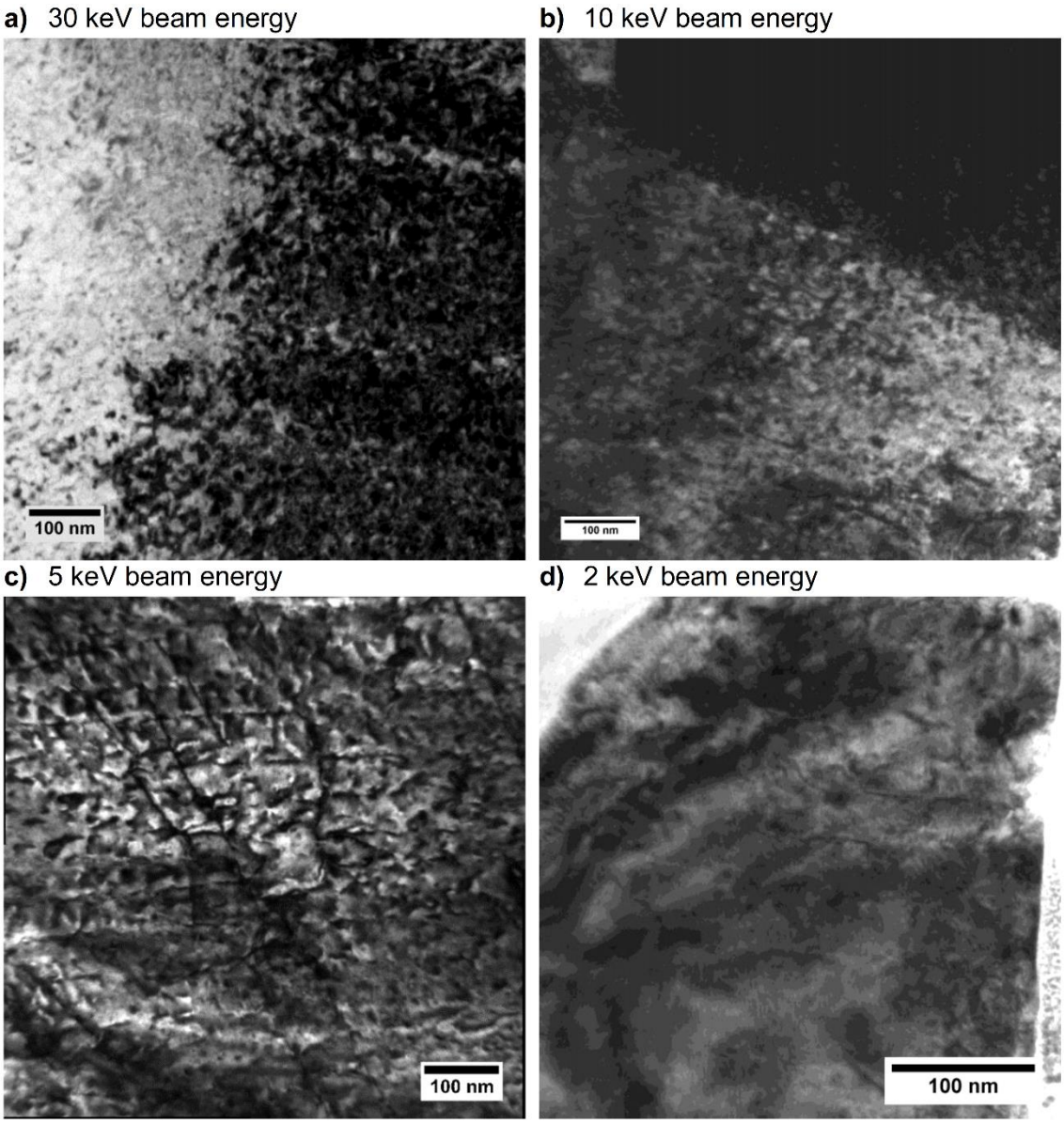
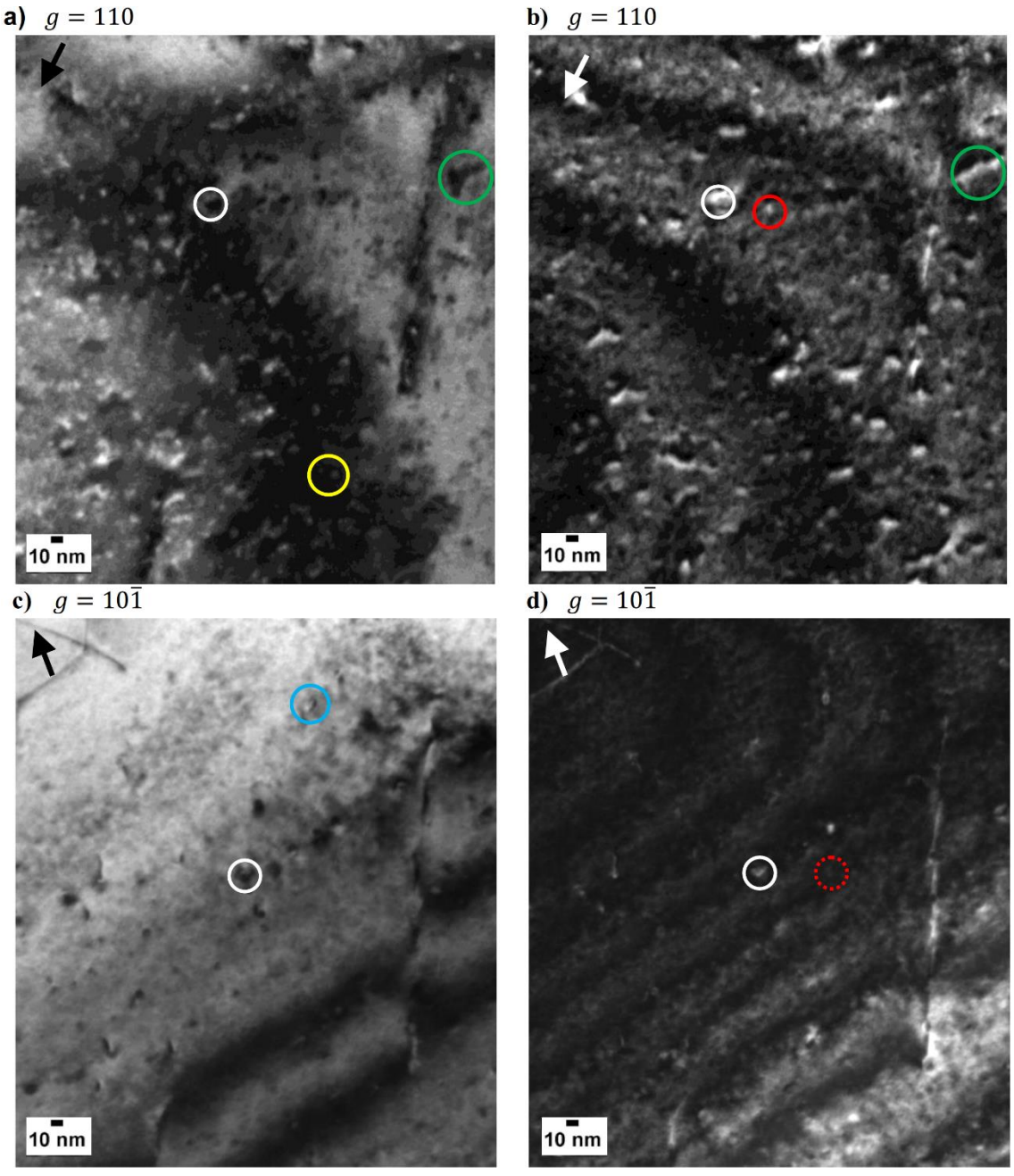


Figure 28: Bright-field down-zone micrographs showing the irradiation-induced damages that correspond to the FIB milling condition used. (a) 30 keV gallium ions beam and incident beam angle, θ = 2°, (b) 10 keV gallium ions beam and incident beam angle, θ = 3°, (c) 5 keV gallium ions beam and incident beam angle, θ = 3°, and (d) 2 keV gallium ions beam and incident beam angle, θ = 10°. These micrographs were imaged at the $< 111 >_{BCC}$ *zone axis.*


a) $g = 110$
b) $g = 110$
c) $g = 10\bar{1}$
d) $g = 10\bar{1}$
10 nm
10 nm
10 nm
10 nm

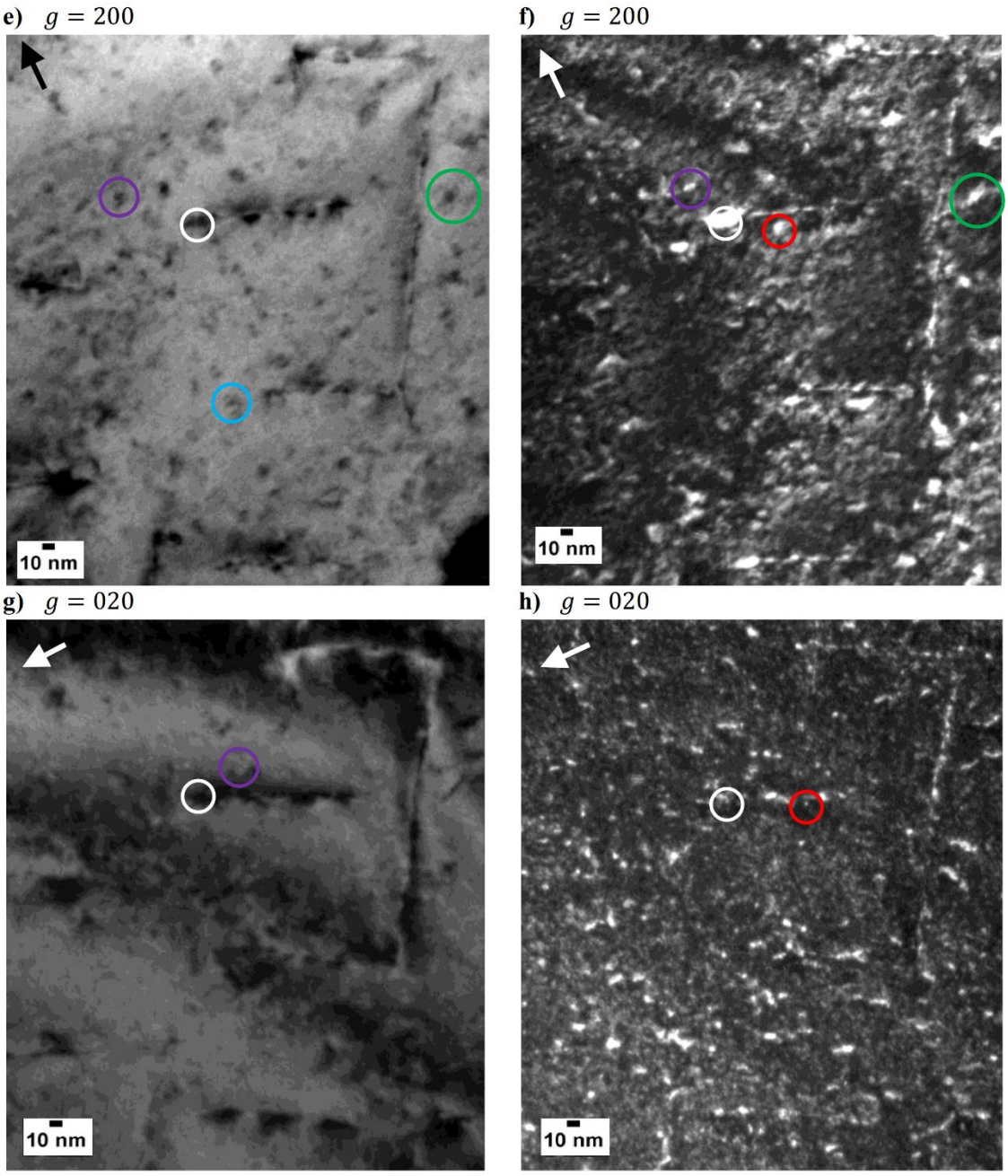


Figure 29: A series of diffraction contrast micrographs imaged from WV weld metal that have been thermally aged for 49,800 hours under two-beam conditions. (a & b) Bright-field and dark-field micrographs imaged using $g = (1\bar{1}0)$, *(c & d) Bright-field and dark-field micrographs imaged using* $g = (10\bar{1})$, *(e & f) Bright-field and dark-field micrographs imaged using* $g = (200)$, *and (g & h) Bright-field and dark-field micrographs imaged using* $g = (020)$.

5.2.2.2.1 Type of matrix defects induced by FIB

A complicated microstructure was observed in the FIB-lift out TEM specimen used to study the matrix defects induced by the ion beam. Note that, this specimen is WV weld steel that has been thermally aged for 49,800 hours. It contains nanometre scale precipitates that were formed during thermal ageing. Some of these precipitates are thought to be coherent with the matrix. Three types of matrix defects that were induced by the FIB in the specimen were identified from the series of diffraction contrast micrographs shown in Figure 29. These matrix defects are amorphous zones, disorder zones and dislocation loops.

5.2.2.2.1.1 Amorphous zones

The evidence for the amorphous zones in the FIB-lift out membrane is shown in Figure 29 (a). This image was obtained in a bright-field under dynamical two-beam conditions, using $g = 1\bar{1}0$. Note that on the brighter side of the thickness fringe, the amorphous zone appears as dark dots against the white background, whereas the contrast is in reverse when it is on the darker side of the thickness fringe. At the transition region, i.e. at the thickness fringe, the amorphous zones appear as dark dots with white centres. One of the examples is marked by a yellow circle in Figure 29 (a). This is a typical contrast for the amorphous zone that arises due to the different structural-factor compared to the matrix, hence, resulting in a different extinction distance, from the surrounding matrix. Further details regarding the structure-factor contrast can be found in Ref. [144].

5.2.2.2.1.2 Disordered zones

The contrast for the disordered zones is very similar compared to the amorphous zones. This is because both defects become visible due to the different structural-factors compared to the matrix. The disordered zone arises due to the displacement cascade events. It is produced at the cascade site and is often observed in ordered

alloys that have been bombarded by fast particles, including heavy-ions. Even though it shows a contrast like the amorphous zones, it can be differentiated by imaging the same region with a kinematical two-beam condition with a different diffraction vector, preferably a non-superlattice reflection. In the kinematical bright field micrograph, dislocation loops were often found to be associated with the disordered zones. The details of identifying the disordered zones are well documented in Ref. [144]. One of the disordered zones was found in Figure 29 (a), marked by a green circle. The corresponding dislocation loop is shown in Figure 29 (h).

5.2.2.2.1.3 Dislocation loops

The contrast of dislocation loops varied according to its nature and type. The well-known two-beam imaging technique used to identify dislocation loops relies on a set of $g.b$ analysis to determine the loop burgers vectors by applying the invisibility criterion $g.b = 0$. The details of this technique are documented in Refs. [144, 177]. Note that it is impossible to differentiate between dislocation loops induced by neutron or ion irradiation.

From the bright-field and dark-field micrographs obtained with different diffraction vectors, as shown in Figure 29, no resolvable dislocation loops, i.e. loops that are bigger than 3-4 nm were found. Non-resolvable dislocation loops, also known as black dots in the bright-field images or white dots in the dark-field images, were observed. One of which is marked by a red circle in Figure 29 (h). Based on Table 12, this white dot is most likely to be a $^1/_2\,[1\bar{1}1]$ type.

Table 12: Values of $g.b$ for Burgers vector determination for dislocation loops in a BCC lattice – low alloy steel

h	k	l	$\frac{1}{2}[111]$	$\frac{1}{2}[\bar{1}11]$	$\frac{1}{2}[1\bar{1}1]$	$\frac{1}{2}[11\bar{1}]$	[100]	[010]	[001]
2	0	0	1	−1	1	1	2	0	0
0	2	0	1	1	−1	1	0	2	0
1	$\bar{1}$	0	0	−1	1	0	1	−1	0
1	0	$\bar{1}$	0	−1	0	1	1	0	−1

5.2.3 Electron beam induced defects/ artefacts

TEM is a technique where an electron beam is transmitted through a thin sample. The sophisticated interactions between electrons and the material generate different signals which allow us to understand the structural information of the material. The interaction of electrons and materials can be categorized to two types – (1) Elastic interaction and (2) Inelastic interaction. These interactions are strongly dependent on the energy of the incident electron beam.

In the elastic interaction, electrons scattered elastically by changing its direction while it passes through the well-organized atoms in a three dimensional spacing. These electrons are involved in the formation of images and diffraction patterns. In the inelastic interaction, electrons scattered in-elastically by changing both its direction and losing energy to atoms that interact with each other and its surroundings. These electrons make chemical analysis, such as EELs and EDS, possible.

If the energy of an incident electron beam is sufficient, i.e. higher than the energy required to knock-off atoms from its equilibrium position at its lattice and/or energy required to sputter atoms close or at the surface from its equilibrium position, both the elastic and inelastic scattered electrons will induce damages, like Frenkel defects, within the sample [178, 179]. This event is the most common type of electron beam irradiation effects. So far, electron beam irradiation effects can be differentiated into 4 types [180]:

1) Ionization effects:

   This induces the decomposition in long polymer chain structures but not metals.

2) Heating effects:

   This is caused by the interaction of incident electrons and phonons in the materials. This effect does not have significant influence on materials with high thermal conductivity, especially metals.

3) Knock-on effects:

   As mentioned earlier, this induces radiation damages, for example small interstitials and vacancies clusters on the sample by knocking-off atoms from its equilibrium position.

4) Sputtering effects:

   This induces displacement of surface atoms and formed pits or cavities on the surface of the sample.

For low-alloy steel, the common electron irradiation effects are knock-on effects and sputtering effects. The defects induced by these effects may be present during the microstructural analysis by TEM.

5.2.3.1 Knock-on effects

The knock-on effects can be described by the following equation,

Equation 2:

$$E_t = \left[\sqrt{100 + AE_d}/5 - 10\right]/20 \quad [180]$$

Where E_t is the transferred energy, Ed is the energy of the incident beam, and A is a constant associated with the chemical element. To allow atoms to be knocked from its equilibrium position from its lattice, the energy of the electron will need to be greater than that of the threshold energy of a material. For low alloyed steel, the threshold

energy for knocking-off an iron atom is an incident electron beam of 400 kV [180]. Hence, an incident electron beam between 200 kV and 300 kV will probably not induce any defects on the sample.

5.2.3.2 Surface sputtering effects

The surface atoms required a lower threshold energy in order for them to be displaced from their equilibrium position. This is due to the unsaturated chemical bonding on the surface [180]. The threshold energy for the iron atom to be displaced from the surface is 4 – 8 eV [180]. The calculated energies transferred to an iron atom for an incident electron beam of 200 kV and 300 kV are 9.4 eV and 15.3 eV, respectively [180]. The calculations suggest that the surface atoms of a low alloyed steel type of TEM specimen will be displaced by an electron beam of 200 kV and 300 kV. Surface damages were observed from low alloyed steel TEM specimen after it was exposed to the electron beam of both 200 kV and 300 kV.

Figure 30 shows two sets of micrographs of areas that were exposed to an incident electron beam of 200 kV for (a & b) less than thirty minutes and (c & d) for more than two hour. No features apart from dislocation lines were shown on Figure 30 (a & b). However, after a long duration of exposure under an electron beam of the same energy as Figure 30 (a & b), i.e. 200 kV, surface features of pits and cavities were visible on a slightly defocus micrograph. Figure 31 shows the surface pits and cavities induced by an electron beam of 300 kV. These surface features became visible after about an hour of exposure under the electron beam. Figure 32 (b) shows the surface pits and cavities in a high angle annular dark field image. The contrast of these surface damage appeared in dark indicating that the average atomic number, Z_{avg}, of the region is lowered compared to its surrounding. This contrast is real due to the projected thickness of the surface pits and cavities is thinner than the surrounding matrix.

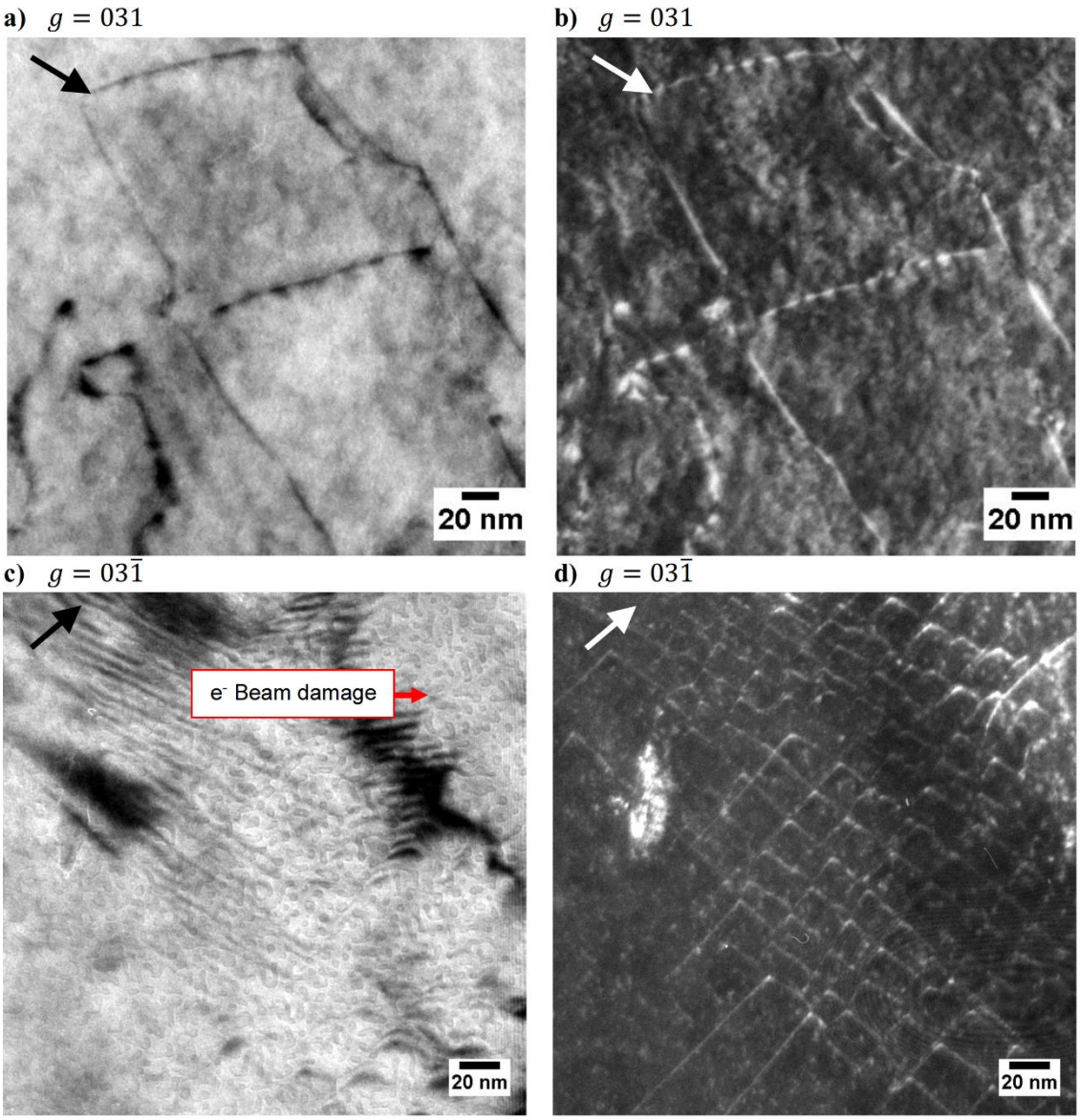


Figure 30: Electron beam damages on the surface of a low alloyed steel TEM specimen caused by a 200 kV electron beam under TEM mode; (a & b) BF and DF micrographs after being exposed to an electron beam for less than thirty minutes; (c & d) BF and DF micrographs after constant exposure under an electron beam for more than two hours. All micrographs were imaged at slightly defocus under a kinematic two-beam condition with $g = 03\bar{1}$.

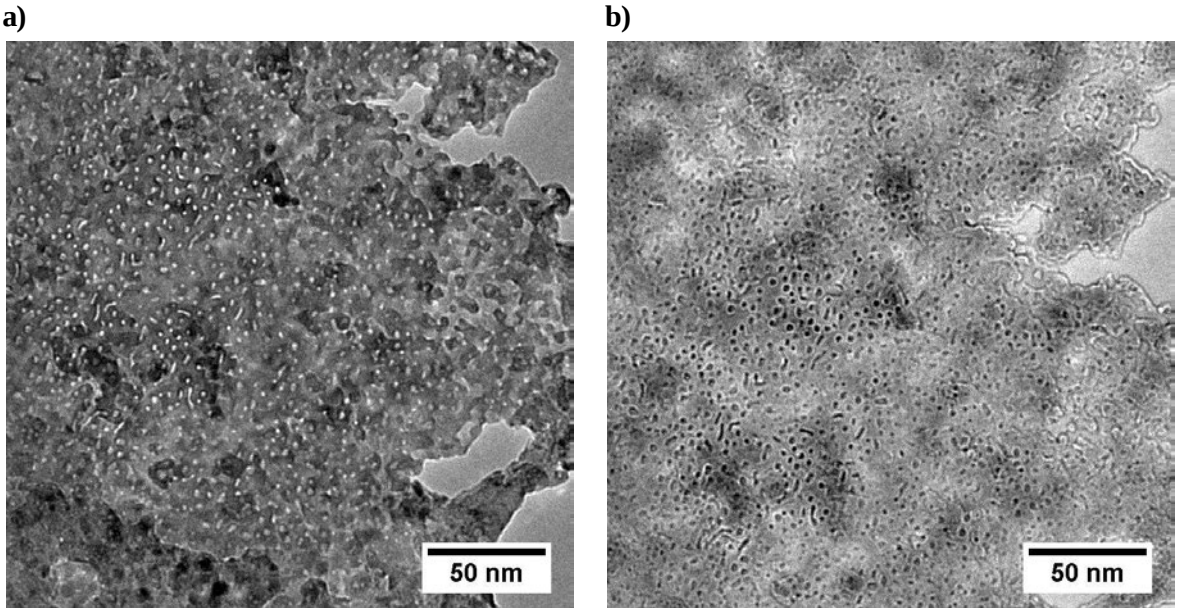


Figure 31: Electron beam damages on the surface of a low alloyed steel TEM specimen induced by a 300 kV electron beam under TEM mode; (a) BF micrograph imaged at underfocus (ΔZ = -2000 nm) and (b) BF micrograph imaged at overfocus (ΔZ = +2000 nm) after being exposed to an electron beam for about an hour.

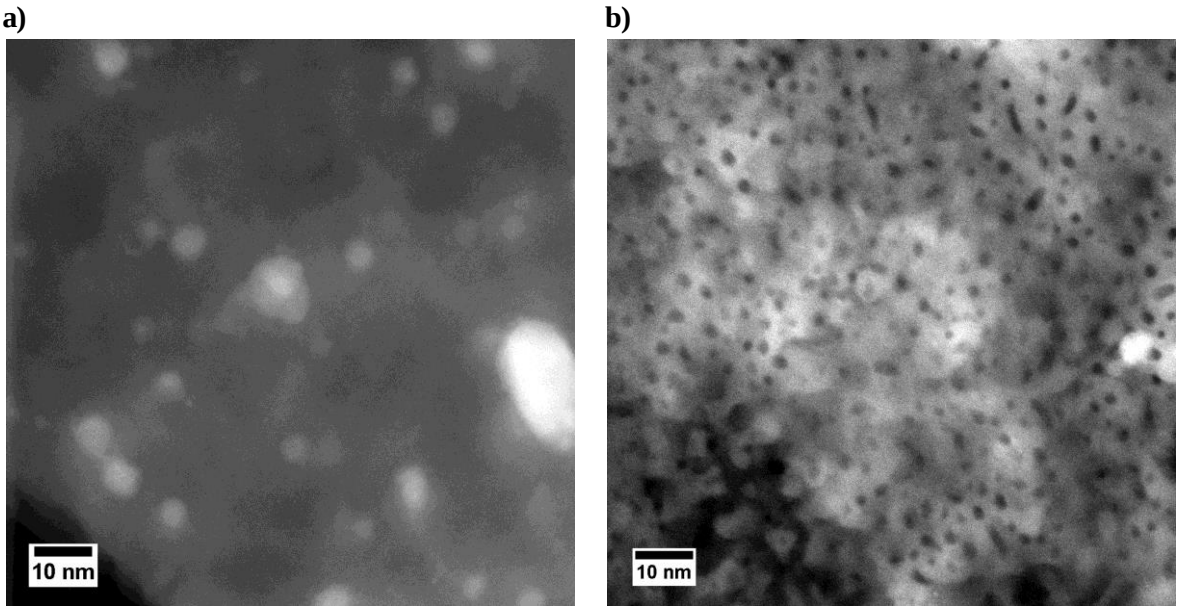


Figure 32: High angle annular dark field image of the region shown in Figure 31 at higher magnification; (a) region free from electron beam induced damages and (b) region with electron beam induced damages

The amount of time required for an electron beam of 200 kV to induce surface pits and cavities of the size that are visible under a transmission electron microscope was approximately twice the amount of time required for an electron beam of 300 kV. This is consistent with the ratio of energies transferred to iron atoms for an incident electron beam of 200 kV and 300 kV.

Previous studies also shown that the energy transfer to surface atoms is dependent on the relative angle between the incident beam and the surface of a TEM specimen [181]. The tilted or oblique surface will decrease the threshold energy required to displace an atom from its surface. Hence, increase the rate of sputtering. This was also observed during the diffraction contrast experiment. Figure 33 shows the surface damages induced by an electron beam of 300 kV after tilting the specimen 15° towards the beam. The structure or shape of the surface damages are elongated compared to those induced at 0°, as shown in Figure 31. This is believed to be due to the projecting angle of the electron beam and surface of the TEM specimen.

Note that the contrast of the surface pits and cavities that are shown under underfocus and overfocus imaging conditions which is very similar to voids and nanometre scaled solute clusters with lower average density and/or average atomic number compared to the iron matrix. It is possible to misinterpret the surface damages induced by an electron beam of high energy ($> E_{threshold}$).

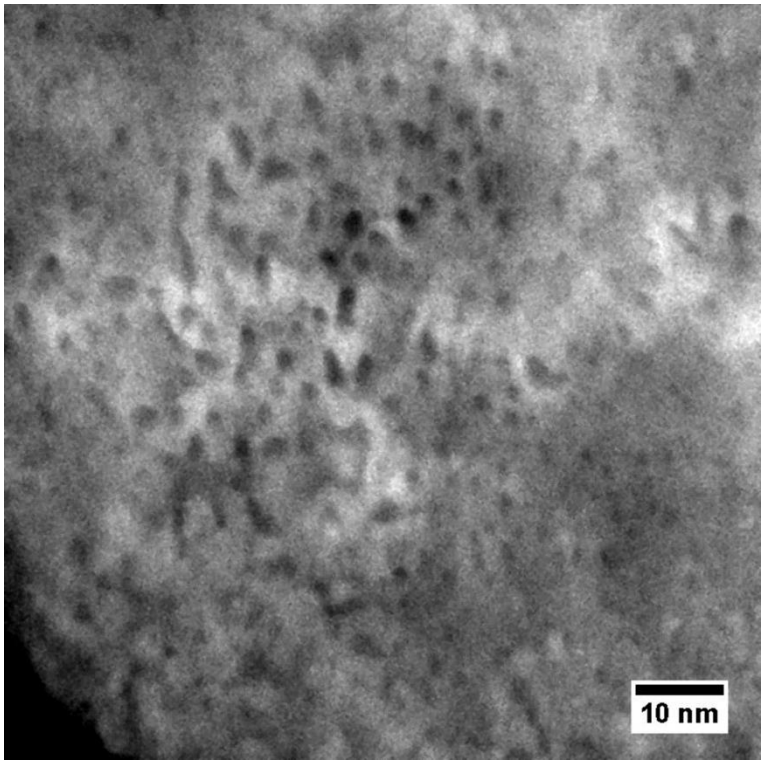


Figure 33: HAADF micrograph that shows the electron beam damages on a tilted surface of a low alloyed steel TEM specimen after being exposed to an electron beam of 300 kV under TEM mode

5.3 RADIATION DAMAGE

The fast neutron irradiation of crystalline materials causes displacement of the lattice atoms. The continuation of this event generates stable matrix defects that cause degradation of mechanical properties in the crystalline materials, hence the term radiation damage. A careful diffraction contrast experiment, i.e. $g.b$ analysis, on suitable flat electron-transparent regions of the thin TEM specimens allows us to characterise the concentration, size, geometry and nature (interstitial or vacancy) of these matrix defects. Note that by using this technique only the matrix defects that are above the visibility limits (≈ 2 nm) can be resolved. So far, several types of matrix defects have been identified in low alloy steels after the sample was neutron irradiated to high neutron fluence. These are mainly dislocation loops and vacancy clusters, also known as nanometre scale voids. Note that, dislocation loops and vacancy clusters are

not the focus of this study. However, it is important to be able to differentiate them from the feature of interest of this study, i.e. nanometre-scale precipitates/solute clusters.

5.3.1 Identifying dislocation loops

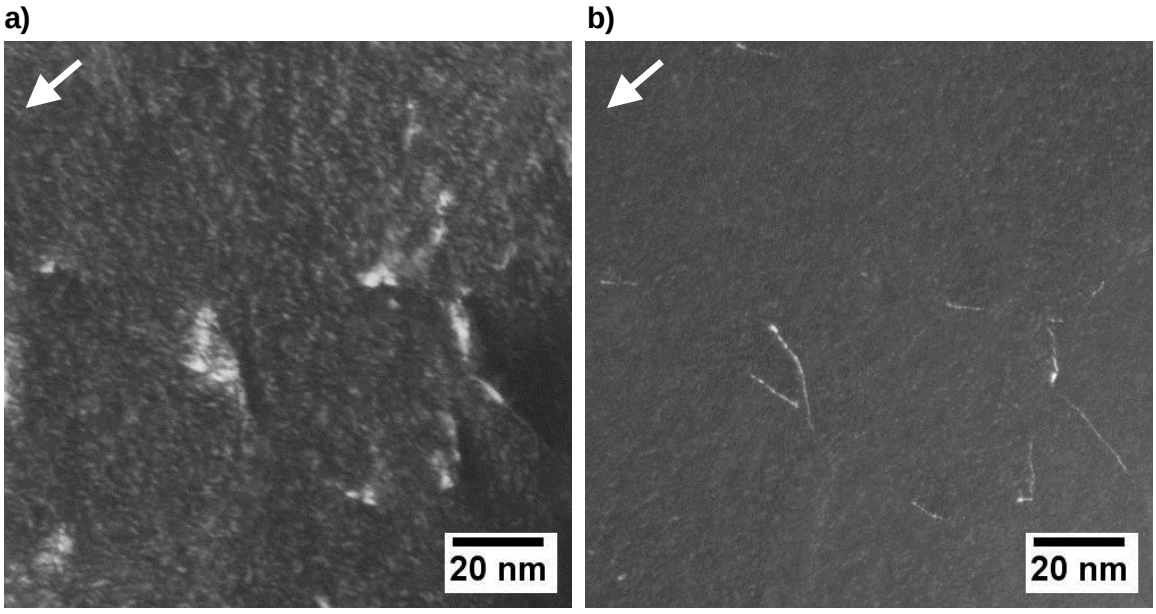


Figure 34: Dark-field micrographs imaged from ANP-6 that have been neutron irradiated up to 5.22 x 10^{23} neutrons.m^{-2}. (a) Dynamical two-beam condition with $s_g \approx 0$ and (b) kinematical two-beam condition with $s_g \approx 2.1\ x\ 10^{-1} nm^{-1}$; with the diffraction vector, $g = 002$.

The method employed to characterise the dislocation loops or point defects clusters are well documented in Refs. [144, 182-184]. The contrast of these loops under the two-beam conditions is generally weak and complicated. This is due to its low elastic strain contrast. Nevertheless, for quantitative measurements, under a suitable condition such as weak beam dark field with a deviation parameter, $|s_g| \geq 2\ x\ 10^{-1} nm^{-1}$, the small dislocation loops will show a better contrast relative to the background. Also, under this condition, the contribution of the oxides fringes onto the background can be minimised. An example is shown in Figure 34. Note that with a background like that of Figure 34 (a), it is difficult to differentiate between the small unresolved dislocation loops and the oxide fringes. The number density and size of the dislocation loops can be measured for the analysis that correlates the number density and size of these

defects with the changes of ductile-brittle transition temperature of the steels after neutron irradiation.

An example of identifying dislocation loops is shown in Section 5.2.2.2.1. Note that the size of the neutron irradiation-induced dislocation loops in the low alloy steels are very small (around the visibility limit of diffraction contrast analysis) even at a high neutron fluence, $\phi t \approx 5 \times 10^{23}$ neutrons.m^{-2} [108, 185].

5.3.2 Identifying voids

'Out-of-focus' imaging was used to identify nanometre-scale voids, if any, from the neutron irradiated materials. It is the same imaging technique used to identify surface features induced during sample preparation or coherent precipitates in the materials. The details of these techniques are documented in Refs. [144, 147]. Note that this technique is capable of imaging voids that are smaller than 5 nm. In order to confirm the presence of small voids, bright-field through-focal series is often recorded with the foil tilted well away from the Bragg condition for all reflections.

The contrast of voids in the out-of-focus micrographs is almost identical to those of surface craters. One of the methods used to differentiate voids and surface craters is to carry out a stereo measurement. Also, another method is to measure the thickness of the over- or under-focus fringes appearing around a void and surface crater. Due to the differences in the change of focus height of surface craters and voids, it is possible to distinguish between those that are surface craters, i.e. surface craters will show thicker out-of-focus fringes compared to those features in the sample.

5.4 Precipitates & Solute Clusters

The identification of precipitates and solute clusters is of great importance for this work. It has been well known that it is extremely difficult to identify irradiation-induced solute clusters or thermally aged coherent precipitates that have been detected by APT using

EM. This is mainly due to the size of these precipitates and the lack of elastic strain of these precipitates in the matrix or their coherent nature. In this study, the author attempts to use various type of conventional and advance electron microscopy techniques to identify nanometre-scale precipitates and solute clusters. The three type of imaging mechanisms and corresponding contrast were used to visualise the precipitates and solute clusters in the materials and are as follows:

1. Diffraction contrast

   This contrast is based on the differences in crystalline structure and/or orientation between the matrix and the precipitates. It is sensitive to lattice misfits, such as dislocations.

2. Phase contrast

   This contrast is based on the interferences between the direct electron beam and diffracted beams.

3. Mass-thickness contrast

   This contrast is based on the differences of absorption of electrons in different materials.

5.4.1 Diffraction (Strain) contrast imaging

The visibility of small coherent precipitates using the matrix deformation or the elastic strain-field of the precipitates is documented in Refs. [145, 186]. With two-beam diffraction conditions, the coherent precipitates appears like a pair of dark lobes separated by a line of no contrast (strain-contrast lobes), as shown in Figure 35. These coherent precipitates are marked by red circles. The direction of the line of no contrast is perpendicular to the direction of g. The smallest coherent precipitate that can be imaged using this technique is ≈ 2 nm. Apart from coherent precipitates, precipitates that were induced by deformation within the surrounding matrix were also visible. This

is due to the lattice misfit between the precipitates and the matrix, resulting in elastic strain induced to the surrounding matrix. The elastic strain contrast of the precipitates is shown in Figure 35. Note that, the contrast of the coherent precipitates could be mistaken as non-edge-type dislocation loops under two-beam diffraction conditions. This is because both of them appear like a pair of dark lobes separated by a dislocation line of no contrast that are perpendicular in the direction of the g-vector used. It is possible to differentiate them from one another. The dislocation loops must satisfy the invisibility criteria of $g.b = 0$ whereas the coherent precipitates do not. Hence, a series of two-beam diffraction condition micrographs is necessary in order to distinguish between these features.

a) $g = 10\bar{1}$ **b)** $g = 10\bar{1}$

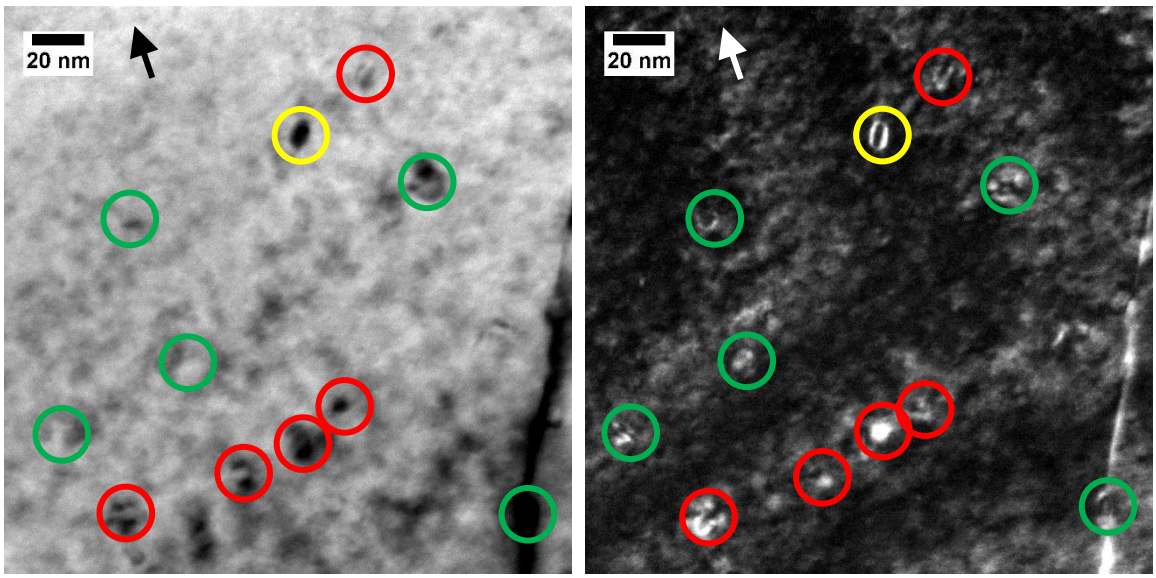


Figure 35: Dynamical two-beam bright field micrographs imaged with $g = 10\bar{1}$ from thermally aged WV weld steels.

5.4.3 Phase contrast imaging

Through-focal series imaging is also used to identify coherent precipitates in the materials. The phase contrast of a coherent precipitates arises from the change in mean inner potential between the precipitates and the matrix. Details of this method are documented in Ref. [147, 187]. The resolution of this technique is governed by the spatial frequency of the exit-wave of the electron beam. With a large spatial frequency, smaller precipitates of less than 2 nm will be visible. The relative atomic density of the precipitates can also be visualised through this techniques. Precipitates that are lighter than the matrix are with bright contrast for under-focused micrograph and dark contrast for over-focused micrograph and are vice versa for those precipitates that are heavier than the matrix.

Those precipitates that are lighter than the matrix share the same transition of fringe contrast from underfocus to overfocus compared to voids and surface craters. The differentiation between the lighter precipitates and surface craters are very similar compared to the differentiation between voids and surface craters. This method is mentioned in Section 5.3.2. As for the methods to make a distinction between voids and lighter precipitates, a persuasive approach is by chemical analysis. If this technique is not available, diffraction contrast imaging will be able pick up the elastic strain field around the lighter precipitates and, as a result, distinguish them from voids.

5.4.4 High resolution electron microscopy (HRTEM)

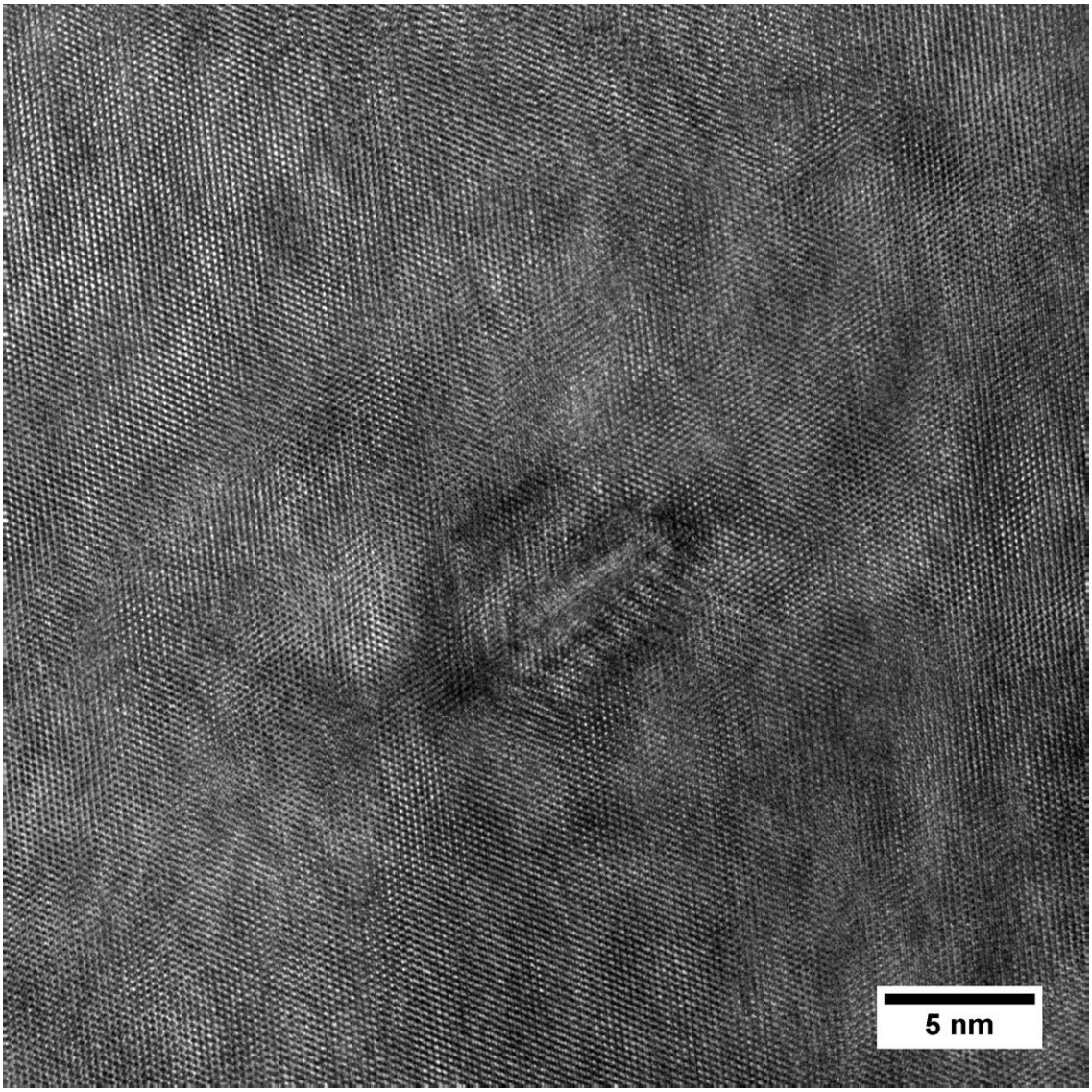


Figure 36: HRTEM micrograph showing a 9R precipitate that formed in WV weld steel that aged for 18,620 hours. This micrograph was imaged at $< 111 >_{BCC}$ *zone axis.*

HRTEM that uses multiple diffracted beams to produce phase contrast images is also employed to visualise the structure of a precipitate. The atomic lattice fringes are useful for identifying the very small second phase precipitates. The lattice images of the surrounding matrix enabled information on the precipitate structure and precipitate-matrix orientation relationship to be deduced. One of the examples is shown in Figure 36. The figure shows a 9R precipitates visible at $< 111 >_{BCC}$ zone axis. Further

structural information of the 9R structure was discussed in Section 3.1.2.1. The description of the HRTEM image theory is documented in Refs. [188, 189].

5.4.5 Scanning transmission electron microscopy (STEM)

It is effective in identifying nanometre-scale precipitates using high angle annular dark field (HAADF) imaging technique. The precipitates will appear in brighter contrast if the precipitates were constituted with heavier solute atoms compared to the matrix and/or with denser structure compared to the matrix. The reverse contrast will observed if the precipitates were constituted with lighter solute atoms and/or loose structure.

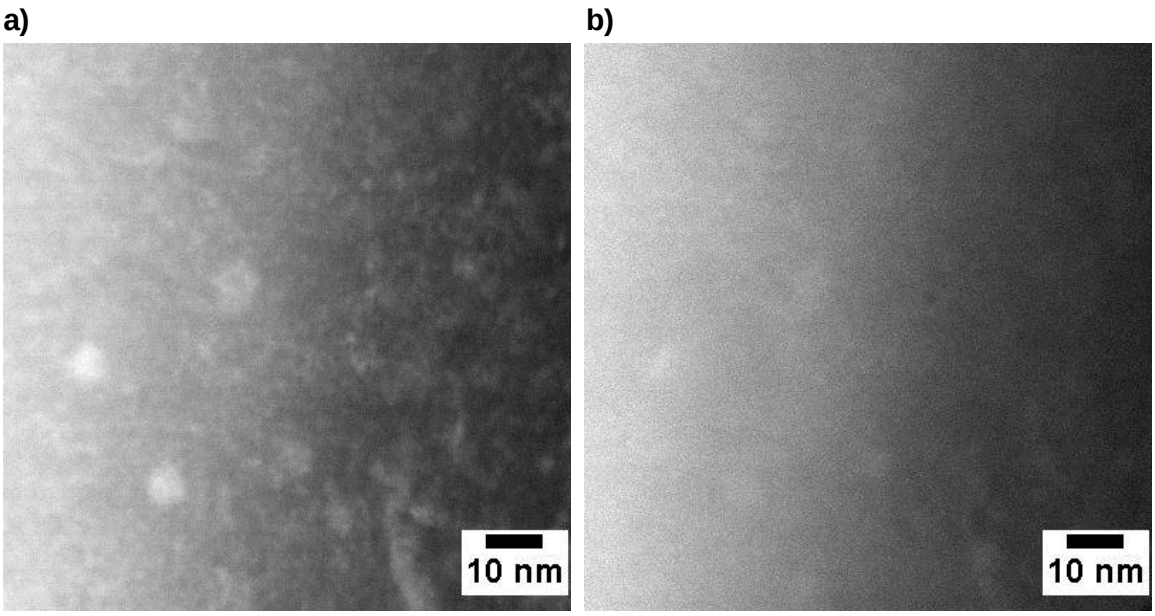


Figure 37: STEM micrographs showing precipitates that formed in the WV weld steel that aged for 49,800 hours. (a) Annular dark field micrograph and (b) High angle annular dark field micrograph.

For precipitates that have similar average Z-number and structure compared to the structure, these precipitates will not be easily identified using Annular Dark Field (ADF) and/or HAADF. An example is shown in Figure 37 (b). The nanometre-scale precipitates have a weak contrast under the HAADF even though they are copper enriched. This is because of these precipitates is located at a relatively thick region. The thicker matrix has significant reduced the contribution of the copper precipitates

onto the average local Z. In order to enhance the contrast of these precipitates, lower angle annular dark field is used, as shown in Figure 37 (a).

5.4.6 Elemental mapping

Chemical analysis is the most effective technique to identify the presence of nanometre-scale precipitates. However, it strongly depends on the availability of EDX or EELS spectrometers on the electron microscope used and the capability of these detectors. A modern EDS or EELS detector permits high resolution chemical analysis on nanometre-scaled precipitates with a diameter that less than 2 nm. One of the EELS results collected is presented in Figure 38 and Figure 39. Note that, the precipitates are not obvious in the HAADF image. They become clearly visible under these elemental maps.

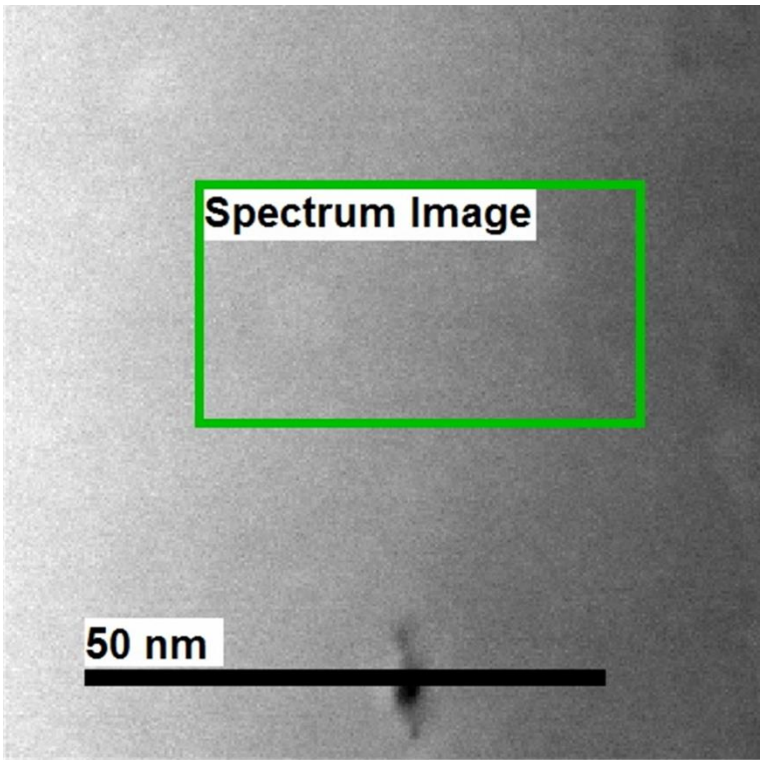


Figure 38: HAADF micrograph showing region of interest that have been analysed by EELS.

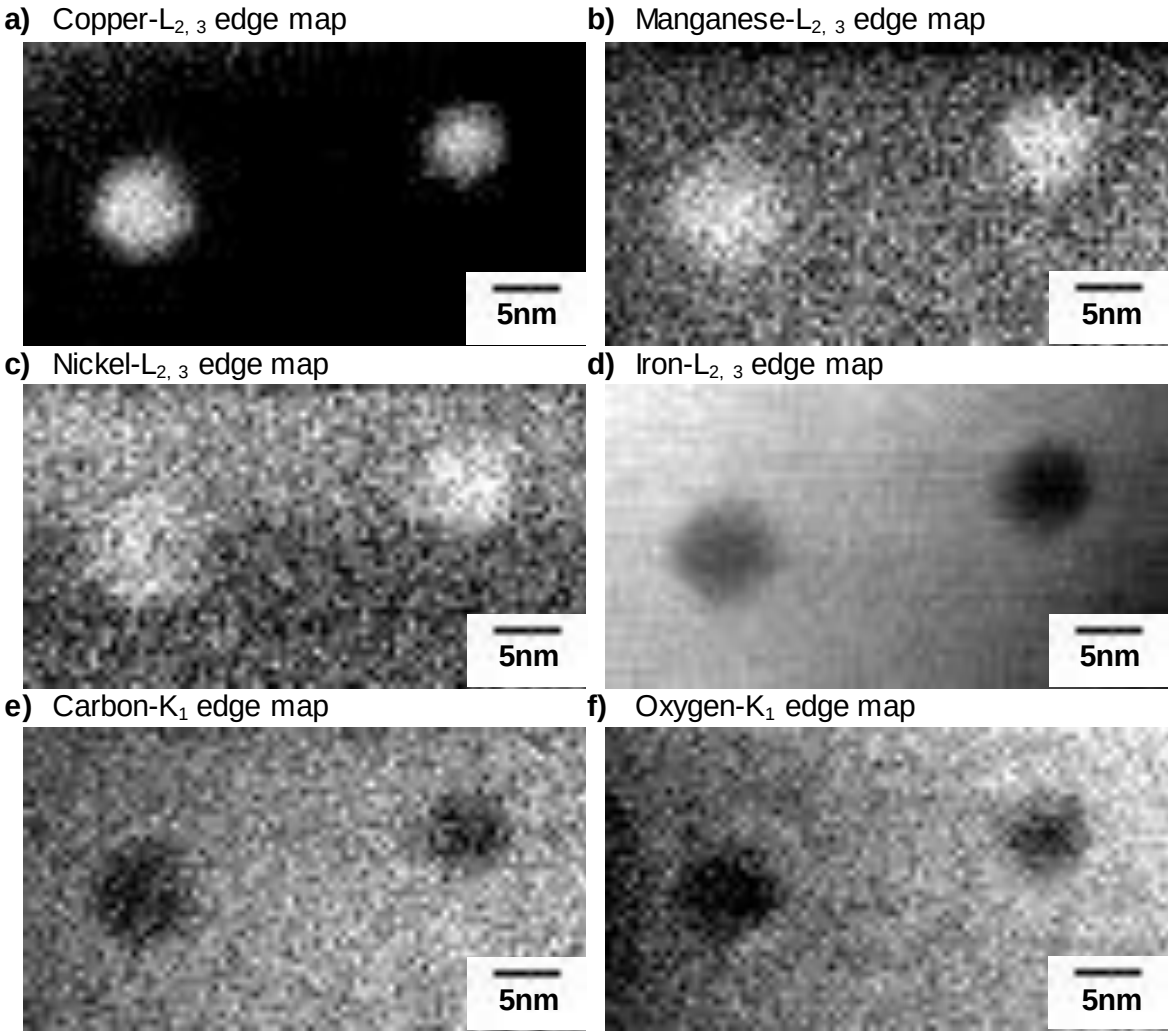


Figure 39: MSA reconstructed elemental maps from the region of interest shown in Figure 38. (a) Copper-L2, 3 edge map, (b) manganese-$L_{2,3}$ edge map, (c) nickel-$L_{2,3}$ edge map, (d) iron-$L_{2,3}$ edge map, (e) carbon-K_1 edge map, and (f) oxygen-K_1 edge map.

6 THERMALLY AGED PRECIPITATE

6.1 INTRODUCTIONS

This chapter describes electron microscopy results from a thermally aged WV weld steel which has been subjected to thermal ageing at 365 °C for 18,620 hours and 49800 hours. The aim of this study was to investigate the effects of long term thermal ageing on the precipitation in a typical nuclear low alloy steel because there is very limited information available on real engineering steels with greater than 20,000 hours ageing at temperature comparable to the operation conditions of the reactor pressure vessel of a nuclear fission power plant. In addition, even though many studies in the past have been performed to understand copper precipitation in Fe-Cu based steels, for example Fe-Cu binary alloys, tertiary Fe-Cu based alloys with the third chemical element being either nickel or manganese, and Fe-Cu-Mn-Ni quaternary alloys, not much information is available on the copper precipitation in real engineering steels, especially on the effect of alloying additions on the precipitation. Weld steels thermally aged for 18,620 hours were previously studied by Dr. G. Sha [190], and so this weld steel thermally aged for 49,800 hours will be the focus for this study. Atom Probe Tomography (APT) analysis on the same material has been carried out by Dr. P. D. Styman and the results can be found in his thesis and are drawn on here to compare with the TEM data presented in this chapter [35].

The details of the manufacturing process and thermal ageing conditions are given in Section 4.1.2.1. Section 6.2 describes the results from experiments carried out using the Conventional Transmission Electron Microscopy (CTEM) technique on material thermally aged for 18,620 hours and 49,800 hours. Information on the precipitate structure was obtained by a combination of bright-field and dark-field imaging with the specimen foil tilted to a series of low-index poles. The results of a High Resolution Transmission Electron Microscopy (HRTEM) investigation into the precipitate

structures is describe in section 6.3. Section **Error! Reference source not found.** hows the results of chemical elemental mapping using EELS and/or EDS in the Scanning Transmission electron Microscopy (STEM) mode. Further discussion on the collected information obtained from these techniques and comparison with the APT results is presented in Section 6.5.

6.2 CONVENTIONAL TRANSMISSION ELECTRON MICROSCOPY

Nanometre scale precipitates are visible under diffraction contrast imaging in the WV weld steel after being thermally aged for both 18,620 hours and 49,800 hours.

WV weld steel after thermal ageing for 18,620 hours

Precipitates formed in the weld steel after thermal ageing for 18,620 hours appear in darker contrast in bright-field down-zone micrographs, as shown in Figure 40 at low magnification. Note that a large number of these precipitates are observed to be associated with dislocation lines. At higher magnification, as shown in Figure 41, the thermally aged precipitates appear as a pair of dark lobes separated by a 'line of no contrast'. One of the examples of this characteristic contrast is marked by a red circle on Figure 41. This contrast is a typical contrast for small coherent or semi-coherent spherical or elliptical precipitates, as discussed by Ashby and Brown [145, 186]. This typical contrast of coherent precipitates is not obvious in Figure 40 mainly due to the effects of magnification and the limited number of pixels available on the Charge-Coupled Device (CCD) camera.

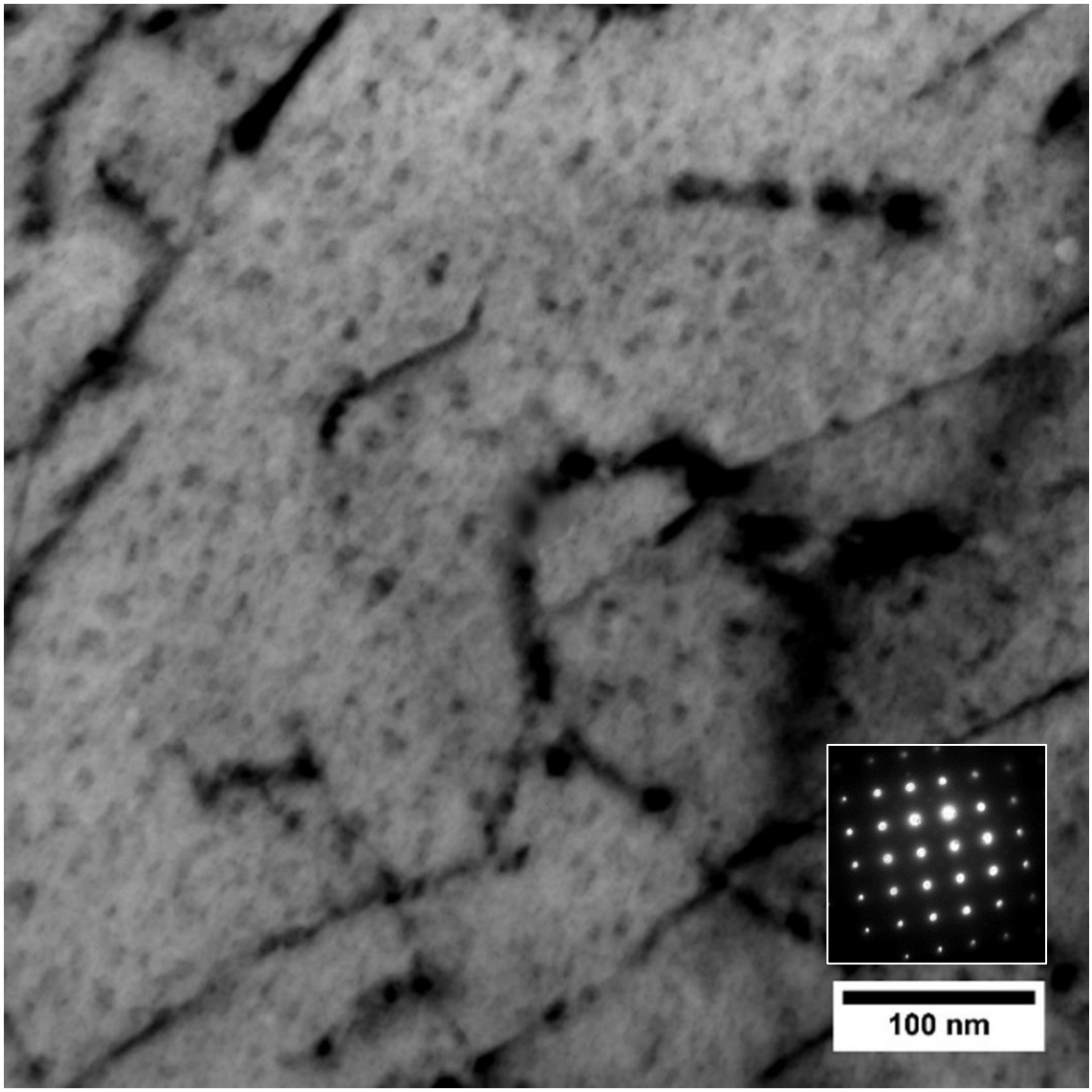


Figure 40: Low magnification micrograph showing precipitates in the WV weld steel after thermal ageing for 18,620 hours at 365 °C, imaged in a bright-field down-zone condition with the foil accurately tilted to the $< 001 >_{BCC}$ pole. Darker contrast features are the thermally aged precipitates.

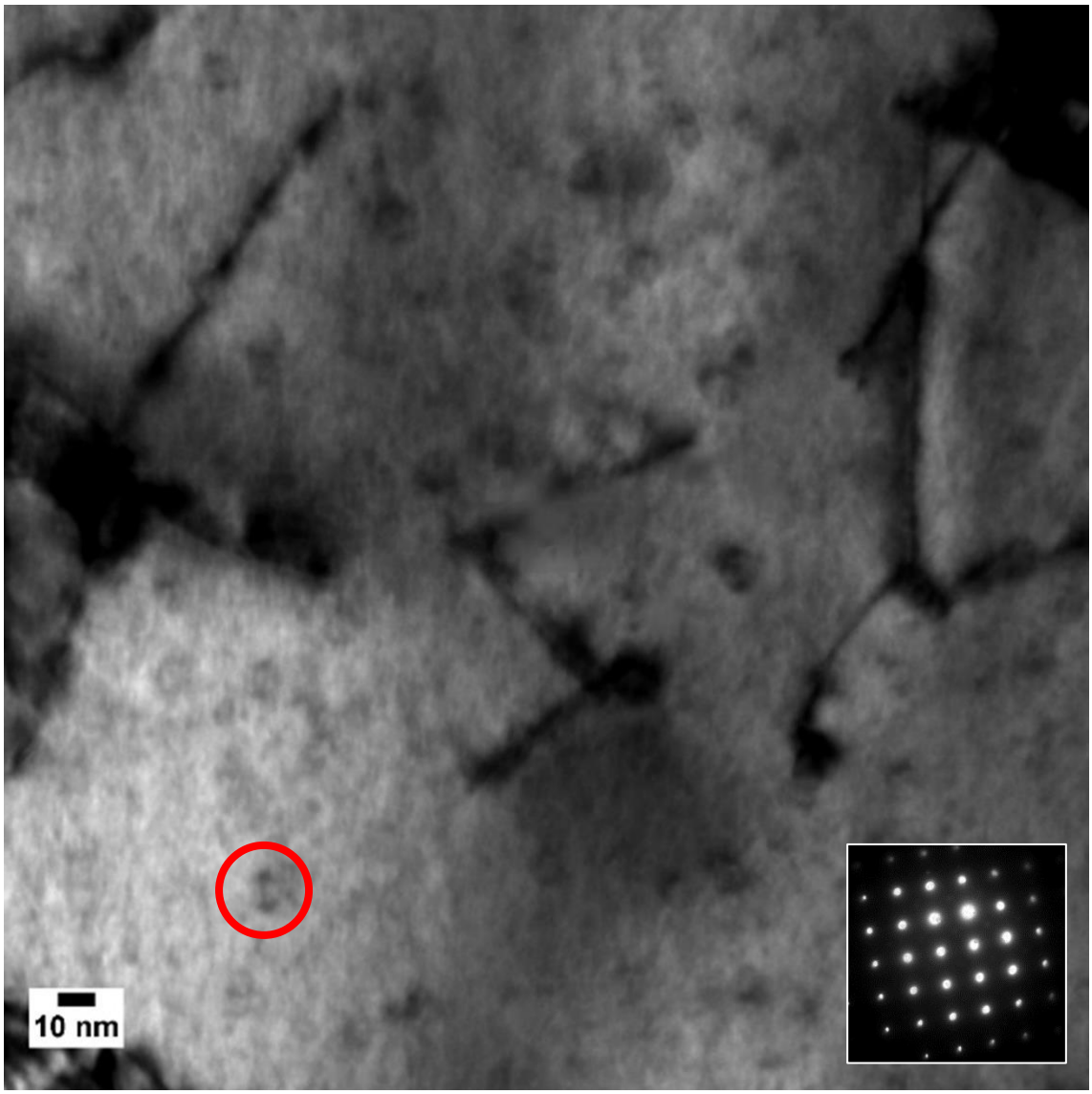


Figure 41: A higher magnification micrograph showing precipitates in the WV weld steel after thermal ageing for 18,620 hours at 365 °C, imaged in a bright-field down-zone condition with the foil accurately tilted to the $< 001 >_{BCC}$ pole; with a focus value, z slightly lower than zero (≥ 50) . Precipitates appears like two dark lobes separated by a line of no contrast, as indicated by the red circle

WV weld steel after being thermally aged for 49, 800 hours

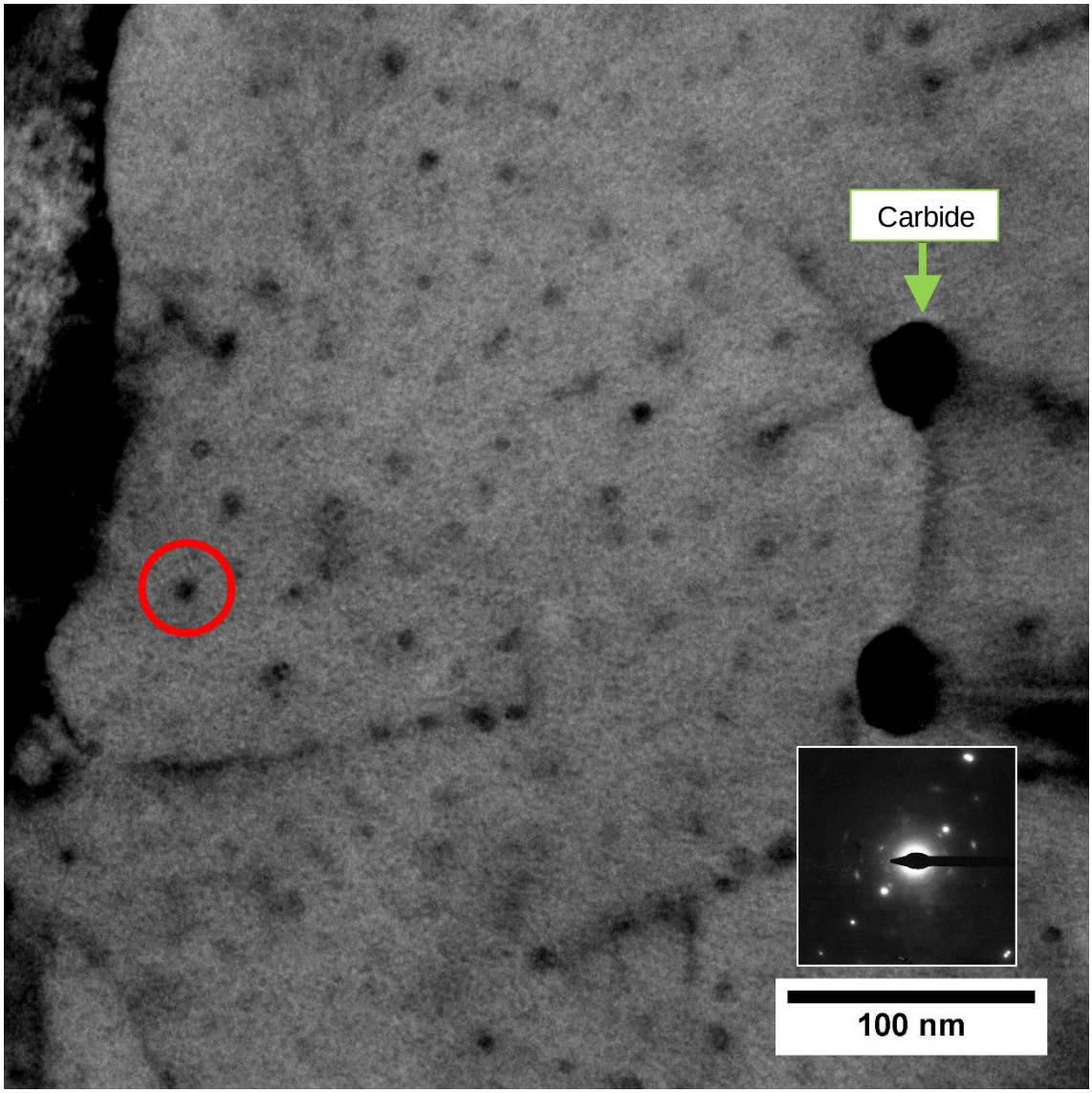


Figure 42: Low magnification bright-field micrograph showing precipitates in the WV weld steel after thermal ageing for 49,800 hours at 365 °C. The small darker contrast spherical features are the thermally aged precipitates, one of them indicated by the red circle.

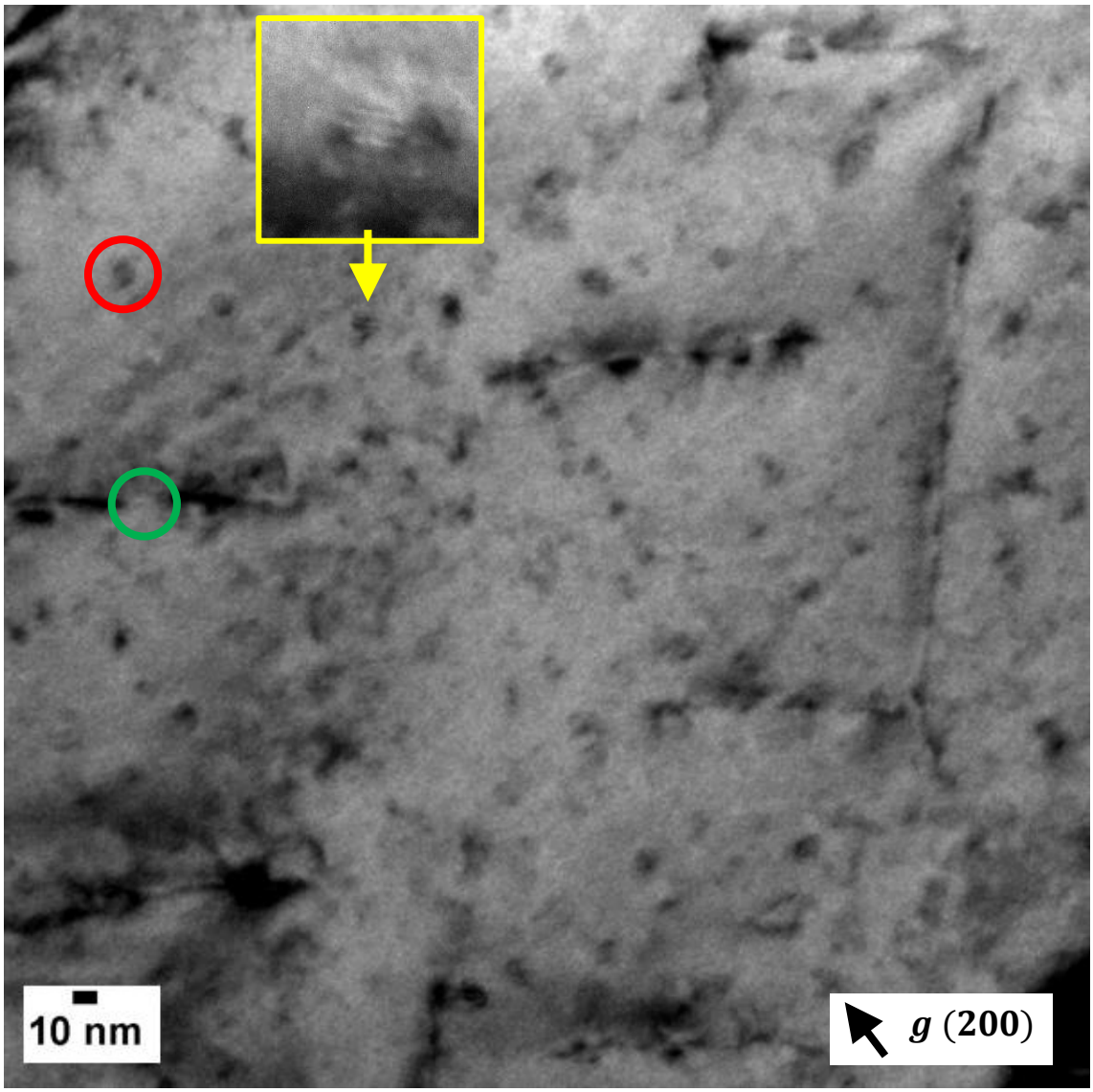


Figure 43: A higher magnification micrograph showing precipitates in the WV weld steel after thermal ageing for 49,800 hours at 365 °C. This micrograph was imaged in a two-beam dynamical bright-field condition, using $g = (200)$ *close to* $< 001 >_{BCC}$ *pole. Precipitates appears like two dark lobes separated by a line of no contrast, as indicated by the red circle. The line of no contrast is perpendicular to the direction of g. This contrast indicates that these precipitates are spherical or elliptical in shape. Some of these precipitates show internal banded contrast, of which one is identified at by the yellow arrow.*

The precipitates formed in weld metal after thermal ageing for 49,800 hours are also visible in a bright-field micrograph, as shown in Figure 42 that was imaged along a random diffraction condition. The precipitates appear as dark spherical features, as one which is marked by a red circle. The visibility of these precipitates is lower compared to those that were imaged in bright-field down-zone condition or in two-beam kinematical or dynamical bright-field condition.

At a higher magnification, a two-beam dynamical bright-field micrograph shows the precipitates appear again as a pair of dark lobes separated by a 'line of no contrast' indicating that these precipitates are coherent or semi-coherent with the matrix, one of which is marked by a red circle in Figure 43. The line of no contrast that is shown on these precipitates is perpendicular to the direction of the reciprocal lattice vector, i.e. *g*-vector used to form the image. This observation is similar to those precipitates observed in weld steels after 18,620 hours. Since this contrast is induced by the strain field of the precipitates in surrounding matrix, the visibility of these precipitates and its direction of the 'line of no contrast' will change according to the diffraction condition set-up and the *g*-vector used.

Precipitates that showed an internal banded contrast were also observed in Figure 43, as indicated by the yellow arrow with an enlarged insert of this image. The same observation was also reported by Othen et al. [65] and will be further discussed in Section 6.2.1. Note also that lower strain contrast or no strain contrast is observed at a dislocation line decorated by a precipitate. An example is indicated by the green circle in Figure 43. The possible explanation for this observation is that the strain fields induced by the dislocation line is relaxed locally by the presence of the precipitates, as a result no or little resulting strain contrast is observed [191].

By comparing these typical micrographs from the weld steel aged for 18,620 hours and 49,800 hours, no distinctive differences was found under both ageing condition, in terms of precipitate coherency with the matrix and distributions of precipitates within a

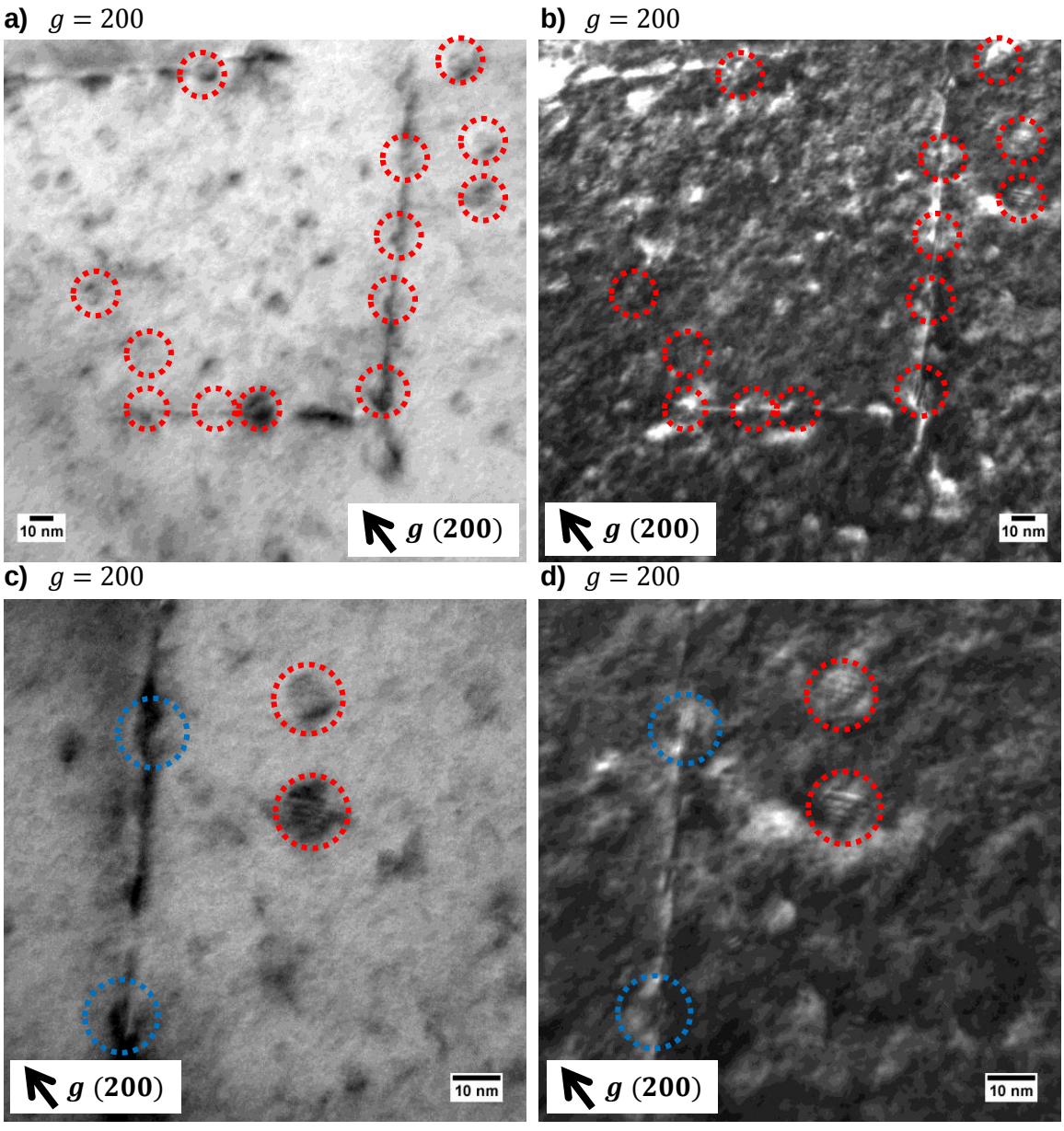
grain. In both materials a significant fraction of precipitates are associated with a dislocation line apparently nucleated at these dislocation lines.

6.2.1 Banded precipitate structure

A series of two-beam dynamical bright-field and dark-field micrographs taken at diffraction conditions with the deviation parameter, $s_g \approx 0$, from the weld steel thermally aged for 49,800 hours are shown as Figure 44. Figure 44 (a, b, c, & d) and (e, f, g, & h) were imaged using a reciprocal lattice vector of $g = (10\bar{1})$ in the $< 101 >_{BCC}$ pole and $g = (200)$ in the $< 001 >_{BCC}$ pole, respectively. Two groups of precipitates can be observed in these micrographs; ones with a banded structure observed within the precipitate in both bright-field and dark-field images, and ones appearing like a pair of dark lobes separated by a 'line of no contrast', also known as 'strain contrast lobes' [53]. After measuring of the diameter of these two groups of precipitates, it was found that average size of the banded structure precipitates were larger than 9 ± 2 nm, whereas the other group of precipitates were smaller than 9 ± 3 nm (the measurement for this group of precipitates was made using the extent of the 'line of no contrast'). It is important to note that these measurements have a high error since they are based on the precipitate contrast shown from the images. This contrast is strongly affected by the depth of the precipitates from the surface of the foil and the precise diffraction condition used [144, 145]. For example the deviation parameter s_g, extinction distance ξ_g, and the reciprocal lattice vector *g*.

The former group of banded structure precipitates were also reported by Othen in his study of phase transformation of copper precipitates in ferritic iron matrix [65]. Othen showed that this banded contrast within the precipitates is due to structural variations within the precipitates rather than a Moiré interference fringe effect, as the banded contrast within the precipitate does not change direction when imaged using a different reciprocal lattice vector, *g,* and only appears when a particular reflection is close to the Bragg condition.

From the diffraction contrast analysis performed in this study, we can see that the visibility of these structural bands in the precipitates is dependent on the reciprocal lattice vector, *g*. The structural bands were observed in most precipitates when a reciprocal lattice vector $g_{BCC} = \{200\}$ in the $< 001 >_{BCC}$ pole was used for imaging. No new diffraction spots from the precipitates could be observed. This is due both to the small volume, and previous studies have shown that a majority of the precipitate reflections for the 9R and FCC structures are very close to the strong matrix reflections at the $< 001 >_{BCC}$ and $< 110 >_{BCC}$ diffraction pattern [65]. Therefore the dim diffraction spots from the precipitates are hidden by the glare of the nearby matrix reflections.



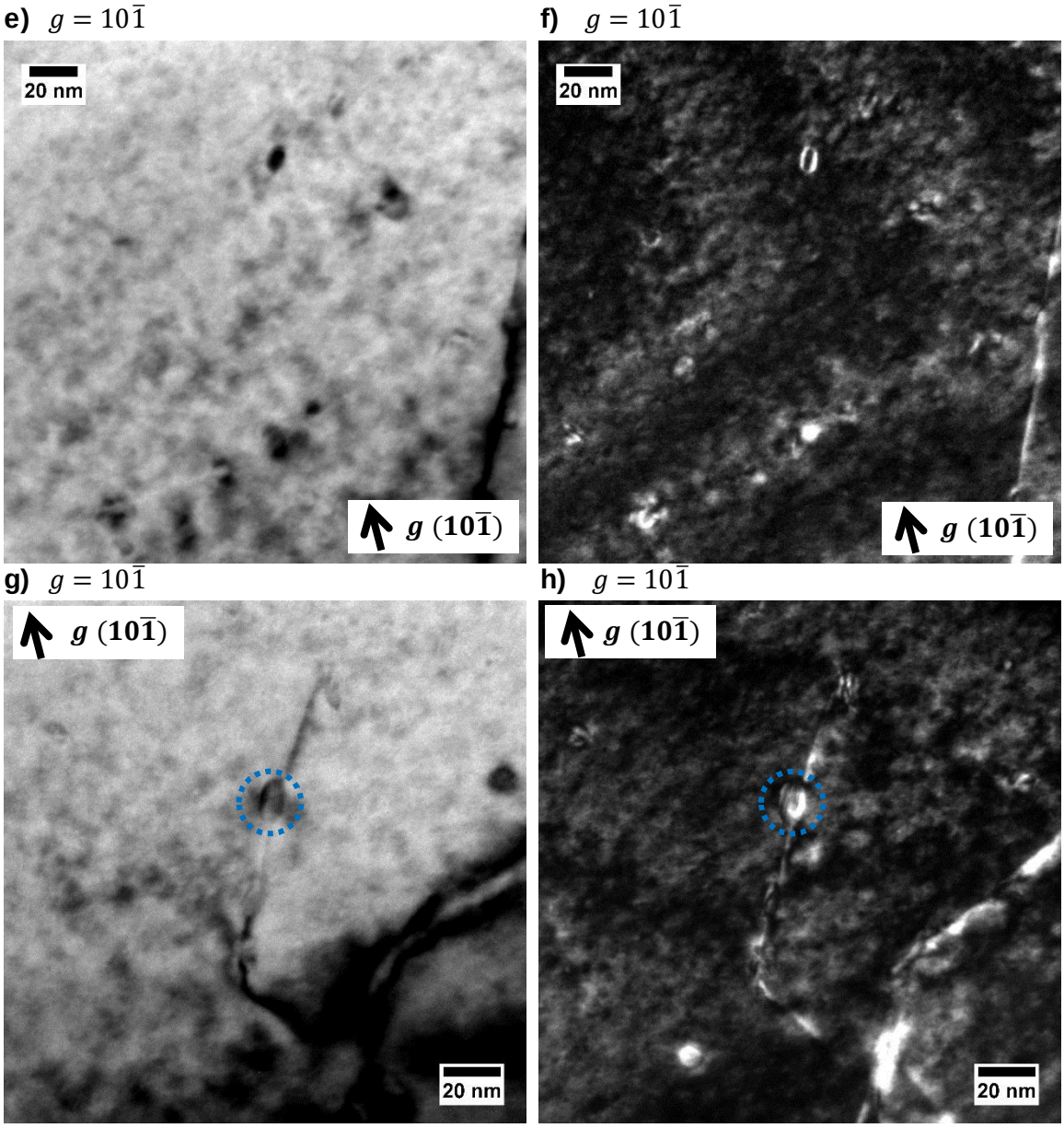


Figure 44: (a, c, e, & g) Series of 2-beam kinematic bright-field micrographs of the same region from the same specimen as Figure 43. These micrographs were imaged using different diffraction vectors. The diffraction vector for (a & d) was $g = (200)$ in the $< 001 >_{BCC}$ pole and (e & g) was $g = (10\bar{1})$ in the $< 101 >_{BCC}$ pole; (b, d, f, & h) Complementary 2-beam kinematic dark-field micrographs for (a, c, e, & g) respectively. Precipitates showing internal banded contrast are marked with red dotted-line circles

6.2.1.1 Banded structure orientation

Two types of structural bands within the precipitate can be observed in Figure 44. Each type of structural bands is marked with a different colour of circles, i.e. red and blue. These structural bands are thought to occur due to twinning and/or stacking faults

observed in the intermediate transformed phases of the copper-rich precipitates, i.e. 9R and 3R structures.

The precipitates marked with red dotted circles are possibly twinned 9R precipitates since the bands in this type of precipitate are parallel to a matrix $< 110 >_{BCC}$ direction lying in the appropriate zone axis. The orientation of these bands was found to be consistent with the orientation of the twins of a twinned 9R structure precipitate reported previously in Refs. [53, 65, 73]. The shape of these precipitates appears to be spherical with an average diameter of 10 ± 2 nm. The average spacing between each band is 1.5 ± 0.2 nm. This spacing between the bands is close to that of twins in 9R precipitates reported in Ref. [53], i.e. 1.4 nm.

Another type of precipitate also shows Moiré fringes. The fringe orientation is independent of the diffraction vector, *g*. These precipitates are marked with blue dotted circles. I believe that these precipitate are untwinned-3R precipitates. These precipitates are elliptical, with the elongated direction parallel to a matrix $< 110 >_{BCC}$ direction, and have an average diameter of 13 ± 2 nm and an average bands spacing of 1.12 ± 0.10 nm. The average Moiré fringe spacing is consistent with the spacing in the 3R structure of Moiré fringes that corresponded to the $(003)_{3R}$ planes [65, 73]. The elongated direction of these precipitates is also consistent with the direction of growth of FCC copper-rich precipitates.

6.3 High Resolution Transmission Electron Microscopy

In order to confirm the nature of the structural bands observed within these precipitates and also the structure of the precipitates in WV weld steel, HRTEM analysis was carried out. The sample foil was tilted to $< 001 >_{BCC}$ or $< 111 >_{BCC}$ zone axes with respect to the matrix.

6.3.1 Un-twinned 9R precipitates

Figure 45 shows high resolution micrographs of the banded structure of typical precipitates imaged along the $< 001 >_{BCC}$ zone axis. These precipitates are close to spherical in shape and have diameters between 3 and 5 nm. From the direction of the $\{110\}_{BCC}$ matrix lattice fringes, it can be seen that the interface between the regions of parallel fringes lies along to one of the matrix $\{110\}_{BCC}$ planes. These fringes are thought to correspond with either the stacking faults present on the $(009)_{9R}$ planes of a 9R precipitate or the uniformly spaced twins that are present in a twinned 9R precipitate. The average fringe spacing is approximately 0.50 ± 0.15 nm. It is useful to note that the stacking faults observed in the HRTEM images reported from previous studies, i.e. Refs. [53, 65], have the same orientation and, within the errors of measurement, the same spacing as the fringes observed these precipitates along the $< 001 >_{BCC}$ zone axis. Therefore, the fringes observed in Figure 45 are likely to be stacking faults on the $(009)_{9R}$ planes of a 9R precipitate.

Figure 46 also shows high resolution micrographs of banded structure precipitates. These precipitates are imaged along the $< 111 >_{BCC}$ zone axis. Similar to those precipitates shown in Figure 45, these are also spherical in shape with a diameter ranging between 5 and 8 nm. The average fringe spacing is about 0.65 ± 0.10 nm. These measurements matches those observed by Nicol [192] in her study of twinned and un-twinned 9R copper-rich precipitates in Fe-Cu alloys. The fringes observed in the precipitates shown in Figure 46 also correspond to stacking faults on the $(009)_{9R}$ planes of a 9R precipitate.

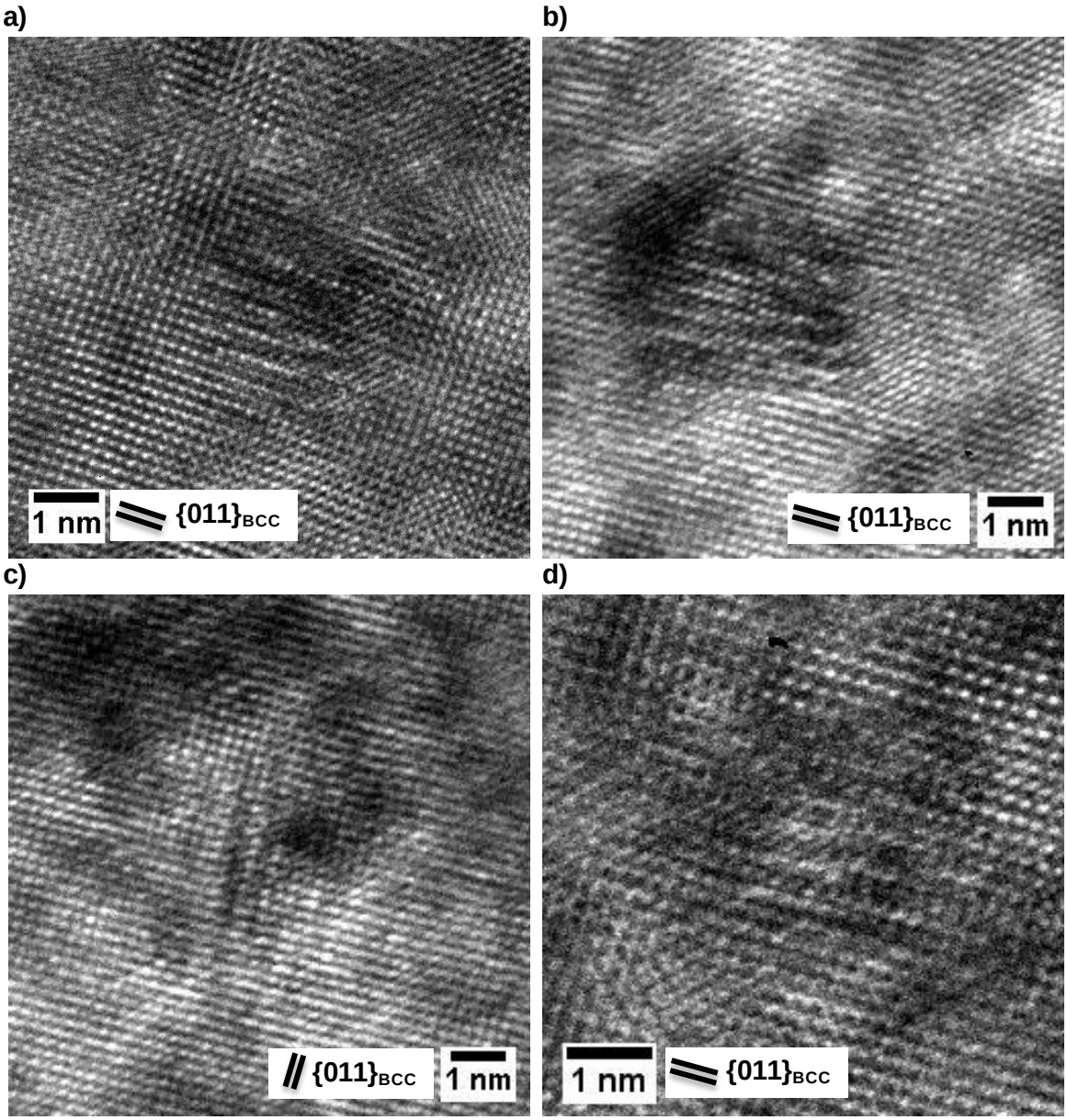


Figure 45: High resolution transmission electron micrographs taken along the $< 001 >_{Fe}$ showing copper-rich precipitates in WV weld steel after thermal ageing for 18,620 hours at 365 °C.

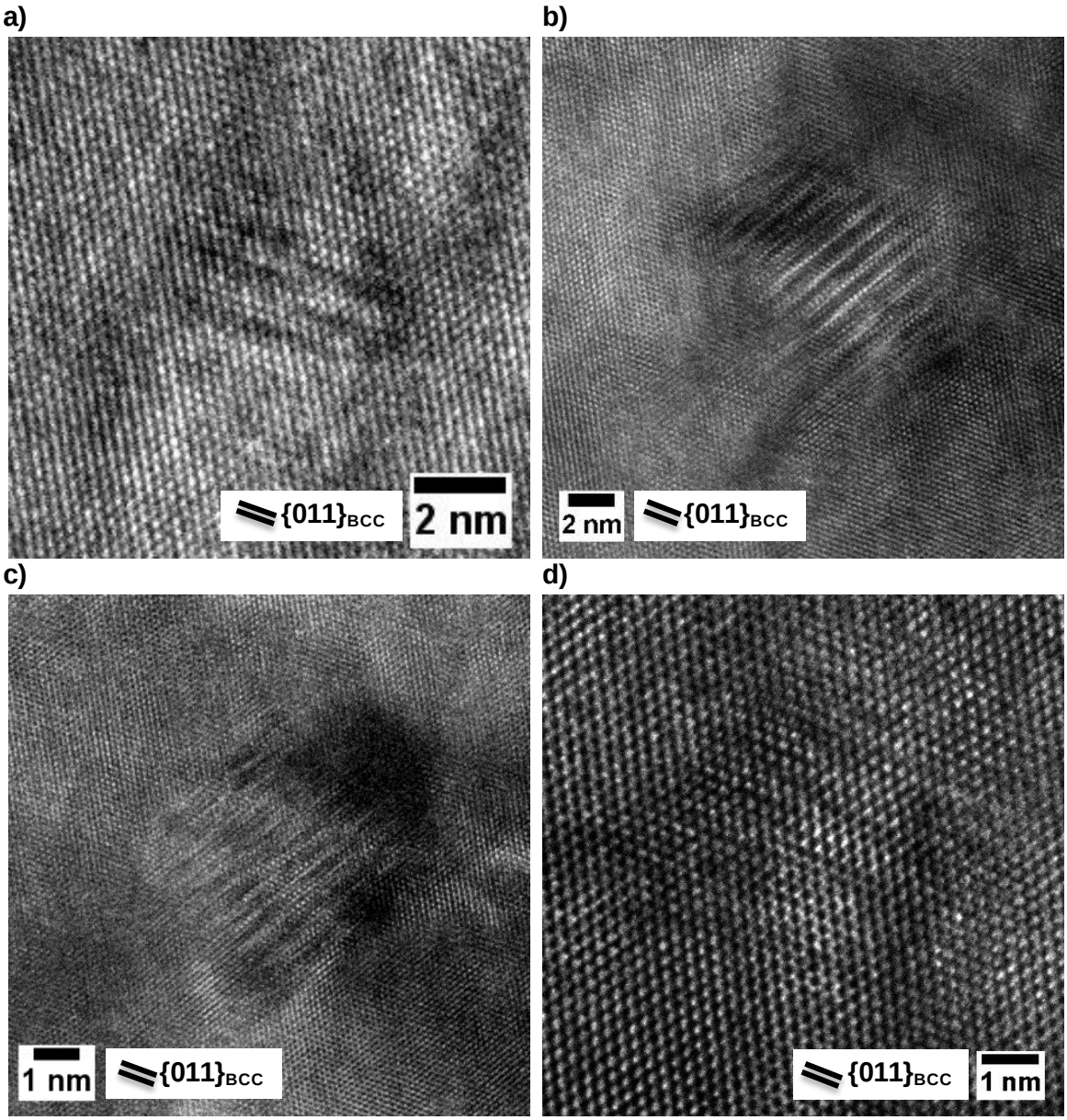


Figure 46: High resolution transmission electron micrographs taken along the $< 111 >_{Fe}$ showing un-twinned copper precipitates in WV weld steel after thermal ageing for 49,800 hours at 365 °C.

6.3.2 Twinned 9R precipitates

Twinned 9R precipitates were also observed in WV weld steel after thermal aging. One of these is shown in Figure 47. This elliptical precipitate exhibits the characteristic herring-bone fringe pattern that allows the immediate identification of a twinned 9R structure as reported by Othen [54, 75]. This means that these banded structure precipitates seen under the conventional TEM (CTEM) are most probably copper-rich precipitates with a distorted FCC structure.

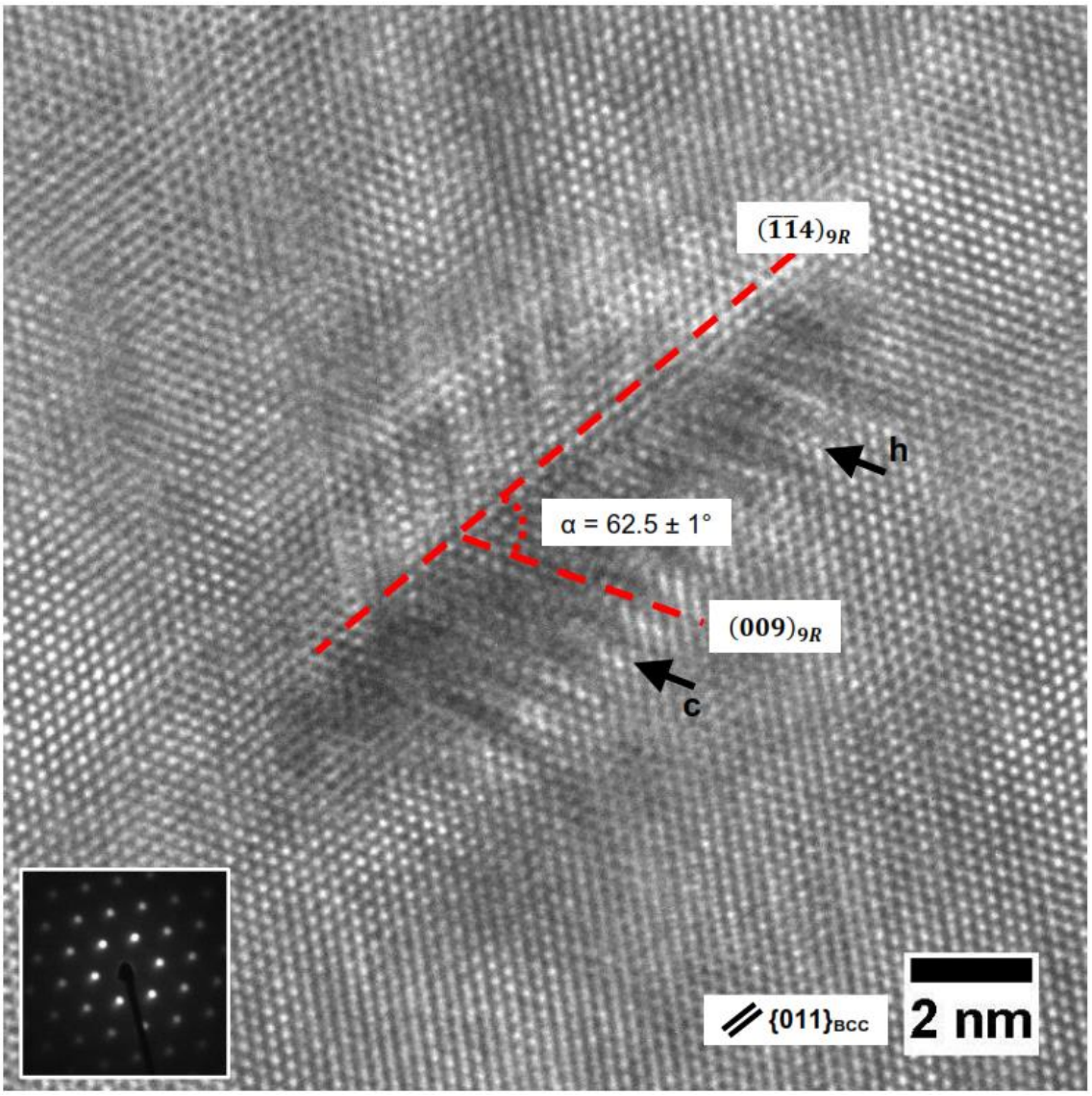


Figure 47: High resolution transmission electron micrograph taken along $< 111 >_{Fe}$ *showing a twinned 9R structure copper-rich precipitate (8 nm) in WV weld steel after thermal ageing for 49,800 hours at 365 °C. The angle α between the* $(009)_{9R}$ *basal and* $(\bar{1}\bar{1}4)_{9R}$ *twin planes is 62.5 ± 1°. The 2-layer fringe spacing at the position of a hexagonal-type stacking fault is indicated. Similarly, the 4-layer fringe spacing at the position of a cubic-type stacking fault is also indicated.*

The diameter of this precipitate is about 10 ± 1 nm (long axis) and about 7 ± 1 nm (short axis). The average fringe spacing is 0.6 ± 0.1 nm. This average fringe spacing is three times the spacing of a $(009)_{9R}$ close packed plane, these observed variations of fringe spacing could be due to different types of stacking fault present in a 9R precipitates. Cubic- and hexagonal-type stacking faults were also observed in this precipitate, as indicated by arrows in Figure 47. Consistent with previous studies, the

twin present in this precipitate lies parallel to a set of matrix $\{110\}_{BCC}$ planes. Hence this precipitate satisfies the orientation relationship that has previously been reported for a typical 9R precipitate with the BCC matrix, i.e. $(011)_{BCC}||(\bar{1}\bar{1}4)_{9R}$ and $[1\bar{1}1]_{BCC}||[\bar{1}10]_{9R}$. The angle, α between the $(009)_{9R}$ close packed plane and the $(\bar{1}\bar{1}4)_{9R}$ twin plane is 62.5 ± 1°. This value suggests that this precipitate has a relaxed twinned 9R structure. It also suggests that the martensitic transformation $BCC \rightarrow 9R$ structure of this precipitates was triggered once it grew and reached a critical size. The further thermal ageing process has then allowed the precipitate to reduce its elastic strains induced during the martensitic transformation by allowing the $(009)_{9R}$ close packed plane to rotate and become closer to the $(\bar{1}\bar{1}4)_{9R}$ plane. Note that a fully relaxed 9R structure has an α angle of 61° [53].

6.3.3 Intermediate structure between 3R and FCC or 3R and FCT

Apart from typical twinned and un-twinned 9R precipitates in this WV weld steel after thermal aging, precipitates with un-twinned intermediate structures between 3R and FCC or 3R and FCT were also observed. One of these is showed in Figure 48. This large precipitate with an average diameter of approximately 18 ± 1 nm exhibits W-shaped diffuse fringes. These fringes provide an indication of that this is a copper-rich precipitate with a distorted FCC structure. These diffuse fringes arise from two types of Moiré fringe formed by the interferences between the $10\bar{1}_{BCC}$ and $\bar{1}\bar{1}1_{Cu}$ reflections and 110_{BCC} and $11\bar{1}_{Cu}$ reflections respectively, as reported previously by Monzen and discussed in detail in Ref. [73].

With an HRTEM image alone it is not possible to determine whether this precipitate possesses an intermediate structure that is closer to a FCC or FCT structure. The degree of tetragonality of an FCT copper-rich precipitates is small. Based on the study reported in Ref. [73], the FCT structure is often found in copper-rich precipitates with sizes ranging from about 26 to 40 nm. It is also suggested that this intermediate structure will transform into an FCC or FCT single crystal when the precipitate

continues to grow by widening the alternate variant fringes/bands at the expense of their neighbours.

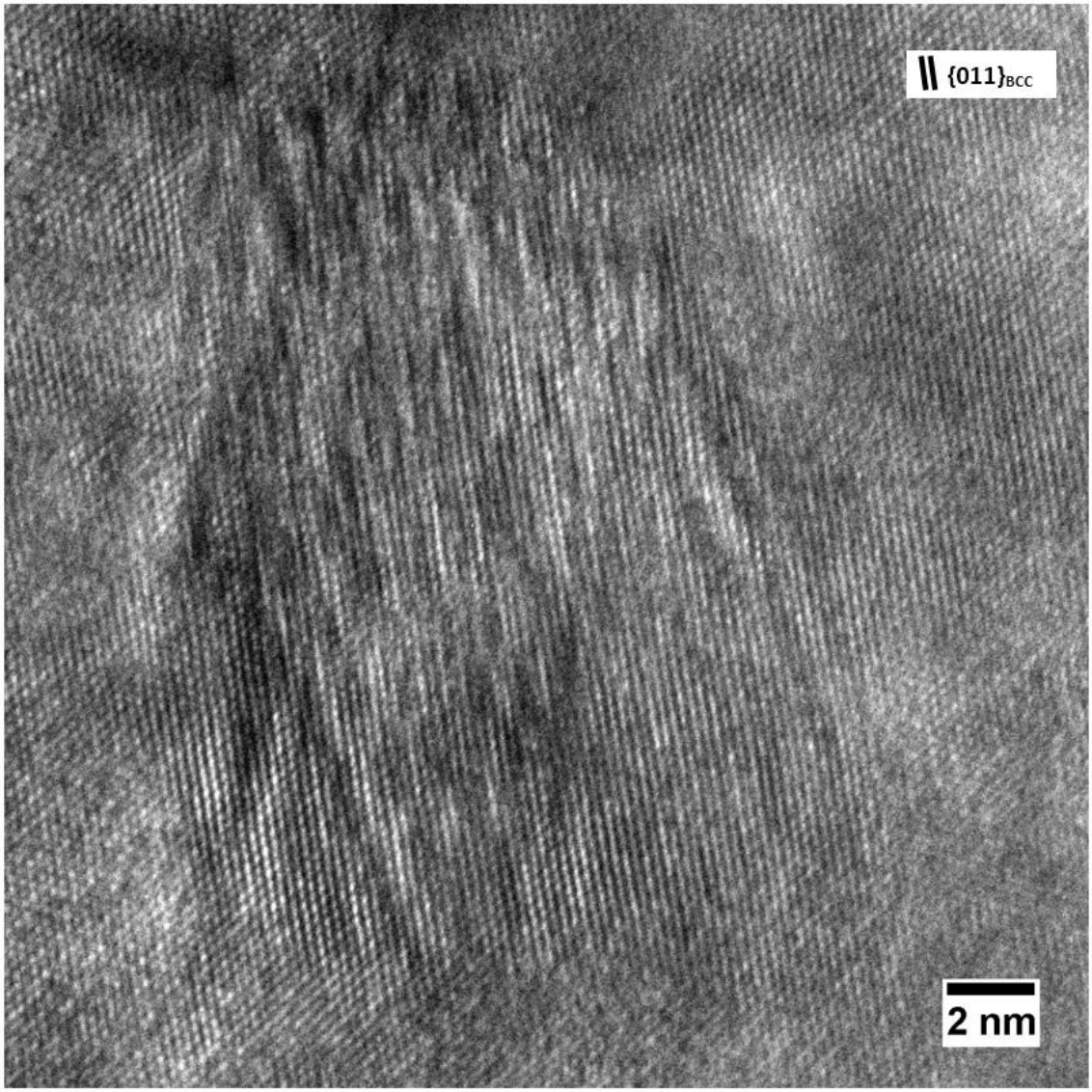


Figure 48: High resolution transmission electron micrograph taken along $< 111 >_{Fe}$ *showing a large copper-rich precipitate (20 nm) in WV weld steel after thermal ageing for 18,620 hours at 365 °C. This precipitate has transformed to intermediate structure between 3R and FCC or 3R and FCT. The W-shaped diffuse fringes shown are the typical contrast for this type of structure.*

6.4 EELS AND EDS SPECTRUM IMAGING

A series of EELS and EDS elemental mapping were performed on WV weld steel thermally aged for two different ageing durations. It is important to note that different electron microscopes and different types of EEL/EDX spectrometers were used to

perform chemical mappings on each sample. The choice of electron microscope and type of EEL/EDX spectrometer used was dependent on the availability of a suitable machine at different stages of my project.

In this section, results of EELS/EDS elemental mapping will be presented according to the ageing duration, i.e. 18,620 hours or 49,800 hours. For the 18,620 hour sample, the EELS elemental maps obtained under TEM mode are presented in Section 6.4.1. As for the sample that was aged for 49,800 hours, the EELS elemental maps obtained under STEM mode can be found in Section 6.4.1.2.

6.4.1 WV weld steel after thermal ageing for 18,620 hours

A JEOL 3000 field emission gun TEM (FEGTEM) was used for the EELS elemental mapping of the sample that was aged for 18,620 hours. The microscope was operated at 297 kV. The EELS data was collected using a post-column Gatan Image Filter (GIF^{TM}) 2000. Note that this mapping is only performed at a relatively low magnification due to the resolution limitations and the problem with the signal-to-noise ratio at high magnification. Whereas, the high magnification EDS elemental maps presented in Section 6.4.1.2 were obtained using a Cs probe corrected JEOL ARM 200 cold field emission gun (S)TEM that was operated at 200 kV.

6.4.1.1 Low magnification elemental mapping

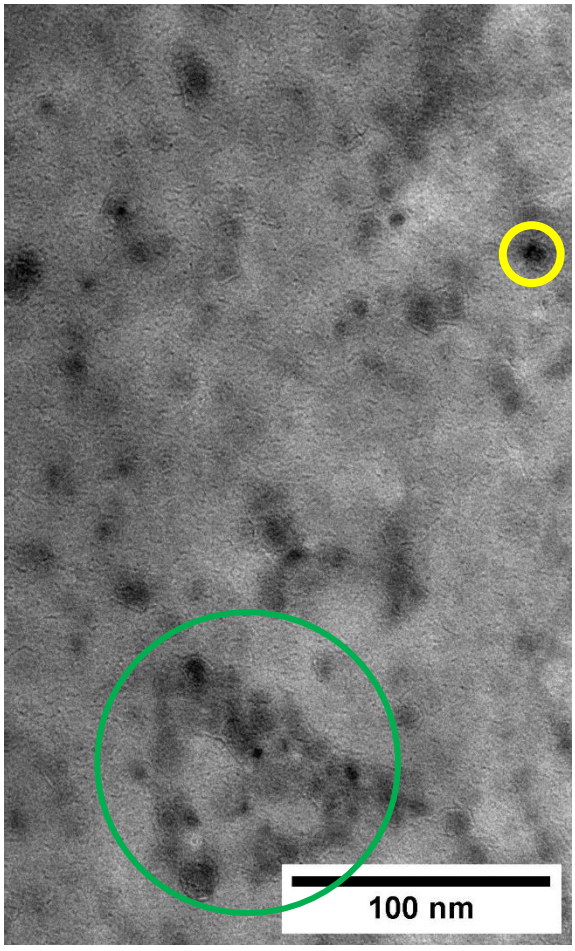
A rather thin area on the specimen that was close to the edge of the hole in a specimen produced during electropolishing was carefully chosen for the EELS elemental mapping. A bright-field micrograph of the mapped region is shown as Figure 49 (a). This region was chosen because it contained distinct features. For example, the surface features induced by the electropolishing process, marked by the green circle in Figure 49 (a), can be used for drift corrections. The average local foil thickness, which was calculated with the use of the Log-Ratio method on the energy-loss spectrum collected, is 25.0 ± 0.2 nm.

The iron-$L_{2,3}$ edge Multivariate Statistical Analysis (MSA) reconstructed elemental map of the corresponding area is shown as Figure 49 (b). Depletion of iron was evident in the nanometre-scale precipitates in the region and these precipitates appear spherical in shape in the iron elemental map. Enrichment of manganese and nickel to the nanometre-scale precipitates was observed in Figure 49 (c) and Figure 49 (d), respectively. Apart from precipitates, manganese and nickel enrichments were also observed to surface features and precipitates re-deposited onto the specimen during electropolishing. In order to distinguish the 'real' precipitates from surface features, as discussed in Section 5.2.2, the iron MSA map is used to compare with both manganese and nickel MSA maps. Note that those surface features or precipitates that re-deposited onto the sample do not show depletion of iron. Hence, a 'real' precipitate will show iron depletion in the iron MSA reconstructed elemental map and enrichment in either the manganese or nickel MSA reconstructed elemental maps or both. One example of a re-deposited precipitate is marked by a yellow circle in Figure 49. The smaller precipitates observed in this set of data is approximately 3.0 ± 0.5 nm and the largest precipitate is 7.0 ± 0.3 nm in diameter. The calculated number density is 2.12 ± 0.3 x 10^{22} m^{-3}.

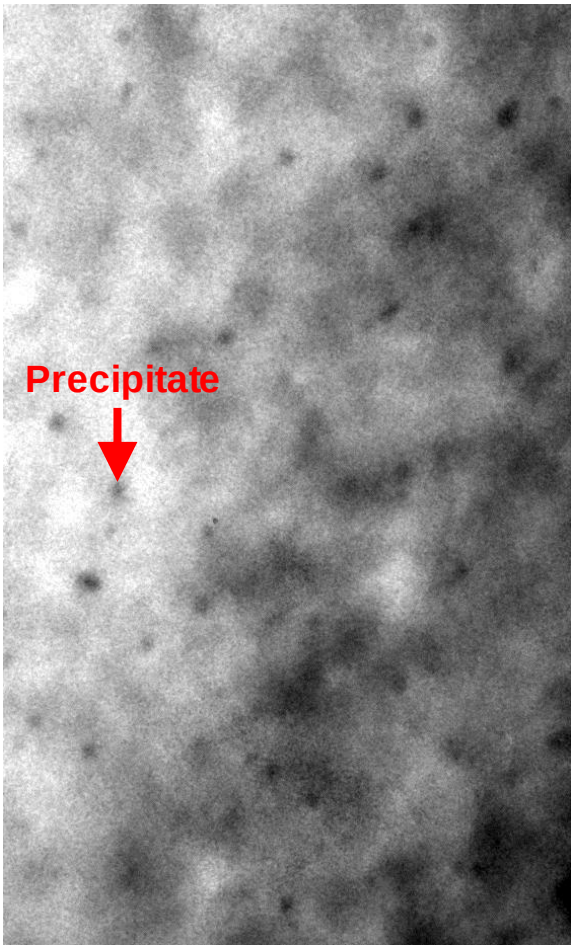
The copper EELS signals are so weak that its elemental map has a poor signal-to-noise ratio. Therefore, it is unsuitable for detailed chemical analyses. There was insufficient signal to image the distribution of the copper with the EFTEM elemental-mapping approach using such short acquisition times, as previously reported in Section 4.3.3. The only indication that these precipitates are copper-rich is by the HREM analysis since the precipitates that have a diameter of greater than 6 nm showed a similar structure to those of copper-rich precipitates studied by other works, i.e. 9R or 3R or intermediate structure between 3R and FCC. Assuming the presence of copper in these nanometre-scale precipitates, it is evident that the nanometre scale precipitates observed in the CTEM analysis and HRTEM analysis are copper-rich

precipitates with the manganese and nickel enrichment shown by EELS analysis. It is impossible to make any assumption that the manganese and nickel is present as a shell or as a co-precipitate on a copper-rich nucleus because the signal for the manganese and nickel in these elemental maps is too weak. Also, the resolution of these elemental maps is too low and as the copper elemental map is un-available.

a) Bright field micrograph



b) Iron-$L_{2,3}$ edge map



c) Manganese-$L_{2,3}$ edge map

d) Nickel-$L_{2,3}$ edge map

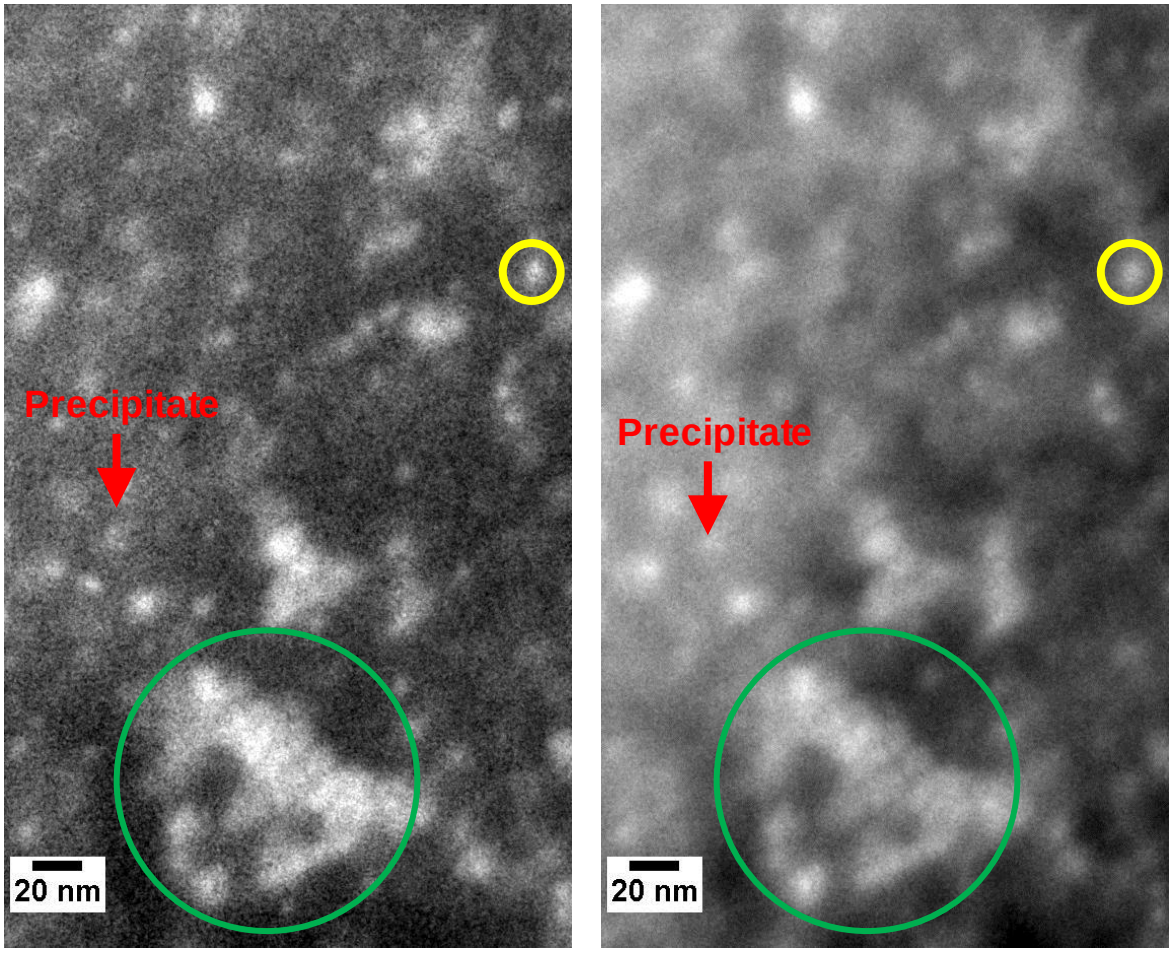


Figure 49: (a) Bright-field micrograph showing the area used for EELS elemental mapping from a WV weld steel specimen that has been thermally aged for 18,620 hours. Corresponding (b) Fe-$L_{2,3}$ (c) Mn-$L_{2,3}$ and (c)Ni-$L_{2,3}$ MSA reconstructed EES elemental maps. The bright-field micrograph was imaged in a slightly over-focussed condition. This is to enhance the contrast of coherent or semi-coherent precipitates in this region. Also, it helps in identifying surface features, for example those marked by a red circle. Apart from precipitates in the sample, both manganese and nickel elemental maps show enrichment in the surface features and re-deposited precipitates that were induced in the electropolishing process.

6.4.1.2 High magnification elemental mapping

High magnification EDS elemental mapping was performed to confirm the presence of copper in these precipitates that were observed in the sample which was aged for 18, 620 hours. The mapping was also performed to confirm whether the presence of manganese and nickel was that of a shell or as a part of the copper-rich nucleus. Figure 50 shows a set of elemental maps of a single precipitate nucleated at the matrix.

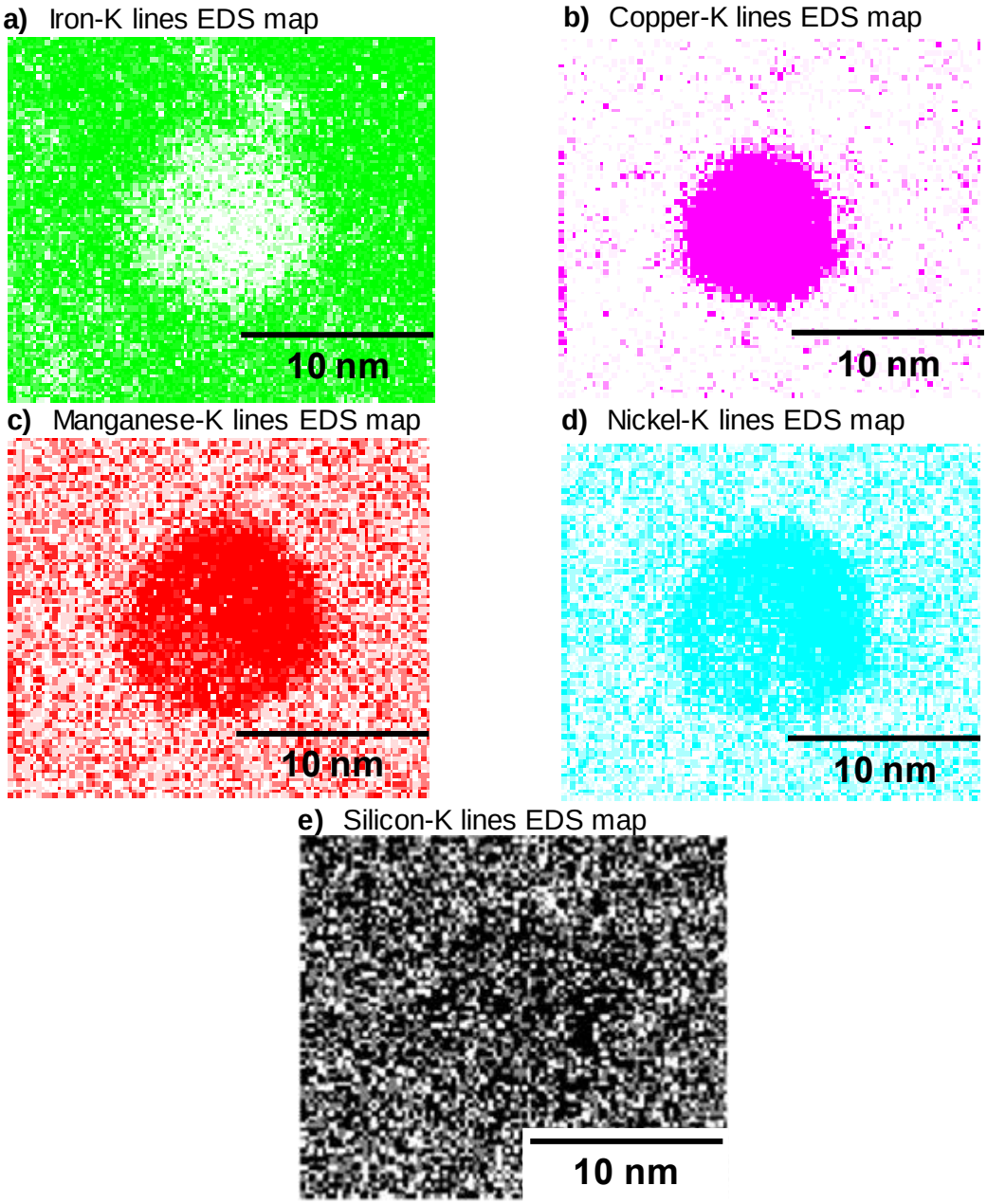


Figure 50: A series of EDS elemental maps corresponding to a thermally aged precipitate nucleated at the matrix of WV weld steel aged for 18, 620 hours. (a) Iron-K line EDS map, (b) Copper-K line EDS map (c) Manganese-K line EDS map, (d) Nickel-K lines EDS map and (e) Silicon-K lines EDS map.

The elemental maps show that the spherical precipitate has a core-shell like structure, i.e. copper-rich core and manganese- and nickel-rich shell. The manganese-K lines and nickel-K lines EDS maps indicate that this precipitate has a manganese and nickel-rich shell that is 1 ± 0.2 nm thick. This confirms that the precipitates observed in the sample that were aged for 18, 620 hours that was presented in Section 6.4.1.1 are

copper enriched and should have crystal structures that are consistent with the HREM analysis presented in Section 6.3 and previous studies summarised in Section 3.

6.4.2 WV weld steel after thermal ageing for 49,800 hours

An aberration corrected JEOL ARM 200 cold field-emission gun (S) TEM was used for the EELS elemental mapping for the sample that was aged for 49,800 hours. The microscope was operated at 200 kV. The EELS data was collected using a Gatan 965 Quantum ER imaging filter. The mappings were obtained in STEM mode at three different magnifications, i.e. low, medium and high magnification, to provide a good overview on the distribution of the precipitates and details of the solute distributions in each precipitate.

6.4.2.1 Low magnification elemental mapping

Figure 51 shows the region of interest for EELS mapping. The brighter contrast features showed in this High Angle Annular Dark-field (HAADF) micrograph are either precipitates or dislocation lines. The brighter contrast on the precipitates indicates that these precipitates have either a higher average atomic-number, Z_{avg}, or higher average local density, ρ_{avg}, whereas the brighter contrast shown by the dislocation lines is due either to the solutes segregation or elastic strain contrast. The strain contrast shown in HAADF micrograph has been further discussed in detail in Section 4.3.2. A suitable region that is relatively thin for EELS mapping is marked by the green box shown in Figure 51. Figure 52 shows a series of MSA reconstructed elemental maps that correspond to the region of interest shown in Figure 51. Copper, manganese and nickel enrichments to the nanometre scale precipitates that were observed in WV weld steel are clearly seen from the respective elemental maps. No enrichment of carbon and oxygen are found in these precipitates, as shown from the carbon and oxygen elemental maps in Figure 52. This means that these precipitates are not carbides or oxides. The silicon EELS signal is weak. As a result, the silicon elemental map has a poor signal-to-noise ratio, and therefore it is unsuitable for detailed chemical analyses.

Both manganese and nickel elemental maps show indications that some of these precipitates are a core-&-shell-like structure. One of the examples is marked by a yellow circle on the manganese and nickel elemental maps. The core-&-shell-like structure has been further investigated by performing EELS mapping at higher magnification, as presented in the next section. The precipitates detected in this EELS data set has an average diameter ranging from 3 ± 1 nm to 13 ± 1 nm. The calculated number density is 1.83 ± 0.1 x 10^{22} m^{-3}. By comparing the HAADF micrograph (Figure 51) and the series of elemental maps (Figure 52), it is important to mention that there are many precipitates located along or at a dislocation line. After a careful measurement, it was found that the ratio of the number density of the precipitates associated with a dislocation line and within the matrix is 7:4, i.e. the number of precipitates located along or at a dislocation line is almost a factor of 2 higher than those that are at the matrix.

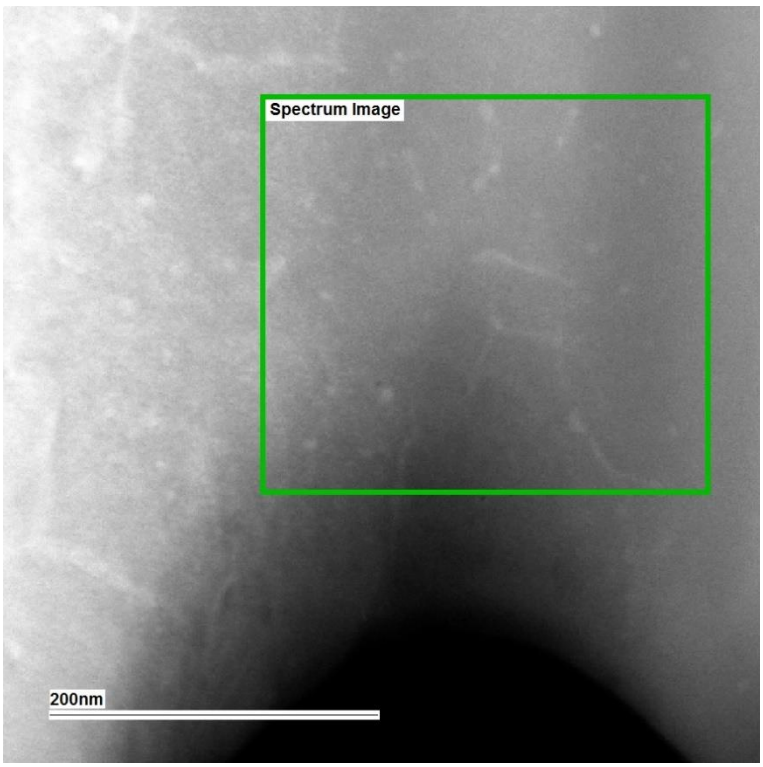


Figure 51: High Angle Annular Dark-field micrograph showing a thinner region, as indicated by the green box that is suitable for EELS mapping, from a WV weld steel specimen that has been thermally aged for 49,800 hours.

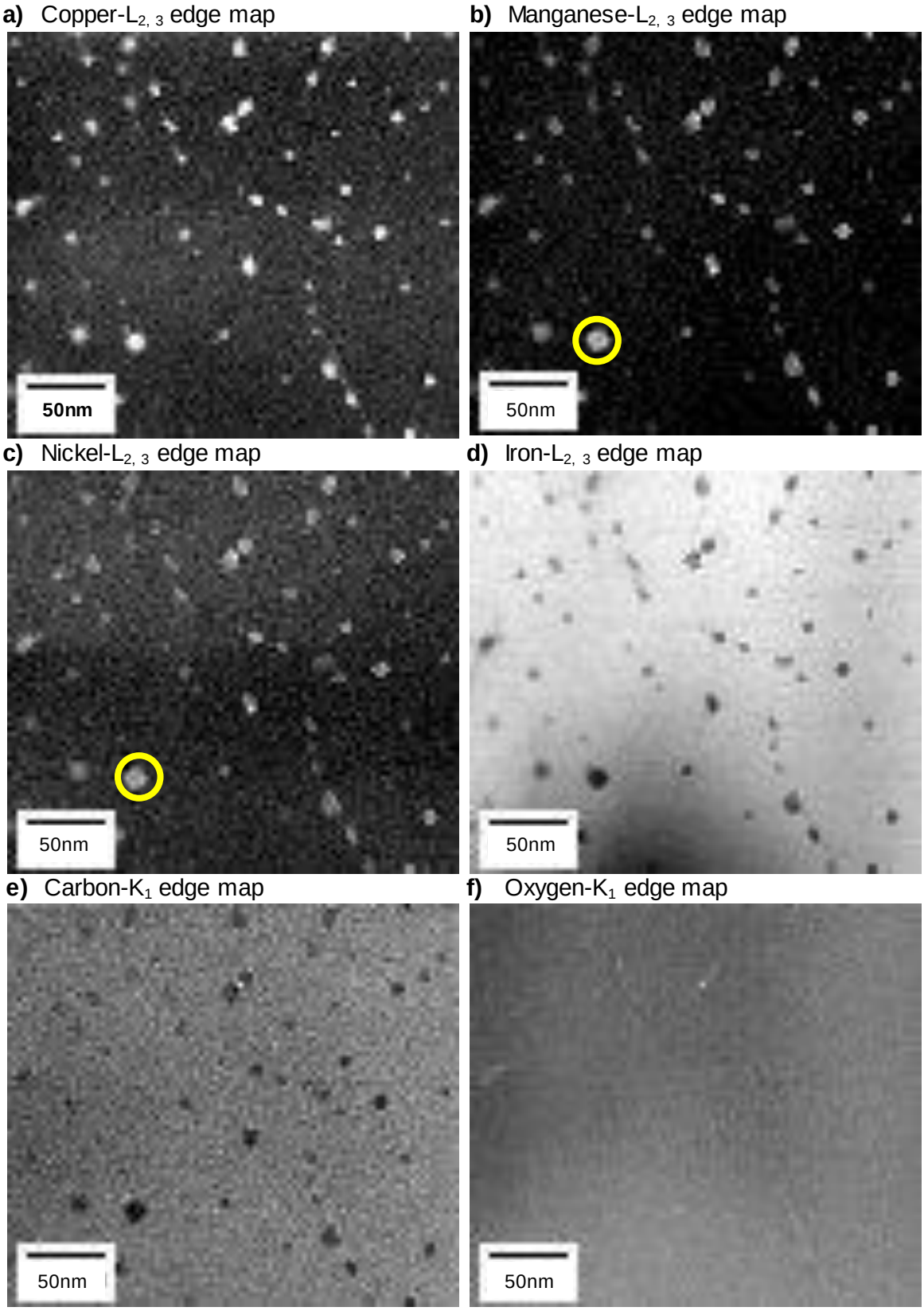


Figure 52: Series of MSA reconstructed elemental maps corresponding to the region shown in Figure 51. (a) Copper-$L_{2,3}$ edge map, (b) Manganese-$L_{2,3}$ edge map, (c) Nickel-$L_{2,3}$ edge, (d) Iron-$L_{2,3}$ edge map, (e) Carbon-K_1 edge map and (f) Oxygen-K_1 edge.

6.4.2.2 Medium magnification elemental mapping

Another EELS elemental mapping experiment was performed at a 'medium' magnification. The region of interest is marked by a green rectangular box in Figure 53. The corresponding series of MSA reconstructed elemental maps are showed in Figure 54. The elemental maps are consistent with the low magnification elemental mapping, i.e. copper, manganese and nickel enrichments within the precipitates were observed.

These maps provide solid evidence that the precipitates in this WV weld steel after thermal ageing for 49,800 hours have a core-&-shell-like structure, i.e. copper-rich (Cu-rich) core and manganese- and nickel-rich (MnNi-rich) shell. The overall shape of these precipitates is faceted but contains a spherical or elliptical copper-rich core. Note that the shape of the precipitates that were nucleated at the matrix and those at the dislocation lines are different. In general, the shape of a precipitate at the matrix is more cuboidal with a spherical copper-rich core. One example is circled in red in Figure 54. The copper-rich core is in good agreement with previous study of the morphology of copper-rich precipitates in Fe-Cu based alloys, as documented in Refs. [65, 99, 192]. As for the precipitates that are associated with a dislocation line, they have an overall shape either rectangular with an elongated elliptical core or a distorted faceted cuboid structure. Further discussion on the change of shape of the precipitates after long term thermal ageing is given in Section 6.5.

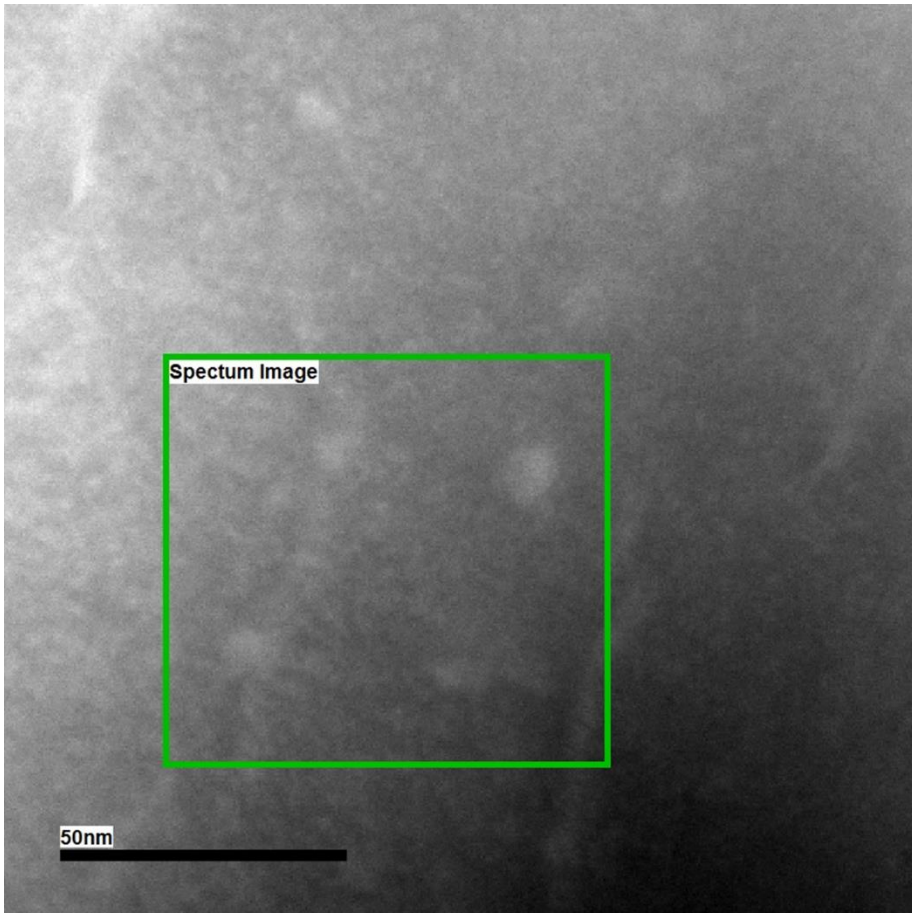


Figure 53: High Angle Annular Dark-field (HAADF) micrograph showing a region of interest for EELS mapping, as indicated by the green box. This region is from a WV weld steel specimen that has been thermally aged for 49,800 hours.

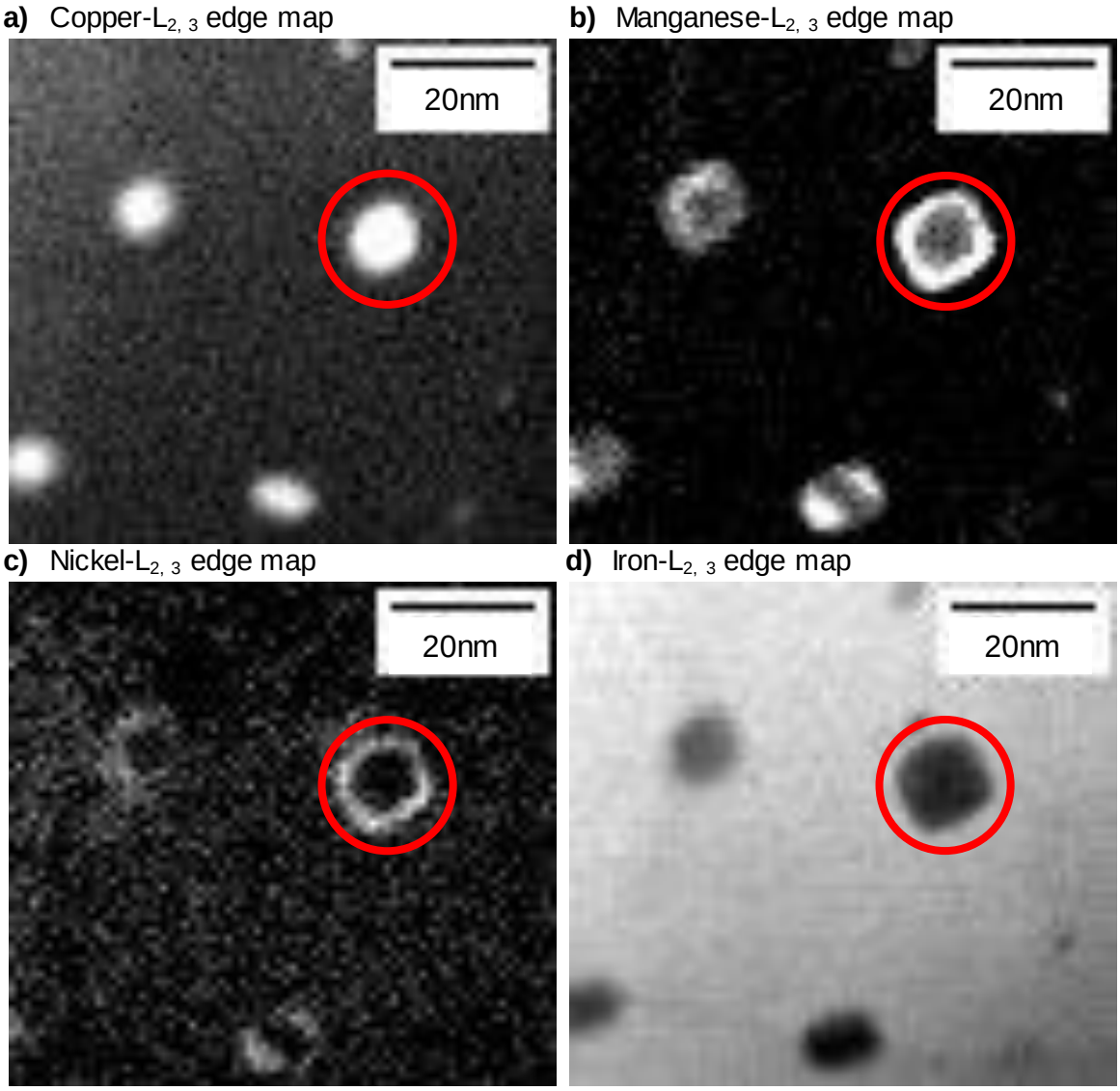


Figure 54: Series of MSA reconstructed elemental maps corresponding to the region shown in Figure 53. (a) Copper-$L_{2,3}$ edge map, (b) Manganese-$L_{2,3}$ edge map, (c) Nickel-$L_{2,3}$ edge, and (d) Iron-$L_{2,3}$ edge map.

6.4.2.3 High magnification elemental mapping

Three sets of high magnification EELS elemental mapping are presented here. The regions that have been mapped are showed in Figure 55 and Figure 57, marked by green boxes. Each set of maps contain an individual precipitate. The corresponding MSA reconstructed elemental maps are presented as Figure 56, Figure 57 and Figure 58. All of these precipitates have copper-rich core and manganese- and nickel-rich (MnNi-rich) shells. This is consistent with those seen in the low and medium magnification elemental mapping images presented in previous sections.

Three of these precipitates are located along a dislocation line. In the respective manganese and nickel elemental maps of these precipitates, preferential enrichment of manganese and nickel or growth of MnNi-rich shells was observed closest to the dislocation line. This could be due to the channelling of solutes through the dislocation line to the precipitates. Note that manganese and nickel enrichment is also observed along the dislocation lines in all three sets of the high magnification EELS elemental maps. Similar observations were also found in APT data as documented in Ref. [35].

By comparing the HAADF contrast of the precipitates and the chemical structure of the precipitates observed from the MSA reconstructed elemental maps presented in Figure 55, Figure 56, Figure 57, Figure 58, and Figure 59, It is obvious that the precipitates show a brighter contrast in the HAADF micrographs in correspondence to the copper-rich core. The MnNi-rich shell has a similar contrast as that of the matrix.

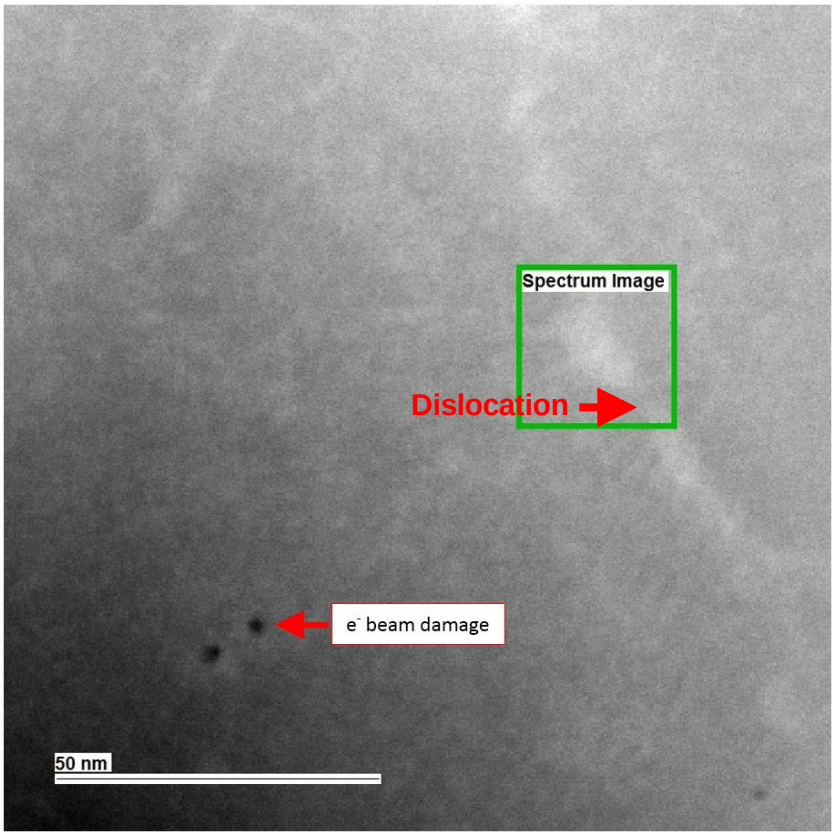


Figure 55: High Angle Annular Dark-field (HAADF) micrograph showing a region for EELS mapping, as indicated by the green box. This region is from a WV weld steel specimen thermally aged for 49,800 hours.

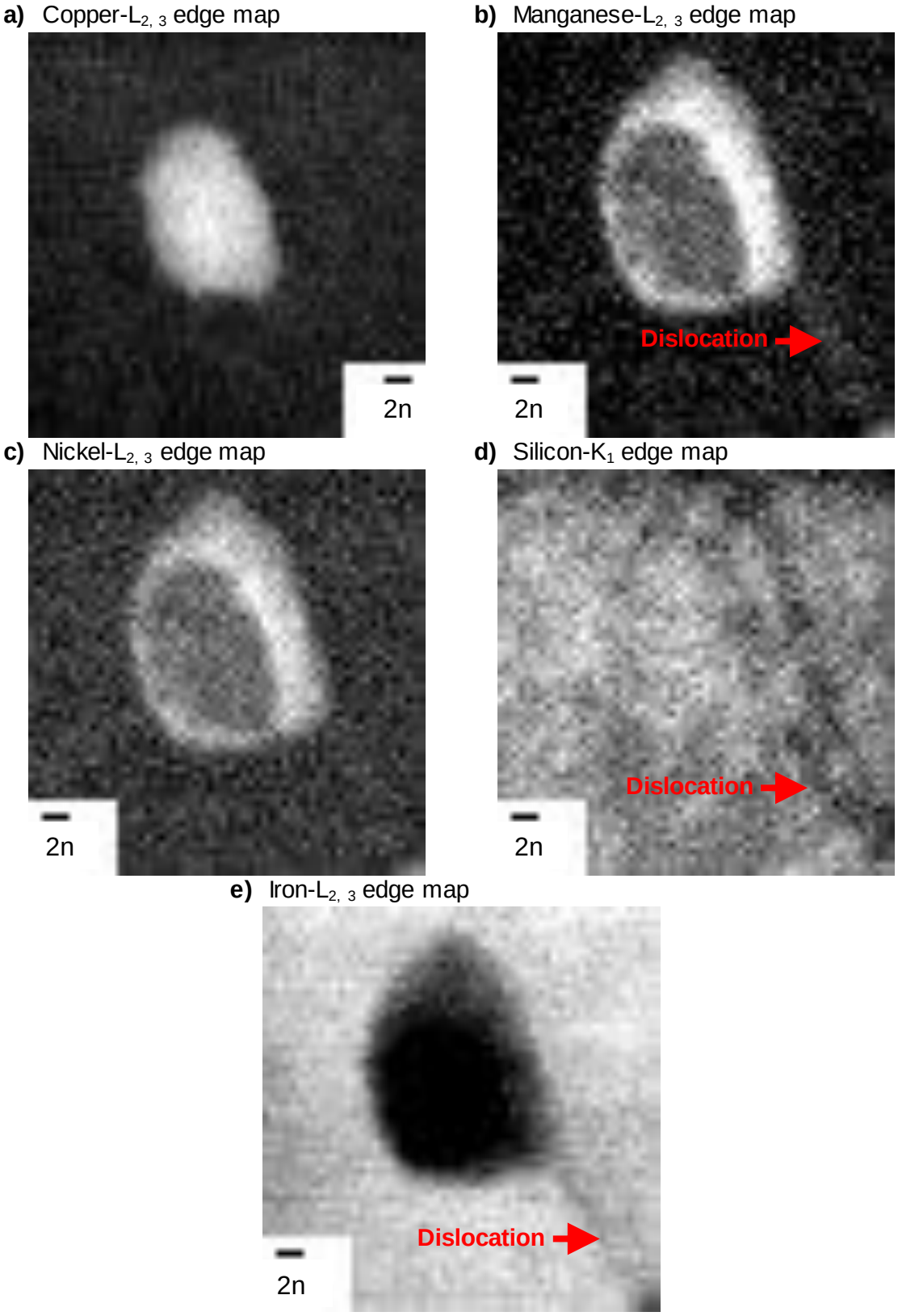


Figure 56: Series of MSA reconstructed elemental maps corresponding to the region shown in Figure 55. (a) Copper-$L_{2,3}$ edge map, (b) Manganese-$L_{2,3}$ edge map, (c) Nickel-$L_{2,3}$ edge, (d) Silicon-K_1 edge map and (e) Iron-$L_{2,3}$ edge map

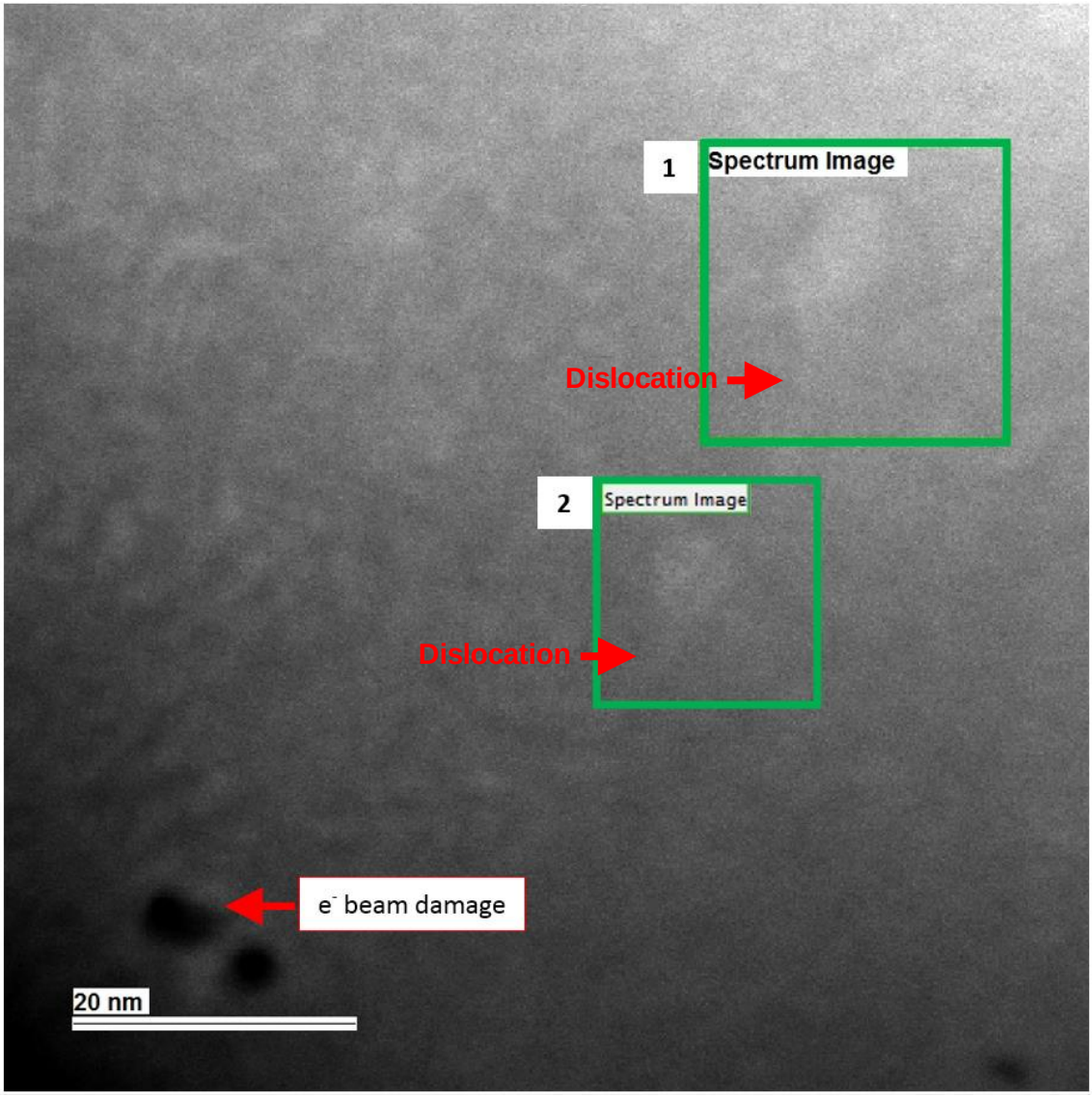


Figure 57: High Angle Annular Dark-field (HAADF) micrograph showing two regions for EELS mapping, as indicated by the green boxes (1) and (2). These regions are from a WV weld steel specimen thermally aged for 49,800 hours.

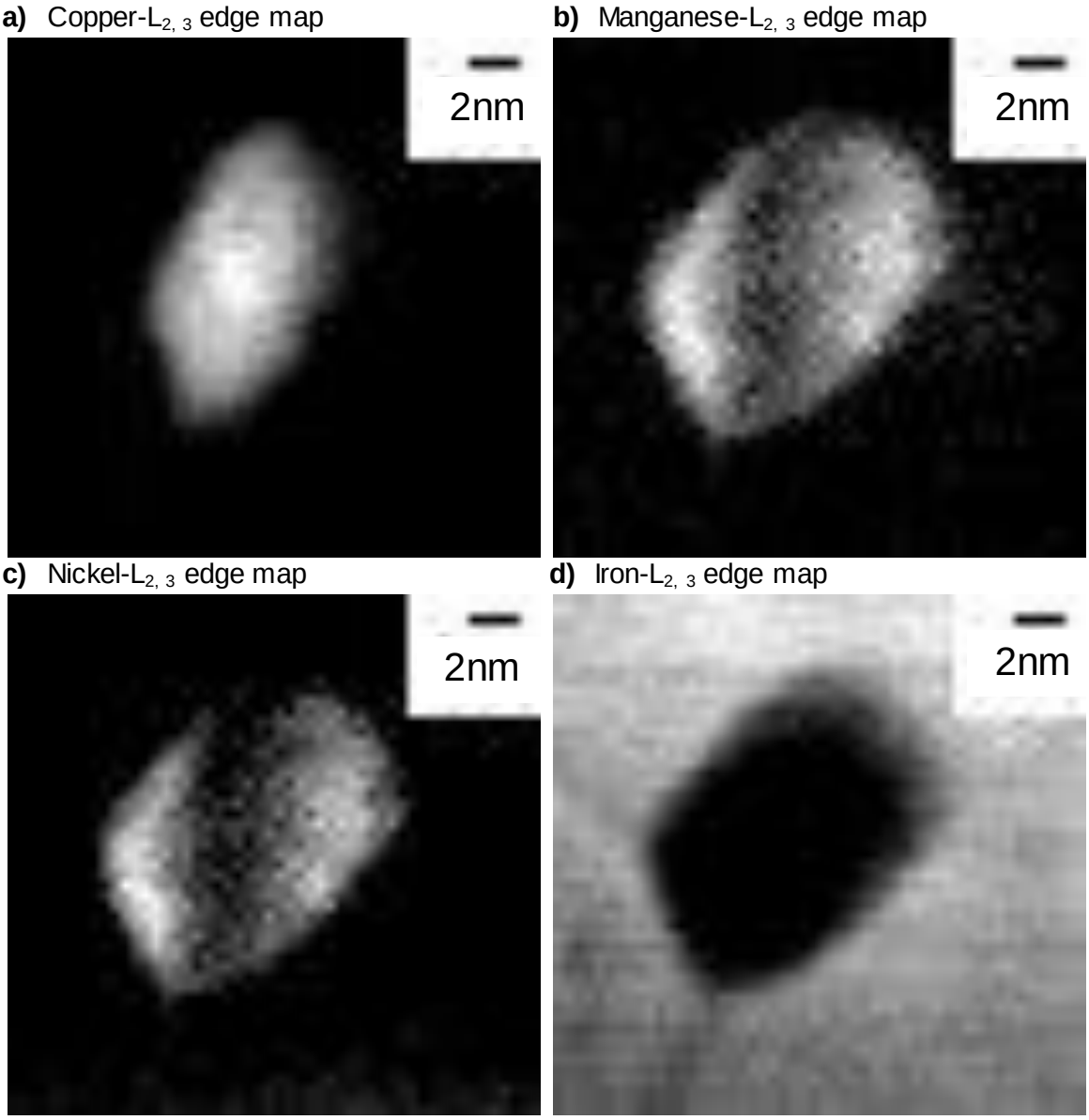


Figure 58: Series of MSA reconstructed elemental maps corresponding to the region shown in Figure 57 (1). (a) Copper-$L_{2,3}$ edge map, (b) Manganese-$L_{2,3}$ edge map, (c) Nickel-$L_{2,3}$ edge, and (d) Iron-$L_{2,3}$ edge map.

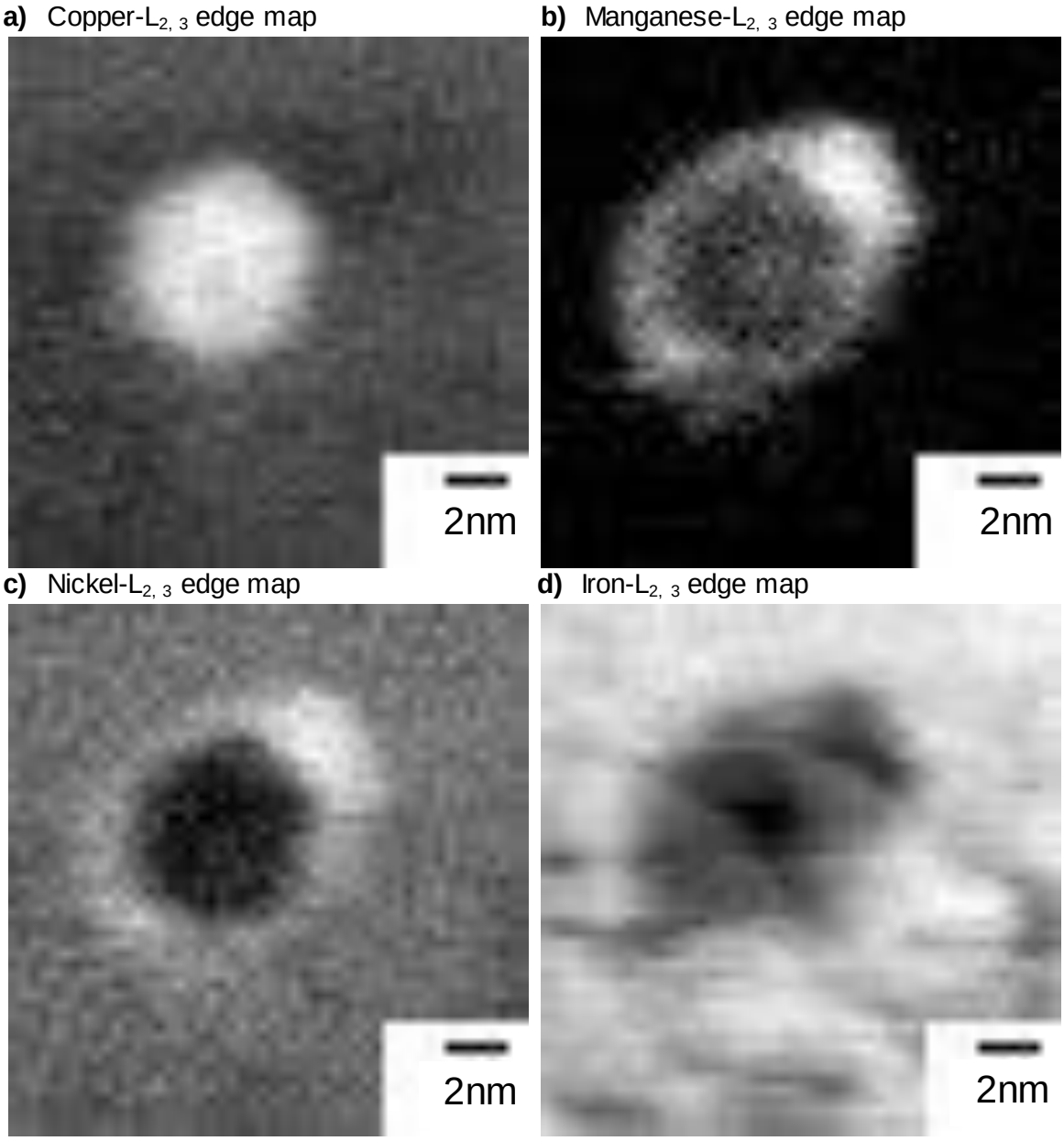


Figure 59: Series of MSA reconstructed elemental maps corresponding to the region shown in Figure 57 (2). (a) Copper-$L_{2,3}$ edge map, (b) Manganese-$L_{2,3}$ edge map, (c) Nickel-$L_{2,3}$ edge, and (d) Iron-$L_{2,3}$ edge map.

6.5 DISCUSSION

Electron microscopy characterisation of WV weld steels that have undergone long term thermal ageing was presented in previous sections. A number of these results need discussing in more detail.

6.5.1 Structure of precipitates

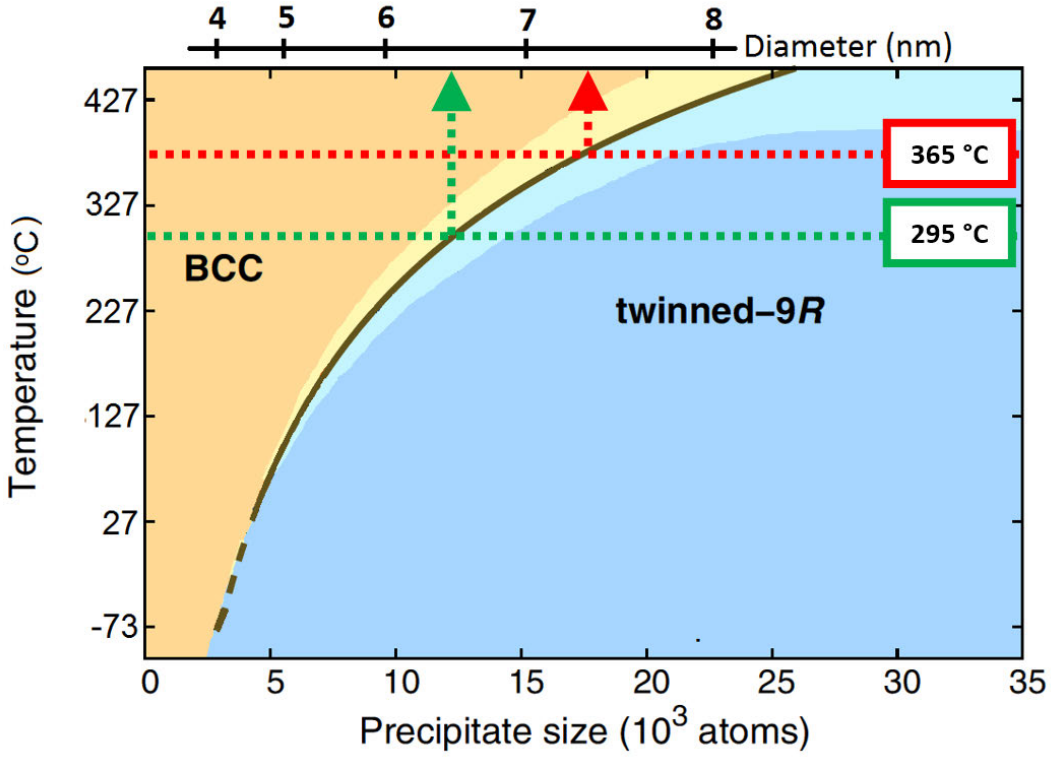


Figure 60: Diagram representing the structure of coper-rich precipitates as a function of temperature and size. This diagram is based on the experimental results obtained by Monzen et al. [53] and simulations performed by Erhart et al. [193]

Results obtained from CTEM and HRTEM analysis have shown that the precipitates formed in WV weld steels after thermal ageing have a typical copper-rich precipitate structure that has been extensively studied and documented in Refs.[53, 65, 73, 99, 192]. Evidence of martensitically transformed 9R, 3R, and intermediate structures between 3R and FCC or 3R and FCC, have been found in the WV weld steels after ageing for both 18,620 hours and 49,800 hours. The micrographs of these structures are presented in Section 6.3. Smaller coherent BCC precipitates are also observed in Section 6.2. The 'Size-Temperature-Transformation' (STT) diagram showing the structure of copper-rich precipitates constructed based on experimental results and simulations are shown as Figure 60. This diagram suggests that at an ageing temperature of 365 °C, the critical size for a coherent BCC copper-rich precipitate to undergo a 9R transformation is 7.4 ± 0.5 nm.

The size of the martensitically transformed precipitates observed under CTEM and HRTEM in this work is in good agreement with the critical size indicated, especially for precipitates with an average diameter of 8nm. A good example is the relaxed twinned 9R precipitate shown in Figure 47. The rotated $(009)_{9R}$ planes (α° < 64.5°) are a good indication that this precipitate was transformed during the thermal ageing process. This observation also confirms that thermal ageing at 365 °C allows the release of strain energy from a 9R precipitate by the martensitic transformation, and results in a reduction of angle, α, between the $(009)_{9R}$ planes and $< \bar{1}\bar{1}4 >_{9R}$ as observed. Transformed precipitates smaller than the critical size, some of these are shown in Figure 45 and Figure 46, are most probably due to either:

- the cooling process after the heat treatment to room temperature, or
- the electropolishing process that required cooling to about – 60 °C, or
- the focussed ion beam milling process, as gallium ions could penetrate the specimen sub-surfaces.

Martensitically transformed precipitates from one of these causes will have an angle of α of 64.5°.

In Section 6.2.1, coherent BCC precipitates were observed with characteristic strain contrast lobes under two-beam dynamical condition. These precipitates are generally smaller than 9 ± 2 nm. This is within the error of the critical size for martensitic transformation at 365 °C, as shown in Figure 60.

Overall observations from CTEM and HRTEM investigations suggest that the structural transformation of the precipitates formed in these WV weld steels during thermal aging at 365 °C are in good agreement with the hypothesis by Monzen et al. [53] that the martensitic transformation from $BCC \rightarrow 9R \rightarrow 3R \rightarrow FCC\ or\ FCT$ is dependent on the size of the precipitate and the ambient temperature.

6.5.2 Chemical composition of precipitates

The EELS and EDS results on WV weld steels after being thermal aged for 18,620 hours and 49,800 hours are consistent with the results from Atom Probe Tomography (APT) characterisation on the same samples performed by Styman [35]. Both techniques show evidence of the enrichment of copper, manganese and nickel within the precipitates in these materials. Core-&-shell like structures were observed from the precipitates in the EELS, EDS and APT results. The core is enriched with copper whereas the shell is enriched with manganese and nickel. There are some minor discrepancies between the results obtained by EELS, EDS and APT, they are as follows:

- Presence of iron in the precipitates (further discussed in Section 6.5.2.1)
- Presence of silicon in the precipitates (further discussed in Section 6.5.2.2)
- Precipitate size and number density distributions (further discussed in Section 6.5.3)

6.5.2.1 Iron concentration in precipitates

The iron concentration of a copper-rich precipitates has been a long-standing issue as was documented in Ref. [194]. This is because the results obtained from APT and SANS are not consistent with each other. The APT suggests that there is a significant amount of iron present within the copper-rich precipitates whereas SANS data once interpreted suggests virtually iron free precipitates. This controversy is directly related to the limitations of both techniques. This has been discussed in detail in Refs. [35, 89].

In this section, the iron concentration in precipitates that formed in WV weld steel thermally aged for 49,800 hours is examined. The results obtained from EELS mapping presented in Section 6.4, were used to measure the iron concentration in the precipitates. The value will then be compared with the APT results reported by Styman [35].

6.5.2.1.1 EELS VS APT results

The relative iron concentration in the precipitates can be measured from the results obtained from EELS mapping. The iron concentration in the precipitates was calculated based on the relative thickness of the matrix in which an embedded precipitate was located using the iron-$L_{2,3}$ edge signal and the size of the corresponded precipitate. Details of this method are well documented in Ref. [92].

By using this method, the iron concentrations of 12 precipitates investigated using EELS at both medium magnifications and high magnifications were calculated. The overall diameter[6] of these precipitates ranged from 6.5 ± 0.7 nm to 12.4 ± 1.0 nm and the overall diameter of the copper-rich cores of these precipitates were between 5.6 ± 0.4 nm and 9.2 ± 1.0 nm. The calculation indicates that the copper core of these precipitates is iron-free. The same calculation was performed on the MnNi-rich shell and it was found that the MnNi-rich shell of these precipitates were also iron-free. The maximum estimated iron concentration in the shell is only 1.3 ± 0.5 %.

For the same material, APT showed that the iron concentration in the precipitates is not zero. The APT detected more than 20 % of iron in precipitates larger than 5 nm in diameter [195]. This strongly suggests that the iron detected by APT in the precipitates was mostly due to the trajectory overlapping effects[7] [196].

The inconsistency between the iron concentrations detected by APT and those measured from the EELS data has raised questions about the accuracy of measurements performed using the method published in Ref. [92]. The iron concentration calculated using this method is strongly dependent on the spatial resolution and detection limits of EELS, the signal-to-noise ratio (SNR) of the EELS data collected, the local thickness measured by EELS and the size of the precipitates

[6] For elliptical precipitate, the diameter is calculated by averaging the length measured from the short and long axes.
[7] Trajectory overlapping effects caused by differences in local magnification can lead to significant proportions of iron being incorrectly positioned within the precipitates.

along the direction of imaging. With the instrument used to collect the EELS data, as previously reported in Section 4.3.3 and Section 6.4, the accumulative errors induced by the first three factors is very low because the quality of the EELS data collected is high, i.e. The SNR for the iron MSA reconstructed elemental map is over 150:1, the size of each pixel used is 0.5 nm (largest), and the relative error (≈ 10 %) induced by the local foil thickness measurement through EELS is corrected by using the correcting factor documented in Ref. [160]. The shape of the copper-rich core is assumed to be either spherical or elliptical based on the observations reported in Sections 6.2, 6.3 and 6.4 as well as the APT studies by Styman [35]. Hence, any error induced due to the assumption made about the shape of the precipitates during the iron concentration calculation using EELS data collected can become significant. Incorrect assumptions might cause an underestimation or overestimation of the iron concentration in the precipitates in the calculation performed. A solution for this is to perform a tomography study and EELS analysis on the precipitates. This will then eliminate the doubts about estimating the thickness of each precipitate from a two-dimensional image. However, this will take significant experimental effort to analyse just a small number of precipitates.

6.5.2.1.2 Correlation between iron concentration & crystal structure

Lozano-Perez et al. [92] have hypothesised that the iron concentration present in the precipitates is dependent on the crystal structure, since different structures can accommodate different concentrations of iron. Based on the STT diagram shown in Figure 60, the critical size for a BCC copper-rich core to martensitically transform into a 9R structure is at 7.4 ± 0.5 nm. It is logical to assume that the precipitates bigger than this size have transformed into a 9R structure and this is also confirmed by the observations from the CTEM and HRTEM analysis summarised in Section 6.5.1. With this information in mind, 11 out of 12 of the precipitates that had their iron concentration measured are assumed to have a 9R structure. As for the precipitate which had a

copper core with an average diameter of 5.6 ± 0.4 nm, this precipitate might remain in the BCC structure. It is important to note that we assume that the $BCC \rightarrow 9R$ martensitic transformation of the precipitates is based on the size of the copper-rich core not the overall size of the precipitates, i.e. the size of the core and shell. All this information suggests that the transformed 9R precipitates could be iron-free.

Even though an iron-free BCC copper-rich precipitate is observed in this analysis, it is still not possible to conclude that *all* the BCC copper-rich precipitates are iron-free. This is due to the poor statistical data available. Also, this precipitate was relatively large compared to the predicted critical size of the $BCC \rightarrow 9R$ transformation and could possibly have rejected iron from its copper-rich core during the growth and coarsening processes during ageing process. Furthermore, we have no information regarding to the effects of the MnNi-shell on the $BCC \rightarrow 9R$ martensitic transformation of copper-rich precipitates, and this might reduce the critical size for the transformation to occur.

6.5.2.2 Silicon concentration of precipitates

APT analysis shows that the precipitates detected in the WV weld steel thermally aged for 49,800 hours contain an average of approximately 3 ± 0.1 at.% of silicon. In the EELS investigations performed, no obvious enrichment of silicon was found in the precipitates. One of the three sets of high magnification EELS mapping presented in Section 6.4.2.3 attempted to investigate the amount of silicon present in a precipitate formed in the same materials as those investigated using APT. The silicon elemental map is presented as Figure 56 (d). This precipitate is located along a dislocation, and it is evident from the map that silicon is depleted at the dislocation line. Apart from that, the silicon is homogeneously distributed in the matrix and the precipitate, with no obvious silicon enrichment observed within the precipitate. Very little difference in the silicon-K_1 edge signal was found between the matrix and within the precipitate. Note that the Signal-to-Noise Ratio (SNR) for the silicon-K_1 edge of all the EELS mapping performed is rather poor. This is because the energy of the core-loss edge of silicon is

relatively high, i.e. the silicon—K_1 edge is at 1839 eV. Hence it is possible that the EELS acquisition conditions used are not able to collect sufficient signal to determine the presence of silicon in the precipitates (average counts for both the silicon signal and noise are below 3000 after MSA reconstruction).

6.5.3 Size of precipitates and number density

Table 13: Number density of the precipitates detected in WV weld steel

Thermal Ageing (hours)	Number density (m^{-3})	
	EELS	***APT***
18,620	2.12×10^{22}	5.88×10^{22}
49,800	1.83×10^{22}	4.13×10^{22}

The number density of the precipitates detected in WV weld steels thermally aged for 18,620 hours and 49,800 hours have been calculated based on the EELS data presented in Section 6.4.. The calculated number densities of the precipitates for the two materials are shown in Table 13, and the differences between the number densities after 18,620 hours and 49,800 hours is small, with a decrease of approximately 14 ± 2 % after more than 30,000 hours further ageing. This suggests that the precipitates formed in this WV weld steel are in the growth and coarsening stage, instead of the nucleation stage, after 20,000 hours. This is in good agreement with the results observed in APT studies [35, 89], which actually show a small decrease in the number density of precipitates after the longer ageing.

Figure 61 shows the overall number density of precipitates detected in the WV weld steel as a function of the diameter of the precipitates. A clear trend can be seen that with an increase in the time of thermal ageing, the size range of the precipitates became wider. The average diameter of precipitates in the steel aged for 49,800 hours is approximately 7 nm, and for 18,620 hours the average diameter was approximately 4.3 nm. Note that the smallest precipitate size detected was 3 nm in materials. This is

the resolution limit of the EELS data that has been collected, and is affected by the electron beam size used during the EELS data acquisition.

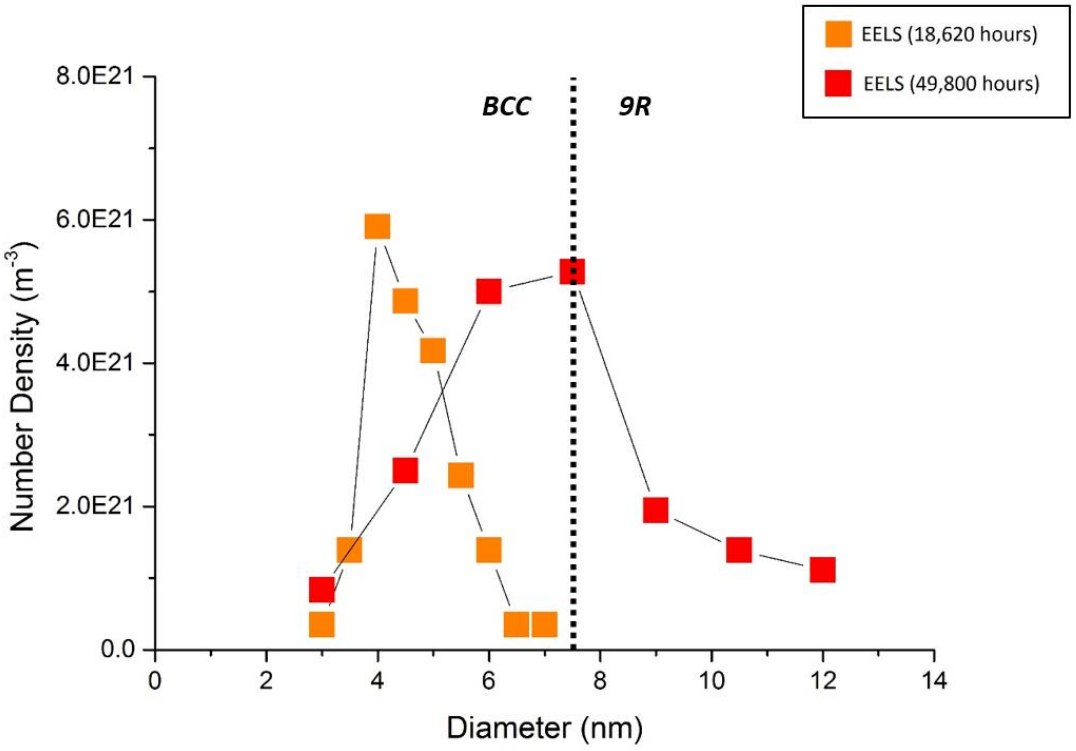


Figure 61: Diagram showing the number density of precipitates detected in WV weld steel after thermal ageing at 365 °C as a function of the diameter of the precipitates.

Based on the STT diagram shown in Figure 60, the critical size for the $BCC \rightarrow 9R$ martensitic transformation at ambient temperature of 365 °C is 7.4 ± 0.5 nm. This means that we might predict that most of the precipitates formed in the WV weld steel that was thermally aged for 18,620 hours still remained in the BCC structure whereas about half of the precipitates in the steel that was thermally aged for 49,800 hours should have transformed into the 9R structure.

6.5.3.1 WV weld steel after being thermally aged for 49,800 hours

It was mentioned in the previous section that most of the precipitates are located along or at a dislocation lines. Based on the WV weld steel thermally aged for 49,800 hours, the number densities of the precipitates in the matrix and those associated with a

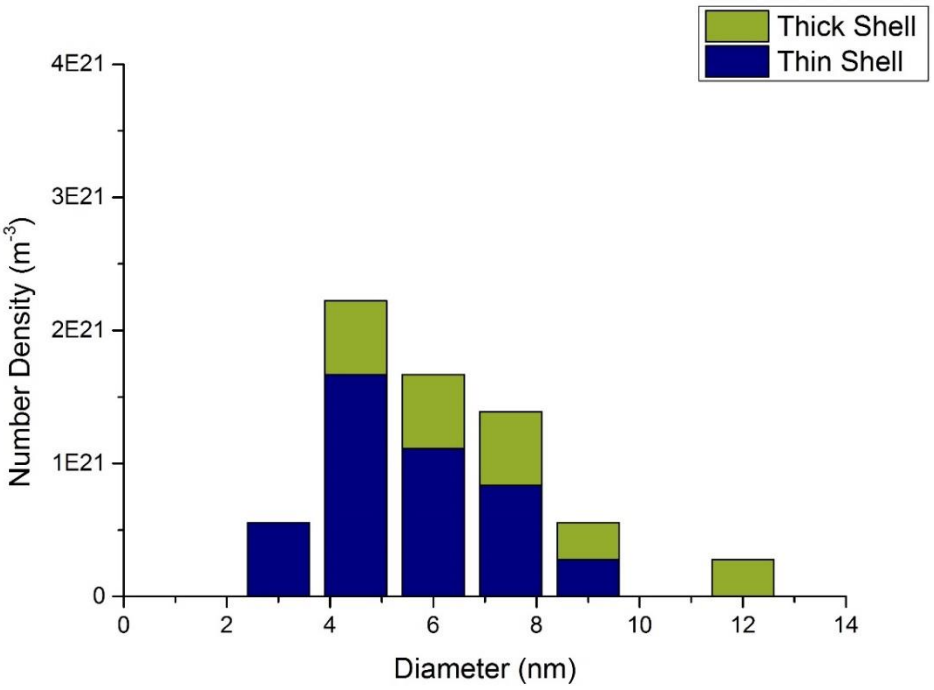
dislocation line were calculated and shown in Table 14. The number density of the precipitates associated with a dislocation line is significantly higher than those that are in the matrix. This indicates that copper-rich precipitates are preferentially heterogeneously nucleated at dislocation lines [191]. This also means that the homogeneity of the precipitate distribution within a grain might be affected by the dislocation distributions in each grain.

Table 14: Number density of the precipitates formed in WV weld steel thermally aged for 49,800 hours (according to the location)

Thermal Ageing (hours)	Number density (m^{-3})	
	Matrix	***Dislocation***
49,800	0.67×10^{22}	1.16×10^{22}

Figure 62 shows the number density of the precipitates as a function of size. Figure 62 (a) represents those precipitates that are in the matrix and Figure 62 (b) represents those precipitates associated with a dislocation line. The precipitates associated with a dislocation are generally bigger than those that are nucleated at the matrix. Also, precipitates with a thicker MnNi-rich shell, i.e. average shell thickness ≥ 1.5 nm, are mostly found to be associated with a dislocation line. This might be due to the dislocation lines acting as a fast diffusion path for solute atoms like manganese and nickel to diffuse easily to a precipitate [197].

a)



b)

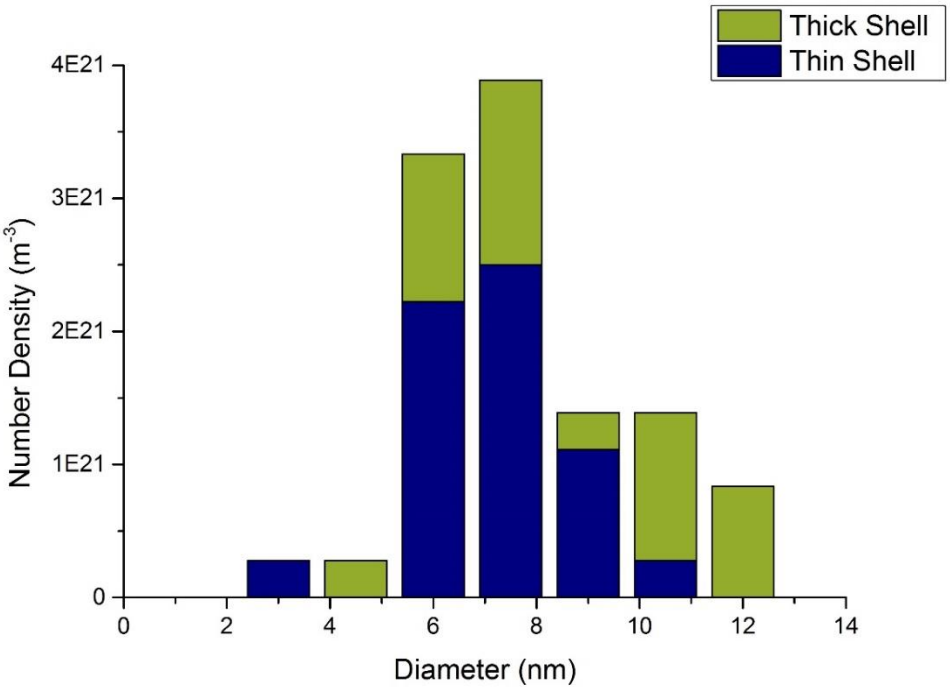


Figure 62: Diagrams showing the number density of precipitates detected as a function of precipitate diameter (a) precipitates in the matrix (b) precipitates that are located at or around a dislocation line. Note that the data in blue indicates that these precipitates have a thin manganese-nickel-rich shell (< 1.5 nm) and the green data indicates that these precipitates have a thick manganese-nickel-rich shell (≥ 1.5nm).

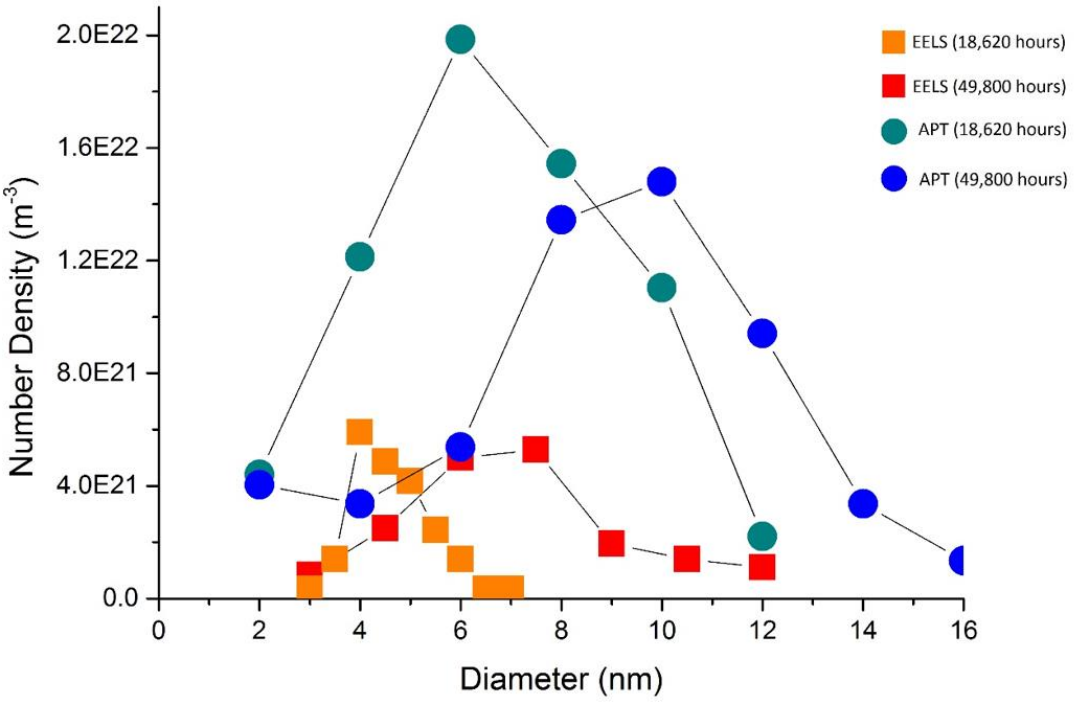


Figure 63: Diagram showing the number density of the precipitates in WV weld steel as a function of diameter of precipitates.

The number densities of precipitates in these WV weld steels measured by APT are shown in Table 13. The number density detected by APT is atleast two times higher than those calculated based on EELS data. In order to understand the reason behind this, precipitate size distribution after both ageing times that measured using APT and EELS were plotted as Figure 63. This figure shows that the higher number density measured using APT is not due to APT detecting precipitates that are smaller than the detection limits of EELS. Instead, the range of precipitates size covered by both APT and EELS analysis are comparable. The higher values in the APT results might be a result of the small sampling value and inhomogeneous distribution of precipitates along microstructural features like dislocation lines. It is worth noting that the trend curve of the precipitate size distribution after both ageing times for APT and EELS data are similar, as shown in Figure 63.

6.5.4 Precipitation under long term thermal ageing

Previous studies on Fe-Cu based steels have confirmed that the BCC copper precipitates are spherical and will only preferentially grow in the $< 011 >_{BCC}$ direction after they have reached a certain size, often occurring after being transformation into a 9R structure [73]. Further thermal ageing will then allow the 9R copper precipitates to continue to grow in the $< 011 >_{BCC}$ direction and become elliptical and eventually rod-shaped [99]. During this shape transition process, the 9R copper precipitates will transform into 3R and the FCC or FCT structures [65, 73].

In the manganese-nickel containing Fe-Cu based steels, for example the WV weld steel studied here, the shape transition is different. It is thought that the spherical BCC copper-rich core is nucleated from either

- matrix defects, i.e. dislocation lines [35] or irradiation induced dislocation loops [123], or
- non-randomly distributed manganese and nickel [45], or
- homogeneously in the matrix lattice[8].

During the growth and coarsening stage, the copper-rich precipitates reject iron, nickel or manganese from the growing core [95]. While the thermal ageing process continues, manganese and nickel are further concentrated at the interface between the copper-rich precipitates and the matrix [198].

[8] Even though that the likely-hood for the homogeneous nucleation of copper-rich precipitates is very low, it is good to include it in the consideration as one of the nucleation mechanism.

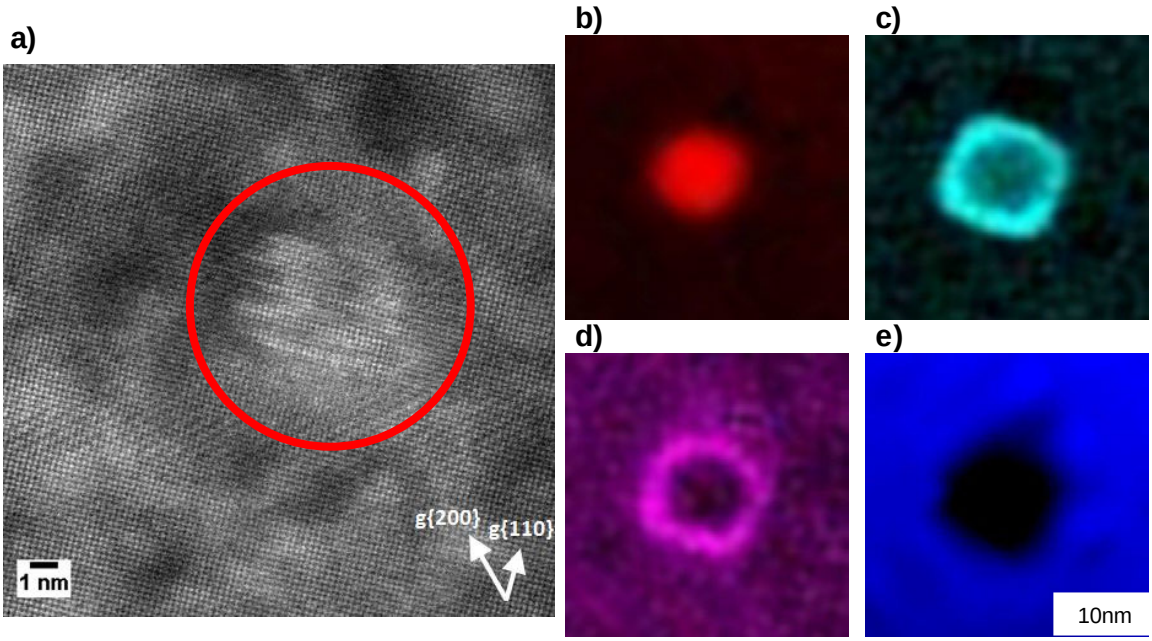


Figure 64: (a) HAADF micrograph showing a martensitically transformed copper precipitate located at the matrix. This image was taken imaged along the <001> zone axis. (b) Copper, (c) manganese, (d) nickel and (e) iron MSA reconstructed elemental maps showing a copper precipitate with a manganese- and nickel-rich shell located in the same grain and orientation as (a). Note that the colour appearing on each elemental maps is an artificial colour added to differentiate the type of element present in each map.

Results obtained from the use of a combination of advance electron microscopy in this study have revealed that the manganese and nickel might not be purely segregated to the interface between the precipitates and the matrix. The MSA reconstructed elemental maps presented in Section 6.4 showed that after approximately 49,800 hours of thermal ageing, precipitates with core-&-shell like structures were observed. The manganese and nickel that were further segregated at the precipitate-matrix interface during the long term thermal ageing process formed a faceted MnNi-rich shell on a spherical or elliptical pure copper precipitate, as shown in Figure 54. Note that one of the precipitates shown in Figure 54 has a copper core partially encased by a MnNi-rich shell. Figure 64 (a) is a HAADF micrograph showing a copper precipitate, marked by a red circle, imaged along the $< 001 >$ zone axis. The brighter fringes shown on this precipitate are similar to those observed from a transformed 9R structure under CTEM and HREM (see Section 6.2 and Section 6.3). In the same grain at the same

condition, similar precipitates were chemical mapped using EELS. The copper, manganese, nickel and iron MSA reconstructed elemental maps are shown as Figure 64 (b), Figure 64 (c), Figure 64 (d), and Figure 64 (e) respectively. By comparing the HAADF micrograph and the manganese elemental map, the faceting on the MnNi-rich shell is parallel to the $\{110\}_{BCC}$ planes. This means that the shell has preferentially grown in the $< 110 >_{BCC}$ direction. Based on these observations, it is logical to suggest that instead of just manganese and nickel segregation, co-precipitation of an ordered MnNi-rich phase on the copper core also occur in this WV weld steel during thermal aging. With this hypothesis, it is then possible to explain the existence of the partial enrichment of manganese and nickel on some of the copper precipitates observed in Section 6.4..

In Section 6.4.2.3, it was found that the brighter contrast of the precipitates under HAADF imaging correspond to the copper-core of the precipitates. The MnNi-rich shell shows a similar contrast to that of the background. This suggests that the fringes shown within the precipitate correspond to the copper-core. The MnNi-shell do not share the same structure as the copper core. Again, this indicates that the MnNi-rich shell is not part of the copper core but an individual phase that precipitates from the copper-core as suggested by Ngayam-Happy et al [114, 115].

6.5.4.1 Potential phase for the MnNi-rich shell of the copper precipitates

6.5.4.1.1 If (γ Mn, Ni) Phase,

The manganese and nickel ratio of the shell that formed in the WV weld steel that has been thermally aged for 49,800 hours was measured from the EELS data collected. Based on a manganese-nickel binary phase diagram published in Refs. [199, 200], the potential phase for the manganese and nickel ratio measured from the shell is likely to be the (γ Mn, Ni) phase. This phase belongs to the FCC system just like the copper phase. Its lattice parameter ranged from 3.5380 to 3.7025 Å (at room temperature),

dependent on the nickel concentration in this phase. The average lattice mismatch between the copper FCC and the FCC (γ Mn, Ni) phase is between 0.05 Å and 0.114 Å, depending on the nickel concentration in it. It is possible that this potential phase to remain in BCC structure while it is relatively small.

6.5.4.1.2 If B2 Phase

According to APT analysis on the same material as reported in Ref. [195], a small proportion of silicon could be present in the MnNi-rich shell of the copper-core precipitates. If we consider that silicon was present in the shell of these copper-rich precipitates, based on a manganese-nickel-silicon tertiary phase diagram published in Refs. [201, 202], the potential phase for the MnNi-shell is likely to be the B2 phase. This phase belongs to the cubic system with the space group of 'Pm3m'.

Based on previous observations shown in Figure 64, the MnNi-rich shell might not contribute as part of the copper-rich precipitates to achieve the critical size for martensitic transformation from $BCC \rightarrow 9R \rightarrow 3R \rightarrow FCC\ or\ FCT$. This indicates that the MnNi-rich shell may not be a FCC structure. Furthermore, B2 phase that is Manganese, Nickel and aluminium enriched was found to be co-precipitated with copper-rich precipitates in aluminium, nickel and manganese containing Fe-Cu based precipitate-hardening (PH) steels after thermal ageing at a relatively high temperature (≈ 500 °C), as reported in Ref. [102]. Note that, these PH steels contain a significant higher concentration of copper, nickel and aluminium. Based on simulations as reported in Refs. [193, 203], this B2 phase could be a 'wetting' layer that plays a crucial role in the $BCC \rightarrow 9R$ transition. This wetting layer stabilised the BCC copper core at an elevated temperature. Also, it was suggested that it was strained to accommodate the misorientation between the transformed 9R lattice of the copper-enriched core and the BCC iron matrix.

We can thus propose that the nucleation of the B2 phase on the copper-rich cores is encouraged by the low energy interfaces formed between equilibrium phases. In order to confirm this, experiments to combine both high resolution chemical mapping and HRTEM imaging required.

6.6 SUMMARY

Nanometre scale precipitates were found in high copper and high nickel low alloy steels that were thermally aged for 18,620 hours and 49,800 hours at a temperature of 365°C. These thermally aged precipitates have a core-&-shell structure. The core of these precipitates are copper-rich, whereas the shell is manganese- and nickel-rich.

A heterogeneous distribution of these precipitates was observed. It was found that these precipitates would preferentially nucleate at dislocations. Data obtained showed that precipitates that nucleated at dislocations possessed a larger precipitates size distribution compared to those that were not associated with dislocations. Furthermore, the precipitates that associate with dislocations have a thicker manganese- and nickel-rich shell compared to those that are not associated with dislocations.

Similar to previous studies on the copper precipitates formed in iron-copper model alloys, the copper-rich core of these nanometre scale precipitates undergo martensitic transformation from $BCC \rightarrow 9R \rightarrow 3R \rightarrow FCC/FCT$ during the process of nucleation, growth and coarsening while under thermal ageing. It is noteworthy that this martensitic transformation is a reversible process and is directly correlated to the size of the copper-rich core of these precipitates observed. The precipitate size dependent $BCC \rightarrow 9R$ martensitic transformation at an ageing temperature of 365 °C that was observed was in good agreement with previous experimental and modelling data, i.e. the precipitate size for a copper-rich core precipitate to undergo the $BCC \rightarrow 9R$ martensitic transformation at an ageing temperature of 365°C is greater and/or equal to 7 ± 1 nm.

The EELS elemental mappings suggest that the copper-rich core of these precipitates with a 9R structure are iron-free. One out of the many of these precipitates that were analysed has a BCC structure and it was found to be also iron-free. As for the manganese- and nickel-rich shell, the EELS analysis indicates that the shell of these precipitates in WV weld metals that were aged for 49, 800 hours contained a very low amount of iron, if any, the iron content would be 1.3 ± 0.5 %. Even though the data was inconclusive, the EELS analysis also suggested that very little or no silicon was detected in these thermally aged precipitates.

The shape of the precipitates is strongly dependent on its nucleating site. In general, the copper-rich core of these precipitates is spherical if these precipitates are not associated with a dislocation. Whereas, if these precipitates nucleated at dislocation, the copper-rich core would be elongated in shape depending on the nature of the dislocation.

The change in shape of the manganese- and nickel-rich shell of these precipitates was also observed after a long term thermal aging. This observation is based on the chemical elemental maps obtained at 18, 620 hours and 49, 800 hours of thermal aging. At 18, 620 hours, the manganese- and nickel-rich shell takes the shape of the copper-rich core. At 49, 800 hours, the manganese- and nickel-rich shell of these precipitates have grown and become faceted, i.e. these precipitates have become cuboidal in shape. A convincing comparison is shown in Figure 50 and Figure 64 The combination of HRTEM analysis and chemical elemental mapping shows that the shell of these precipitates tend to grow on the $\{110\}_{BCC}$ plane.

7 IRRADIATION-INDUCED SOLUTE CLUSTERS

7.1 INTRODUCTION

This chapter presents an analysis of irradiation-induced solute clusters formed in low copper and high nickel low alloy steels neutron irradiated to high neutron fluence, $\phi t \approx 5 \times 10^{23}$ neutrons.m^{-2}. The weld metals studied are part of the materials from the LONGLIFE project. The aim of this study is to identify any irradiation-induced solute clusters in the weld metals. No observation on nanometre scale solute clusters have been reported in the past from neutron irradiated low copper (> 0.1 at.%) low alloyed steels using electron microscopy. So far, Atom probe tomography (APT) is the only technique that allows us to directly visualise the distribution of these nanometre scale solute clusters[9]. Hence, the question to be answered is can EM techniques analyse the nature of these solute clusters in low copper steels [123, 204].

The details of the manufacturing process, irradiation conditions and the change of Charpy 41-J transition temperature shifts for the materials studied are given in Section 4.1.1.1. Sections 7.2 and 7.3 describe the results from electron microscopy investigations on the neutron irradiated weld metals of ANP-2 and ANP-6, as listed in Table 4 and Table 5, respectively. Further discussion on the information obtained from both weld steels and the comparison with the APT results are presented in Section 7.4.

[9] The term 'solute cluster' is used for the precipitate-like feature that detected in neutron irradiated steels by APT. This is because of no structural information can be obtained by APT.

7.2 NEUTRON IRRADIATED ANP-2 WELD STEEL

7.2.1 Diffraction contrast imaging

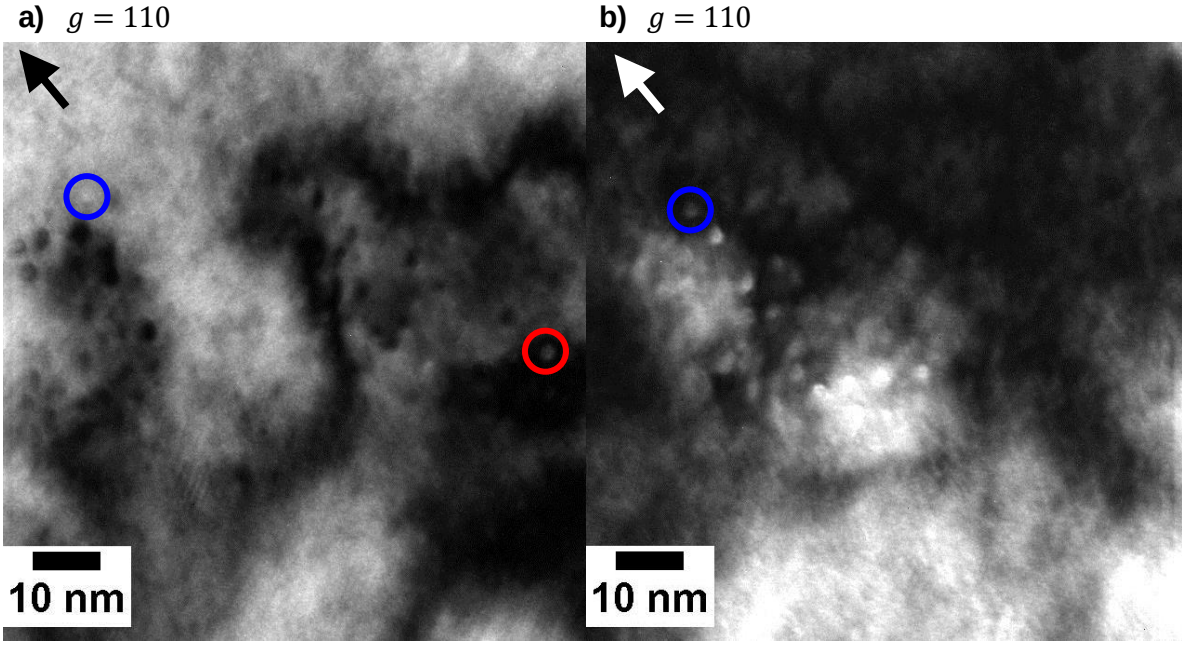


Figure 65: Nanometre-scale solute clusters in neutron irradiated ANP-2 weld metal ($\phi t \approx 5.0 \times 10^{23}$ n.m^{-2}) imaged in dynamical two-beam condition, $s_g \approx 0$. (a) Bright-field image and (b) dark-field image of the area where the clusters can be detected using g = (110) at relatively high-index zone axis.

Spherical nanometre scale solute clusters were detected in neutron irradiated ANP-2 weld metal ($\phi t \approx 5 \times 10^{23}$ neutrons.m^{-2}) using the diffraction contrast imaging technique described in the previous section. Figure 65 shows bright-field and dark-field images of an area in the neutron irradiated ANP-2 weld metal with a thickness of about 60 ± 10 nm, imaged with a dynamical two beam condition, $s_g \approx 0$. It is important to note that these nanometre scale solute clusters only became apparent when imaged along a relatively high-index zone axis and with strong contrast at this particular diffraction vector, g = (110). The dark wavy line across the bright-field image diagonally shown in the Figure 65 (a) is the contour fringe, resulting from a combination of local sample bending and in-homogeneous thickness. The nanometre scale solute clusters detected were found to have a better contrast around the contour fringe, where $s_g \approx 0$. Note that the contrast from the nanometre scale solute clusters inverted from dark to white after

passing through the thickness fringe along the direction of the g-vector used (one of which was marked with the blue circle). The contrast from solute clusters obtained using dark-field imaging (Figure 65 (b)) exhibited weaker contrast than that for the bright-field image. However, some of the detected solute clusters were reflecting and showed as bright on the dark background of the matrix in the dark field image.

In the transition region at the centre of the contour fringes, some solute clusters imaged as dark dots with a white centre, one of which is marked by the red circle on the bright-field image of Figure 65. This observation was not surprising, especially for small clusters like those found in the irradiated ANP-2 weld metal ($\phi t \approx 5.0 \times 10^{23}$ n.m^{-2}). Similar phenomena have also be observed in amorphous zones in silicon, formed by a process of direct-impact amorphisation after an irradiation with 60 keV Bi_2 ions and imaged in structure-factor contrast [205]. However, this observation found in the ANP-2 weld metal does not indicate that these detected dark features are amorphous zones. The solute cluster's contrast is dark with a white centre (amorphous-like contrast) at the contour fringe and is simply due to the thickness effect and different crystal structure to the matrix.

7.2.2 Phase contrast imaging

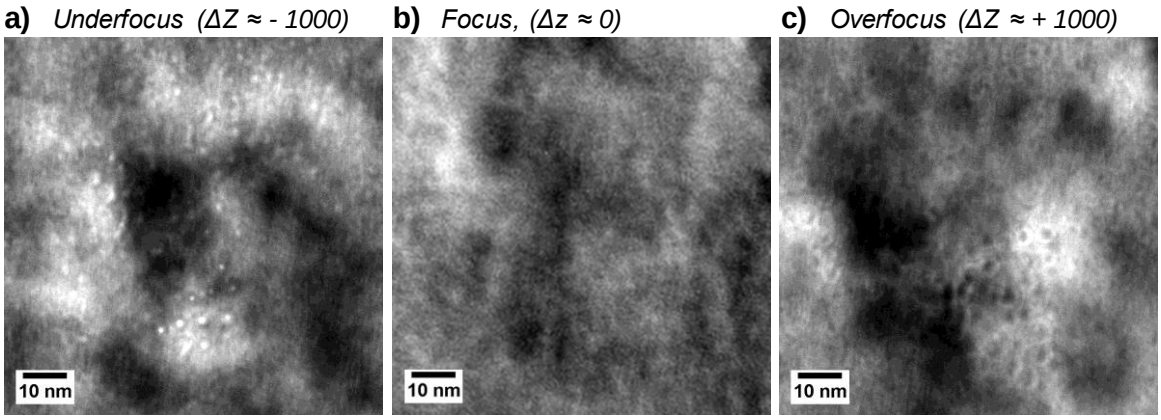


Figure 66: The same area as shown in Figure 65 at a similar magnification, imaged in bright-field conditions in both (a) underfocus (ΔZ = - 1000 nm), (b) focus (ΔZ ≈ 0 nm) and (c) overfocus (ΔZ = + 1000 nm) condition with g = 110 and with $s_g > 0$. The nanometre-scale solute clusters observed in the Figure 65 showed phase contrast behaviour typical of voids.

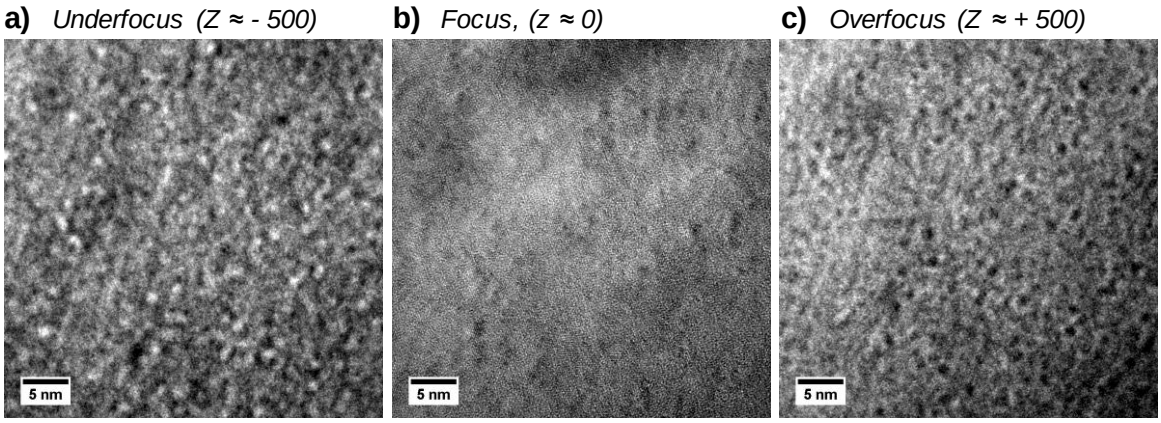


Figure 67: The same area as shown in Figure 65 at a similar magnification, imaged in a bright-field condition away from Bragg condition. (a) Underfocus (ΔZ = - 1000 nm), (b) focus (ΔZ ≈ 0 nm) and (c) overfocus (ΔZ = + 1000 nm).

A through-focal series was performed on the same area analysed in Figure 65 with the same diffraction condition. The nanometre scale solute clusters detected previously were visible at high values of defocus, as shown in Figure 66. These solute clusters are white for an under-focused image and dark for the over-focused image, i.e. showing the same phase contrast behaviour typical of void. Based on the theoretical phase contrast calculations in Ref. [147], it is reasonable to assume that these observed clusters are less dense than the matrix. Note that some of the features seen in the Figure 66 might be surface cavities. The size and shape of these clusters cannot be determined from these highly defocused images. By comparing the over-focus image Figure 66 (c) and the diffraction contrast images of the same area, as shown in Figure 65, it is possible to identify nanometre scale solute clusters that are further from the contour fringe. Due to the high number density of clusters present in the irradiated ANP-2 weld metal, it is not possible to clearly identify all the clusters from the over-focus and under-focus images shown. Nevertheless, the distribution of these nanometre scale clusters is clearly shown in these images.

Another through-focal series was also performed on the same area as in Figure 65, but this time with a condition far away from the Bragg condition, as shown in Figure 67. No nanometre scale solute clusters were visible under this condition apart from surface

craters induced during sample preparation. This means that similar to diffraction contrast imaging, these nanometre-scale solute clusters formed in neutron irradiated ANP-2 weld steels are only visible in phase contrast imaging under certain diffraction conditions. Phase contrast arises from the change in mean inner potential between the feature of interest and the matrix. Hence, this indicates that far from the Bragg condition, both the solute clusters and the matrix have similar mean inner potentials. However, when at a Bragg condition like that shown in Figure 65, the mean inner potential between the solute clusters and the matrix is different, and this difference causes a phase shift between electrons which traverse the solute clusters and those that pass through the matrix.

7.2.3 High angle annular dark field imaging

Figure 68 shows the presence of dark contrast features with diameters ranged from approximately 1 to 4 nm. This area corresponds to the region shown in Figure 65. Note that the locations of the dark contrast features correlate with the features identified as nanometre scale solute clusters visible in the diffraction contrast images. One of the examples is circled in red. It is therefore plausible that these dark features detected using HAADF imaging are the nanometre scale solute clusters. The contrast of these solute clusters suggests that they either have a lower average projected atomic number (Z_{avg}), a lower than average local density (ρ_{avg}), or both. This is consistent with the phase contrast behaviour shown by these solute clusters in Figure 66, i.e. lower average density compared to the matrix of the irradiated ANP-2 weld steel.

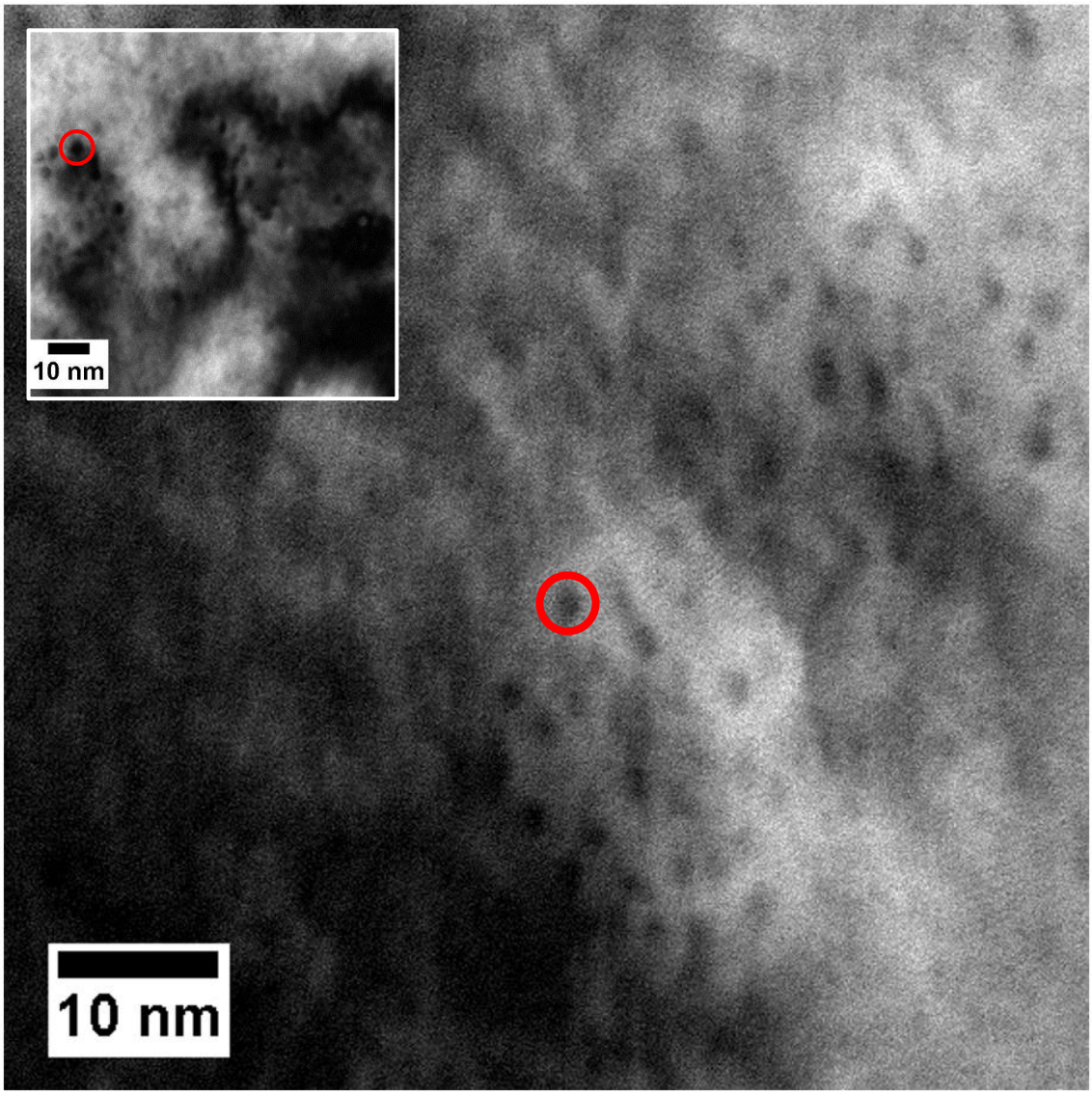


Figure 68: HAADF micrograph showing the nanometre-scale solute clusters formed in the ANP-2 weld metal imaged at the same area as shown in *Figure 65* (Small insert on the top left corner). A pair of the solute clusters that have been identified are circled in red.

7.3 Neutron Irradiated ANP-6 Weld Steel

7.3.1 High angle annular dark field imaging

A typical area of the neutron irradiated ANP-6 weld steel analysed by HAADF imaging is shown in Figure 69. Relatively coarse elongated precipitates (about 70nm by 7nm) can be seen on the grain boundary. These could be second phase particles formed during heat treatment. Small regions, with slightly brighter contrast compared to their surroundings, were also observed in the image (one of them is identified by a yellow

circle). These regions are often seen in electropolished specimens, and could be due to contamination from electropolishing, contamination from specimen storage in anhydrous iso-propanol or sample preparation induced defects. The latter seems to be most likely as specimens prepared by electropolishing are likely to have slightly rough surfaces if perfect electropolishing conditions are not achieved [206]. Slight changes in thickness (≈ ± 10 nm) would not usually be observed under conventional TEM imaging, but are seen with HAADF.

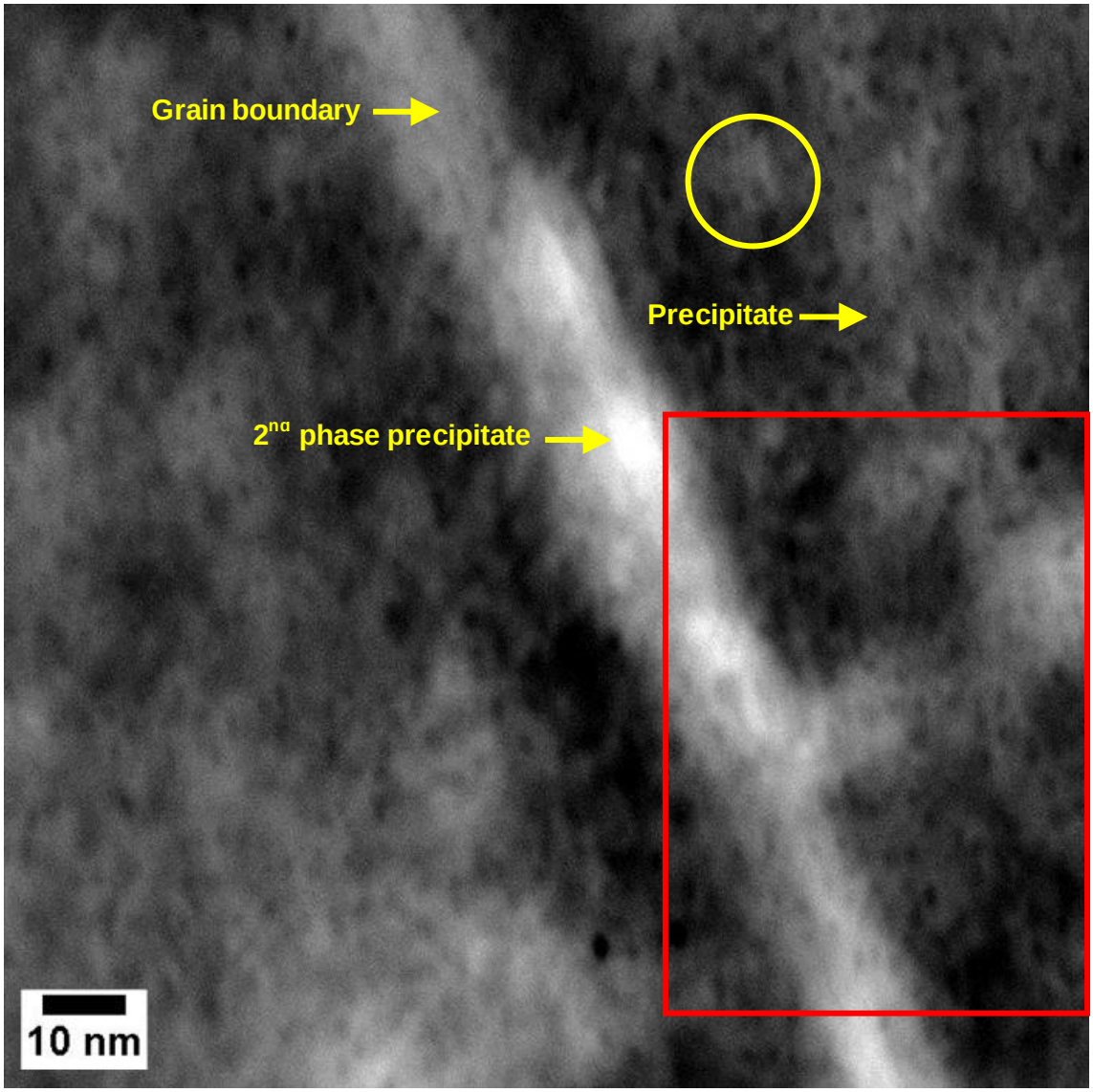


Figure 69: A typical HAADF STEM image of an area investigated at high magnification showing a grain boundary and second phase particles.

Across the whole imaged region in Figure 69, darker contrast features that range from approximately 1 to 4 nm in diameter are clearly visible. The contrast of these features are comparable with those seen in the neutron irradiated ANP-2 weld steel shown in Figure 68. This suggests that they could possibly be the nanometre-scale solute clusters. The average thickness of the region shown in Figure 69 is about 30 ± 10 nm. Note that, the nanometre scale solute clusters can be imaged easily in thinner regions, when local foil thickness < 40nm, as this avoids strong contributions from the thermal scattering and diffraction contrast. The contrast of these features indicates that the nanometre-scale solute clusters either have a lower than average projected atomic number (Z), a lower than average local density (ρ_{avg}), or both. By measuring the full width at half maximum (FWHM) of these features, their mean diameter can be estimated to be approximately 2 ± 0.5 nm.

7.3.2 Electron energy loss spectroscopy

EELS elemental mapping was performed under TEM mode using a JEOL 3000 field-emission gun TEM (FEGTEM) with a post-column Gatan Image Filter (GIF^{TM}) 2000. The specimen area used for acquiring the EELS elemental map is indicated by the red box in Figure 69. This region was carefully chosen because it has a fairly uniform thickness below 50 nm. It also contains distinct features, such as local damage from the electron beam during analysis of the grain boundary chemistry and second phase particles (as marked). The TEM bright field image and the corresponding iron-$L_{2,3}$ edge MSA reconstructed map of the area are shown in Figure 70.

Depletion of iron was evident in the second phase particles (presumably carbides), on the grain boundary (although the surroundings seem enriched) and in the solute clusters observed in the HAADF image. The diameter of these solute clusters, which lie at the same locations as the dark contrast features in the HAADF image (see Figure 69), was measured from line profiles on the iron elemental map. Based on the FWHM value, the mean diameter of these Fe-depleted features is 3 ± 0.5 nm. Although

included for completeness, the manganese and nickel signals are so weak that their elemental maps have poor Signal-to-Noise ratios (SNR) and therefore both are unsuitable for detailed chemical analyses.

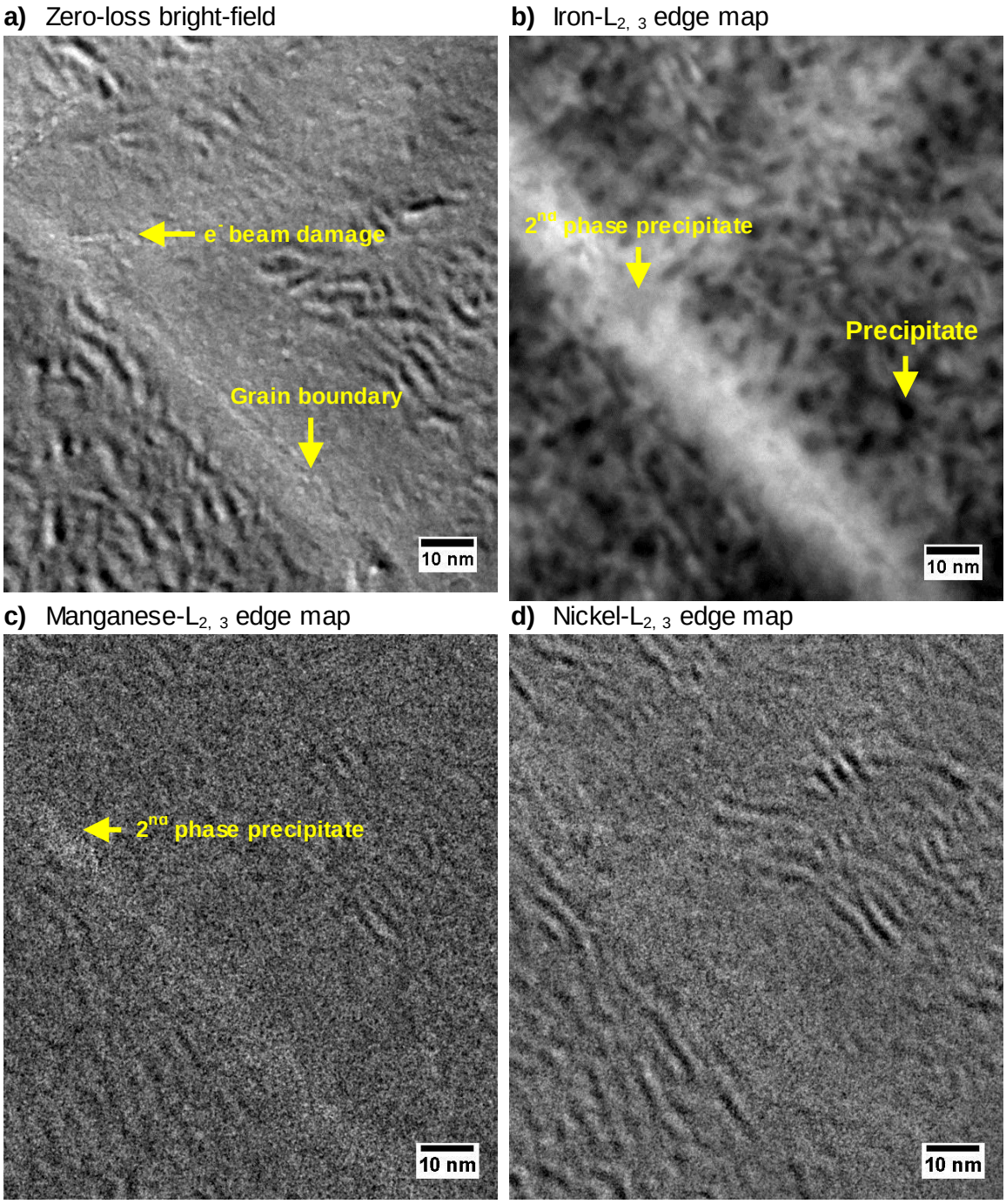


Figure 70: Area investigated in the HAADF image. (a) TEM bright field image, (b) Iron-$L_{2,3}$ edge EELS MSA reconstructed map.

There was an insufficient signal to image the distribution of the elements, apart from iron, with the EFTEM elemental-mapping approach using short acquisition times. The only indication of the ultrafine features observed in the HAADF image from the data set obtained was the depletion of iron. This kind of evidence is insufficient to prove that the features observed in the HAADF images and iron elemental map are enriched with copper, manganese, nickel, or silicon. Nevertheless, it is evident that the nano-scale sized features observed in the Fe elemental maps and HAADF images are iron-depleted and have a lower projected Z_{avg} and/or a lower local ρ_{avg}.

7.4 DISCUSSION

7.4.1 Analytical methods

Strong evidence for the presence of irradiation-induced nanometre scale solute clusters was found in the irradiated weld metals analysed using different EM techniques. It should be noted that not all of these techniques were able to provide accurate estimates of the number density of solute clusters. For example the diffraction contrast analysis will require consistent diffraction conditions over the area of interest in order to reveal the nanometre scale solute clusters in the weld metals. Furthermore, the spatial resolution and detection limit of the analytical techniques used play a major role in determining the detectability of small solute clusters. Consequently one would anticipate results from the TEM analytical techniques to be an underestimate of the true number density of precipitates &/or solute clusters. Similarly, estimates of number density of the solute clusters from APT are also subject to uncertainties since the precise number of solute clusters identified will depend on the criteria chosen during the cluster search methodology [207].

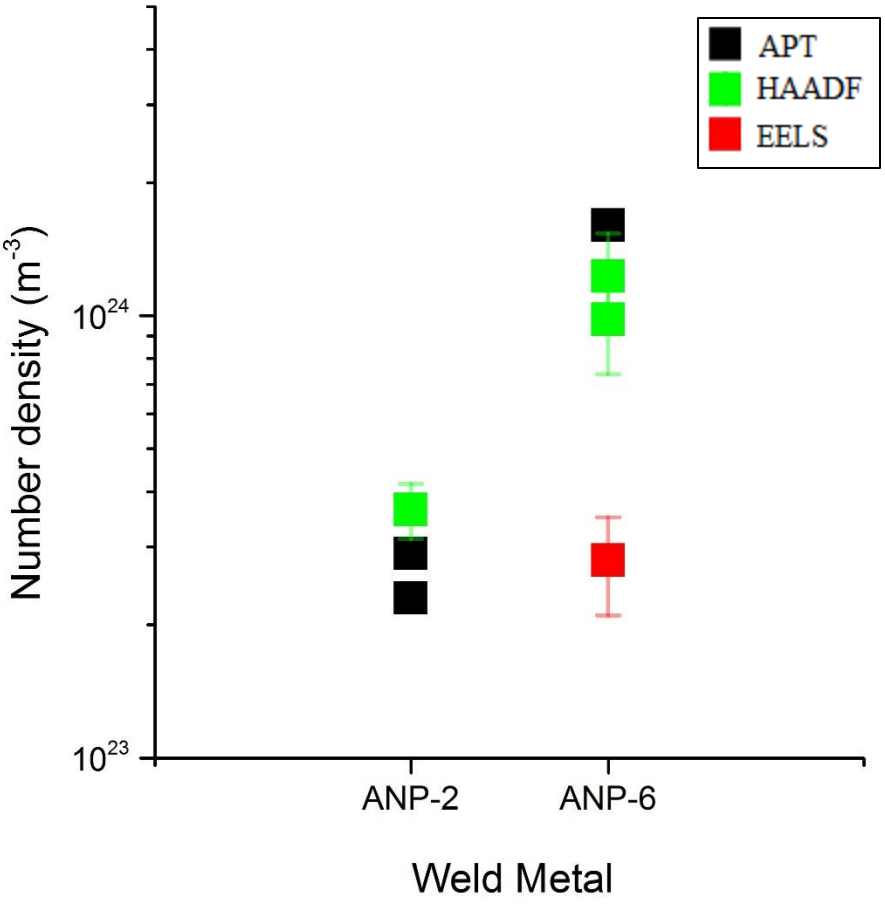


Figure 71: Summary of number densities of the solute clusters formed in neutron irradiated ANP-2 and ANP-6 measured using different analytical techniques. *The APT data is collected from Ref. [108]. Note that the y-axis has a log-scale.*

Table 15: Nanometre scale solute clusters detection percentage of each analytical technique performed in this study. Assuming that the cluster number of density that detected in APT is absolute, i.e. 100%.

Analytical Techniques	**Percentage of APT clusters No. density detected by TEM techniques, %**
HAADF (ANP-6)	72 ± 10
EFTEM Fe $L_{2,3}$-edge elemental map (ANP-6)	20 ± 5

Nonetheless it is instructive to compare the estimates of the number densities of solute clusters obtained by each technique. All the measurements are shown in Figure 71. The number density of the solute clusters measured from the ANP-2 weld steel are reasonably consistent from both APT and the HAADF images shown in Sections 7.2.3 and 7.3.1. However, the number density measurements from neutron irradiated ANP-6 weld steel are less consistent. The HAADF results were obtained from two different regions and may indicate area to area variability.

In Table 15, taking the APT data as a reference shows that measurements made from both EM techniques under-estimate the number of nanometre scale solute clusters present in neutron irradiated ANP-6 weld metal. It is probable that the under-estimation is largely due to the fact that the smallest detectable solute cluster size by EELS elemental mapping with the microscope used in this study is approximately 3 ± 0.5 nm. The underestimate of number density of precipitates using HAADF is not related to spatial resolution as the technique revealed solute clusters as small as approximately 1 nm in diameter. However, diffraction contrast and an inhomogeneous sample thickness mask the true variations in the signal from embedded nanometre scale solute clusters. An improved sample preparation approach, most likely involving a focused ion beam (FIB) will be required to overcome this problem.

7.4.2 Chemical composition of solute cluster

Due to poor signal-to-noise ratio from the elemental maps that were shown in Section 7.3.2, we were unable to determine the chemical distribution of these solute clusters. Based on the results from the APT analysis obtained in the LONGLIFE project, it has been confirmed that these solute clusters are manganese, nickel and silicon enriched. A small amount of copper was also present in these solute clusters, i.e. less than 6 at. %, if assumed that iron as an artefact resulted from trajectory aberration effects. Based on the study of thermally aged precipitate that was reported in Section 6 and the APT results from the LONGLIFE project, it strongly indicated that the presence of copper in

these solute clusters act as a heterogeneous nucleation site for manganese- and nickel-rich phase to form. Results from the LONGLIFE project further suggested that copper was involved at the initial stage of solute clustering, hence, the higher the concentration of copper in the material, the higher the volume fraction of solute clusters formed in a low alloyed steel (See Section 11.1, Appendix A, Section I.VII). The experiments performed in the LONGLIFE project also showed that the chemical composition of these solute clusters is bulk chemistry dependent. The bulk chemistry of low alloyed steel has a strong influence on the number density of solute clusters formed during neutron irradiation. The effect of bulk chemistry of a low alloyed steel on the number density of the solute clusters are reported in Section 11.1, Appendix A.

7.5 SUMMARY

This is the first time that irradiation-induced solute clusters were visualised using techniques other than APT, i.e. transmission electron microscopy. These solute clusters are only visible when certain diffraction conditions were achieved. These solute clusters shown stronger contrast against the background at Bragg conditions. This suggests that these solute clusters have a weak strain field around the matrix. Phase contrast analysis shows that these solute clusters have a different mean inner potential compared to the matrix when certain diffraction conditions were met. Phase shift between electrons that traverse the solute clusters and matrix were only observed at a suitable diffraction condition. HAADF shows that these solute clusters have either a lower average atomic density, or average Z_{avg}, or both compared to the matrix.

It is important to note that not all electron microscopy techniques are capable of providing accurate estimates of the number density of solute clusters, as discussed in Section 7.4.1. It was found that chemical sensitive electron microscopy techniques such as EELS/EDS mapping and HAADF imaging are a better option in measuring the number density of solute clusters.

The number density of solute clusters measured from neutron irradiated ANP-2 and ANP-6 using electron microscopy techniques are comparable with those that were measured by APT. It is noteworthy that the differences between the number density measured by electron microscopy techniques and APT could be due to the heterogeneous nucleation of these solute clusters and the differences in sampling size of both techniques.

8 ELECTRON BEAM INDUCED DAMAGE TO PRECIPITATES &/OR SOLUTE CLUSTERS

8.1 INTRODUCTION

Electron beam induced surface damage to TEM samples of low alloy steels has been discussed in Section 5.2.3. This surface damage was observed on low alloy steels that have been neutron irradiated or thermally aged. The damage is caused by the energy of the electron beams used in TEM analysis as it possesses enough energy to displace surface atoms or atoms from their equilibrium lattice sites. In the study of the chemical composition of precipitates in thermally aged and solute clusters in neutron irradiated low alloy steels, preferential electron beam damage sites were observed during Energy-dispersive X-ray (EDX) analysis using very finely focussed probes. The following sections describe and discuss the damage observed in the specimens analysed.

8.1.1 Experimental procedures for EDX-line scans

EDX-line scans were performed on both neutron irradiated and thermally aged low alloy steels in which nanometre scale solutes clusters and precipitates were observed. The spot-size of the electron beam used for EDX-line scans was 0.5 ± 0.1 nm with an electron beam energy of 297 kV. The electron beam current used was 400pA. Each set of EDX-line scans were drift corrected with multiple sub-pixels (32 x 32 sub-pixels) per nanometre in STEM imaging mode. The electron beam scanned an area of one square nanometre within each pixel in one second before moving on to the next pixel. Hence, in one cycle, each square nanometre pixel will be exposed to the electron beam for an average of one second. The number of cycles per line-scan determine the total time of a square nanometre pixel exposed to the electron beam.

8.2 OBSERVATIONS

8.2.1 Neutron irradiation-induced precipitates

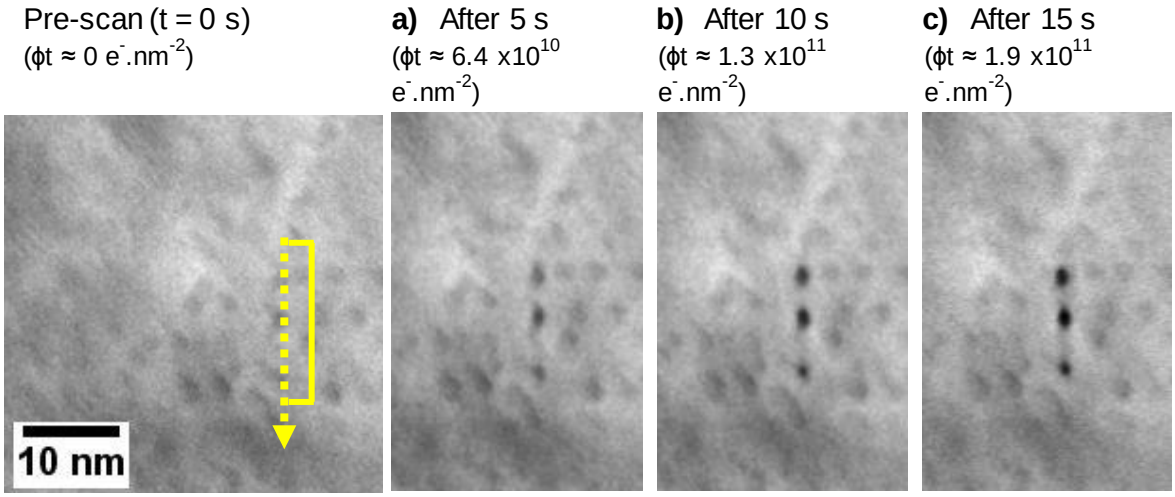


Figure 72: HAADF micrograph of the region shown in Figure 65. The yellow arrow indicates the scanning direction of the electron beam. The yellow box indicates the region scanned.

The nanometre scale solute clusters were observed in both neutron irradiated ANP-2 and ANP-6 weld steels, as shown in Sections 7.2 and 7.3. EDX-line scans were performed across these solute clusters.

Figure 72 shows one of the examples of the EDX-line scan that performed. The area chosen for the EDX-line scan is marked by a yellow box. The yellow dotted line arrow indicates the scanning direction. Notes that the contrast of the solute clusters located along the EDX-line scan became stronger during the scans. This was observed in all the EDX-line scans performed on neutron irradiated weld steels. Electron beam damage was found at the area where the solute clusters are located after EDX-line scans. This was confirmed by a through-focal series performed on the region investigated, as shown in Figure 73, where surface craters were found where the electron beam had been focussed.

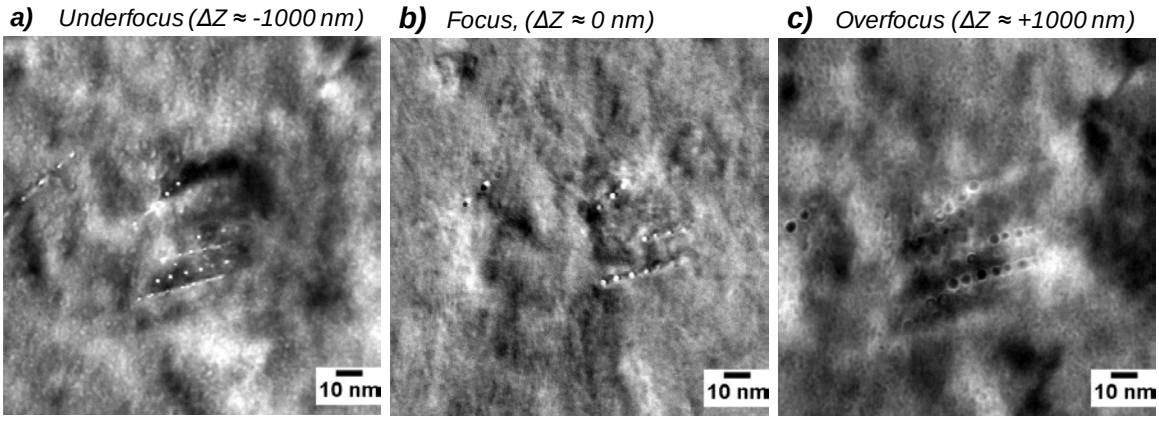


Figure 73: A through-focal series of the region where EDX-line scans were performed on neutron irradiated ANP-2 weld steels. (a) Underfocus (ΔZ = -1000 nm) bright-field micrograph, (b) focus (ΔZ = 0 nm) bright-field micrograph, and (b) overfocus (ΔZ = + 1000 nm) bright-field micrograph.

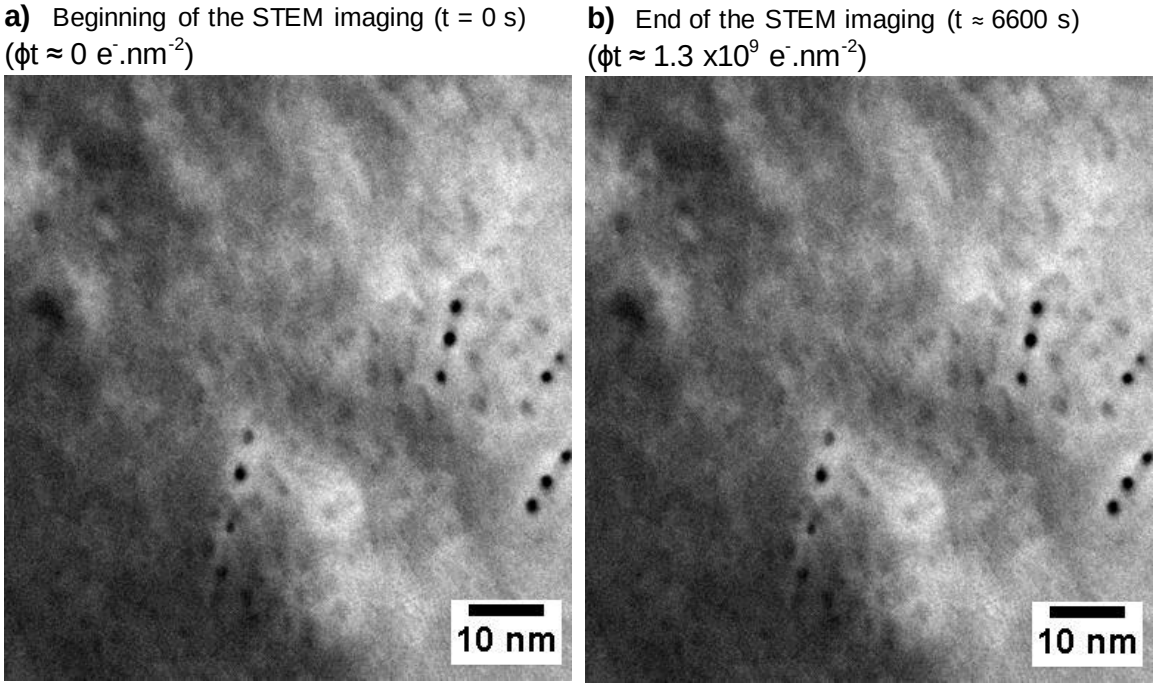


Figure 74: HAADF micrographs showing the region exposed to constant electron beam for 110 minutes. (a) Pre-scan and (b) after 110 minutes.

It was thought that electron beam damage on the solute clusters will become visible after a duration of exposure to the electron beam. In order to determine this threshold dose for visible electron beam damage, the region shown in Figure 72 was subjected to constant electron beam scanning under the STEM mode for 110 minutes, i.e. electron fluence, $\phi t \approx 1.3 \times 10^{9}$ $e^{-}.nm^{-2}$. The spot size and energy of electron beam used were the same as those used for the EDX-line scans. The results were shown in Figure 74.

No obvious change in contrast was observed while comparing the pre-scan micrographs and that after 110 minutes. Hence it is thought that the threshold for electron beam damage on these precipitates is over an electron fluence of 1.3 x 10^{9} e^{-}.nm^{-2}.

8.2.2 Thermally aged precipitates

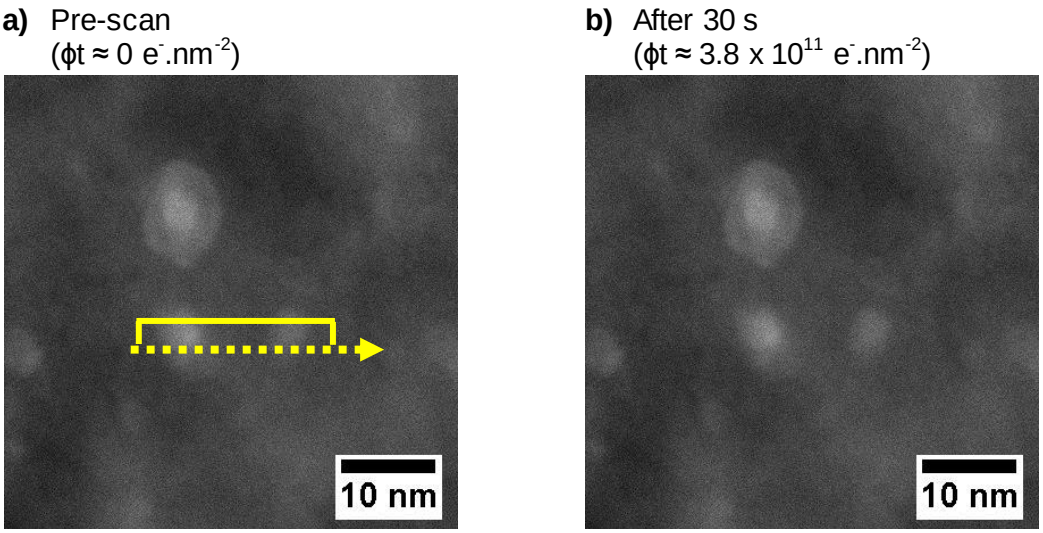


Figure 75: HAADF micrographs showing thermally aged precipitates that have been EDX-line scanned. The yellow arrow indicates the scanning direction. The yellow box indicates the region scanned.

EDX-line scans were also performed on precipitates found in thermally aged WV weld steel. The conditions for EDX-line scans were the same as those used in for neutron irradiated weld steels. One of the examples is shown in Figure 75. It is important to note that no electron beam induced damage could be observed at both the core and shell of the thermally aged precipitates that have been EDX-line scanned for 30 seconds, i.e. electron fluence, ϕt ≈ 3.8 x 10^{11} e^{-}.nm^{-2}.

8.3 Discussion

8.3.1 Irradiation-induced solute clusters & thermally aged precipitates

Electron beam damage was evident on solute clusters observed in both neutron irradiated ANP-2 and ANP-6 weld steels. No evidence of electron beam damage was

observed on thermally aged precipitates, even after twice the exposure time or doubles the electron fluence. This indicates that solute clusters/precipitates formed under the condition of irradiation and thermal ageing are different. Hence it is necessary to understand the differences between the solute clusters formed under irradiation and precipitates formed under thermal aging.

8.3.1.1 Chemical composition

Based on APT analysis on the same neutron irradiated weld steels reported in this study, the average chemical composition of the solute clusters formed in both the neutron irradiated weld steels, ANP-2 and ANP-6, is $Mn_{36}Ni_{49}Si_{10}(Cu_YP_Z)$, where Y and Z are approximately 5 [208]. As for the precipitates formed in the thermally aged WV weld steels, the average chemical composition for precipitates with core-shell structure is $Mn_{23}Ni_{30}Si_5Cu_{42}$ after 18,620 hours and $Mn_{21}Ni_{26}Si_5Cu_{44}$ after 49,800 hours [195]. The average chemical composition for the shell of the precipitates formed after 18,620 hours and 49,800 hours respectively is $Mn_{40}Ni_{52}Si_8$ and $Mn_{41}Ni_{50}Si_9$ respectively. Note that all the iron that detected in these precipitates are assumed to be artefact induced during the evaporation process during APT analysis.

The average chemical composition of the irradiation-induced solute clusters and thermally aged precipitates detected using APT are thus very similar, if we assumed that copper detected in these precipitates is the core. The chemical composition of these precipitates are also similar to precipitates/solute clusters identified as manganese-nickel-rich precipitates (MNPs) in low copper weld steels reported in Refs. [1, 9, 108]. These precipitates/solute clusters are predicted to have slow kinetics of nucleation and growth, hence, it is known as ‘late blooming precipitates’ [5, 9, 123].

8.3.1.2 Structure of the precipitates/solute clusters

Previous chapters have shown that in thermally aged Fe-Cu (> 0.1 at.%) based steel, precipitates were found after a long term thermal ageing to have a copper enriched

core with a BCC structure during the nucleation process. Once the copper core grows and reaches a critical size, it will transform to a FCC or FCT structure via 9R and 3R structures.

The shell of these thermally aged precipitates is manganese and nickel-rich. It is possible that a MnNi-rich phase to precipitate at the interface between the copper-enriched nucleus and the matrix, as discussed in Section 6.5.4.1. APT analysis shows that the chemical composition of the solute clusters in the neutron irradiated materials is very similar to the MnNi-rich phase formed under thermal ageing in high copper containing steel. Hence, it is reasonable to assume that the irradiation-induced solute clusters share the same phase as those formed under thermally ageing, with the exception that the solute clusters form might be a dis-ordered structure or phase.

8.3.1.3 Formation of precipitates/solute clusters

The formation of the ordered MnNi-rich phase under thermal ageing conditions is known to be based on the 'substitution diffusion mechanisms'. This is because of the manganese and nickel are of similar size as iron atoms. It was found that these MnNi-phase is preferentially nucleated on the copper-enriched precipitates [209]. The EELS results that presented in Section 6.4 show that thicker MnNi-rich phase is frequently found on those copper precipitates that preferentially nucleated at dislocation lines. Also, the EELS results indicate that the kinetic of nucleation and growth for the MnNi-rich phase is much slower compared to the copper-rich phase. This is because copper in the iron matrix is in a supersaturated state (high thermodynamic driving force for precipitation). Additionally, the non-randomly distributed nickel and manganese after the initial stress relief heat treatments provide heterogeneous nucleation sites for the copper precipitation [45].

Previous studies on the precipitation in low copper (> 0.1 at.%) steels suggested that the mechanism behind irradiation induced solute clusters is that point defect clusters

formed during the fast neutron bombardment induced displacement cascade events [121, 210, 211]. The MnNi-rich phase then precipitates on the point defect clusters by heterogeneous nucleation. Atomistic Kinetic Monte Carlo simulations also indicate that most of the MnNi-rich phase is associated with self-interstitials atom (SIA) clusters and the copper phase is associated with vacancies [114, 115, 123]. This means that the MnNi-rich phase formed under neutron irradiation might be a disordered phase that associates with SIA clusters and vacancies.

8.3.2 Plausible explanation for the electron beam damage on irradiation-induced solute clusters

The electron beam damage observed on the irradiation-induced solute clusters at lower electron fluence compared to the thermally aged MnNi-rich phase that has a similar chemical composition, as presented in Section 8.2.1 and Section 8.2.2. This observation suggests that the solute clusters formed under neutron irradiation are different compared to the MnNi-rich precipitates that are formed under thermal ageing.

Based on the observation mentioned, it is clear that the irradiation-induced solute clusters have a lower threshold energy to displace atoms at the MnNi-rich solute clusters compared to thermally aged MnNi-rich precipitates. This lower in threshold energy for atoms displacement indirectly suggests that the local chemical bonding between atoms within the MnNi-rich solute clusters is weaker compared to the thermally aged MnNi-rich precipitates. This weaker local chemical bonding could be due to the association of a significant amount of point defects induced during neutron irradiation. Further experiments are required in order to confirm this.

9 FUTURE WORK

The work presented in this thesis has attempted to answer some of the outstanding questions concerning the differences between the precipitates and solute clusters formed under neutron irradiation and thermal aging, and also, the effects of chemical elements on neutron irradiation-induced microstructure. However, during the course of this research project some new avenues for investigation have arisen which could not be fully completed within the time-frame of this project. Similarly, there are still some outstanding issues in the existing work which could warrant further analysis.

9.1 CHEMICAL ANALYSIS

Despite the fact that significant information on the precipitates and solute clusters that formed in low alloy steels under thermal ageing and neutron irradiation was obtained in the past years, there is still inconsistency in the chemical composition of the precipitates and solute clusters that formed in low alloy steels, especially regarding the concentration of iron within these clusters. Only recently has electron microscopy had the technology, i.e. higher detection efficiency and faster read-out EDX detector and EEL spectrometer, to obtain chemical information at a resolution and sensitivity that is comparable with APT as demonstrated in this work. With these new capabilities, we are now able to provide chemical information on these precipitates and solute clusters with reasonable confidence.

In order to improve further the confidence of the results obtained, it is important to understand the detection limits of these new detectors, especially using these detectors to detect manganese, nickel, copper, silicon and phosphorus. By doing so, we would be able to improve our understanding on the differences in chemical information on the precipitates and solute clusters obtained using the latest EDX detector, EEL

spectrometer and APT. For example, the concentration of silicon in thermally aged precipitates.

To understand the limitation of these new detectors, the author proposes an experiment to study a series of Fe-based model alloys with known chemistry and with a variation of a limited amount of manganese, nickel, copper, silicon and phosphorus that remained in the solid solution. The analytical techniques involved in this experiment would be APT and TEM that with a high detection efficiency fast read-out EDX detector and EELS spectrometer installed.

9.2 THERMALLY AGED PRECIPITATION

The author has demonstrated that the martensitic transformed copper-rich precipitate observed in the thermally aged low alloy steels are iron free. However, very little information on the iron concentration of BCC copper-rich precipitates is available. To improve the understanding of the iron concentration of the copper-rich precipitates before transformation, precipitates of less than 7nm in diameter , for those samples that are thermally aged at 365 ˚C, should be analysed. This is possible by using the latest EEL spectroscopy installed in a TEM with a probe size of less than 0.5nm.

Furthermore, it is important to obtain information on the nucleation process of the manganese- and nickel-rich phase formed in the WV weld metal during the thermal aging process. With a high chemically sensitivity EDX detector and EELS spectrometer on a TEM, it is important to re-examine WV weld metal that has been thermally aged for less than 18,000 hours. This proposed experiment will allow us to observe the initial stage of the precipitation of manganese- and nickel-rich phase on the copper-rich precipitate and this can be compared with the APT results obtained by Morley [89].

The crystal structure of the manganese- and nickel-rich phase is also important for the understanding of the hardening effect of this phase in a low alloy steel. The author is currently involved in an experiment that has an objective of discovering the structure of

this manganese- and nickel-rich phase in a long term thermal aged WV weld metal. In this experiment, a series of atomic resolution chemical spectrum images and micrographs of core-shell precipitates would be obtained using a TEM and compared with simulated TEM micrograph to confirm the structure and chemical distribution of these core-shell precipitates. Also, this experiment will provide information of the presence of a 'wetting' layer for the BCC → 9R transition of the copper-rich core of these precipitates, as mentioned in Section 6.5.4.1.

9.3 NEUTRON IRRADIATION-INDUCED SOLUTE CLUSTERING

The mechanism of formation of these irradiation-induced solute clusters still remains unclear. However, the author believed that if convincing data on the presence of point defects and presence of iron in solute clusters can be obtained, it is possible to improve our understanding on the mechanism of its formation. This is potentially possible using a combination of advanced electron microscopy analytical techniques such as exit wave reconstruction, atomic resolution high angle annular dark field imaging and atomic resolution chemical elemental mapping. It is important to note that these techniques present challenges for sample preparation as they demand a TEM specimen that is very thin, i.e. less than 40nm in thickness, and with an almost defect free surface. Also, as the materials that are to be analysed are radioactive, radioactive safety rules and regulation of an institution may have restrictions on the manipulation of these radioactive materials and this indirectly limits the sample preparation techniques that one could use to prepare a suitable TEM specimen for these proposed experiments.

10 REFERENCES

[1] G.R. Odette, G.E. Lucas, Recent progress in understanding reactor pressure vessel steel embrittlement, Radiation Effects and Defects in Solids 144 (1998) 189-231.
[2] G.R. Odette, G.E. Lucas, Embrittlement of nuclear reactor pressure vessels, JOM 53 (2001) 18-22.
[3] R. Ngayam-Happy, C.S. Becquart, C. Domain, L. Malerba, Formation and evolution of MnNi Clusters in neutron irradiated dilute Fe alloys modelled by a first principle-based AKMC method, Journal of Nuclear Materials 426 (2012) 10.
[4] C.L. Liu, G.R. Odette, B.D. Wirth, G.E. Lucas, A lattice Monte Carlo simulation of nanophase compositions and structures in irradiated pressure vessel Fe-Cu-Ni-Mn-Si steels, Materials Science and Engineering A 238 (1997) 202-209.
[5] G.R. Odette, B.D. Wirth, A computational microscopy study of nanostructural evolution in irradiated pressure vessel steels, Journal of Nuclear Materials 251 (1997) 157-171.
[6] M.G. Burke, The origin of the term 'End-of-life' of a nuclear power plant, in: J.J.H. Lim (Ed.)IGRDM-18, Miyazaki, Japan, 2014.
[7] Nuclear power plant life management processes: Guidelines and practices for heavy water reactors, IAEA, Vienna, Austria, 2006.
[8] R.K. Nanstad, M.A. Sokolov, D.E. McCabe, Applicability of the fracture toughness master curve to irradiated highly embrittled steel and intergranular fracture, JAI 5 (2008) 14.
[9] G.R. Odette, R.K. Nanstad, Predictive reactor pressure vessel steel irradiation embrittlement models: Issues and opportunities, JOM 61 (2009) 17-23.
[10] M.K. Miller, K.A. Powers, R.K. Nanstad, P. Efsing, Atom probe tomography characterizations of high nickel, low copper surveillance RPV welds irradiated to high fluences, Journal of Nuclear Materials 437 (2013) 107-115.
[11] E.D. Eason, G.R. Odette, R.K. Nanstad, T. Yamamoto, A physically-based correlation of irradiation-induced transition temperature shifts for RPV steels, Journal of Nuclear Materials 433 (2013) 240-254.
[12] Integrity of Reactor Pressure Vessels in Nuclear Power Plants: Assessment of Irradiation Embrittlement Effects in Reactor Pressure Vessel Steels, IAEA Nuclear Energy, Vienna, April 2009.
[13] Standard practice for neutron radiation damage simulation by charged particle irradiation, Annual book of ASTM Standards, ASTM International, American Society for Testing and Materials, ASTM E521, West Conshohocken, PA, 2002.
[14] G.R. Odette, G.E. Lucas, in: J.T.A. Roberts, J.R. Weeks, G.J. Theus (Eds.) Proc. 2nd Int. Symp. on Environmental Degradation of Materials in Nuclear-Water ReactorsLaGrange Park, IL USA, 1986, pp. 345.
[15] T.J. Williams, P.R. Burch, C.A. English, P.H.N. De la cour Ray, in: G.J. Theus, J.R. Weeks (Eds.) Proc. 3rd Int. Symp. on Environmental Degradation of Materials in Nuclear Reactors - Water Reactors, The Metallurgical Society, Warrendale, PA, 1988, pp. 121.
[16] G.R. Odette, G.E. Lucas, Embrittlement of LWR pressure vessel steels, EPRI NP 6114, Electric Power Research Institute (1989).
[17] G.R. Odette, G.E. Lucas, in: G.J. Theus, J.R. Weeks (Eds.) Proc. 3rd Int. Symp. on Environmental Degradation of Materials in Nuclear Reactors - Water Reactors, The Metallurgical Society, Warrendale, PA. USA, 1988, pp. 345.
[18] G.R. Odette, G.E. Lucas, in: N.H. Packan, R.E. Stoller, A.S. Kumar (Eds.) The effects of radiation on materials: 14th Int. Symp. , ASTM-STP-1046 (American Society for Testing and Materials), Philadelphia, PA. USA, 1990, pp. 323.

[19] G.R. Odette, E.V. Mader, G.E. Lucas, W.J. Phythian, C.A. English, D.S. Gelles, R.K. Nanstad, The effects of radiation on materials, in: E.A. Little (Ed.) 16th International Symposium of Radiation Damage of Materials Philadelphia, USA, 1993, pp. 323.
[20] G.R. Odette, G.E. Lucas, D.K. Klingensmith, Effects of Irradiation on Materials, in: D.S. Gelles, R.K. Nanstad, A.V. Kumar, E.A. Little (Eds.) 17th Int. Symp. ASTM-STP-1270West Conshohoken, PA, USA, 1996, pp. 606.
[21] G.R. Odette, G.E. Lucas, Current understanding of the effects of environmental and metallurgical variables on RPV embrittlement, Proc. of the US NRC 24th Water Reactor Safety Information Meeting, 1997, pp. 1.
[22] P. Pareige, Etude a la sonde atomique de l'evolution microstructurale sous irradiation d'alliages ferritiques Fe-Cu et d'aciers de cuve de reacteurs nucleaires, Universite de Rouen, Rouen, 1994.
[23] P. Pareige, F. Perocheau, P. Auger, S. Jumel, H. Bernas, Nuclear Instruments and Methods in Physics Research B 178, (2001) 233.
[24] G.R. Odette, B.D. Wirth, A computational microscopy study of nanostructural evolution in irradiated pressure vessel steels, Journal of Nuclear Materials 251 (1997) 157-171.
[25] M.A. Puigvi, Y.N. Osetsky, A. Serra, Interactions between vacancy and glissile interstitial clusters in iron and copper, Materials Science and Engineering A 365 (2004) 101-106.
[26] M.A. Puigvi, A. Serra, N. De Diego, Y.N. Osetsky, D.J. Bacon, Features of the interactions between a vacancy and interstitial loops in metals, Philosophical Magazine Letters 84 (2004) 257-266.
[27] E. Kuramoto, K. Ohsawa, T. Tsutsumi, Computer simulation of defects interacting with a dislocation in Fe and Ni, Journal of Nuclear Materials 283-287 (2000) 778-783.
[28] E. Kuramoto, K. Ohsawa, T. Tsutsumi, Computer simulation of fundamental behaviors of point defects, clusters and interaction with dislocations in Fe and Ni, CMES - Computer Modeling in Engineering and Sciences 3 (2002) 193-200.
[29] R. Bullough, B.L. Eyre, R.C. Perrin, Growth and stability of voids in irradiated metals, Nucl Appl Technol 9 (1970) 346-355.
[30] V.G. Kapinos, Y.N. Osetskii, P.A. Platonov, The mechanism of nucleation of vacancy loops with burgers vectors 〈100〉 in BCC metals, Journal of Nuclear Materials 173 (1990) 229-242.
[31] V.G. Kapinos, D.J. Bacon, Model for vacancy-loop nucleation in displacement cascades, Physical Review B 52 (1995) 4029-4043.
[32] J.H. Shim, D.I. Kim, W.S. Jung, Y.W. Cho, K.T. Hong, B.D. Wirth, Atomistic study of temperature dependence of interaction between screw dislocation and nanosized bcc Cu precipitate in bcc Fe, Journal of Applied Physics 104 (2008).
[33] H.K. Hardy, T.J. Heal, Report on precipitation, Progress in Metal Physics 5 (1954) 143-278.
[34] R.W. Cahn, P. Haasen, Physical metallurgy, 4th revised & enhanced ed., North-Holland, Amsterdam, 1996.
[35] P.D. Styman, Atomic scale studies of thermally aged reactor pressure vessel steels, Department of Materials, University of Oxford, Oxford, 2013.
[36] P.D. Styman, J.M. Hyde, K. Wilford, A. Morley, G.D.W. Smith, Precipitation in long term thermally aged high copper, high nickel model RPV steel welds, Progress in Nuclear Energy 57 (2012) 86-92.
[37] J. Walmsley, S. Fisher, P. Spellward, Microstructural and microchemical characterisation of ferritic ex-service Magnox Control Rod sheath material, Effects of Radiation on Materials: 18th International Symposium 1325 (1999) 869-881.
[38] S.B. Fisher, J.E. Harbottle, N. Aldridge, Radiation hardening in magnox pressure -vessel steels, Philosophical Transactions of the Royal Society of London. Series A, Mathematical and Physical Sciences 315 (1985) 301-332.

[39] M.R. Wootton, R. Moskovic, C.J. Bolton, P.E.J. Flewitt, Magnox Steel Reator Pressure Vessel Monitoring Schemes - An Overview, 24th Symposium on Effects of Radiation on Nuclear Materials and the Nuclear Fuel Cycle, ASTM, Denver, Colorado, USA, 2008.
[40] G.R. Odette, On the dominant mechanism of irradiation embrittlement of reactor pressure vessel steels, Scripta Metallurgica 17 (1983) 1183-1188.
[41] M.K. Miller, K.F. Russell, Atom probe characterization of copper solubility in the Midland weld after neutron irradiation and thermal annealing, Journal of Nuclear Materials 250 (1997) 223-228.
[42] M.K. Miller, K.F. Russell, R.E. Stoller, P. Pareige, Atom probe tomography characterisation of the solute distribution in a neutron-irradiated and annealed pressure vessel steel weld, Rep. NUREG/CR-6629, ORNL/TM-13768, Oak Ridge, TN, 1999.
[43] M.K. Miller, B.D. Wirth, G.R. Odette, Precipitation in neutron-irradiated Fe-Cu and Fe-Cu-Mn model alloys: a comparison of APT and SANS data, Materials Science and Engineering a-Structural Materials Properties Microstructure and Processing 353 (2003) 133-139.
[44] S.C. Glade, B.D. Wirth, G.R. Odette, P. Asoka-Kumar, P.A. Sterne, R.H. Howell, Positron annihilation spectroscopy and small-angle neutron scattering characterisation of the effect of Mn on nanostructural features formed in irradiated Fe-Cu-Mn alloys, Philos. Mag. 85 (2005) 10.
[45] A. Cerezo, S. Hirosawa, I. Rozdilsky, G.D.W. Smith, Combined atomic-scale modelling and experimental studies of nucleation in the solid state, Philosophical Transactions of the Royal Society of London. Series A, Mathematical and Physical Sciences 361 (2003) 14.
[46] A. Cerezo, S. Hirosawa, G. Sha, G.D.W. Smith, 3-D atomic-scale experimental and modelling studies of the early stages of precipitation, Minerals, Metals & Materials Soc, Warrendale, 2005.
[47] A. Seko, N. Odagaki, S.R. Nishitani, I. Tanaka, H. Adachi, Free-energy calculation of precipitate nucleation in an Fe-Cu-Ni alloy, Materials Transactions 45 (2004) 1978-1981.
[48] A.T. Al-Motasem, M. Posselt, F. Bergner, Nanoclusters in BCC-Fe containing vacancies, copper and nickel: structure and energetics, Journal of Nuclear Materials 418 (2011) 215-222.
[49] R.P. Kolli, R.M. Wojes, S. Zaucha, D.N. Seidman, A subnanoscale study of the nucleation, growth, and coarsening kinetics of Cu-rich precipitates in a multicomponent Fe-Cu based steel, Int. J. Mater. Res. 99 (2008) 513-527.
[50] F. Maury, N. Lorenzelli, C.H. De Novion, Influence of Mn and Ni on Cu precipitation in dilute iron alloys during electron irradiation: A small-angle neutron scattering study, Journal of Nuclear Materials 183 (1991) 217-220.
[51] H. Kawanishi, M. Suzuki, Microstructure and hardening in thermally aged and neutron-irradiated Fe-Cu model alloy, in: M.L. Hamilton, A.S. Kumar, S.T. Rosinski, M.L. Grossbeck (Eds.), Effects of Radiation on Materials: 19th International Symposium, American Society Testing and Materials, W Conshohocken, 2000, pp. 492-515.
[52] V.N. Urtsev, D.A. Mirzaev, I.L. Yakovleva, N.A. Tereshchenko, K.Y. Okishev, On the mechanism of nucleation of copper precipitates upon aging of Fe-Cu Alloys, Phys. Metals Metallogr. 110 (2010) 346-355.
[53] R. Monzen, M.L. Jenkins, A.P. Sutton, The bcc-to-9R martensitic transformation of Cu precipitates and the relaxation process of elastic strains in an Fe-Cu alloy, Philosophical Magazine A 80 (2000) 711-723.
[54] P.J. Othen, M.L. Jenkins, G.D.W. Smith, W.J. Phythian, Transmission electron microscope investigations of the structure of copper precipitates in thermally-aged Fe—Cu and Fe—Cu—Ni, Philosophical Magazine Letters 64 (1991) 383-391.
[55] M.K. Miller, B.D. Wirth, G.R. Odette, Precipitation in neutron-irradiated Fe-Cu and Fe-Cu-Mn model alloys: A comparison of APT and SANS data, Materials Science and Engineering A 353 (2003) 133-139.

[56] P.J. Othen, A study of copper precipitation in Fe-Cu and Fe-Cu-Ni model alloys, Department of Materials, University of Oxford, Oxford, 1992.
[57] Y.U. Heo, Y.K. Kim, J.S. Kim, J.K. Kim, Phase transformation of Cu precipitates from bcc to fcc in Fe–3Si–2Cu alloy, Acta Materialia 61 (2013) 519-528.
[58] D.E. Alexander, B.J. Kestel, P.R. Jemian, G.R. Odette, D. Klingensmith, D. Gragg, Anomalous small-angle x-ray scattering characterization of model pressure vessel alloy microstructures, in: S.J. Zinkle, G.E. Lucas, R.C. Ewing, J.S. Williams (Eds.), Microstructural Processes in Irradiated Materials1999, pp. 415-420.
[59] Y.R. Wen, Y.P. Li, A. Hirata, Y. Zhang, T. Fujita, T. Furuhara, C.T. Liu, A. Chiba, M.W. Chen, Synergistic alloying effect on microstructural evolution and mechanical properties of Cu precipitation-strengthened ferritic alloys, Acta Mater. 61 (2013) 7726-7740.
[60] A.C. Nicol, Aspects of copper precipitation and irradiation hardening in Fe-Cu alloys, in: M.L.t.a. Jenkins, S. University of Oxford. Faculty of Physical, C. Oriel, M. University of Oxford. Department of (Eds.), Thesis (D.Phil.)--University of Oxford, 2000., 2000.
[61] J.T. Buswell, C.A. English, M.G. Hetherington, W.P. Phythian, G.D.W. Smith, G.M. Worrall, Proc. 14th Int. Symp. on Effects of Radiation in Materials, Andover, Massachussetts, 1988.
[62] J.T. Buswell, C.A. English, M.G. Hetherington, W.J. Phythian, G.D.W. Smith, G.M. Worrall, An analysis of small clusters formed in thermally aged and irradiated Fe-Cu and Fe-Cu-Ni model alloys, in: N.H. Packan, R.E. Stoller, A.S. Kumar (Eds.) Effects of Radiation on Materials: 14th International Symposium, ASTM, 1990.
[63] P. Erhart, J. Marian, B. Sadigh, Thermodynamic and mechanical properties of copper precipitates in a-iron from atomistic simulations, Physical Review B 88 (2013) 024116.
[64] P. Erhart, B. Sadigh, Low-temperature criticality of martensitic transformations of Cu nanoprecipitates in a-Fe, Physical Review Letters 111 (2013) 025701.
[65] P.J. Othen, A study of copper precipitation in Fe-Cu and Fe-Cu-Ni model alloys, Department of Materials, University of Oxford, Oxford, 1992.
[66] Z. Nishiyama, S. Kajiwara, Japan. J. appl. Phys. 2 (1963) 478.
[67] S. Kajiwara, Z. Nishiyama, Japan. J. appl. Phys. 12 (1964) 749.
[68] Nishiyam.Z, J. Kakinoki, S. Kajiwara, Stacking faults in martensite of Cu-Al alloy, J. Phys. Soc. Jpn. 20 (1965) 1192-&.
[69] L.S. Ramsdell, Studies on silicon carbide, American Mineralogist 32 (1947) 64-82.
[70] P. Krishna, D. Pandey, Close-Packed Structures, International Union of Crystallography.
[71] M. Andrade, M. Chandrasekaran, L. Delaey, The basal-plane stacking-faults in 18R martensite of copper base alloys, Acta Metallurgica 32 (1984) 1809-1816.
[72] H.A. Hardouin Duparc, R.C. Doole, M.L. Jenkins, A. Barbu, A high-resolution electron microscopy study of copper precipitation in Fe-1.5 wt% Cu under electron irradiation, Philosophical Magazine Letters 71 (1995) 325-333.
[73] R. Monzen, M. Iguchi, M.L. Jenkins, Structural changes of 9R copper precipitates in an aged Fe-Cu alloy, Philosophical Magazine Letters 80 (2000) 137-148.
[74] Y.R. Wen, A. Hirata, Z.W. Zhang, T. Fujita, C.T. Liu, J.H. Jiang, M.W. Chen, Microstructure characterization of Cu-rich nanoprecipitates in a Fe–2.5 Cu–1.5 Mn–4.0 Ni–1.0 Al multicomponent ferritic alloy, Acta Materialia 61 (2013) 2133-2147.
[75] P.J. Othen, M.L. Jenkins, G.D.W. Smith, High-resolution electron microscopy studies of the structure of Cu precipitates in α-Fe, Philosophical Magazine A 70 (1994) 1-24.
[76] Y.N. Osetsky, A.G. Mikhin, A. Serra, Study of copper precipitates in alpha-iron by computer-simulation 1: interatomic potentials and properties of Fe and Cu, Philos. Mag. A-Phys. Condens. Matter Struct. Defect Mech. Prop. 72 (1995) 361-381.
[77] S. Kajiwara, Theoretical-analysis of crystallography of martensitic-transformation of BCC to 9R close-packed structure, Transactions of the Japan Institute of Metals 17 (1976) 435-446.
[78] A. Sato, N. Ishikawa, T. Mori, Nucleation and growth of defect clusters in an electron-irradiated Cu-Fe alloy, Materials Science and Engineering 81 (1986) 427-432.

[79] W.E. King, R. Benedek, K.L. Merkle, M. Meshii, Damage effects of high-energy electrons on metals, Ultramicroscopy 23 (1987) 345-353.
[80] E. Hornbogen, R.C. Glenn, A metallographic study of precipitation of copper from alpha iron, Transactions of the American Institute of Mining and Metallurgical Engineers 218 (1960) 1064-1070.
[81] H.R. Habibi-Bajguirani, M.L. Jenkins, High-resolution electron microscopy analysis of the structure of copper precipitates in a martensitic stainless steel of type PH 15-5, Philosophical Magazine Letters 73 (1996) 155-162.
[82] T. Harry, D.J. Bacon, Computer simulation of the core structure of the {111} screw dislocation in α-iron containing copper precipitates: II. dislocation–precipitate interaction and the strengthening effect, Acta Materialia 50 (2002) 209-222.
[83] T. Harry, D.J. Bacon, Computer simulation of the core structure of the {111} screw dislocation in α-iron containing copper precipitates:: I. structure in the matrix and a precipitate, Acta Mater. 50 (2002) 195-208.
[84] D.J. Bacon, Y.N. Osetsky, Hardening due to copper precipitates in alpha-iron studied by atomic-scale modelling, Journal of Nuclear Materials 329 (2004) 1233-1237.
[85] D.J. Bacon, Y.N. Osetsky, Modelling dislocation-obstacle interactions in metals exposed to an irradiation environment, Materials Science and Engineering a-Structural Materials Properties Microstructure and Processing 400 (2005) 353-361.
[86] S. Lozano-Perez, M.L. Jenkins, J.M. Titchmarsh, Evidence for deformation-induced transformations of Cu-rich precipitates in an aged FeCu alloy, Philosophical Magazine Letters 86 (2006) 367-374.
[87] J.M. Hyde, C.A. English, An analysis of the structure of irradiation induced Cu-enriched clusters in low and high nickel welds, Microstructural Processes in Irradiated Materials - 2000. Symposium (Mater. Res. Soc. Proceedings Vol. 650) (2001) R6.6.1-R6.612R616.612.
[88] J.M. Hyde, A. Cerezo, T.J. Williams, Statistical analysis of atom probe data: Detecting the early stages of solute clustering and/or co-segregation, Ultramicroscopy 109 (2009) 502-509.
[89] A. Morley, Thermal ageing of low alloy steels, Department of Materials, University of Oxford, Oxford, 2008.
[90] J.M. Hyde, G. Sha, E.A. Marquis, A. Morley, K.B. Wilford, T.J. Williams, A comparison of the structure of solute clusters formed during thermal ageing and irradiation, Ultramicroscopy 111 (2011) 664-671.
[91] M.E. Fine, J.Z. Liu, M.D. Asta, An unsolved mystery: The composition of bcc Cu alloy precipitates in bcc Fe and steels, Materials Science and Engineering: A 463 (2007) 271-274.
[92] S. Lozano-Perez, J.M. Titchmarsh, M.L. Jenkins, Determination of the Fe content of embedded Cu-rich particles in ferritic alloys using energy-filtered TEM, Ultramicroscopy 106 (2006) 75-91.
[93] B.D. Wirth, P. Asoka-Kumar, R.H. Howell, G.R. Odette, P.A. Sterne, Positron annihilation spectroscopy and small angle neutron scattering characterisation of nanostructural features in irradiated Fe-Cu-Mn alloys, in: G.E. Lucas, M.A. Snead, M.A. Kirk, R.G. Elliman (Eds.) Materials Research Society Symposium Proceedings, Materials Research Society, Boston, MA, 2001.
[94] E. Kozeschnik, Thermodynamic prediction of the equilibrium chemical composition of critical nuclei: BCC Cu precipitation in α-Fe, Scripta Materialia 59 (2008) 1018-1021.
[95] P.J. Pareige, K.F. Russell, M.K. Miller, APFIM studies of the phase transformations in thermally aged ferritic FeCuNi alloys: Comparison with aging under neutron irradiation, Applied Surface Science 94-5 (1996) 362-369.
[96] T. Koyama, H. Onodera, Computer simulation of phase decomposition in Fe-Cu-Mn-Ni quaternary alloy based on the phase-field method, Materials Transactions 46 (2005) 1187-1192.
[97] T. Koyama, K. Hashimoto, H. Onodera, Phase-field simulation of phase transformation in Fe-Cu-Mn-Ni quaternary alloy, Materials Transactions 47 (2006) 2765-2772.

[98] K. Osamura, H. Okuda, K. Asano, M. Furusaka, K. Kishida, F. Kurosawa, R. Uemori, SANS study of phase-decomposition in Fe-Cu alloy with Ni and Mn addition, ISIJ Int. 34 (1994) 346-354.
[99] R. Monzen, K. Takada, C. Watanabe, Coarsening of spherical Cu particles in an alpha-Fe matrix, ISIJ Int. 44 (2004) 442-444.
[100] D. Isheim, R.P. Kolli, M.E. Fine, D.N. Seidman, An atom-probe tomographic study of the temporal evolution of the nanostructure of Fe-Cu based high-strength low-carbon steels, Scripta Materialia 55 (2006) 35-40.
[101] R.P. Kolli, D.N. Seidman, The temporal evolution of the decomposition of a concentrated multicomponent Fe-Cu-based steel, Acta Materialia 56 (2008) 2073-2088.
[102] Z.W. Zhang, C.T. Liu, M.K. Miller, X.L. Wang, Y.R. Wen, T. Fujita, A. Hirata, M.W. Chen, G. Chen, B.A. Chin, A nanoscale co-precipitation approach for property enhancement of Fe-base alloys, Sci Rep 3 (2013) 6.
[103] G. Sha, A. Morley, A. Cerezo, G.D.W. Smith, Partitioning and segregation of trace element Sn in a low-alloy steel, Philosophical Magazine Letters 87 (2007) 327-339.
[104] J.T. Buswell, P.J.E. Bischler, S.T. Fenton, A.E. Ward, W.J. Phythian, Microstructural developments in neutron-irradiated mild steel submerged-arc weld metal, Journal of Nuclear Materials 205 (1993) 198-205.
[105] A.F. Calder, D.J. Bacon, Computer simulation study of the effects of copper solutes on cascade damage in Fe-Cu alloys, in: I.M. Robertson, G.S. Was, L.W. Hobbs, T.D. DelaRubia (Eds.), Microstructure Evolution during Irradiation, Materials Research Society, Warrendale, 1997, pp. 521-526.
[106] M.L. Jenkins, Irradiation-induced precipitates: diffraction contrast, in: J.J.H. Lim (Ed.)Department of Materials, Oxford University, 2013.
[107] D.A. Porter, Phase transformations in metals and alloys, 2nd.ed.. ed., Cheltenham : Thornes, Cheltenham, 2000.
[108] M. Serrano, M. Hernández-Mayoral, H. Hein, P. Todeschini, T. Planman, F. Bergner, A. Ulbricht, A. Wagner, R. Chaouadi, B. Radiguet, S. Cammelli, F. Danoix, P. Pareige, G. Torok, F. Gillemot, R. Szekely, J. Rouden, K. Wilford, C. Grovenor, E. Meslin, LONGLIGE Project Deliverable 3.9: final report on neutron radiation induced microstructure of RPV materials for long term operation, LONLIGE Project Deliverable, 2013.
[109] E. Meslin, B. Radiguet, P. Pareige, A. Barbu, Kinetic of solute clustering in neutron irradiated ferritic model alloys and a French pressure vessel steel investigated by atom probe tomography, Journal of Nuclear Materials 399 (2010) 137-145.
[110] A.V. Barashev, S.I. Golubov, D.J. Bacon, P.E.J. Flewitt, T.A. Lewis, Copper precipitation in Fe–Cu alloys under electron and neutron irradiation, Acta Materialia 52 (2004) 877-886.
[111] M.K. Miller, K.F. Russell, M.A. Sokolov, R.K. Nanstad, APT characterization of irradiated high nickel RPV steels, Journal of Nuclear Materials 361 (2007) 248-261.
[112] M.K. Miller, P. Pareige, Atomic level characterization of neutron irradiated pressure vessel steels, in: G.E. Lucas, L.L. Snead, M.A. Kirk, R.G. Eliman (Eds.) Materials Research Society Symposium Proceedings, Materials Research Society, Boston, MA, 2001.
[113] M.K. Miller, K.F. Russell, M.A. Sokolov, R.K. Nanstad, Atom probe tomography of radiation-sensitive KS-01 weld, Philos. Mag. 85 (2005) 401-408.
[114] R. Ngayam-Happy, C.S. Becquart, C. Domain, L. Malerba, Formation and evolution of MnNi clusters in neutron irradiated dilute Fe alloys modelled by a first principle-based AKMC method, Journal of Nuclear Materials 426 (2012) 198-207.
[115] R. Ngayam-Happy, C.S. Becquart, C. Domain, First principle-based AKMC modelling of the formation and medium-term evolution of point defect and solute-rich clusters in a neutron irradiated complex Fe-CuMnNiSiP alloy representative of reactor pressure vessel steels, Journal of Nuclear Materials 440 (2013) 143-152.

[116] G.R. Odette, Radiation induced microstructural evolution in reactor pressure vessel steels, in: I.M. Robertson, L.E. Rehn, S.J. Zinkle, W.J. Phythian (Eds.) Materials Research Society Symposium Proceedings, Materials Research Society, Boston, MA, 1995, pp. 137-148.
[117] M.K. Miller, A.A. Chernobaeva, Y.I. Shtrombakh, K.F. Russell, R.K. Nanstad, D.Y. Erak, O.O. Zabusov, Evolution of the nanostructure of VVER-1000 RPV materials under neutron irradiation and post irradiation annealing, Journal of Nuclear Materials 385 (2009) 615-622.
[118] E. Meslin, B. Radiguet, P. Pareige, C. Toffolon, A. Barbu, Irradiation-induced solute clustering in a low nickel FeMnNi ferritic alloy, Experimental Mechanics 51 (2011) 1453-1458.
[119] M.K. Miller, K.F. Russell, J. Kocik, E. Keilova, Embrittlement of low copper VVER 440 surveillance samples neutron-irradiated to high fluences, Journal of Nuclear Materials 282 (2000) 83-88.
[120] P. Auger, P. Pareige, S. Welzel, J.C. Van Duysen, Synthesis of atom probe experiments on irradiation-induced solute segregation in French ferritic pressure vessel steels, Journal of Nuclear Materials 280 (2000) 331-344.
[121] P. Pareige, J.C. Vanduysen, P. Auger, An APFIM study of the microstructure of a ferrite alloy after high fluence neutron irradiation, Applied Surface Science 67 (1993) 342-347.
[122] E. Meslin, M. Lambrecht, M. Hernandez-Mayoral, F. Bergner, L. Malerba, P. Pareige, B. Radiguet, A. Barbu, D. Gomez-Briceno, A. Ulbricht, A. Almazouzi, Characterization of neutron-irradiated ferritic model alloys and a RPV steel from combined APT, SANS, TEM and PAS analyses, Journal of Nuclear Materials 406 (2010) 73-83.
[123] L. Malerba, Are late blooming phsaes a real concern? Some considerations based on atomistic simulation, IAEA TM Vienna, 2013.
[124] P. Auger, P. Pareige, M. Akamatsu, D. Blavette, APFIM investigation of clustering in neutron-irradiated FeCu alloys and pressure vessel steels, Journal of Nuclear Materials 225 (1995) 225-230.
[125] P.D. Styman, Atomic scale studies of thermally aged reactor pressure vessel steels, Dept. of Materials University of Oxford Oxford 2013.
[126] U.S.N.R. Commision, Radiation Embrittlement of Reactor Vessel Materials, Regulatory Guide 1.99, Revision 2, in: U.S.N.R. Commission (Ed.) Washington, D.C., 1988.
[127] P. Efsing, C. Jansson, T. Mager, G. Embring, Analysis of the ductile-to-brittle transition temperature shift in a commercial power plant with high nickel containing weld material, in: R.G. Lott, J.T. Busby (Eds.), Effects of Radiation on Materials: 23rd International Symposium, American Society Testing and Materials, W Conshohocken, 2008, pp. 44-55.
[128] H. Hein, E. Keim, H. Schnabel, T. Seibert, A. Gundermann, Final results from the crack initiation and arrest of irradiated steel materials project on fracture mechanical assessments of pre-irradiated RPV steels used in German PWR, Journal of ASTM International 6 (2009) JAI101962 (101918 pp.)-JAI101962 (101918 pp.).
[129] H. Hein, E. Keim, H. Schnabel, J. Barthelmes, C. Eiselt, F. Obermeier, J. Ganswind, M. Widera, Final results from the CARINA project on crack initiation and arrest of irradiated German RPV steels for neutron fluences in the upper bound, 26th Symposium on Effects of Radiation on Nuclear Materials Indianpolis, Indiana, USA, 2013.
[130] A.D. Romig, J.I. Goldstein, Determination of the Fe-Ni and Fe-Ni-P phase diagrams at low temperatures (700 to 300 degrees Celsius), Metallurgical Transactions a-Physical Metallurgy and Materials Science 11 (1980) 1151-1159.
[131] A.D. Romig, J.I. Goldstein, Determination of Fe-rich portion of Fe-Ni-C phase diagram, Metallurgical Transactions a-Physical Metallurgy and Materials Science 9 (1978) 1599-1609.
[132] T.B. Massalski, H. Okamoto, P.R. Subramanian, L. Kacprzak, Binary alloy phase diagrams, 2nd Edition ed., ASM International Ohio 1990.
[133] A. Morley, Thermal ageing of low alloy steels, Dept. of Materials, Oxford University, 2008.
[134] Struer tenupol 5 instruction manual, Struer.

[135] O. Instruments, Electrolytic polishing and etching - sample preparation for EBSD.
[136] L.A. Giannuzzi, F.A. Stevie, Introduction to focused ion beams : instrumentation, theory, techniques and practice, Springer, New York, 2005.
[137] L.R. Herlinger, S. Chevacharoenkul, D.C. Erwin, TEM sample preparation using a focused ion beam and a probe manipulator, ASM International1996.
[138] F.A. Stevie, C.B. Vartuli, L.A. Giannuzzi, T.L. Shofner, S.R. Brown, B. Rossie, F. Hillion, R.H. Mills, M. Antonell, R.B. Irwin, B.M. Purcell, Application of focused ion beam lift-out specimen preparation to TEM, SEM, STEM, AES and SIMS analysis, Surface and Interface Analysis 31 (2001) 345-351.
[139] L.A. Giannuzzi, B.W. Kempshall, C.A. Urbanik, B.I. Prenitzer, J.L. Drown, T. Shofner, S.R. Brown, R.B. Irwin, F.A. Stevie, Aesf, TEM analysis of galvanized steel using the FIB lift-out specimen preparation technique, 1999.
[140] F.A. Stevie, R.B. Irwin, T.L. Shofner, S.R. Brown, J.L. Drown, L.A. Giannuzzi, Plan view TEM sample preparation using the focused ion beam lift-out technique, in: D.G. Seiler, A.C. Diebold, W.M. Bullis, T.J. Shaffner, R. McDonald, E.J. Walters (Eds.), Characterization and Metrology for Ulsi Technology, Amer Inst Physics, Melville, 1998, pp. 868-872.
[141] L.A. Giannuzzi, F.A. Stevie, A review of focused ion beam milling techniques for TEM specimen preparation, Micron 30 (1999) 197-204.
[142] B.I. Prenitzer, C.A. Urbanik-Shannon, L.A. Giannuzzi, S.R. Brown, R.B. Irwin, T.L. Shofner, F.A. Stevie, The correlation between ion beam/material interactions and practical FIB specimen preparation, Microsc. microanal. 9 (2003) 216-236.
[143] J. Mayer, L.A. Giannuzzi, T. Kamino, J. Michael, TEM sample preparation and FIB-induced damage, MRS Bull. 32 (2007) 400-407.
[144] M.L. Jenkins, M.A. Kirk, Characterisation of radiation damage by transmission electron microscopy, Institute of Physics Publishing, Bristol and Philadelphia, 2001.
[145] M.F. Ashby, L.M. Brown, Diffraction contrast from spherically symmetrical coherency strains, Philos. Mag. 8 (1963) 1083-&.
[146] P. Guyot, Theory of orientation contrast from inclusions, Physica Status Solidi 28 (1968) 349-&.
[147] A. Charai, C. Boulesteix, Visualization and study of the shape and size of very small coherent precipitates by a phase-contrast method, Physica Status Solidi a-Applied Research 80 (1983) 333-341.
[148] S.J. Pennycook, P.D. Nellist, Z-contrast scanning transmission electron microscopy, in: D.G. Rickerby, G. Valdre, U. Valdre (Eds.), Impact of Electron and Scanning Probe Microscopy on Materials Research, Springer, Dordrecht, 1999, pp. 161-207.
[149] S.J. Pennycook, D.E. Jesson, A.J. McGibbon, P.D. Nellist, High angle dark field STEM for advanced materials, Journal of Electron Microscopy 45 (1996) 36-43.
[150] S. Hillyard, R.F. Loane, J. Silcox, Annular dark-field imaging: Resolution and thickness effects, Ultramicroscopy 49 (1993) 14-25.
[151] P. Hartel, H. Rose, C. Dinges, Conditions and reasons for incoherent imaging in STEM, Ultramicroscopy 63 (1996) 93-114.
[152] Electron Energy Filter, in: E.M.F. Director (Ed.), Marine Geoscience Electron Microscopy Facility, http://www7430.nrlssc.navy.mil/facilities/emf/gif.htm, 2005.
[153] A. Berger, H. Kohl, Elemental mapping using an imaging energy filter - image formation and resolution limits, Microscopy Microanalysis Microstructures 3 (1992) 159-174.
[154] R.F. Egerton, P.A. Crozier, The effect of lens aberrations on the spatial resolution of an energy-filtered TEM image, Micron 28 (1997) 117-124.
[155] S. Lozano-Perez, V.D. Bernal, R.J. Nicholls, Achieving sub-nanometre particle mapping with energy-filtered TEM, Ultramicroscopy 109 (2009) 1217-1228.
[156] N. Bonnet, E. Simova, S. Lebonvallet, H. Kaplan, New applications of multivariate statistical analysis in spectroscopy and microscopy, Ultramicroscopy 40 (1992) 1-11.

[157] P.M. Rice, R.E. Stoller, J. Bentley, Energy-filtered imaging of precipitates in FeCuN alloys, in: G.W. Bailey, M.H. Ellisman, R.A. Hennigar, N.J. Zaluzec (Eds.) Proc. microscopy and microanalysis, Jones and Begell Publishing, Kansas City, Missouri, 1995, pp. 542-543.
[158] R.F. Egerton, Electron energy-loss spectroscopy in the electron microscope, New YorkL Plenum1996.
[159] M.H. Loretto, Electron beam analysis of materials, 2nd ed. ed., London : Chapman & Hall, London, 1994.
[160] H.R. Zhang, R.F. Egerton, M. Malac, Local thickness measurement through scattering contrast and electron energy-loss spectroscopy, Micron 43 (2012) 8-15.
[161] B. Dziunikowski, Energy dispersive X-ray fluorescence analysis, Oxford : Elsevier Amsterdam, 1989.
[162] J.C. Russ, Fundamentals of energy dispersive x-ray analysis, Boston : Butterworths, London, 1984.
[163] D.B. Williams, C.B. Carter, Transmission electron microscopy: a textbook for materials science, Springer, USA, 1996.
[164] H. Boersch, H. Hamisch, D. Wohlleben, K. Grohmann, Antiparallele weisssche bereiche als biprisma fur elektroneninterferenzen, Zeitschrift Fur Physik 159 (1960) 397-404.
[165] P.B. Hirsch, A. Howie, R.B. Nicholson, D.W. Pashley, M.J. Whelan, Electron microscopy of thin crystals, 2nd ed., Krieger, Huntington, New York, 1977.
[166] Ann. Rep, Nat. Chem. Lab., 1964.
[167] U.R. Evans, Th corrosion and oxidation of metals: first supplementary volume, Edward Arnold Ltd., London, 1968.
[168] K. Sachs, G.T.F. Jay, Journal of Iron Steel Institute 190 (1960).
[169] H.R. Nelson, The primary oxide film on iron, The Journal of Chemical Physics 5 (1937) 252-259.
[170] R. Grau-Crespo, A.-B.A. Y., I. Saadoune, N.H.D. Leeuw, Vacancy ordering and electronic structure of γ-Fe_2O_3 (maghemite): a theoretical investigation, University College London, Department of Chemistry, London.
[171] W. Mi, Z. Guo, Q. Wang, T. Yang, H. Bai, Charge ordering in reactive sputtered (100) and (111) oriented epitaxial Fe_3O_4 films, Scripta Materialia 68 (2013).
[172] M. Iizumi, T.F. Koetzle, G. Shirane, S. Chikazumi, M. Matsui, S. Todo, Structure of magnetite (Fe_3O_4) below the verwey transition-temperature, Acta Crystallogr. Sect. B-Struct. Commun. 38 (1982) 2121-2133.
[173] L.A. Giannuzzi, F.A. Stevie, Introduction to focussed ion beams: Instrumentation, theory, techniques and practice, Springer, New York, 2005.
[174] G.S. Was, Fundamentals of radiation materials science : Metals and alloys, Springer, New York, 2007.
[175] J.F. Ziegler, J.P. Biersack, M.D. Ziegler, TRIM - Setup and Input, SRIM The Stopping and Range of Ions in Matter, SRIM co., MD, USA, 2008.
[176] L.A. Giannuzzi, J.R. Michael, Comparison of channeling contrast between ion and electron images, Microsc. microanal. 19 (2013) 344-349.
[177] X. Yi, Electron microscopy study of radiation damage in tungsten and alloys, Department of Materials, The University of Oxford, Oxford, 2013.
[178] R.F. Egerton, P. Li, M. Malac, Radiation damage in the TEM and SEM, Micron 35 (2004) 399-409.
[179] R.F. Egerton, F. Wang, P.A. Crozier, Beam-induced damage to thin specimens in an intense electron probe, Microsc. microanal. 12 (2006) 65-71.
[180] D.M. Tang, In situ transmission electron microscopy studis of carbon nanotube nucleation mechanism and carbon nanotube-clamped metal atomic chains, Springer2013.
[181] R.F. Egerton, Knock-on and ionisation damage in the TEM, Weekly Colloquim in Materials departmentOxford, UK, 2012.

[182] C.A. English, B.L. Eyre, S.M. Holmes, Electron microscope image contrast from small dislocation loops. IV. Application of theoretical predictions for non-edge loops to defect analysis in irradiated molybdenum, Journal of Physics F: Metal Physics 10 (1980) 1065-1080.
[183] D.M. Maher, B.L. Eyre, Neutron irradiation damage in molybdenum, Philos. Mag. 23 (1971) 409-438.
[184] D.K. Saldin, M.J. Whelan, The construction of displacement fields of dislocation loops and stacking-fault tetrahedra from angular dislocation segments, Phil. Mag. R. Soc. London (1979).
[185] M. Hernández-Mayoral, D. Gómez-Briceño, Transmission electron microscopy study on neutron irradiated pure iron and RPV model alloys, Journal of Nuclear Materials 399 (2010) 146-153.
[186] M.F. Ashby, L.M. Brown, On diffraction contrast from inclusions, Philos. Mag. 8 (1963) 1649-&.
[187] A. Charai, C. Boulesteix, Determination of the size and the form of small coherent precipitates by phase-contrast (Fresnel fringes), Journal De Microscopie Et De Spectroscopie Electroniques 8 (1983) A8-A8.
[188] J.C.H. Spence, Experimental high-resolution electron microscopy, 2nd ed.. ed., Oxford University Press, New York, Oxford, 1988.
[189] J.C.H.a. Spence, High-resolution electron microscopy, Fourth edition.. ed., Oxford : Oxford University Press2013.
[190] G. Sha, A. Cerezo, G.D.W. Smith, Characterisation and modelling of thermally aged pressure vessel steel: A research progress report between Jan. 2004 and May. 2004, Department of Materials, Oxford University, Oxford, 2004, pp. 18.
[191] M.L. Jenkins, Diffraction contrast of dislocations and precipitates, in: J.J.H. Lim (Ed.), 2014.
[192] A.C. Nicol, Aspects of copper precipitation and irradiation hardening in Fe-Cu alloys, Department of Materials, The University of Oxford, Oxford, 2000.
[193] P. Erhart, B. Sadigh, Low-temperature criticality of martensitic transformations of Cu nanoprecipitates in ferritic Fe, Physical Review Letters 111 (2013) 025701.
[194] J.M. Hyde, M.G. Burke, G.D.W. Smith, P. Styman, H. Swan, K. Wilford, Uncertainties and assumptions associated with APT and SANS characterisation of irradiation damage in RPV steels, Journal of Nuclear Materials (2013).
[195] P.D. Styman, Collection of APT data on WV weld steels aged at 365 degree Celsius, University of Oxford, Oxford, 2013.
[196] P. Wells, N.J. Cunningham, G.R. Odette, B. Geiser, Towards understanding atom probe artifacts: measuring and modeling the effects of trajectory aberrations and variable field evaporation potentials, IGRDM-17, UC Santa Barbara, Embiez Island, France, 2013.
[197] G.D. Smith, Preferential growth direction for the Mn-Ni shell, in: J.J.H. Lim (Ed.)Oxford, 2014.
[198] D. Isheim, M.S. Gagliano, M.E. Fine, D.N. Seidman, Interfacial segregation at Cu-rich precipitates in a high-strength low-carbon steel studied on a sub-nanometer scale, Acta Materialia 54 (2006) 841-849.
[199] T.B. Massalski, H. Okamoto, P.R. Subramanian, L. Kacprzak, Binary alloy phase diagrams, 2nd ed., ASM International, Materials Park, Ohio.
[200] N.A. Gokcen, The Mn-Ni (Manganese-Nickel) System, JPE 12 (1991) 313-321.
[201] H. Ke, W. Xiong, L. Barnard, R. Krishnamurthy, D. Morgan, CALPHAD and Cluster Dynamics modeling of Ni-Mn-Si rich precipitates in RPV steels, University of Wisconsin, Madison, WI USA, 2013.
[202] B. Hu, H.H. Xu, S.H. Liu, Y. Du, C.Y. He, C.S. Sha, D.D. Zhao, Y.B. Peng, Experimental investigation and thermodynamic modeling of the Mn-Ni-Si system, Calphad-Comput. Coupling Ph. Diagrams Thermochem. 35 (2011) 346-354.

[203] P. Erhart, J. Marian, B. Sadigh, Thermodynamic and mechanical properties of copper precipitates in alpha-iron from atomistic simulations, Physical Review B 88 (2013) 024116.
[204] E. Altstadt, F. Bergner, H. Hein, Asme, Irradiation damage and embrittlement in RPV steels under the aspect of long term operation - overview of the FP7 project LONGLIFE, Amer Soc Mechanical Engineers, New York, 2011.
[205] L.M. Howe, M.H. Rainville, H.K. Haugen, D.A. Thompson, Collision cascades in silicon, Nuclear Instruments & Methods 170 (1980) 419-425.
[206] A. Bhuyan, B. Gregory, H. Lei, S.Y. Yee, Y.B. Gianchandani, Pulse and DC electropolishing of stainless steel for stents and other devices, University of Michigan, USA.
[207] E.A. Marquis, J.M. Hyde, Applications of atom-probe tomography to the characterisation of solute behaviours, Materials Science and Engineering R: Reports 69 (2010) 37-62.
[208] J.J.H. Lim, J.M. Hyde, S. Lozano-Perez, C.R.M. Grovenor, Microstructural characterisation of irradiation-induced MnNi-rich solute cluster in highly neutron-irradiated MnNiMo alloyed weld metals, in: M.A. Kirk, E. Lucon (Eds.) 26th Symposium on Effects of Radiation on Nuclear Materials, ASTM international, West Conshohochen, PA, Indianapolis, Indiana, 2013, pp. 18.
[209] L. Malerba, Are late-blooming phases a real concern? Some considerations based on atomistic simulation, IAEA annual meeting, IAEA, Vienna, 2013.
[210] B. Radiguet, P. Pareige, A. Barbu, Irradiation induced clustering in low copper or copper free ferritic model alloys, Nucl. Instrum. Methods Phys. Res. Sect. B-Beam Interact. Mater. Atoms 267 (2009) 1496-1499.
[211] K. Fujii, K. Fukuya, Characterization of defect clusters in ion-irradiated A533B steel, Journal of Nuclear Materials 336 (2005) 323-330.

11 APPENDICES

11.1 APPENDIX A: LONGLIFE DELIVERABLE REPORT 3.6 - CHEMICAL EFFECTS ON IRRADIATION-INDUCED PRECIPITATION

(See next page)



TREATMENT OF LONG TERM IRRADIATION EMBRITTLEMENT EFFECTS IN RPV SAFETY ASSESSMENT



Grant Agreement Number: 249360

Chemical Effects on Neutron Induced Microstructure

Deliverable D3.5

Author(s): J. J. H. Lim (UOXF, UK), S. R. Ortner (NNL, UK), C. R. M. Grovenor (UOXF, UK), S. Lozano-Perez (UOXF, UK), K. Wilford (RRs, UK), F. Bergner (FZD, DE), E. Altstadt (FZD, DE) , H. Hein (ANP-G, DE), B. Radiguet (CNRS, FR), M. Hernandez-Mayoral (CIEMAT, ES), M. Serrano (CIEMAT, ES)

Date of issuance of this report: 11 October 2013 (revised on 10 December 2013)

Project co-funded by the European Commission under the Euratom for Nuclear Research and Training Activities within the Seventh Framework Programme (2007-2011)		
Dissemination Level		
PU	Public	**X**
RE	Restricted to a group specified by the partners of the LONGLIFE project	
CO	Confidential, only for partners of the LONGLIFE project	

ABBREVIATIONS & ACRONYMS

LONGLIFE	Treatment of LONG term irradiation embrittLement effect In RPV saFEty assessment
RPV	Reactor Pressure Vessel
APT	Atom Probe Tomography
SANS	Small Angle Neutron Scattering
BM	Base Metal
WM	Weld Metal
[CC]	All alloying elements
[SC]	All clustering elements, i.e. Cu, Ni, Mn, Si and P
LBP	Late blooming phase
LBE	Late blooming effect
SC	Solute Cluster
VF	Volume Fraction

FIGURES & TABLES

Figure i: Correlation between (a) no. density of clusters and fluence, (b) volume fraction of clusters and fluence, (c) mean diameter of clusters and fluence, and (d) volume fraction and Charpy-V shift values for ANP-4 and ANP-5. (Data label = Flux) xi

Figure ii: Size distributions of irradiation-induced defect/solute clusters calculated from the magnetic scattering contributions for (a) ANP-4 and (b) ANP-5. The volume fractions per radius interval were calculated using the assumption of non-magnetic scattering features [1]. xii

Figure iii: Correlation between square root of volume fraction measured using SANS data and Charpy-V shift values for ANP-4 and ANP-5. (Data label = Fluence)..... xiii

Figure iv: Correlation between (a) number density of clusters and fluences, (b) volume fraction of clusters and fluence, (c) mean diameter of clusters and fluence, and (d) volume fraction and Charpy-V shift values for EDF-2 and EDF-3. (Data label = Flux or/& Temperature) xv

Figure v: Size distributions of irradiation-induced defect/solute clusters calculated from the magnetic scattering contributions for (a) EDF-2 and (b) EDF-3. The volume fractions per radius interval were calculated using the assumption of non-magnetic scattering features [1]. xvi

Figure vi: Correlation between (a) number density of clusters and fluence, (b) volume fraction of clusters and fluence, (c) mean diameter of clusters and fluence, and (d) volume fraction and Charpy-V shift values for EDF-2 and EDF-3. (Data label = Flux or/& Temperature) xvii

Figure vii: Correlation between (a) number density of clusters and fluence, (b) volume fraction of clusters and fluence, (c) mean diameter of clusters and fluence, and (d) volume fraction and Charpy-V shift values for FZD-1a and FZD-1b. (Data label = Flux or/& Temperature) xx

Figure viii: Size distributions of irradiation-induced defect/solute clusters calculated from the magnetic scattering contributions for (a) FZD-1a and (b) FZD-1b. The volume fractions per radius interval were calculated using the assumption of non-magnetic scattering features [1]. xxi

Figure ix: Correlation between (a) number density of clusters and fluence, (b) volume fraction of clusters and fluence, (c) mean diameter of clusters and fluence, and (d) volume fraction and Charpy-V shift values for ANP-2 and ANP-6. (Data label = Flux or/& Temperature) xxiv

Figure x: Correlation between square root of volume fraction measured using APT data and Charpy-V shift values for ANP-2 and ANP-6. (Data label = Fluence)..... xxv

Figure xi: Correlation between (a) number density of clusters and fluence, (b) volume fraction of clusters and fluence, (c) mean diameter of clusters and fluence, and (d) volume fraction and Charpy-V shift values for AEK-1 and VTT-1. (Data label = Flux or/& Temperature) xxvii

Figure xii: Size distributions of irradiation-induced defect/solute clusters calculated from the magnetic scattering contributions for AEK-1. The volume fractions per radius interval were calculated using the assumption of non-magnetic scattering features [1]..... xxviii

Figure xiii: Size distributions of irradiation-induced defect/solute clusters calculated from the magnetic scattering contributions for VTT-1. The volume fractions per radius interval were calculated using the assumption of non-magnetic scattering features [1]..... xxviii

Figure xiv: Correlation between square root of volume fraction measured using APT data and Charpy-V shift values for AEK-1 and VTT-1..... xxx

Figure xv: Correlation between (a) number density of clusters and fluence, (b) volume fraction of clusters and fluence, (c) mean diameter of clusters and fluence, and (d) volume fraction and Charpy-V shift values for AEK-1 and NRI-1. (Data label = Flux or/& Temperature)..... xxxii

Figure xvi: Magnitude of (a) number density and (b) volume fraction of solute cluster detected in ANP-6 and NRI-1 as a function of neutron fluence. (Data label = Flux) xxxv

Figure xvii: Average solute cluster chemistry for ANP-6 and NRI-1 detected using APT.. xxxvi

Figure xviii: Correlation between (a) number density of clusters and fluence, (b) volume fraction of clusters and fluence, (c) mean diameter of clusters and fluence, and (d) square root of volume fraction and Charpy-V shift values for EDF-2, EDF-3, ANP-2 and ANP-6. Data used was obtained from APT. (Data label = Flux or/& Temperature) xxxix

Figure xix: Correlation between (a) number density of clusters and fluence, (b) volume fraction of clusters and fluence, (c) mean diameter of clusters and fluence, and (d) square root of volume fraction and Charpy-V shift values for EDF-2 and FZD-1b. (Data label = Flux or/& Temperature) xliii

Figure xx: Correlation between volume fraction and number density of clusters for all RPV steels. (Data label = Fluence) xlv

Figure xxi: Tertiary diagram of Cu, Ni and Mn that provides indication of the type of solute clusters detected in all RPV steels at ϕt between 4 & 6E23 $n.m^{-2}$, based on average chemical compositions detected using APT. l

Figure xxii: Potential phases of the SCs detected in all RPV steels of ϕt between 4 & 6E23 $n.m^{-2}$, based on average chemical composition detected using APT. The tertiary diagram was obtained from Ref. [18, 19]. li

Figure xxiii: Correlation between mean (a) [Cu] (b) [Ni] (c) [Mn] (d) [Si] and (e) [P] of solute clusters and fluence for all RPV steels analysed by using APT. liii

Figure xxiv: Correlation between square root of volume fraction (in %) and Charpy-V shift values for all metals analysed using (a) APT and (b) SANS. The different coloured labels represent each data point according to type of RPV steels. liv

Figure xxv: Correlation between square root of volume fraction (in %) and Charpy-V shift values for all metals analysed using (a) APT and (b) SANS. The different coloured labels represent each data point according to the Cu concentration in RPV steels before neutron irradiation. lv

Figure xxvi: Correlation between square root of volume fraction (in %) and Charpy-V shift values for all metals analysed using (a) APT and (b) SANS. The different coloured labels represent each data point according to the ratio of Ni/Mn concentration in RPV steels before neutron irradiation. lv

Figure xxvii: (a) Number density and (b) volume fraction of clusters against neutron fluence for ANP-2, EDF-2 & NRI-1 lvi

Figure xxviii: (a) Number density and (b) volume fraction of solute clusters against neutron fluence for ANP-2 and NRI-1 lvii

Figure xxix: Correlation between (1) volume fraction of solute clusters and neutron fluence and (2) square root of volume fraction and Charpy-V shift values for EDF-2. (Data label = Fluence) lviii

Figure xxx: (a) Number density and (b) volume fraction of clusters against ϕt for all RPV steels lix

Table i: Nominal chemical compositions of ANP-4 and ANP-5 x

Table ii: Summary of chemical composition differences between ANP-4 and ANP-5 x

Table iii: Summary of neutron irradiation conditions for ANP-4 and ANP-5 x

Table iv: A-ratio summary for ANP-4 and ANP-5 xii

Table v: Nominal chemical compositions of EDF-2 and EDF-3 xiv

Table vi: Summary of chemical composition differences between EDF-2 and EDF-3 xiv

Table vii: Summary of neutron irradiation conditions for EDF-2 and EDF-3 xiv

Table viii: A-ratio summary for EDF-2 and EDF-3 xvi

Table ix: Nominal chemical compositions of FZD-1a and FZD-1b xix

Table x: Summary of chemical composition differences between FZD-1a and FZD-1b xix

Table xi: Summary of neutron irradiation conditions for FZD-1a and FZD-1b xix

Table xii: A-ratio summary for FZD-1a and FZD-1b xxi

Table xiii: Nominal chemical compositions of ANP-2 and ANP-6 xxiii

Table xiv: Summary of chemical composition differences between ANP-2 and ANP-6 xxiii

Table xv: Summary of neutron irradiation conditions for ANP-2 and ANP-6 xxiii

Table xvi: Nominal chemical compositions of AEK-1 and VTT-1 xxvi

Table xvii: Summary of chemical composition differences between AEK-1 and VTT-1 xxvi

Table xviii: Summary of neutron irradiation conditions for AEK-1 and VTT-1 xxvi

Table xix: A-ratio summary for AEK-1 and VTT-1 xxix

Table xx: Nominal chemical compositions of AEK-1 and NRI-1 xxxi

Table xxi: Summary of chemical composition differences between AEK-1 and NRI-1 xxxi

Table xxii: Summary of neutron irradiation conditions for AEK-1 and NRI-1 xxxi

Table xxiii: Nominal chemical compositions of ANP-6 and NRI-1 xxxiv

Table xxiv: Summary of chemical composition differences between ANP-6 and NRI-1 xxxiv

Table xxv: Summary of neutron irradiation conditions for ANP-6 and NRI-1 xxxiv

Table xxvi: Nominal chemical compositions of EDF-2, EDF-3, ANP-2 and ANP-6 xxxvii

Table xxvii: Summary of chemical composition differences between ANP-2, ANP-6, EDF-2 and EDF-3 xxxviii

Table xxviii: Summary of neutron irradiation conditions for EDF-2, EDF-3, ANP-2 and ANP-6 xxxviii

Table xxix: Nominal chemical compositions of EDF-2 and FZD-1b..... xlii

Table xxx: Summary of chemical composition differences between EDF-2 and FZD-1b..... xlii

Table xxxi: Summary of neutron irradiation conditions for EDF-2 and FZD-1b..... xlii

Table xxxii: Nominal chemical composition of RPV steels..... xlv

Table xxxiii: Summary of average chemical composition of solute clusters detected in RPV steels (only considering ϕt range of interest, $4 < \phi t < 6 \times 10^{23}$ n.m^{-2}, E>1MeV)..... xlix

Table xxxiv: Summary of average chemical composition of solute clusters considering only of nickel, manganese & silicon, detected in RPV steels (only considering ϕt range of interest, $4 < \phi t < 6 \times 10^{23}$ n.m^{-2}, E>1MeV)..... li

Table xxxv: RPV steels that showed potential incubation effects in either Charpy-V notch testing or APT analysis or both. lvi

CONTENTS

I. Introduction

II. Chemical effects on irradiation-induced microstructures

II. I. NiMoCr steels

II. II. 16MND5 steels

II. III. A533B steels

II. IV. S3NiMo steels

II. V. Kh2MF steels

II. VI. Synergistic effects of Ni, Mn and Si for high Ni steels

II. VII. Synergistic effects of Ni, Mn and Si for low & high Ni steels

II. VIII. Temperature effects for low Ni steels

III. Irradiation-induced solute clusters

IV. Irradiation-induced solute cluster chemistry

V. Irradiation-induced cluster hardening capability

VI. Incubation period for irradiation-induced cluster nucleation and growth

VII. References

I. Introduction

Deliverable 2.2 in the LONGLIFE project was a report on the previous understanding of the effect of the chemical composition of RPV steels on the development of microstructure and properties in service conditions.

This report collates the new results from the LONGLIFE project. We have chosen to concentrate on comparisons between materials where there are clear chemical differences so that we can study the effect of as few independent variables as possible. The primary clustering elements that have been considered are copper, phosphorus, nickel, manganese and silicon.

In the following sections, we will discuss the correlation between the number density, volume fraction and size of irradiation-induced clusters and chemical compositions for RPV steels that have been analysed by either APT or SANS or both analytical techniques. Furthermore, we will discuss the incubation period for irradiation-induced cluster nucleation and growth and compare these with the literature available. Finally, this report will conclude with a summary of average solute cluster chemistry.

II. Chemical effects on irradiation-induced precipitation

Sections II. I to II. V are analyses performed on data sets separated by alloying chemical composition, i.e. type of steel. The synergistic effect of Ni, Mn and Si is studied in sections II. VI and II. VII. An attempt to study the effect of temperature on irradiation-induced microstructure was performed and is summarized in section II. VIII. Note that the volume fraction of clusters is the main output variable used for comparison in this report. This is because of the number density of clusters is found to be rather sensitive to irradiation flux.

II. I. NiMoCr steels

ANP-4 & ANP-5 are 22NiMoCr3-7 type steels. ANP-5 with 0.22 wt.% Cu is the metal studied in LONGLIFE with the highest copper content. Both metals have been neutron irradiated to different fluences and at different fluxes. The chemical compositions and irradiation conditions for ANP-4 and ANP-5 are summarised as follows:

Total concentration of clustering elements[1]:

(1) ANP-4 (BM): 2.140 at%
(2) ANP-5 (WM): 2.728 at%

Table i: Nominal chemical compositions of ANP-4 and ANP-5

Materials	[C]	[Si]	[Mn]	[P]	[S]	[Cr]	[Mo]	[Ni]	[Cu]	[V]	[Al]
	at%	at%	at%	at%	at%	at%	at%	at%	at%	at%	at%
ANP-5 (WM)	0.371	0.298	1.156	0.027	0.023	0.793	0.348	1.054	0.193	0.011	0.027
ANP-4 (BM)	0.969	0.434	0.858	0.011	0.010	0.413	0.318	0.793	0.044	0.011	0.029

Table ii: Summary of chemical composition differences between ANP-4 and ANP-5

Materials	*Higher content*	*Lower content*
ANP-4 (BM)	C, Si	Cu, Ni, Mn, Cr
ANP-5 (WM)	Cu, Ni, Mn, Cr	C, Si

Table iii: Summary of neutron irradiation conditions for ANP-4 and ANP-5

Materials	*ϕt (n.m^{-2})*	*ϕ (n.m^{-2}.s^{-1})*	*T_{irra} (˚C)*
ANP-4 (BM)	1.05E23	1.95E16	285
	4.24E23	1.95E16	
ANP-5 (WM)	2.20E23	6.00E14	285-290
	2.20E23	2.10E16	

[1] Total concentration of solute elements that involved in clustering, i.e. Cu, Ni, Mn, Si and P

SANS results from ANP-4 and ANP-5

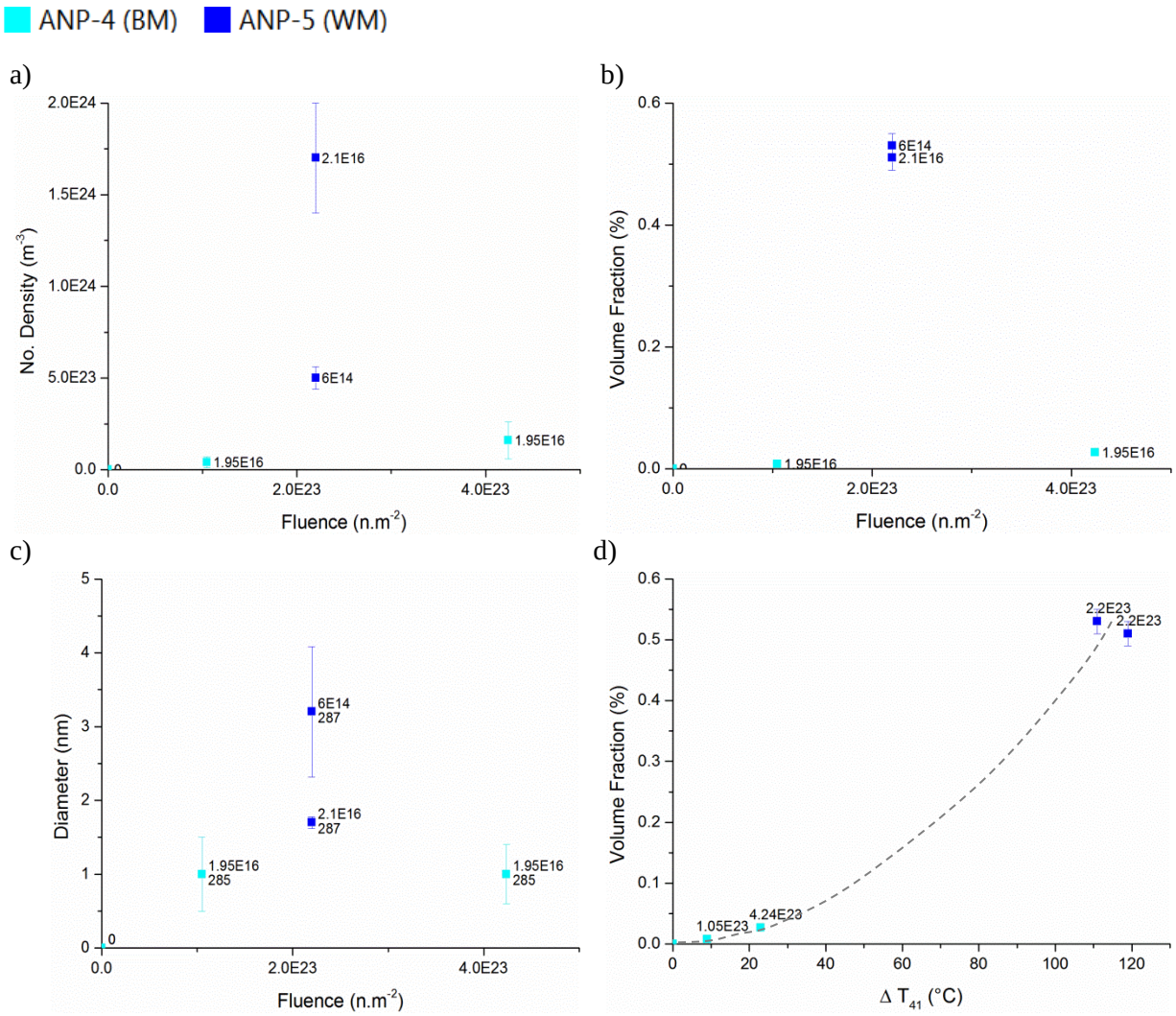


Figure i: Correlation between (a) no. density of clusters and fluence, (b) volume fraction of clusters and fluence, (c) mean diameter of clusters and fluence, and (d) volume fraction and Charpy-V shift values for ANP-4 and ANP-5. (Data label = Flux)

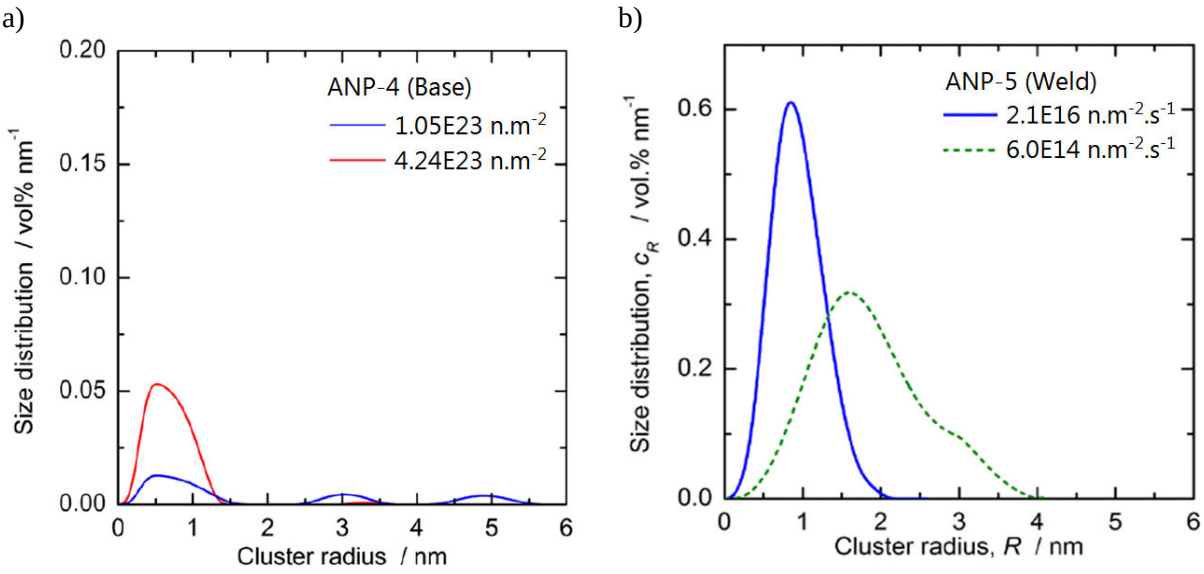


Figure ii: Size distributions of irradiation-induced defect/solute clusters calculated from the magnetic scattering contributions for (a) ANP-4 and (b) ANP-5. The volume fractions per radius interval were calculated using the assumption of non-magnetic scattering features [1].

Table iv: A-ratio summary for ANP-4 and ANP-5

Materials	*ϕt, (n.m^{-2})*	*A-ratio*
ANP-4 (BM)	1.05E23	1.5 ± 0.2
	4.24E23	N/A
ANP-5 (WM)	2.2E23 (low ϕ)	2.5 ± 0.1
	2.2E23 (high ϕ)	2.3 ± 0.1

ANP-5 with higher Cu (0.22 wt.%), Ni & Mn content compared to ANP-4 contains a higher number density and volume fraction of irradiation-induced solute clusters even at lower fluence ($\phi t \approx$ 2.2E23 n.m^{-2}) compared to ANP-4 irradiated to $\phi t \approx$ 4.2E23 n.m^{-2} (Figure i (a) & Figure i (b)). Based on previous studies on the neutron irradiation effect on high Cu steels, we can conclude that this higher volume fraction of irradiation-induced clusters in ANP-5 is primarily due to the high Cu content. Also, the larger concentration of clustering solute atoms in ANP-5 allowed larger irradiation-induced clusters to form during irradiation under similar conditions, i.e. similar irradiation temperature (± 5 ˚C) & irradiation flux ($\phi \approx$ 2E16 n.m^{-2}.s^{-1}) (Figure i (c)).

Irradiation-induced cluster hardening capability:

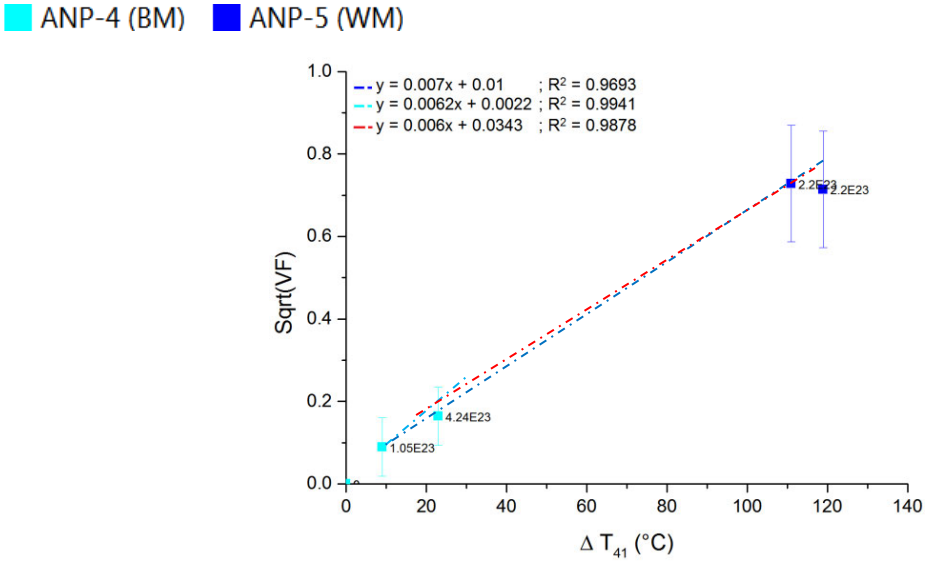


Figure iii: Correlation between square root of volume fraction measured using SANS data and Charpy-V shift values for ANP-4 and ANP-5. (Data label = Fluence)

The correlation between the square root of volume fraction and the shift in the Charpy-V transition temperature is linear for ANP-4 and ANP-5 (Figure iii) even though these metals have different chemical compositions and are irradiated to different neutron fluences. This suggests that the increase in Charpy-V transition temperature for both ANP-4 and ANP-5 are induced by same or similar hardening mechanisms.

II. II. 16MND5 steels (Low Nickel)

EDF-2 and EDF-3 are 16MND5 type steels irradiated to similar neutron fluences. The chemical compositions of these metals have slight differences in clustering element content (especially for Cu and Si), Cr and C. Note that the differences in Cu and Si concentrations in both steels are typical for base and weld RPV metals. The chemical compositions and irradiation conditions for EDF-2 and EDF-3 are summarised as follows:

Total concentration of clustering elements:

(1) EDF-2: 2.491 at%
(2) EDF-3: 2.775 at%

Table v: Nominal chemical compositions of EDF-2 and EDF-3

Materials	[C]	[Si]	[Mn]	[P]	[S]	[Cr]	[Mo]	[Ni]	[Cu]	[V]	[Al]
	at%	at%	at%	at%	at%	at%	at%	at%	at%	at%	at%
EDF-2 (BM)	0.638	0.436	1.335	0.011	0.010	0.214	0.313	0.653	0.056	0.006	0.029
EDF-3 (WM)	0.250	0.694	1.429	0.016	0.019	0.021	0.331	0.607	0.029	0.006	0.006

Table vi: Summary of chemical composition differences between EDF-2 and EDF-3

Materials	***Higher content***	***Lower content***
EDF-2 (BM)	C , Cr, Cu, (~Ni)	Mn, Si
EDF-3 (WM)	Mn, Si	C, Cr, Cu, (~Ni)

Table vii: Summary of neutron irradiation conditions for EDF-2 and EDF-3

Materials	***ϕt (n.m^{-2})***	***ϕ (n.m^{-2}.s^{-1})***	***T_{irra} (°C)***
EDF-2 (BM)	1.71E23	1.9E15	286
	5.22E23	2.1E15	
	6.95E23	2.0E15	
EDF-3 (WM)	1.26E23	1.4E15	286
	3.86E23	1.6E15	
	5.13E23	1.5E15	

SANS results from EDF-2 and EDF-3

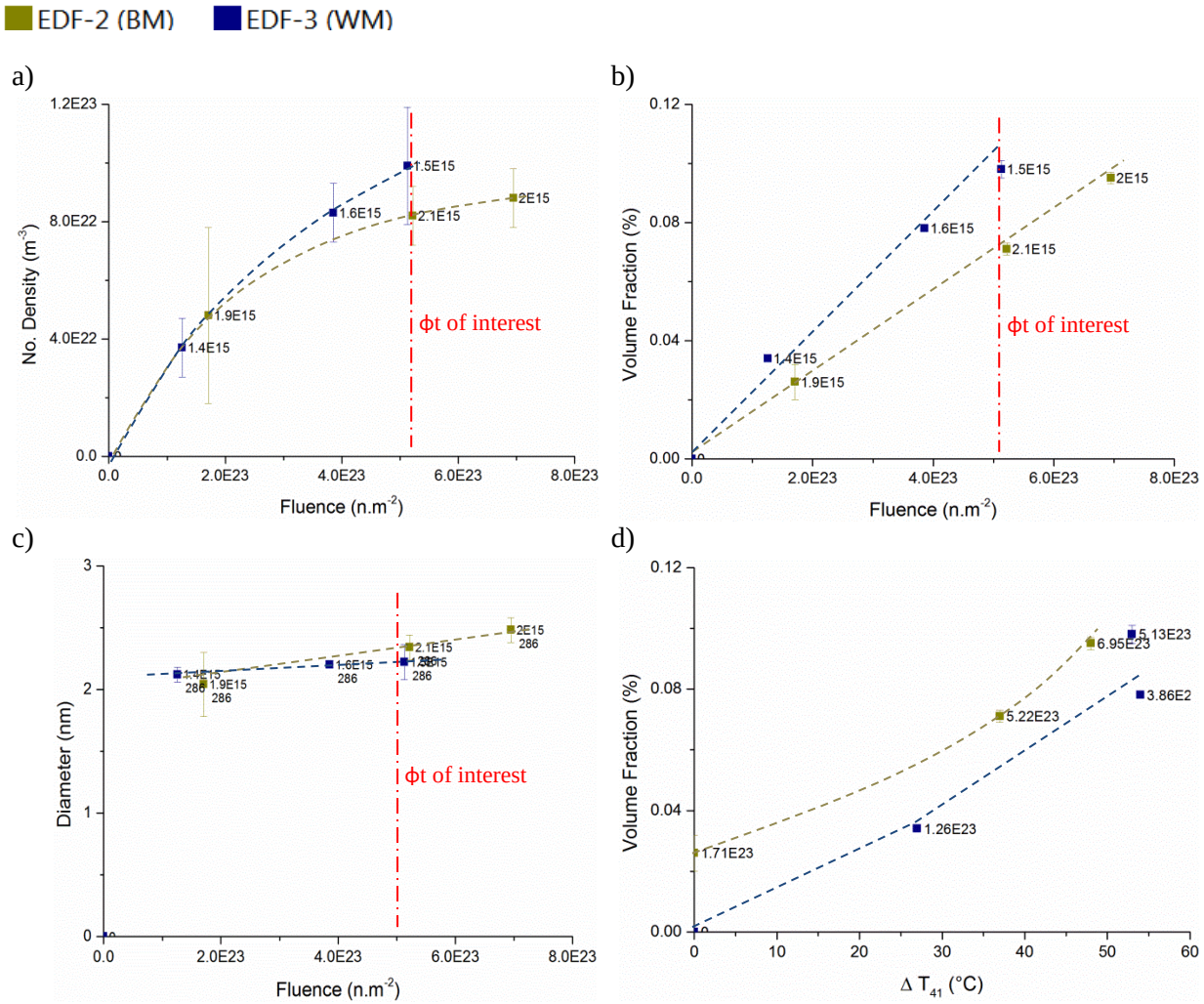


Figure iv: Correlation between (a) number density of clusters and fluences, (b) volume fraction of clusters and fluence, (c) mean diameter of clusters and fluence, and (d) volume fraction and Charpy-V shift values for EDF-2 and EDF-3. (Data label = Flux or/& Temperature)

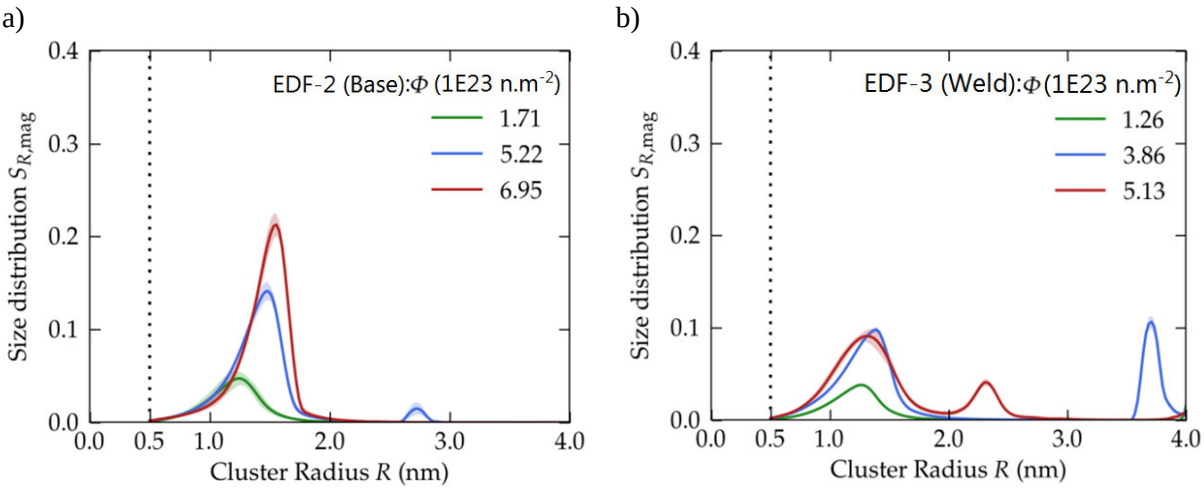


Figure v: Size distributions of irradiation-induced defect/solute clusters calculated from the magnetic scattering contributions for (a) EDF-2 and (b) EDF-3. The volume fractions per radius interval were calculated using the assumption of non-magnetic scattering features [1].

Table viii: A-ratio summary for EDF-2 and EDF-3

Materials	ϕt, (n.m^{-2})	A-ratio
EDF-2 (BM)	1.71E23	2.1 ± 1.1
	5.22E23	3.4 ± 0.3
	6.95E23	3.3 ± 0.2
EDF-3 (WM)	1.26E23	5.3 ± 0.5
	3.86E23	5.1 ± 0.2
	5.13E23	7.5 ± 0.8

EDF-2 has a higher C content compared to EDF-3, but the effect of C is assumed to be offset by higher Cr content to form Cr-rich carbides in EDF-2.

Clear differences were observed in the number density and volume fraction of clusters measured by SANS as a function of neutron fluence for EDF-2 and EDF-3 (Figure iv (a) & Figure iv (b)). Note that 2 populations of irradiation-induced clusters were detected in EDF-2 and EDF-3 at a neutron fluence of ϕt ≈ 5E23 n.m^{-2} (Figure v (a) and Figure v (b)).

EDF-2 with slightly higher Cu content and lower Mn and Si content contains a lower number density and volume fraction of clusters using SANS compared to EDF-3 that

contains a slightly higher Mn and Si content. These observations at $\phi t \approx 5E23$ n.m^{-2} are consistent with APT results from EDF-2 and EDF-3.

APT results from EDF-2 and EDF-3

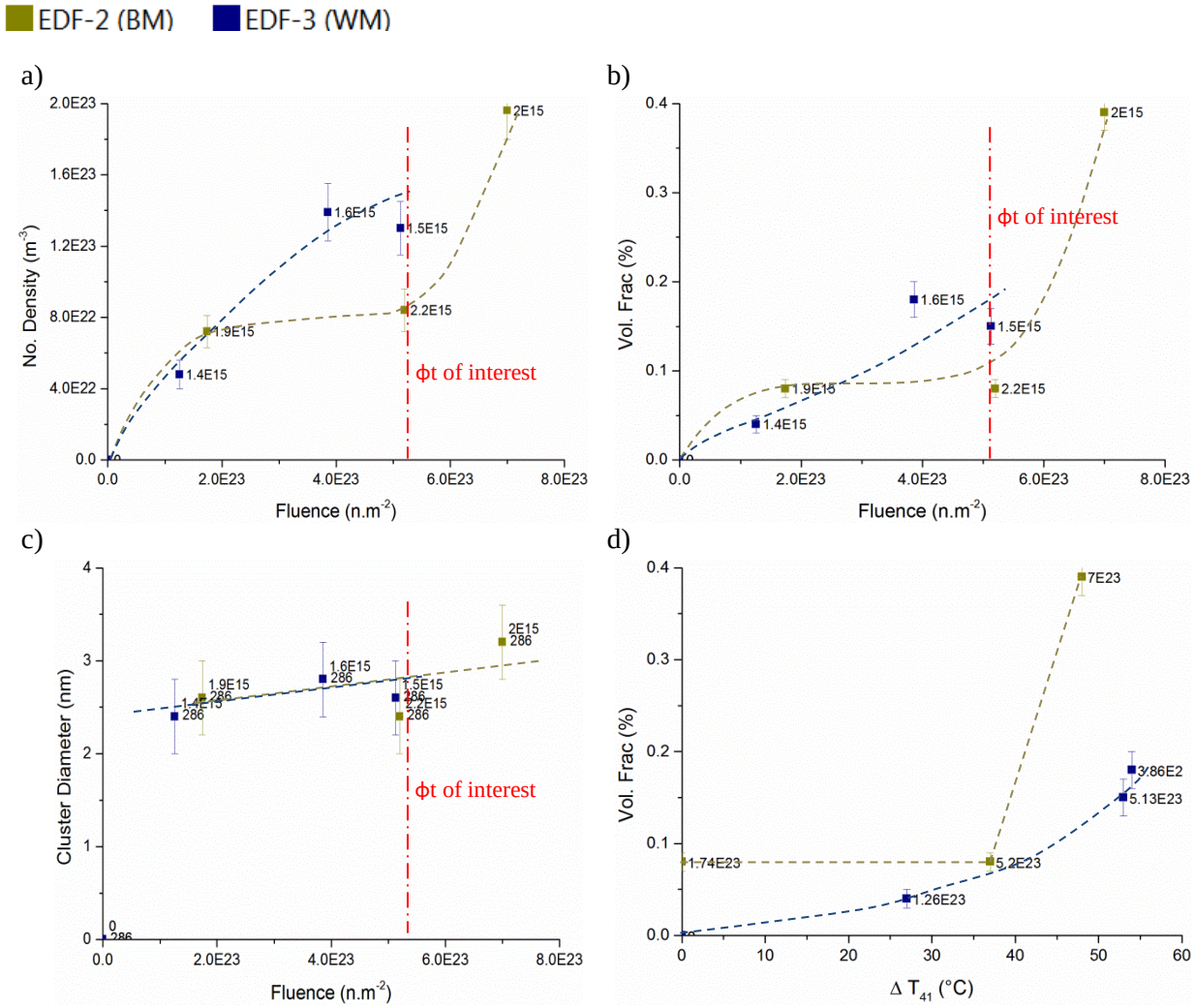


Figure vi: Correlation between (a) number density of clusters and fluence, (b) volume fraction of clusters and fluence, (c) mean diameter of clusters and fluence, and (d) volume fraction and Charpy-V shift values for EDF-2 and EDF-3. (Data label = Flux or/& Temperature)

The number density and volume fraction of clusters detected using APT is also generally lower for EDF-2 than EDF-3 (Figure vi (a) and Figure vi (b)). Note that in these APT results, we assumed that only 1 population of irradiation-induced solute clusters was detected by considering that clusters formed in the matrix and those precipitated at /or associated with dislocations are the same type of cluster, since they have similar chemical composition. (See Section IV)

From these observations, it is reasonable to speculate that in low copper and low nickel steels, nucleation and growth of solute clusters induced during neutron irradiation depends on [Mn] and [Si]. Increasing the Mn and Si contents in a low Ni steel encourages the nucleation of more solute clusters.

Similar observations can be made by comparing neutron irradiated AEK-1 and NRI-1 (see section – Kh2MF steels (CrMoV alloyed steels)). Comparison between AEK-1 and NRI-1 indicates that lower volume fraction of solute clusters are observed in steels with high Ni content but lower concentrations of Mn and/or Si.

A sudden increase in number density and volume fraction of clusters was detected using APT in EDF-2 at $\phi t \approx 7E23$ n.m^{-2} after an incubation period from $\phi t \approx 2E23$n.m^{-2} to $\phi t \approx 5E23$ n.m^{-2} (see Figure vi (a) and Figure vi (b)). This sudden increase of number density and volume fraction of clusters is not detected by SANS. This sudden increase of volume fraction of cluster observed in APT data may due to the data scattering caused by the volume sampling limitation of the APT technique.

Both APT and SANS results show that the mean diameters of the solute clusters detected in EDF-2 and EDF-3 increased with increasing neutron fluence. The average cluster sizes in EDF-2 and EDF-3 are comparable; possibly because of the similar concentration of clustering elements, (See Figure iv (c) and Figure vi (c)). This relationship of cluster size and clustering element content is consistent with the data from the analysis of the NiMoCr steels.

II. III. A533B steels (Low Nickel)

FZD-1a and FZD-1b are A533B type steels. Both metals have been irradiated to similar neutron fluence. The only significant chemical composition difference between these metals is the phosphorus content. The chemical compositions and irradiation conditions for FZD-1a and FZD-1b are summarised as follows:

Total concentration of clustering elements:

(1) FZD-1a: 2.540 at%
(2) FZD-1b: 2.531 at%

Table ix: Nominal chemical compositions of FZD-1a and FZD-1b

Materials	[C]	[Si]	[Mn]	[P]	[S]	[Cr]	[Mo]	[Ni]	[Cu]	[V]	[Al]
	at%	at%	at%	at%	at%	at%	at%	at%	at%	at%	at%
FZD-1a (BM)	0.921	0.473	1.309	0.036	0.007	0.181	0.329	0.698	0.024	0.005	0.062
FZD-1b (BM)	0.877	0.474	1.332	0.010	0.009	0.171	0.318	0.690	0.025	0.007	0.062

Table x: Summary of chemical composition differences between FZD-1a and FZD-1b

Materials	*Higher content*	*Lower content*
FZD-1a (BM)	P	-
FZD-1b (BM)	-	P

Table xi: Summary of neutron irradiation conditions for FZD-1a and FZD-1b

Materials	*ϕt (n.m^{-2})*	*ϕ (n.m^{-2}.s^{-1})*	*T_{irra} (°C)*
FZD-1a (BM)	5.7E23	2.2E16	255
	8.9E23	3.5E16	
FZD-1b (BM)	5.7E23	2.2E16	255
	8.9E23	3.5E16	

SANS results from FZD-1a and FZD-1b

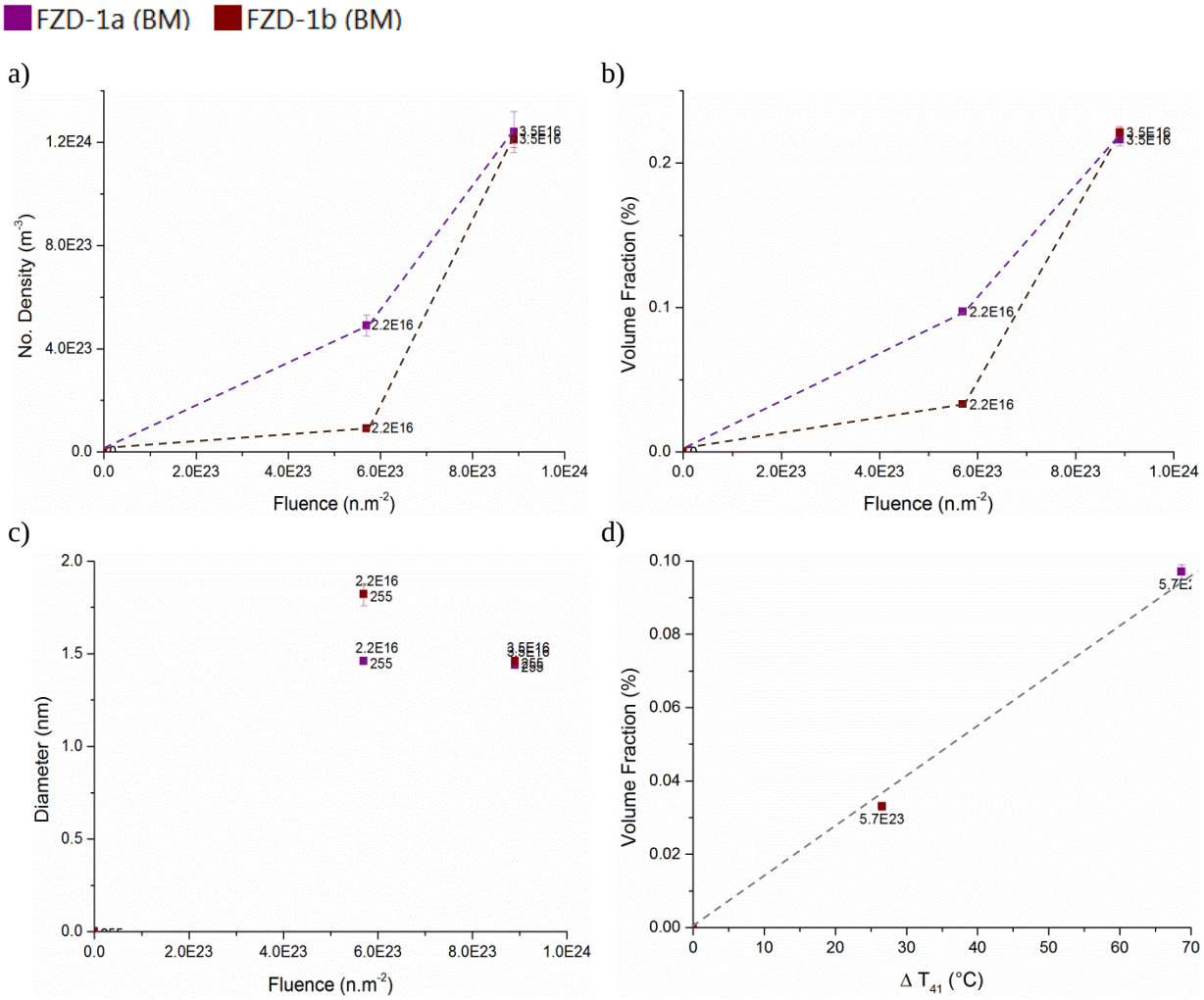


Figure vii: Correlation between (a) number density of clusters and fluence, (b) volume fraction of clusters and fluence, (c) mean diameter of clusters and fluence, and (d) volume fraction and Charpy-V shift values for FZD-1a and FZD-1b. (Data label = Flux or/& Temperature)

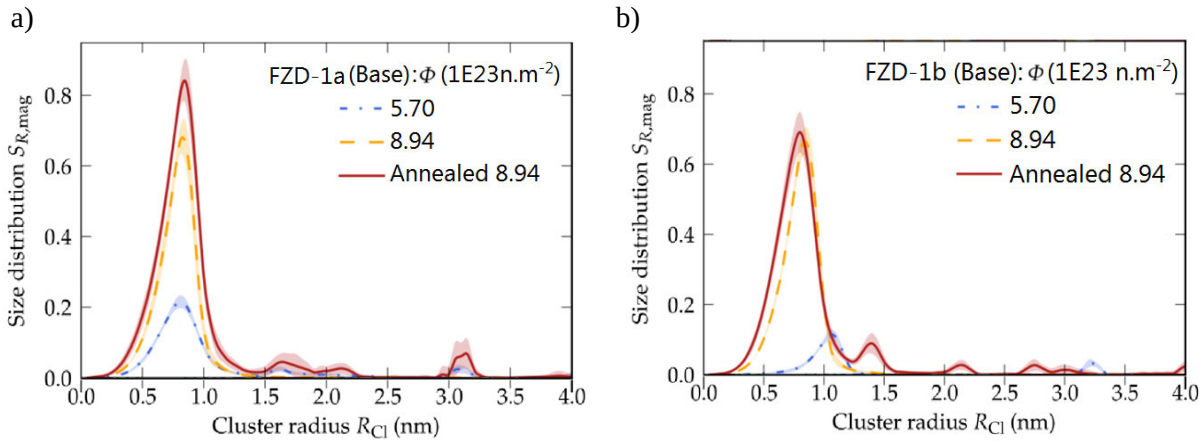


Figure viii: Size distributions of irradiation-induced defect/solute clusters calculated from the magnetic scattering contributions for (a) FZD-1a and (b) FZD-1b. The volume fractions per radius interval were calculated using the assumption of non-magnetic scattering features [1].

Table xii: A-ratio summary for FZD-1a and FZD-1b

Materials	ϕt, (n.m^{-2})	A-ratio
FZD-1a (BM)	5.7E23	2.2 ± 0.13
	8.9E23	2.0 ± 0.10
FZD-1b (BM)	5.7E23	1.9 ± 0.16
	8.9E23	2.2 ± 0.11

A higher number density and volume fraction of irradiation-induced clusters were detected in FZD-1a with higher P content compared to FZD-1b at ϕt ≈ 5.7E23 n.m^{-2} (Figure vii (a) and Figure vii (b)). However, the magnitude of the differences of number density and volume fraction of clusters between FZD-1a and FZD-1b at ϕt ≈ 9E23n.m^{-2} is much smaller than at ϕt ≈ 5.7E23 n.m^{-2} (Figure vii (a) and Figure vii (b)).

The same observation applies to the cluster size detected in highly neutron irradiated FZD-1a and FZD-1b (see Figure vii (c)) However, at ϕt ≈ 5.7E23 n.m^{-2} in FZD-1b which contains a lower P content, a bigger mean cluster size was measured compared to FZD-1a with higher P content. A similar analysis cannot be performed on our APT data because of

the absence of FZD-1b data. The APT results show no increase of P content in solute clusters precipitated in FZD-1a (high P) neutron irradiated up to $\phi t \approx 5.7E23 n.m^{-2}$.

Figure viii (a) and Figure viii (b) also indicate that a higher P content does not increase the overall number density and volume fraction of clusters induced during neutron irradiation to $\phi t \approx 9E23\ n.m^{-2}$, but at $\phi t \approx 5.7E23 n.m^{-2}$ more clusters are detected in FZD-1a than in FZD-1b.

Note that it was mentioned that the effects of P on irradiation-induced clusters are normally associated with Cu-rich precipitate [2], and it is possible that the clusters detected from FZD-1a & FZD-1b are NiMnSi-rich clusters; and since no P effect was observed on the clusters (Figure viii (a) and Figure viii (b)) we may suggest that NiMnSi-rich cluster precipitation is not affected by P [2].

II. IV. S3NiMo steels (High Nickel)

ANP-2 and ANP-6 are S3NiMo type steels. Both metals have been irradiated to similar neutron fluence. ANP-6 is the metal with the highest total concentration of clustering elements, i.e. amount of Cu, Ni, Mn, Si and P, in the list of LONGLIFE materials. The chemical compositions and irradiation conditions for ANP-2 and ANP-6 are summarised as follows:

Total concentration of clustering elements:

(1) ANP-2: 2.357 at%
(2) ANP-6: 3.428 at%

Table xiii: Nominal chemical compositions of ANP-2 and ANP-6

Materials	[C]	[Si]	[Mn]	[P]	[S]	[Cr]	[Mo]	[Ni]	[Cu]	[V]	[Al]
	at%	at%	at%	at%	at%	at%	at%	at%	at%	at%	at%
ANP-2 (WM)	0.232	0.239	1.097	0.034	0.016	0.107	0.361	0.961	0.026	0.011	0.025
ANP-6 (WM)	0.232	0.298	1.432	0.022	0.012	0.075	0.267	1.606	0.070	0.004	0.046

Table xiv: Summary of chemical composition differences between ANP-2 and ANP-6

Materials	***Higher content***	***Lower content***
ANP-2 (WM)	Mo, Cr, P	Cu, Ni, Mn, Si
ANP-6 (WM)	Cu, Ni, Mn, Si	Mo, Cr, P

Table xv: Summary of neutron irradiation conditions for ANP-2 and ANP-6

Materials	***ϕt (n.m^{-2})***	***ϕ (n.m^{-2}.s^{-1})***	***T_{irra} (˚C)***
ANP-2 (WM)	9.80E22	2.50E16	285
	4.97E23	2.33E16	
ANP-6 (WM)	4.10E22	1.06E16	280-300
	1.16E23	2.96E16	
	5.22E23	2.41E16	

APT results from ANP-2 and ANP-6

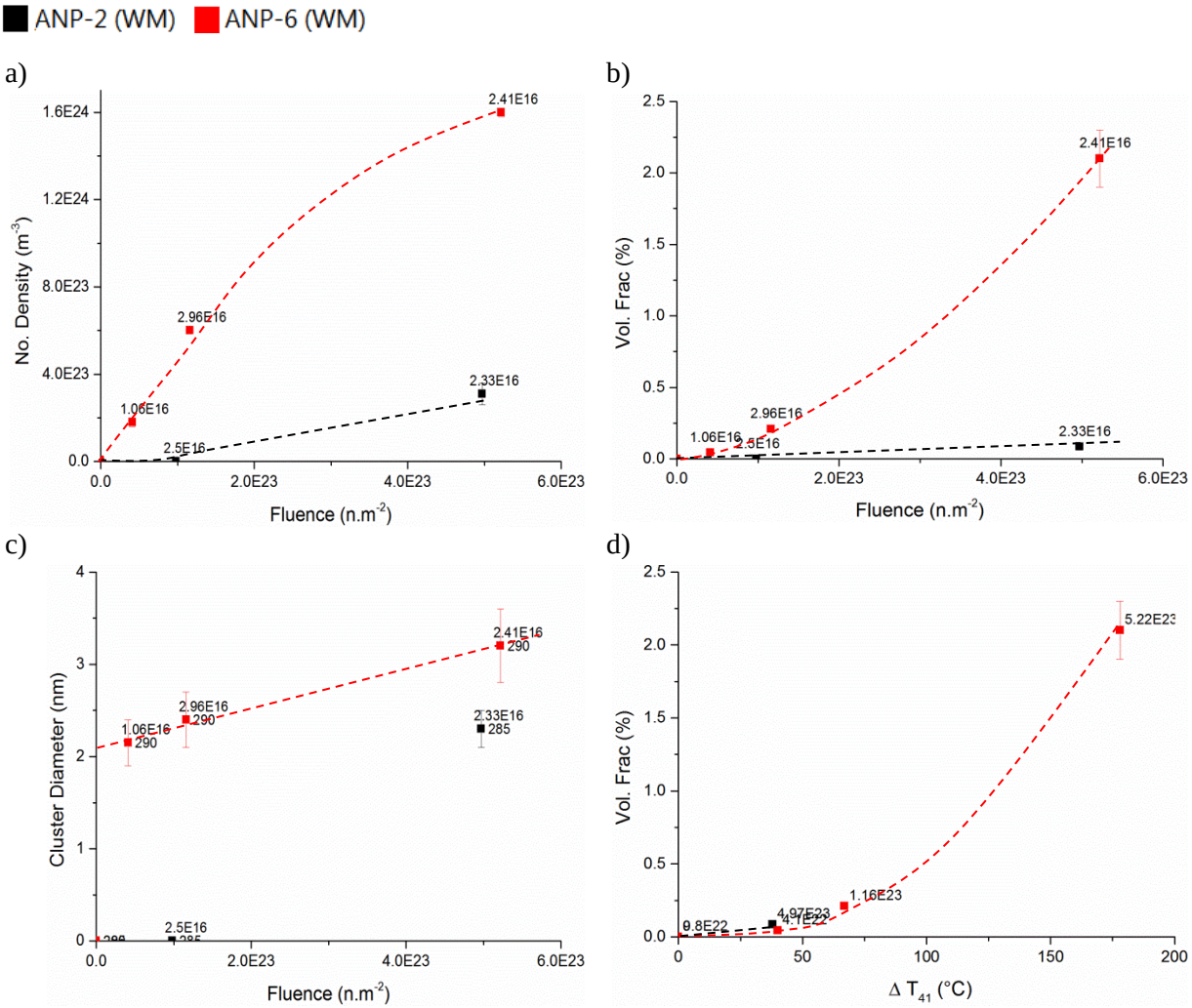


Figure ix: Correlation between (a) number density of clusters and fluence, (b) volume fraction of clusters and fluence, (c) mean diameter of clusters and fluence, and (d) volume fraction and Charpy-V shift values for ANP-2 and ANP-6. (Data label = Flux or/& Temperature)

APT detected 4 times more irradiation-induced solute clusters in ANP-6 which has a significantly higher concentration of Ni and relatively higher concentrations of Mn, Si and Cu compared to ANP-2 (Figure ix (a) and Figure ix (b)). This observation indicates, unsurprisingly, that higher Cu, Ni, Mn and Si contents will increase the number density and volume fraction of clusters induced during irradiation. However, due to insufficient data, we were unable to separate the individual effects of Ni, Mn and Si. Note that clusters found in both steels are NiMnSi-rich.

Figure ix (c) shows that the sample with higher concentration of clustering elements also induced larger clusters under neutron irradiation. This observation is consistent with analysis performed on 22NiMoCr3-7 type steels. It is important to note that at $\phi t \approx 1E23$ $n.m^{-2}$ no solute clusters were detected in ANP-2.

Irradiation-induced cluster hardening capability:

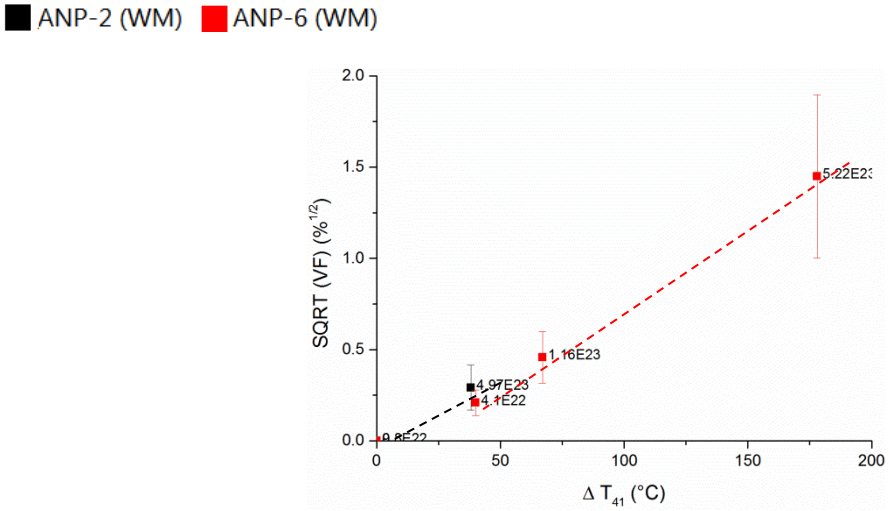


Figure x: Correlation between square root of volume fraction measured using APT data and Charpy-V shift values for ANP-2 and ANP-6. (Data label = Fluence)

Figure x shows the correlation between square root of volume fraction measured using APT and Charpy-V shift values for ANP-2 and ANP-6.

II. V. Kh2MF steels (CrMoV)

AEK-1, NRI-1 and VTT-1 are Kh2MF type steels. These metals have been irradiated to different neutron fluences at different temperatures. Here we will compare the materials where the irradiation conditions are as similar as possible AEK-1 and VTT-1, and separately AEK-1 and NRI-1.

The chemical compositions and irradiation conditions for AEK-1 and VTT-1 are summarised as follows:

Total concentration of clustering elements:

(1) AEK-1: 1.292 at%
(2) VTT-1: 2.589 at%

Table xvi: Nominal chemical compositions of AEK-1 and VTT-1.

Materials	[C]	[Si]	[Mn]	[P]	[S]	[Cr]	[Mo]	[Ni]	[Cu]	[V]	[Al]
	at%	at%	at%	at%	at%	at%	at%	at%	at%	at%	at%
AEK-1 (BM)	0.738	0.572	0.544	0.032	0.023	2.823	0.393	0.066	0.078	0.304	0.000
VTT-1 (WM)	0.185	1.185	1.07	0.036	0.045	1.674	0.269	0.123	0.175	0.218	0.000

Table xvii: Summary of chemical composition differences between AEK-1 and VTT-1

Materials	***Higher content***	***Lower content***
AEK-1 (BM)	C, Cr, Mo, V	Cu, Ni, Mn, Si
VTT-1 (WM)	Cu, Ni, Mn, Si	C, Cr, Mo, V

Table xviii: Summary of neutron irradiation conditions for AEK-1 and VTT-1

Materials	***ϕt (n.m^{-2})***	***ϕ (n.m^{-2}.s^{-1})***	***T_{irra} (°C)***
AEK-1 (BM)	1.83E24	3.11E16	280
	5.95E24	2.12E16	
	9.06E24	3.23E16	
VTT-1 (WM)	1.60E23	1.00E15	270
	2.80E23	1.10E16	
	4.00E23	1.60E16	
	4.20E23	2.80E15	

SANS results from AEK-1 and VTT-1

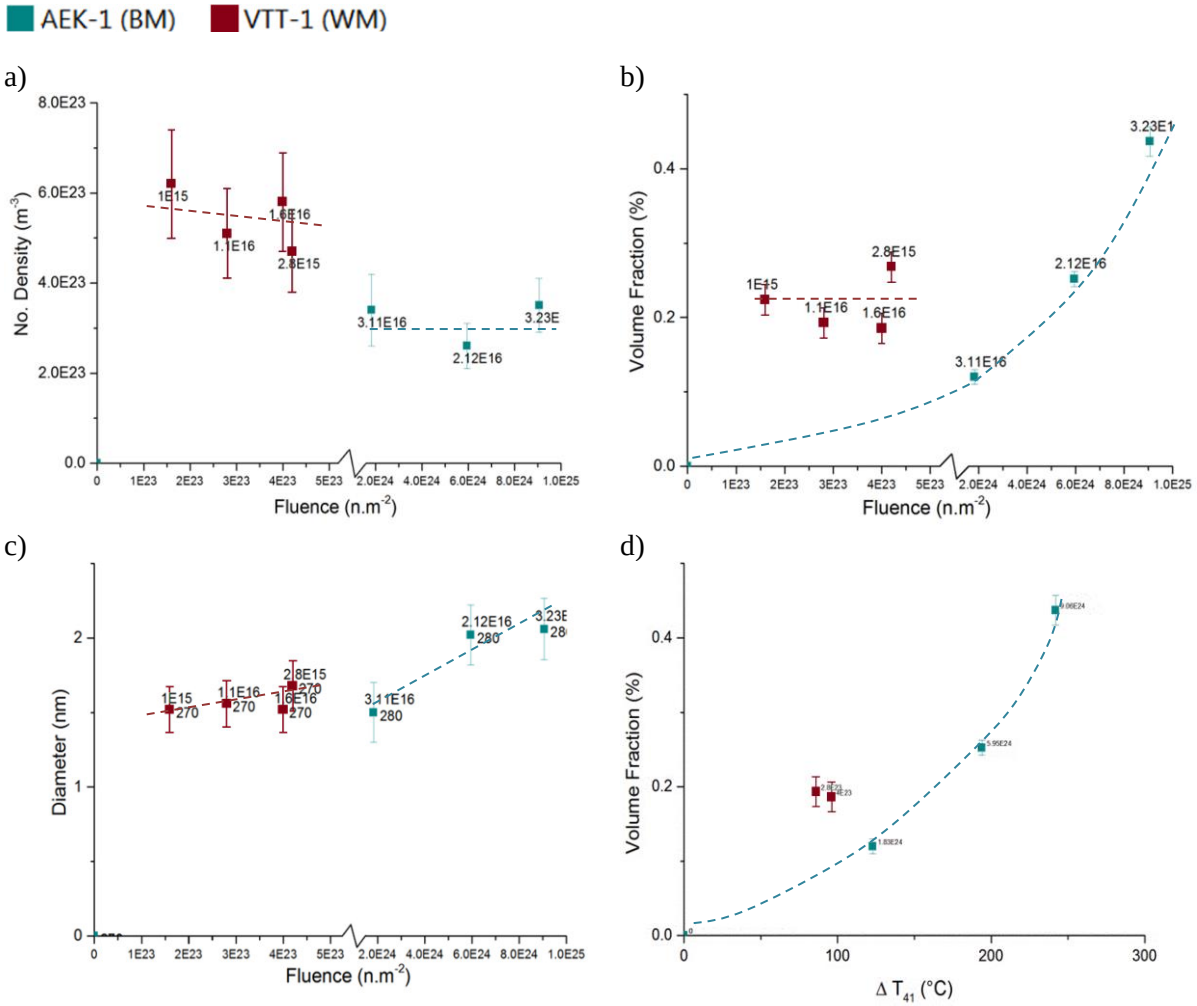


Figure xi: Correlation between (a) number density of clusters and fluence, (b) volume fraction of clusters and fluence, (c) mean diameter of clusters and fluence, and (d) volume fraction and Charpy-V shift values for AEK-1 and VTT-1. (Data label = Flux or/& Temperature)

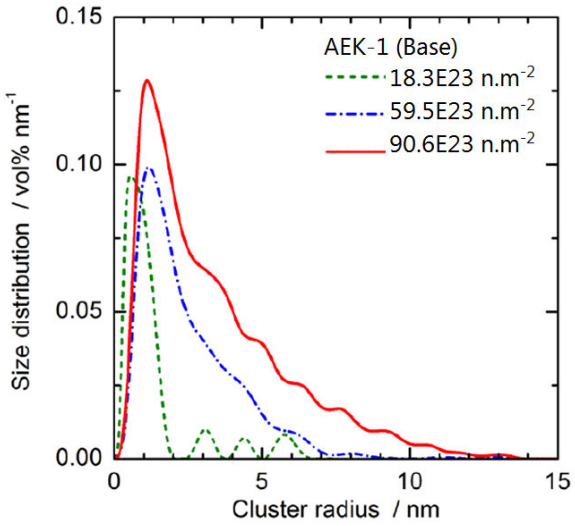


Figure xii: Size distributions of irradiation-induced defect/solute clusters calculated from the magnetic scattering contributions for AEK-1. The volume fractions per radius interval were calculated using the assumption of non-magnetic scattering features [1]

a) b)

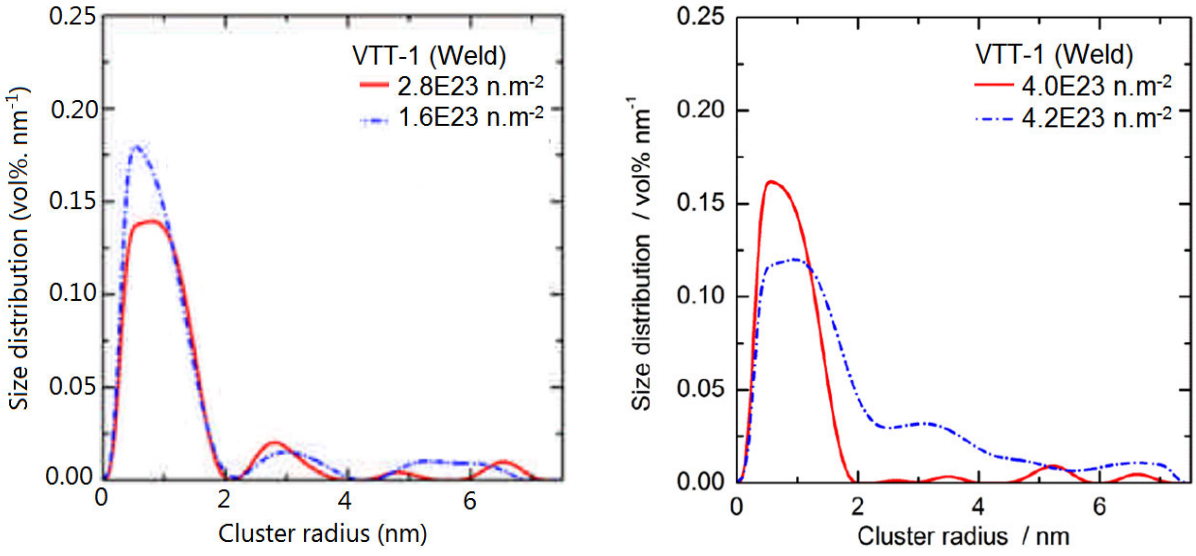


Figure xiii: Size distributions of irradiation-induced defect/solute clusters calculated from the magnetic scattering contributions for VTT-1. The volume fractions per radius interval were calculated using the assumption of non-magnetic scattering features [1].

Table xix: A-ratio summary for AEK-1 and VTT-1

Materials	ϕt (n.m^{-2})	A-ratio
AEK-1 (BM)	1.83E24	1.7 ± 0.1
	5.95E24	2.2 ± 0.1
	9.06E24	2.1 ± 0.1
VTT-1 (WM)	2.80E23	1.6 ± 0.1
	4.00E23	2.0 ± 0.1

Different populations of irradiation-induced clusters were detected in CrMoV-alloyed steels using SANS (Figure xii and Figure xiii). This observation is consistent with the results obtained from APT and TEM analysis on neutron irradiated AEK-1 and on neutron irradiated NRI-1. The types of irradiation-induced defect detected are solute clusters, solute atom enriched dislocation loops, vanadium-rich precipitates and solute atom-enriched grain-boundaries.

The number density, volume fraction and size of these clusters are plotted as a function of neutron fluence in Figure xi (a), Figure xi (b) and Figure xi (c). These figures show that VTT-1 at $\phi t \approx 4E23 n.m^{-2}$ with a higher Cu, Ni, Mn and Si content has a higher number density and volume fraction of irradiation-induced defect/clusters compared to AEK-1 after $\phi t \approx 1E24 n.m^{-2}$, which has a lower Cu, Ni, Mn, and Si content.

This observation is further evidence that an increase of Cu, Ni, Mn, and Si content in steels will encourage more irradiation-induced defect/clusters to form/precipitate at a lower neutron fluence. This indication is consistent with the analysis above on S3NiMo type steels.

Irradiation-induced cluster hardening capability:

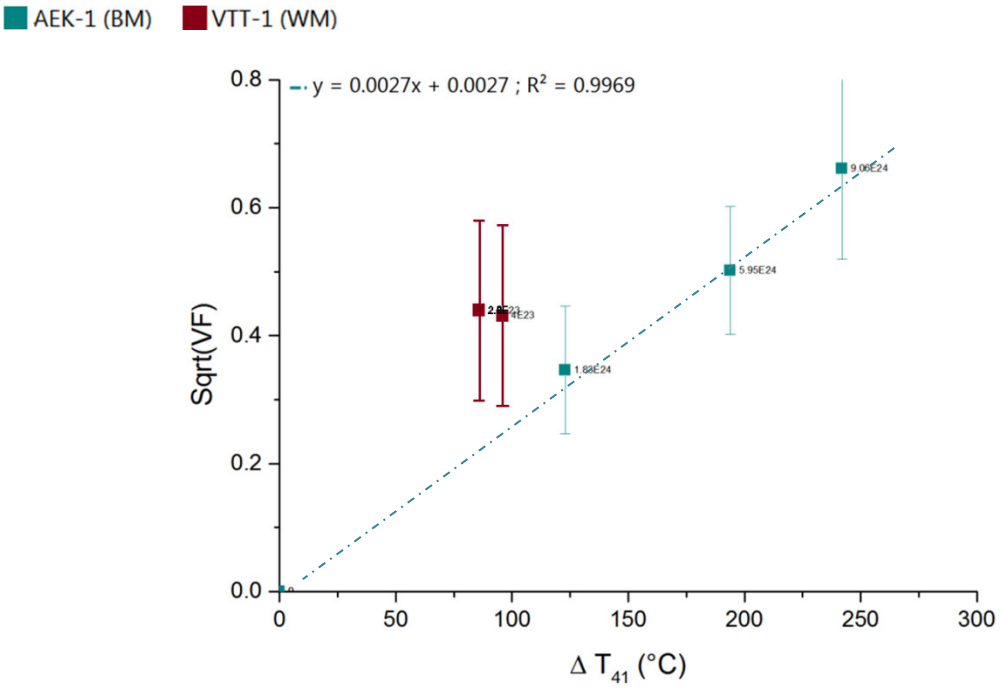


Figure xiv: Correlation between square root of volume fraction measured using APT data and Charpy-V shift values for AEK-1 and VTT-1.

The correlation between square root of volume fraction measured using SANS data and Charpy-V shift values is linear for AEK-1 (Figure xiv). Figure xiv also shows that AEK-1 has a higher Charpy-V transition temperature shift with a lower volume fraction of clusters compared to VTT-1.

AEK-1 and NRI-1

The chemical compositions and irradiation conditions for AEK-1 and NRI-1 are summarised as follows:

Total concentration of clustering elements:

(1) AEK-1: 1.292 at%
(2) NRI-1: 3.110 at%

Table xx: Nominal chemical compositions of AEK-1 and NRI-1.

Materials	[C]	[Si]	[Mn]	[P]	[S]	[Cr]	[Mo]	[Ni]	[Cu]	[V]	[Al]
	at%	at%	at%	at%	at%	at%	at%	at%	at%	at%	at%
AEK-1 (BM)	0.738	0.572	0.544	0.032	0.023	2.823	0.393	0.066	0.078	0.304	0.000
NRI-1 (WM)	0.324	0.733	0.749	0.011	0.014	1.990	0.394	1.582	0.035	0	0

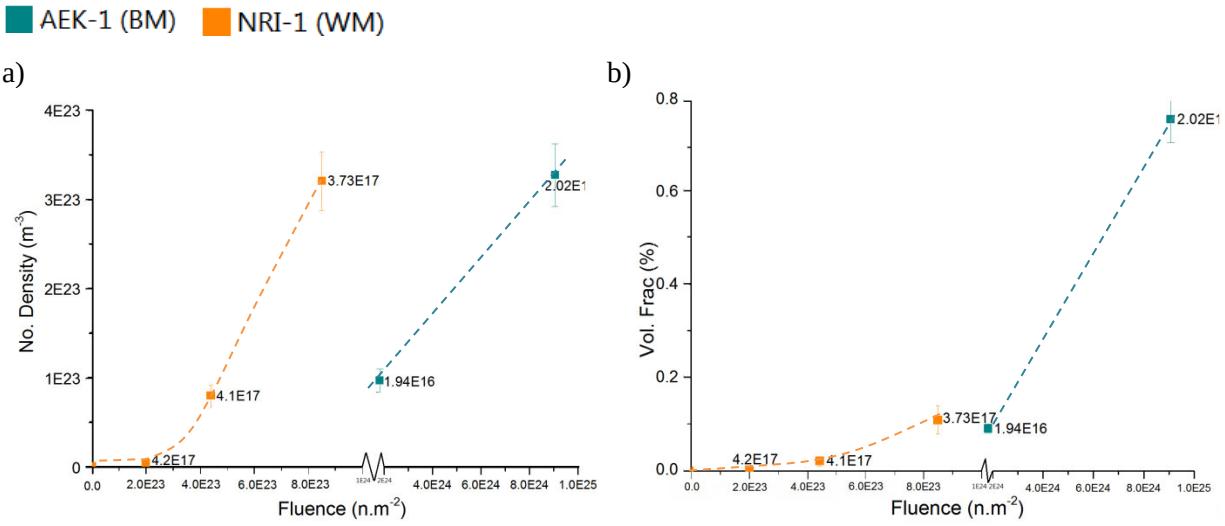
Table xxi: Summary of chemical composition differences between AEK-1 and NRI-1

Materials	***Higher content***	***Lower content***
AEK-1 (BM)	Cu, C, Cr, V	Ni, Mn, Si
NRI-1 (WM)	Ni, Mn, Si	Cu, C, Cr, V

Table xxii: Summary of neutron irradiation conditions for AEK-1 and NRI-1

Materials	***ϕt (n.m^{-2})***	***ϕ (n.m^{-2}.s^{-1})***	***T_{irra} (°C)***
AEK-1 (BM)	1.83E24	3.11E16	280
	9.06E24	3.23E16	
NRI-1 (WM)	2.00E23	4.20E17	290
	4.40E23	4.10E17	
	8.50E23	3.73E17	

APT results from AEK-1 and NRI-1



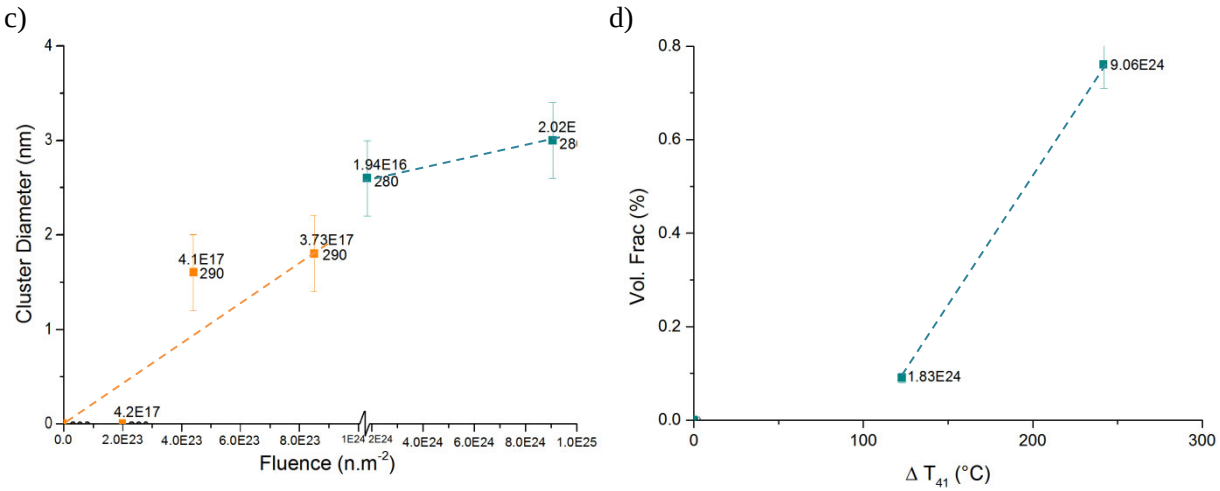


Figure xv: Correlation between (a) number density of clusters and fluence, (b) volume fraction of clusters and fluence, (c) mean diameter of clusters and fluence, and (d) volume fraction and Charpy-V shift values for AEK-1 and NRI-1. (Data label = Flux or/& Temperature)

The number density, volume fraction and size of irradiation-induced solute clusters detected using APT as a function of neutron fluence are plotted in Figure xv (a), Figure xv (b), and Figure xv (c) respectively. Even though AEK-1 and NRI-1 have been irradiated to difference fluences, the chemical effects on irradiation-induced clusters are clearly shown in this data. NRI-1 with a higher Ni, Mn and Si content compared to AEK-1 contains a significantly higher number density of solute clusters at ϕt values between ≈ 8E23 $n.m^{-2}$ and ≈ 1E24 $n.m^{-2}$. Similar observations are seen in the volume fraction of clusters detected in NRI-1 and AEK-1.

The contrast between the differences in number density and volume fraction of solute clusters detected in NRI-1 and AEK-1 may be partly due to flux effects. The flux used to irradiate NRI-1 ($\phi \approx 1E17 n.m^{-2}.s^{-1}$) is of an order of magnitude higher compared to AEK-1 ($\phi \approx 1E16\ n.m^{-2}.s^{-1}$). Based on the results from ANP-5, a higher flux will induce a higher number density of clusters and a smaller mean solute cluster size. However, a steel irradiated by a higher flux will have similar volume fraction of clusters compared to a steel of same chemical composition that has been neutron irradiated by a lower flux but to the same neutron fluence.

Another important factor that can cause differences in number density and volume fraction of solute clusters detected in NRI-1 and AEK-1 is the difference in chemical composition. One might expect the higher concentration of Ni, Mn and Si will induce a higher volume fraction of solute clusters in NRI-1 compared to AEK-1. However, Figure xvi (b) shows that the differences in volume fraction of clusters detected in NRI-1 is relatively small compared to AEK-1 at similar ϕt (8E23 $n.m^{-2}$ < ϕt < 1E24 $n.m^{-2}$). A similar observation was found from data of 16MND5 type steels (Figure iv).

It is important to note very few solute clusters are detected in NRI-1 at $\phi t \approx$ 2E23 $n.m^{-2}$. This observation is similar to ANP-2 and will be further discussed in Section III.

II. VI. Synergistic effects of Ni, Mn and Si for high Ni steels

To further analyse the synergistic effects of Ni, Mn and Si, ANP-6 and NRI-1 are selected. Both ANP-6 and NRI-1 contain a high concentration of nickel (≈1.6 at.%), but different contents of Mn and Si. The chemical compositions and irradiation conditions for ANP-6 and NRI-1 are summarised as follows:

Total concentration of clustering elements:

(1) ANP-6: 3.428 at.%
(2) NRI-1: 3.110 at.%

Table xxiii: Nominal chemical compositions of ANP-6 and NRI-1

Materials	[C]	[Si]	[Mn]	[P]	[S]	[Cr]	[Mo]	[Ni]	[Cu]	[V]	[Al]
	at%	at%	at%	at%	at%	at%	at%	at%	at%	at%	at%
ANP-6 (WM)	0.232	0.298	1.432	0.022	0.012	0.075	0.267	1.606	0.070	0.004	0.046
NRI-1 (WM)	0.324	0.733	0.749	0.011	0.014	1.990	0.394	1.582	0.035	0	0

Table xxiv: Summary of chemical composition differences between ANP-6 and NRI-1

Materials	*Higher content*	*Lower content*
ANP-6 (WM)	Cu, Mn	Si, Cr, Mo, C
NRI-1 (WM)	Si, Cr, Mo, C	Cu, Mn

Table xxv: Summary of neutron irradiation conditions for ANP-6 and NRI-1

Materials	*ϕt ($n.m^{-2}$)*	*ϕ ($n.m^{-2}.s^{-1}$)*	*T_{irra} (°C)*
ANP-6 (WM)	4.10E22	1.06E16	290-300
	1.16E23	2.96E16	
	5.22E23	2.41E16	
NRI-1 (WM)	2.00E23	4.20E17	290
	4.40E23	4.10E17	
	8.50E23	3.73E17	

APT results from ANP-6 and NRI-1

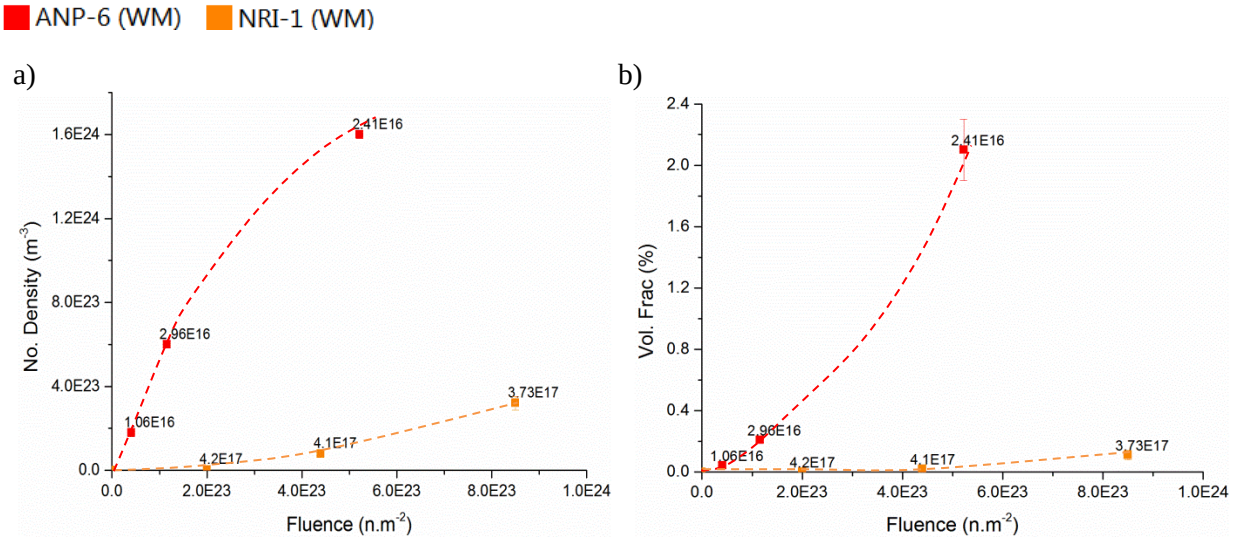


Figure xvi: Magnitude of (a) number density and (b) volume fraction of solute cluster detected in ANP-6 and NRI-1 as a function of neutron fluence. (Data label = Flux)

Figure xvi shows that ANP-6 with a higher Mn content has a significantly higher number density and volume fraction of solute clusters compared to NRI-1 with a lower Mn content but a higher concentration of Si. This observation is consistent with the analysis performed on 16MND5-type (EFD-2 & EDF-3) and Kh2MF-type (AEK-1 & NRI-1) steels. Assuming that [Cr] has very little effect, it suggests that the concentration of Mn is the stronger influencing factor that encourages solute clusters to nucleate and grow during neutron irradiation. Figure xvii also suggests that an increase in Si content in steels with low Mn content will not encourage more solute clusters to form during neutron irradiation in materials with the same Ni concentration.

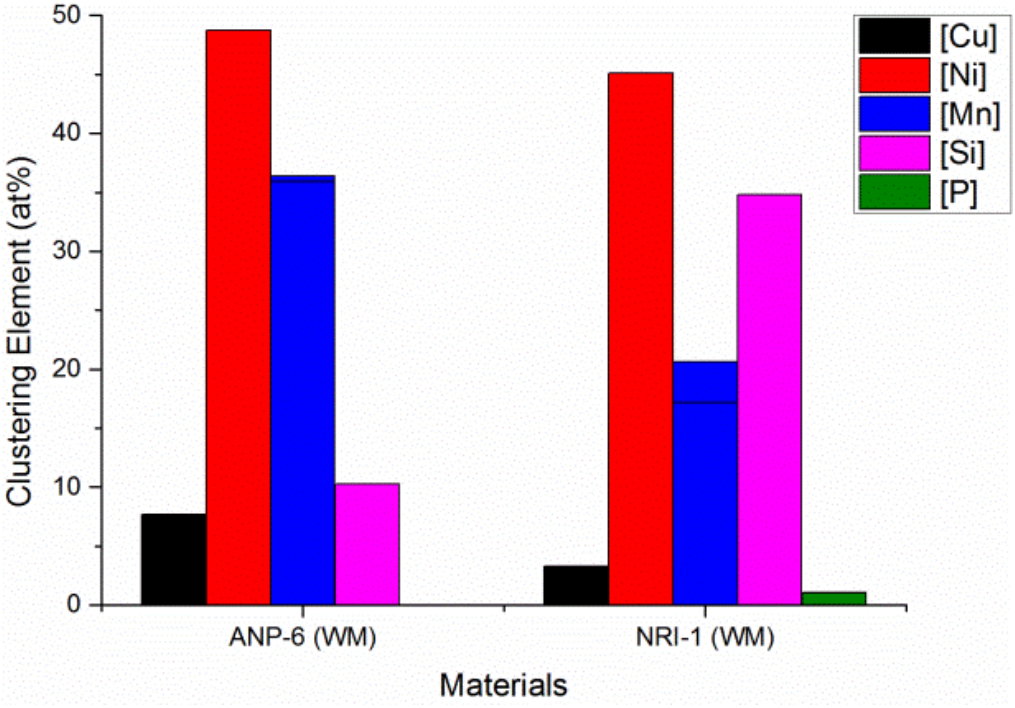


Figure xvii: Average solute cluster chemistry for ANP-6 and NRI-1 detected using APT.

The ratio of Cu, Ni, Mn, Si and P content of solute clusters detected in ANP-6 and NRI-1 is shown in Figure xvii. The composition of the solute clusters clearly follows the bulk alloy composition quite faithfully.

II. VII. Synergistic effects of Ni, Mn & Si for low & high Ni steels

This analysis is to study the effect of Ni on irradiation-induced solute clusters detected in MnNiMo-alloy steels. The metals selected from the list of materials available are ANP-2, ANP-6, EDF-2 and EDF-3. These metals have been irradiated to a similar neutron fluence, but at different neutron fluxes. The neutron fluence range is between $\phi t \approx 0$ n.m^{-2} and $\phi t \approx$ 5E23 n.m^{-2}. The chemical compositions and irradiation conditions for ANP-2, ANP-6, EDF-2 and EDF-3 are summarised as follows:

Total concentration of clustering elements in metal:

1) EDF-2: 2.491 at%
2) EDF-3: 2.775 at%
3) ANP-2: 2.357 at%
4) ANP-6: 3.428 at%

Note: FZD-1a & FZD-1b are not included in this assessment because their irradiation temperature is much lower (255˚C).

Table xxvi: Nominal chemical compositions of EDF-2, EDF-3, ANP-2 and ANP-6

Materials	[C]	[Si]	[Mn]	[P]	[S]	[Cr]	[Mo]	[Ni]	[Cu]	[V]	[Al]
	at%	at%	at%	at%	at%	at%	at%	at%	at%	at%	at%
EDF-2 (BM)	0.638	0.436	1.335	0.011	0.010	0.214	0.313	0.653	0.056	0.006	0.029
EDF-3 (WM)	0.250	0.694	1.429	0.016	0.019	0.021	0.331	0.607	0.029	0.006	0.006
ANP-2 (WM)	0.232	0.239	1.097	0.034	0.016	0.107	0.361	0.961	0.026	0.011	0.025
ANP-6 (WM)	0.232	0.298	1.432	0.022	0.012	0.075	0.267	1.606	0.070	0.004	0.046

Table xxvii: Summary of chemical composition differences between ANP-2, ANP-6, EDF-2 and EDF-3

Copper		
Low [Cu]	***Medium [Cu]***	***High [Cu]***
ANP-2	EDF-2	ANP-6
EDF-3		
Nickel		
Low [Ni]	***Medium [Ni]***	***High [Ni]***
EDF-2	ANP-2	ANP-6
EDF-3		
Manganese		
Low [Mn]	***High [Mn]***	
ANP-2	EDF-2	
	EDF-3	
	ANP-6	
Silicon		
Low [Si]	***Medium [Si]***	***High [Si]***
ANP-2	EDF-2	EDF-3
ANP-6		

Table xxviii: Summary of neutron irradiation conditions for EDF-2, EDF-3, ANP-2 and ANP-6

Materials	*ϕt ($n.m^{-2}$)*	*ϕ ($n.m^{-2}.s^{-1}$)*	*T_{irra} (°C)*
EDF-2 (BM)	1.71E23	1.90E15	286
	5.22E23	2.10E15	
	6.95E23	2.00E15	
EDF-3 (WM)	1.26E23	1.40E15	286
	3.86E23	1.60E15	
	5.13E23	1.50E15	
ANP-2 (WM)	9.80E22	2.50E16	285
	4.97E23	2.33E16	
ANP-6 (WM)	4.10E22	1.06E16	280-300
	1.16E23	2.96E16	
	5.22E23	2.41E16	

APT results from EDF-2, EDF-3, ANP-2 and ANP-6

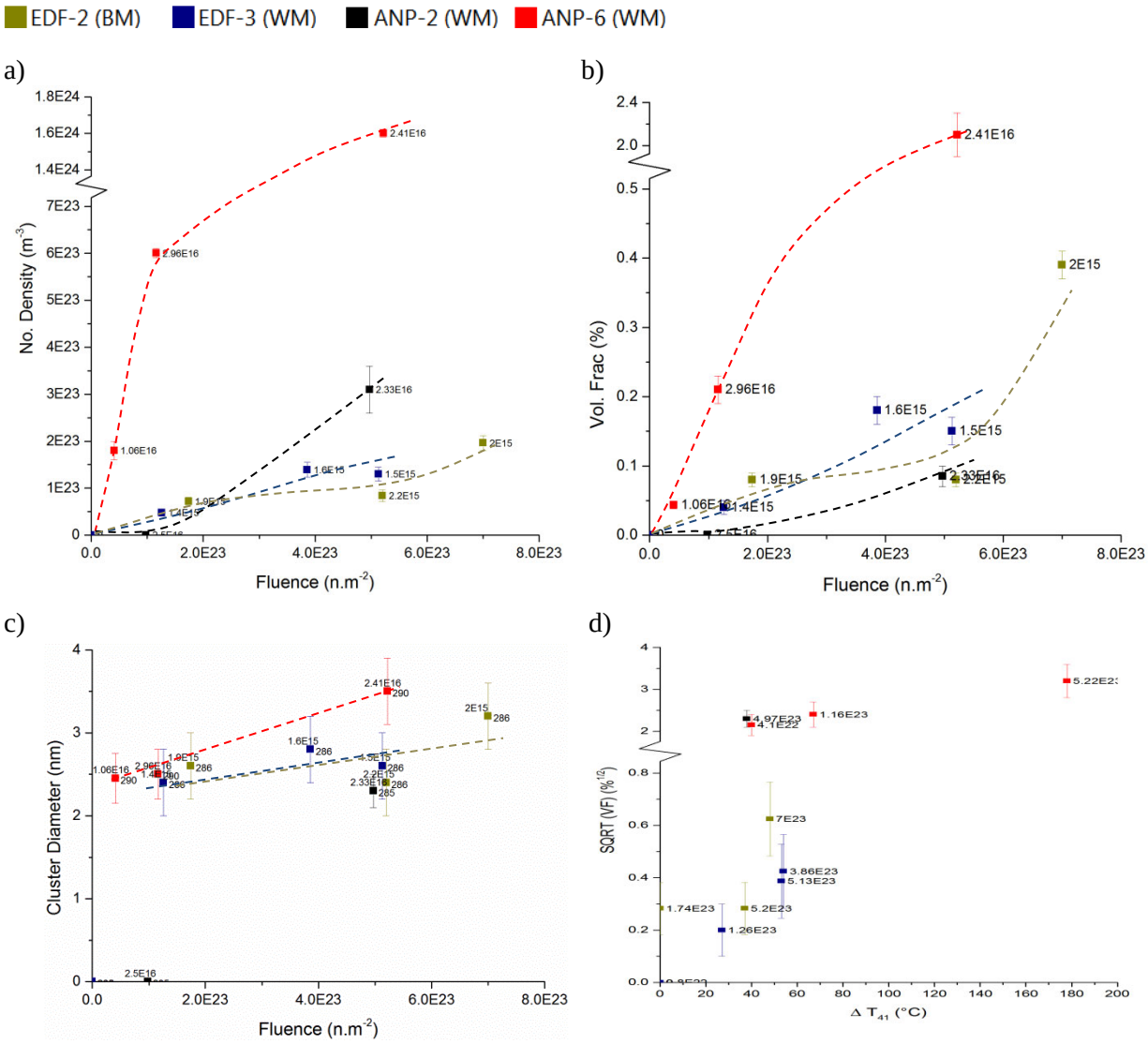


Figure xviii: Correlation between (a) number density of clusters and fluence, (b) volume fraction of clusters and fluence, (c) mean diameter of clusters and fluence, and (d) square root of volume fraction and Charpy-V shift values for EDF-2, EDF-3, ANP-2 and ANP-6. Data used was obtained from APT. (Data label = Flux or/& Temperature)

The number density, volume fraction and size of solute clusters as a function of neutron fluence for ANP-2, ANP-6, EDF-2 and EDF-3 are plotted as Figure xviii (a), Figure xviii (b) and Figure xviii (c) respectively. The flux effect on the number density of clusters can be seen in Figure xviii (a). High [Ni] ANP-6 and ANP-2 irradiated at a higher neutron flux contained a significantly higher number of clusters at a neutron fluence, $\phi t \approx 5E23 n.m^{-2}$, compared to EDF-2 and EDF-3 that have been irradiated at a lower neutron flux.

A strong correlation of chemical effects on the volume fraction of irradiation-induced clusters was observed in Figure xviii (b). The correlation found is strongly dependent on the concentration of Cu, Ni, Mn and, possibly, Si.

At low neutron fluence, between $\phi t \approx 0$ n.m^{-2} and $\phi t \approx$ 2E23 n.m^{-2}, the volume fraction of solute clusters detected in these metals, from lowest to highest, is ANP-2, EDF-3, EDF-2 and ANP-6. This sequence is identical to the variation Cu content in these steels. This observation raises the question as to whether the Cu is involved at the initial stage of solute clustering so that higher concentrations of Cu (but < 0.1 at%) will increase the rate of clustering at low fluence.

This observation may support the simulation results from previous studies on irradiation-induced Cu-rich cluster precipitation processes. Simulations suggest that mono-vacancy defects induced by neutron irradiation prefer to couple with Cu atoms since the Cu-vacancy couple has the lowest interaction energy compared to Mn-vacancy or Ni-vacancy defects [3].

At higher neutron fluence, i.e. $\phi t \approx$ 5E23 n.m^{-2}, the highest volume fraction of solute clusters was detected in ANP-6 that contains the highest concentration of Cu, Ni and Mn. An interesting outcome in the synergistic effect of Ni, Mn and Si is shown in Figure xviii (b). ANP-2 with a higher Ni content and a lower Mn and Si content has a lower volume fraction of solute clusters compared to EDF-2 and EDF-3 that contain a lower Ni content and higher Mn and Si content. This observation is consistent with previous analysis on ANP-6 and NRI-1 and 16MND5-type steels.

The mean cluster size increases with increasing neutron fluence (Figure xviii (c)). ANP-6 with the highest concentration of clustering elements has the largest mean cluster diameter

even though it was neutron irradiated by a higher flux compared to EDF-2 and EDF-3. This indicates that cluster size also depends on the concentration of clustering elements, and is consistent with previous analysis on NiMoCr-alloyed steels.

II. VIII. Temperature Effect for low Ni steels

The main purpose of this analysis is to study the effect of temperature on irradiation-induced microstructure of ferritic steels with similar chemical compositions. Metals selected are EDF-2 and FZD-1b. However, these metals have been irradiated to different neutron fluence using different flux. The chemical compositions and irradiation conditions for EDF-2 and FZD-1b are summarised as follows:

Total concentration of clustering elements:

(1) EDF-2: 2.491 at%
(2) FZD-1b: 2.531 at%

Table xxix: Nominal chemical compositions of EDF-2 and FZD-1b

Materials	[C]	[Si]	[Mn]	[P]	[S]	[Cr]	[Mo]	[Ni]	[Cu]	[V]	[Al]
	at%	at%	at%	at%	at%	at%	at%	at%	at%	at%	at%
EDF-2 (BM)	0.638	0.436	1.335	0.011	0.010	0.214	0.313	0.653	0.056	0.006	0.029
FZD-1b (BM)	0.877	0.474	1.332	0.010	0.009	0.171	0.318	0.690	0.025	0.007	0.062

Table xxx: Summary of chemical composition differences between EDF-2 and FZD-1b

Materials	***Higher content***	***Lower content***
EDF-2 (BM)	Cu, Cr	Ni, Si, C
FZD-1b (BM)	Ni, Si, C	Cu, Cr

Table xxxi: Summary of neutron irradiation conditions for EDF-2 and FZD-1b

Materials	***ϕt (n.m^{-2})***	***ϕ (n.m^{-2}.s^{-1})***	***T_{irra} (˚C)***
EDF-2 (BM)	1.71E23	1.9E15	286
	5.22E23	2.1E15	
	6.95E23	2.0E15	
FZD-1b (BM)	5.70E23	2.2E16	255
	8.90E23	3.5E16	

SANS results from EDF-2 and FZD-1b

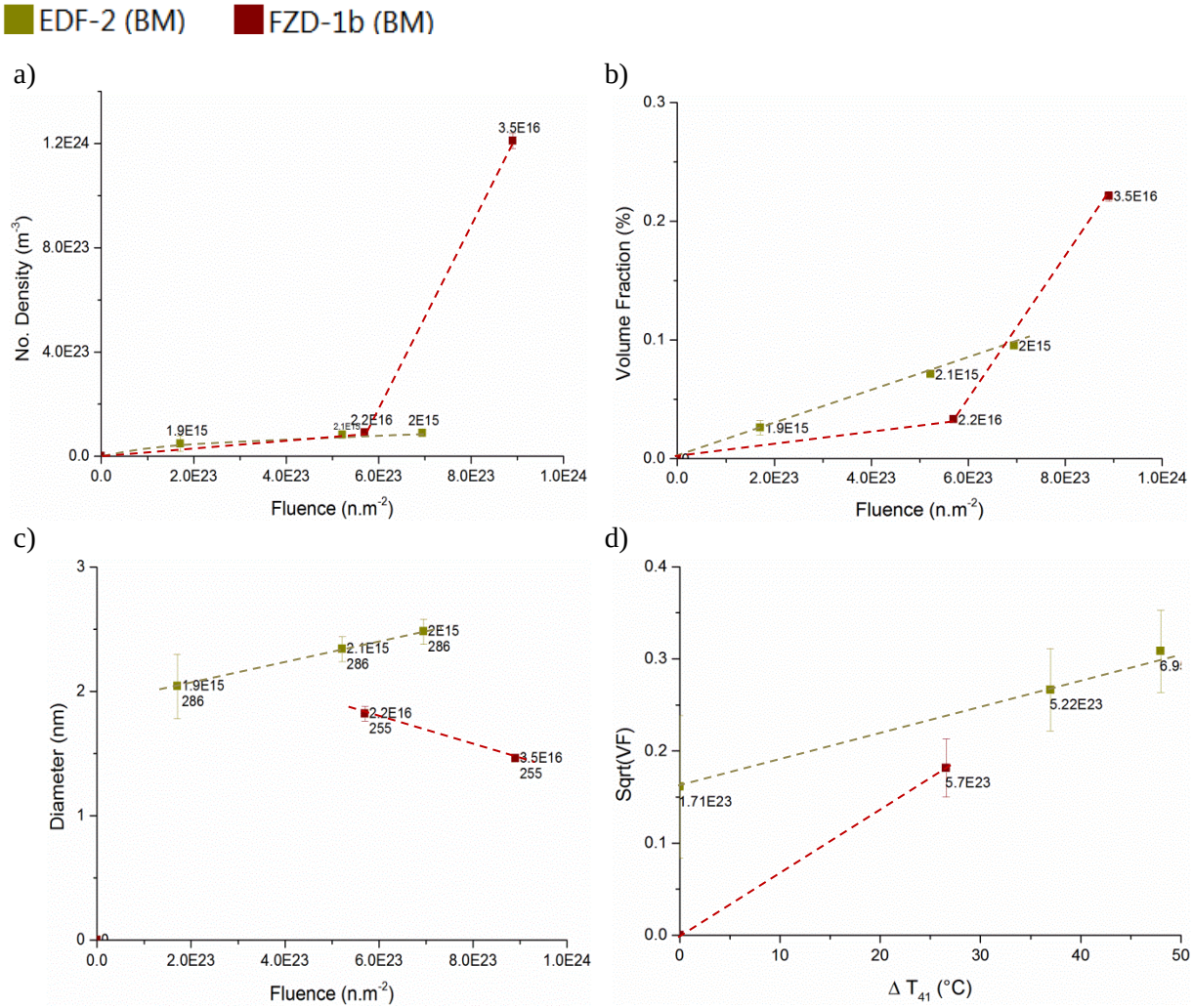


Figure xix: Correlation between (a) number density of clusters and fluence, (b) volume fraction of clusters and fluence, (c) mean diameter of clusters and fluence, and (d) square root of volume fraction and Charpy-V shift values for EDF-2 and FZD-1b. (Data label = Flux or/& Temperature)

Number density, volume fraction and size of irradiation-induced clusters detected in EDF-2 and FZD-1b as a function of neutron fluence are plotted as Figure xix (a), Figure xix (b) and Figure xix (c) respectively. No obvious differences were found between the number densities of clusters detected in EDF-2 and FZD-1b at neutron fluences between $\phi t \approx 0 n.m^{-2}$ and $\phi t \approx 6E23\ n.m^{-2}$. It is not possible to include neutron fluences greater than $\phi t \approx 6E23\ n.m^{-2}$ into the comparison as both metals covered a different range of neutron fluence.

Figure xix (b) shows that the volume fraction of clusters detected in EDF-2 is significant higher compared to FZD-1b at a neutron fluence $\phi t \approx 5E23 n.m^{-2}$. This difference in

volume fraction of clusters could partly be due to the difference in irradiation temperature between EDF-2 and FZD-1b since their chemical compositions are quite similar.

The mean cluster diameter detected in EDF-2 and FZD-1b is also different. FZD-1b shows a smaller mean cluster size compared to EDF-2. This difference in cluster diameter may be the effect of neutron flux.

III. Irradiation-induced solute clusters

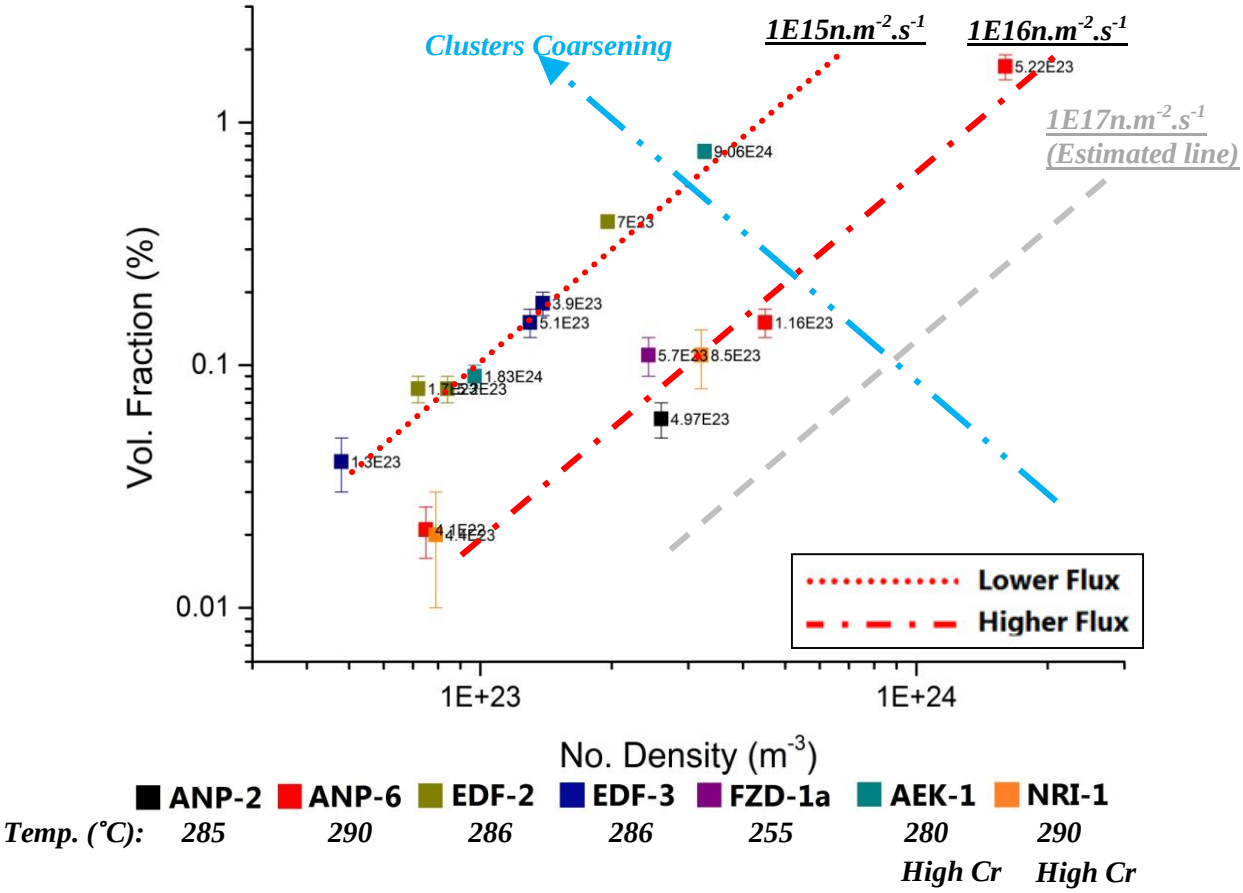


Figure xx: Correlation between volume fraction and number density of clusters for all RPV steels. (Data label = Fluence)

Table xxxii: Nominal chemical composition of RPV steels

	Chemical Elements (at%)								
	C	*Si*	*Mn*	*P*	*Cr*	*Mo*	*Ni*	*Cu*	*V*
EDF-2	0.638	0.436	1.335	0.011	0.214	0.313	0.653	0.056	0.006
EDF-3	0.250	0.694	1.429	0.016	0.021	0.331	0.607	0.029	0.006
AEK-1	0.738	0.572	**0.544**	0.032	**2.823**	0.393	0.066	0.078	0.304
ANP-2	0.232	0.239	1.097	0.034	0.107	0.361	0.961	0.026	0.011
ANP-6	0.232	0.298	1.432	0.022	0.075	0.267	1.606	0.070	0.004
FZD-1a	0.921	0.473	1.309	0.361	0.181	0.329	0.698	0.024	0.005
NRI-1	0.324	0.733	**0.749**	0.011	**1.990**	0.394	1.582	0.035	0.000

Figure xx shows the correlation between volume fraction and number density of clusters detected from all RPV steels studied in LONGLIFE. The correlation observed in this Figure is complicated as it summarises the synergistic effects of flux, fluence, temperature

and chemical composition on irradiation-induced solute clusters. Two trends were observed, as shown by the red lines in Figure xx. These trends are believed to provide reliable data on the effect of flux on the RPV steels that have been analysed.

All steels that have been neutron irradiated at fluxes that are in the order of 1E15n.m^{-2}.s^{-1} and 1E16n.m^{-2}.s^{-1} are well aligned, as shown by the red-dotted line and red-dash-dotted line respectively. These trends indicate that, in general, RPV steels that have been neutron irradiated at a higher flux have a higher number density of clusters than RPV steels that have been neutron irradiated at a lower flux, at a given neutron fluence. This observation is similar to the flux effects observed from ANP-5 and Deliverable 3.4 report.

However, two steels, AEK-1 and NRI-1, do not fit into the trends observed in Figure xx. Both AEK-1 and NRI-1 data points fall onto the flux lines an order of magnitude lower than their own fluxes, i.e. AEK-1 that has been irradiated at a flux of 1E16n.m^{-2}.s^{-1} is lined up at the flux line of 1E15n.m^{-2}.s^{-1} ; Similarly, NRI-1 with a flux of 1E17n.m^{-2}.s^{-1} is lined up at the flux line of 1E16n.m^{-2}.s^{-1}.

After a careful cross-examination, it was found that the only possible explanation for these ‘apparent flux effects shifts’ observed from AEK-1 and NRI-1 is related to the effects of Cr and Mn on irradiation-induced clusters, since differences of these steels to the others lie in the Cr and Mn concentrations, i.e. AEK-1 and NRI-1 contain ≈ 2 at.% of Cr and ≈ 0.5 at% and 0.7 at.% of Mn, respectively.

III. I) Effects of Chromium on Irradiation-induced Solute Clusters

Most of the effects of Cr found are on radiation sensitivity [4], void-swelling [5, 6] and irradiation-induced dislocation loops [7]. No microstructural studies of the effects of Cr on irradiation-induced MnNiSi-rich clusters can be found from the literature. However, a

study on semi-mechanistic models of radiation damage [4] showed that chromium has a positive effect on reducing the basic matrix damage rate constant and the precipitation term. It would be useful to note that this study also mentions that the positive effect of Cr is limited to concentration of approximately 2 wt%. Higher concentration, i.e. 6-18 wt% would have an detrimental effect [8].

Apart from that, previous studies on chemical effects on irradiation-induced hardening and irradiation-induced microstructure based on different combination of Fe-based binary alloys [9-11] indicate that vacancies induced by irradiation were 'trapped' by Cr solute atoms and thus, reduce swelling. Hence, it is reasonable to speculate that this 'vacancy trapping' might indirectly affect solute cluster formation. This speculation will only be possible if the mechanism of formation of solute clusters involve coupling of solute atoms with vacancies and subsequent mobility of irradiation-induced vacancies as suggested in the modeling studies of solute cluster formation during neutron irradiation [3].

Nevertheless, evidence is still limited and more research is required in order to quantify whether the 'apparent flux effects shift' is caused by the Cr present in AEK-1 and NRI-1.

III. II) Effects of Manganese on Irradiation-induced Solute Clusters

Apart from high Cr concentrations in AEK-1 and NRI-1, both metals have relatively low Mn concentrations, i.e. less than 1 at%. Based on Section II, there is evidence for the effects of Mn on irradiation-induced solute clusters. Increasing the Mn concentration in steel that contain reasonable concentration of Ni will significantly increase the volume fraction of solute clusters induced during long-term neutron irradiation.

Moreover, similar studies based on Fe-based binary alloys [9, 12, 13] show that increasing the Mn concentration in Fe will significantly increase irradiation-induced hardening. These

studies have also shown that irradiation-induced hardening provoked by Mn is comparable to the hardening induced by Cu at high neutron fluence and/or dpa.

Yabuuchi et al.[14] discussed the effects of Mn on the mobility of dislocation loops. They have found that the size distribution of dislocation loops formed in an irradiated Fe-1at% Mn binary alloy is smaller compared to those found in an irradiated pure Fe. Also, the 1-D motion of dislocation loops found in a Fe-1at% Mn binary alloy occur at higher annealing temperature compared to pure Fe. This finding suggests that reducing the Mn concentration in steel will potentially increase the rate of diffusion of solute atoms and as a result larger solute clusters can be formed, i.e. cluster coarsening as shown by the light-blue line in Figure xx.

However, these are just indications that show the effects of Mn on irradiation-induced defects. Evidence is still limited and more research is required in order to quantify whether the ‘apparent flux effects shift’ is caused by the Mn or the synergistic effects of Mn, Cr present in AEK-1 and NRI-1.

IV. Solute Cluster Chemistry

Solute clusters were detected in all of the neutron irradiated RPV steels analysed by using APT except ANP-2 ($\phi t \approx 1E23$ n.m^{-2}) & NRI-1 ($\phi t \approx 2E23$ n.m^{-2}). Based on APT reconstructed data, 6 chemical elements, i.e. copper, nickel, manganese, silicon, phosphorus & iron were found in the irradiation-induced clusters. There is considerable discussion in the literature [15, 16] concerning the concentration of Fe detected in these clusters which may result from trajectory aberration effects. Hence, in this analysis, only the ratios of the solute elements, excluding Fe, were considered. After removing iron from the solute cluster composition, the average chemistry of solute clusters could be compared for RPV steels neutron irradiated to ϕt between 4 and 6 x 10^{23} n.m^{-2}, E > 1MeV, and are summarized in Table xxxiii. For most materials studied the solute cluster chemistry was rather similar after removing Fe (e.g. ANP-2 & ANP-6).

Table xxxiii: Summary of average chemical composition of solute clusters detected in RPV steels (only considering ϕt range of interest, 4 < ϕt < 6 x 10^{23} n.m^{-2}, E>1MeV).

Mat.	Fluence	Flux	[Cu]	[Ni]	[Mn]	[Si]	[P]
	x 10^{23} n.m^{-2}	X 10^{16} n.m^{-2}.s^{-1}	at%	at%	at%	at%	at%
ANP-2 (Weld)	4.97	2.33	2.2 ± 0.2	49.5 ± 0.5	35.5 ± 0.4	10.8 ± 1.1	2.2 ± 0.2
ANP-6 (Weld)	5.22	2.41	5.1 ± 0.5	48.7 ± 4.9	35.9 ± 3.6	10.3 ± 1.0	0.0 ± 0.0
EDF-2 (Base)	5.20	0.22	6.1 ± 2.0	38.1 ± 5.6	26.9 ± 4.6	28.9 ± 4.6	0.0 ± 0.0
EDF-3 (Weld)	5.10	0.15	1.4 ± 0.5	28.5 ± 1.4	26.6 ± 1.4	40.6 ± 1.9	2.9 ± 0.5
FZD-1a (Base)	5.70	2.20	0.4 ± 0.2	40.9 ± 1.8	40.3 ± 1.8	17.8 ± 1.2	0.6 ± 1.2
AEK-1 (Base)	18.3	1.60	33.8 ± 3.2	12.2 ± 1.8	22.1 ± 2.7	30.2 ± 2.7	1.8 ± 0.9
NRI-1 (Weld)	4.40	40.5	3.3 ± 1.1	44.0 ± 4.9	20.7 ± 3.3	31.0 ± 2.2	1.1 ± 0.5

Based on the definition of copper-rich clusters (CRPs) and manganese, nickel and silicon-rich clusters (MNPs) suggested by Odette *et. al.* in [17], solute clusters detected in all the metals analysed by APT in this project are MNP, apart from AEK-1 (Figure xxi). It is difficult to classify the type of clusters precipitated in AEK-1, since the mean chemical ratio of Cu and the combination of Ni and Mn is 50:50.

Apart from Fe as an artefact induced by APT during the evaporation process, there are on-going discussions about whether copper & phosphorus are part of the solute clusters (especially for MNP). If we remove Cu and P from the cluster composition, we can summarise the average solute cluster chemistry of different RPV steels in Table xxxiv.

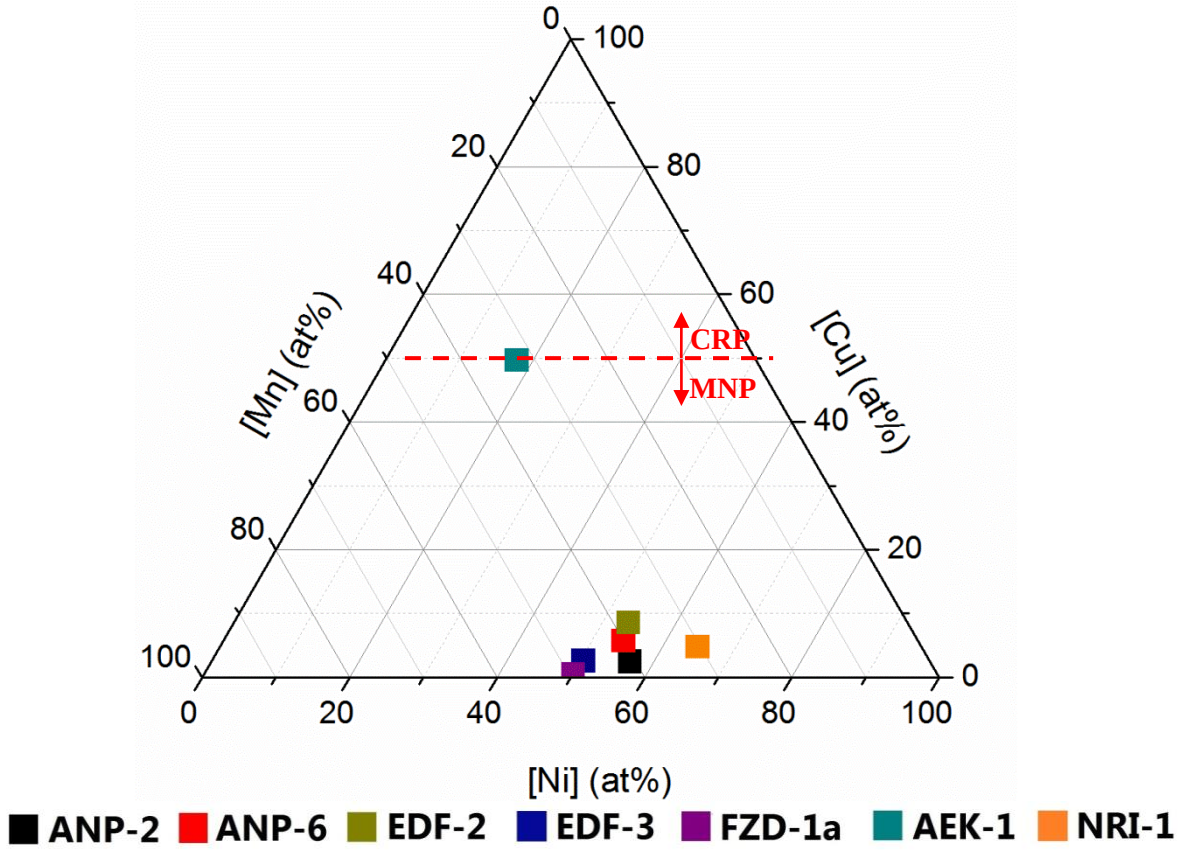


Figure xxi: Tertiary diagram of Cu, Ni and Mn that provides indication of the type of solute clusters detected in all RPV steels at ϕt between 4 & 6E23 n.m^{-2}, based on average chemical compositions detected using APT.

Note that the solute cluster compositions from ANP-2 & ANP-6 are very similar and almost identical if we considered a typical error bar, even though ANP-6 has much higher nickel, manganese and copper content in the bulk compared to ANP-2.

Table xxxiv: Summary of average chemical composition of solute clusters considering only of nickel, manganese & silicon, detected in RPV steels (only considering ϕt range of interest, 4 < ϕt < 6 x10^{23} n.m^{-2}, E>1MeV).

Mat.	Fluence	Flux	[Ni]	[Mn]	[Si]
	x 10^{23} n.m^{-2}	X 10^{16} n.m^{-2}.s^{-1}	at%	at%	at%
ANP-2 (Weld)	4.97	2.33	51.7 ± 0.5	37.1 ± 0.4	11.2 ± 1.1
ANP-6 (Weld)	5.22	2.41	51.4 ± 5.1	37.8 ± 3.8	10.8 ± 1.1
EDF-2 (Base)	5.20	0.22	40.5 ± 5.9	28.6 ± 4.9	30.8 ± 4.9
EDF-3 (Weld)	5.10	0.15	29.8 ± 1.5	27.8 ± 1.5	42.4 ± 2.0
FZD-1a (Base)	5.70	2.20	41.3 ± 1.8	40.7 ± 1.8	18.0 ± 1.2
AEK-1 (Base)	18.3	1.60	18.9 ± 2.8	34.3 ± 4.2	46.9 ± 4.2
NRI-1 (Weld)	4.40	40.5	46.0 ± 5.1	21.6 ± 3.4	32.4 ± 2.3

IV. I) Potential phase for solute cluster precipitates in RPV steels

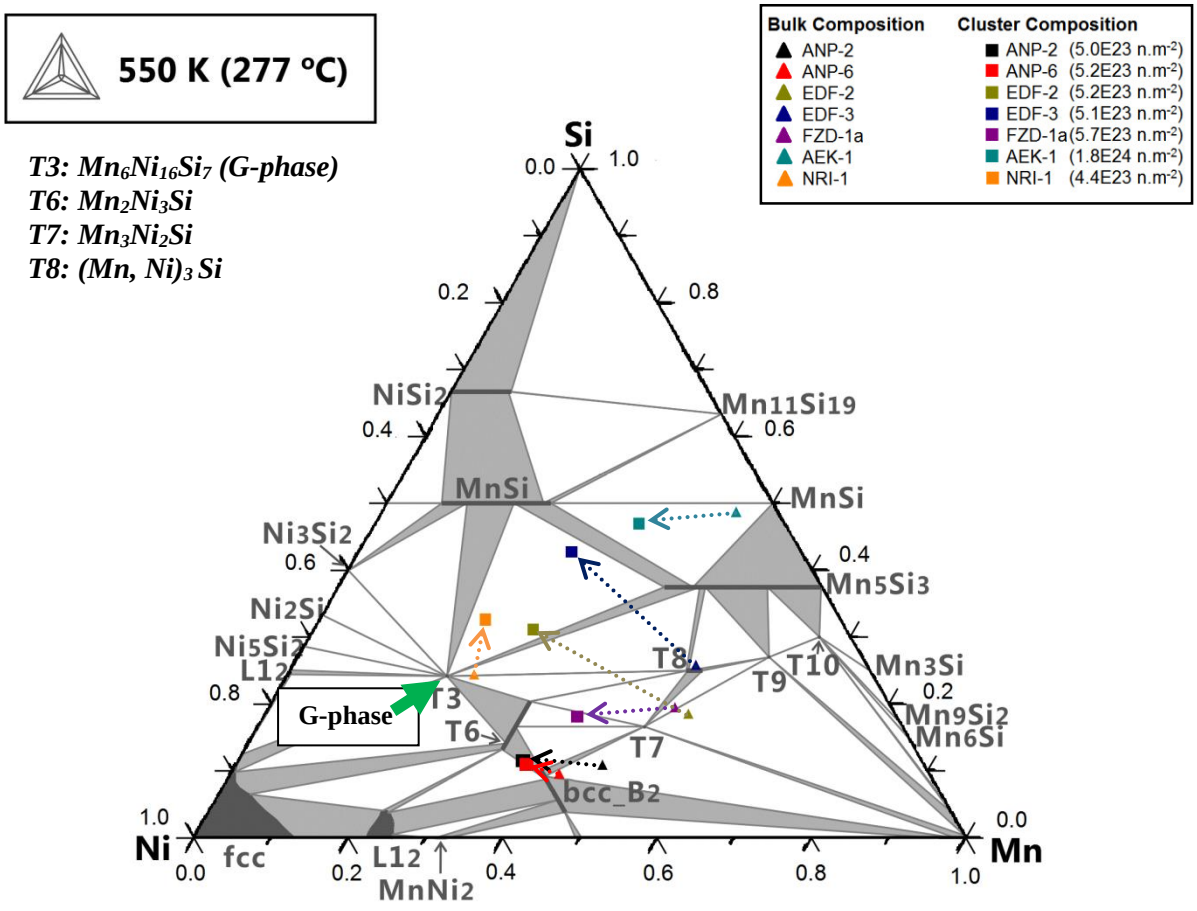


Figure xxii: Potential phases of the SCs detected in all RPV steels of ϕt between 4 & 6E23 n.m^{-2}, based on average chemical composition detected using APT. The tertiary diagram was obtained from Ref. [18, 19].

Odette *et. al*. suggested that MNPs are a G-phase. G-phase was first found in the ferritic part of thermally aged duplex stainless steels by Allsop & Brown in the 1960s [20, 21]. By comparing the chemical data for the G-phase ($Mn_6Ni_{16}Si_7$) from the literature with the average solute cluster composition of all RPV steels detected by using APT, none of the average chemical compositions detected (Table xxxiv) match well with the G-phase composition. The potential phase of solute clusters detected from the RPV steels analysed is shown in Figure xxii. Note that, based on the nominal chemical composition of NRI-1, G-phase is most likely to be induced during neutron irradiation (Figure xxii). However, the mean chemical composition of solute clusters detected in NRI-1 has shifted away from the G-phase.

Malerba *et al.* [22] presented the possibility for nickel-manganese phases to precipitate at RPV temperatures if the local concentration of nickel and manganese exceed 2%. The presence of matrix damage or dislocation loops will shift the solubility limit, and as a result, we might expect these solute clusters to become stable at RPV operating temperatures.

IV. II) Effect of fluence on solute cluster chemistry

Figure xxiii shows the correlation between the mean chemical composition of solute clusters, for the chemical elements, Cu, Ni, Si, Mn and P, present in these clusters, and fluence for all RPV steels. Ni, Mn, Si and P data has no obvious correlation with neutron fluence. Figure xxiii (a) shows that the mean Cu concentration of solute clusters decreases with the increase of neutron fluence for all RPV steels. It is important to note that the solute cluster chemistry might depend on the APT specimen erosion mode, parameters used during the APT specimen erosion and parameters used in the cluster analysis algorithm for raw APT data reconstruction.

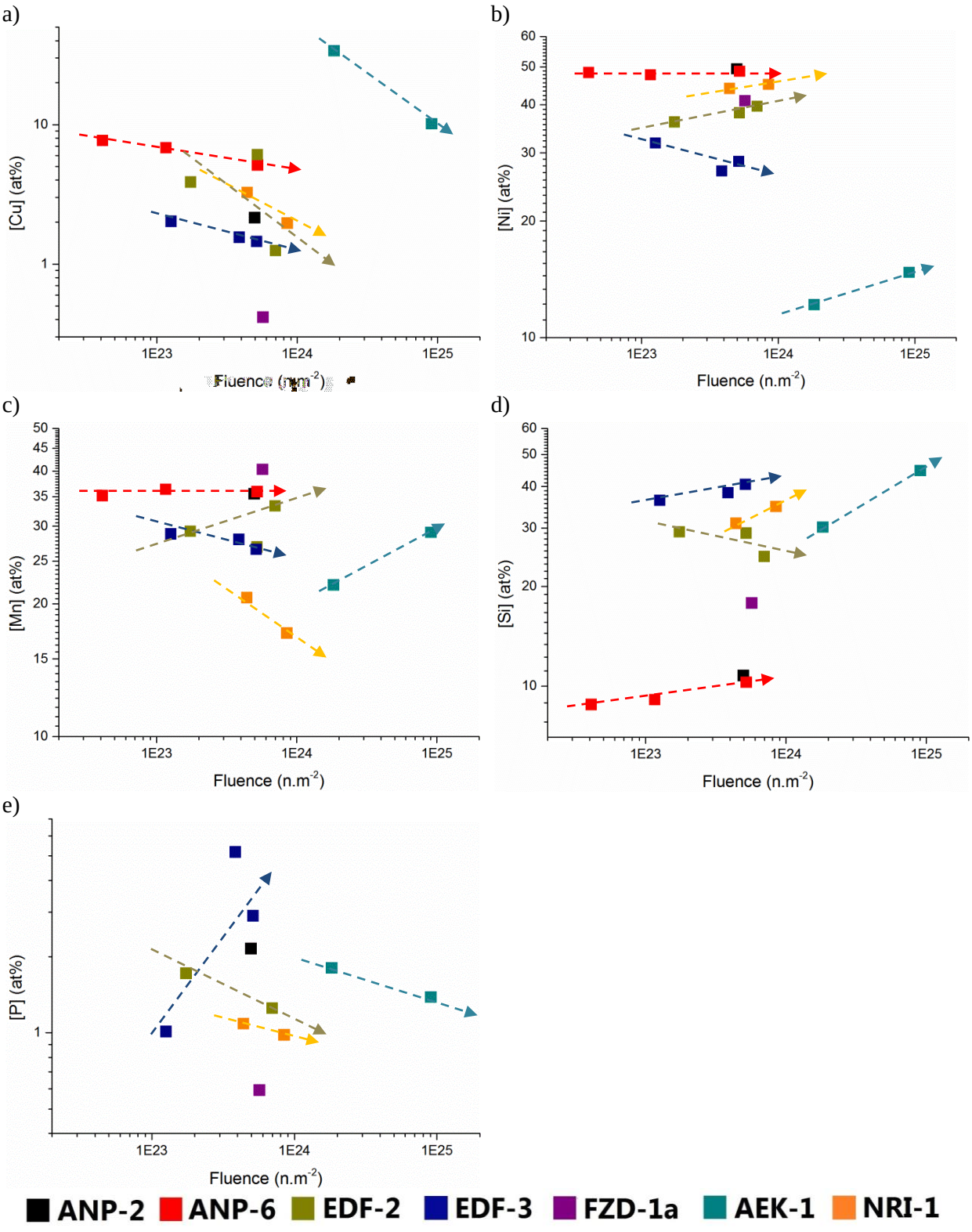


Figure xxiii: Correlation between mean (a) [Cu] (b) [Ni] (c) [Mn] (d) [Si] and (e) [P] of solute clusters and fluence for all RPV steels analysed by using APT.

V. Irradiation-induced cluster hardening capability

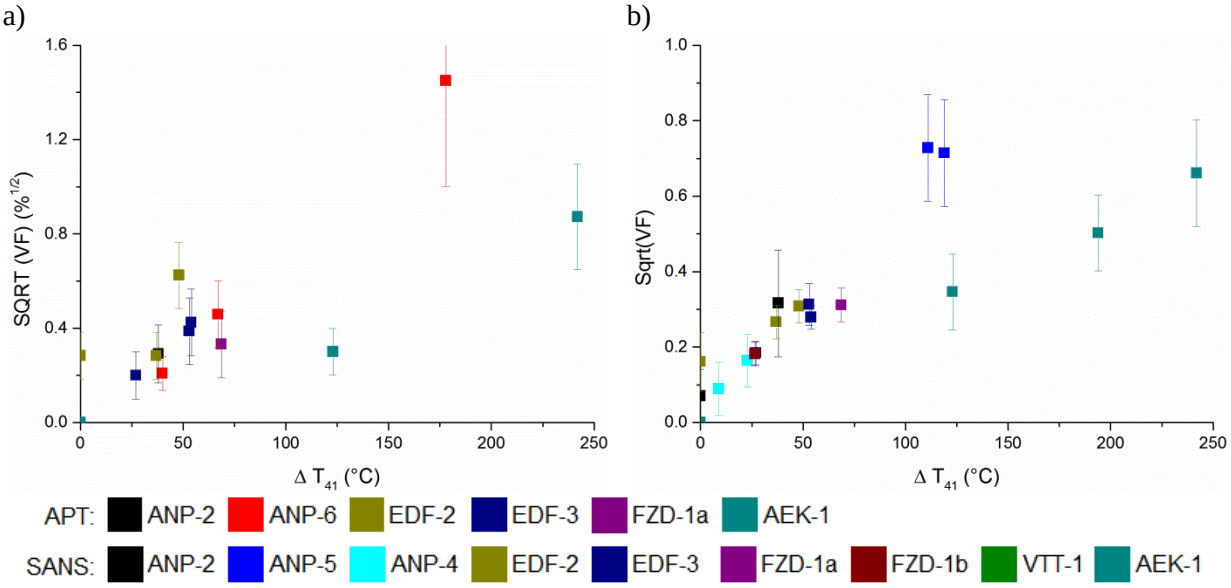


Figure xxiv: Correlation between square root of volume fraction (in %) and Charpy-V shift values for all metals analysed using (a) APT and (b) SANS. The different coloured labels represent each data point according to type of RPV steels.

Figure xxiv (a) and Figure xxiv (b) show the correlation between square root of volume fraction and Charpy-V shift values for all the metals analysed using APT and SANS respectively. It is difficult to find any relationships from these figures. Similar figures have been plotted and each data point was colour labelled according to its Cu concentration (Figure xxv (a) and Figure xxv (b)) and according to the ratio of Ni/Mn concentration (Figure xxvi (a) and Figure xxvi (b)) in the bulks metals before neutron irradiation.

Figure xxvi shows that the correlation between square root of volume fraction and Charpy-V shift values might be influenced by the [Ni] / [Mn] ratio.

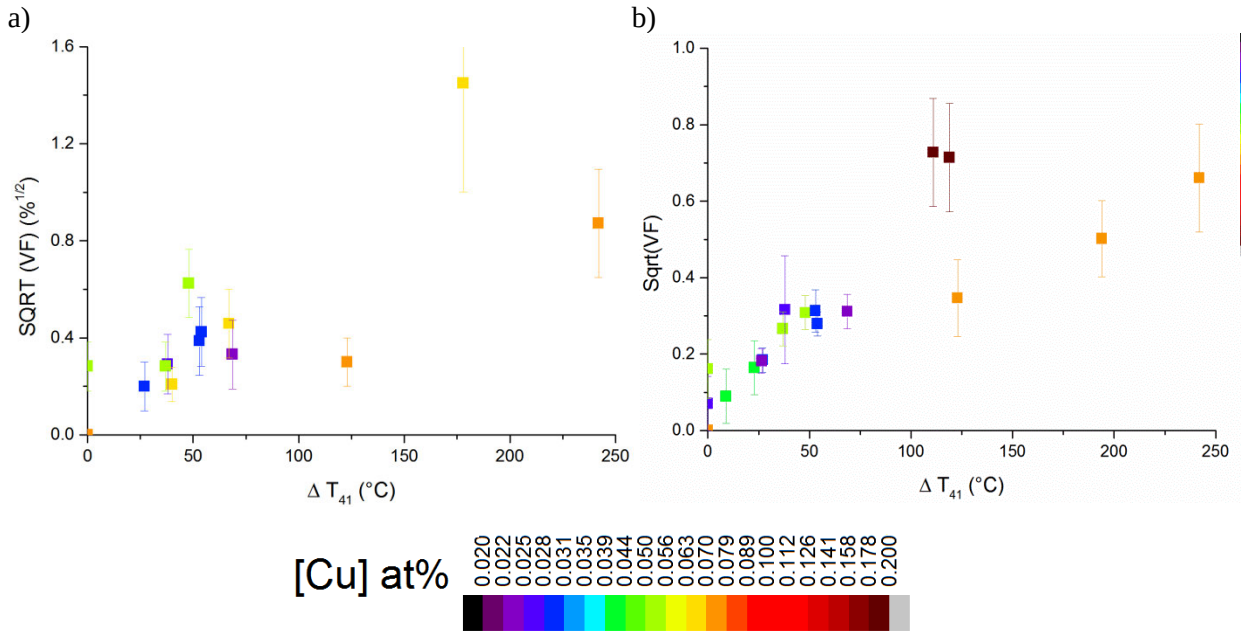


Figure xxv: Correlation between square root of volume fraction (in %) and Charpy-V shift values for all metals analysed using (a) APT and (b) SANS. The different coloured labels represent each data point according to the Cu concentration in RPV steels before neutron irradiation.

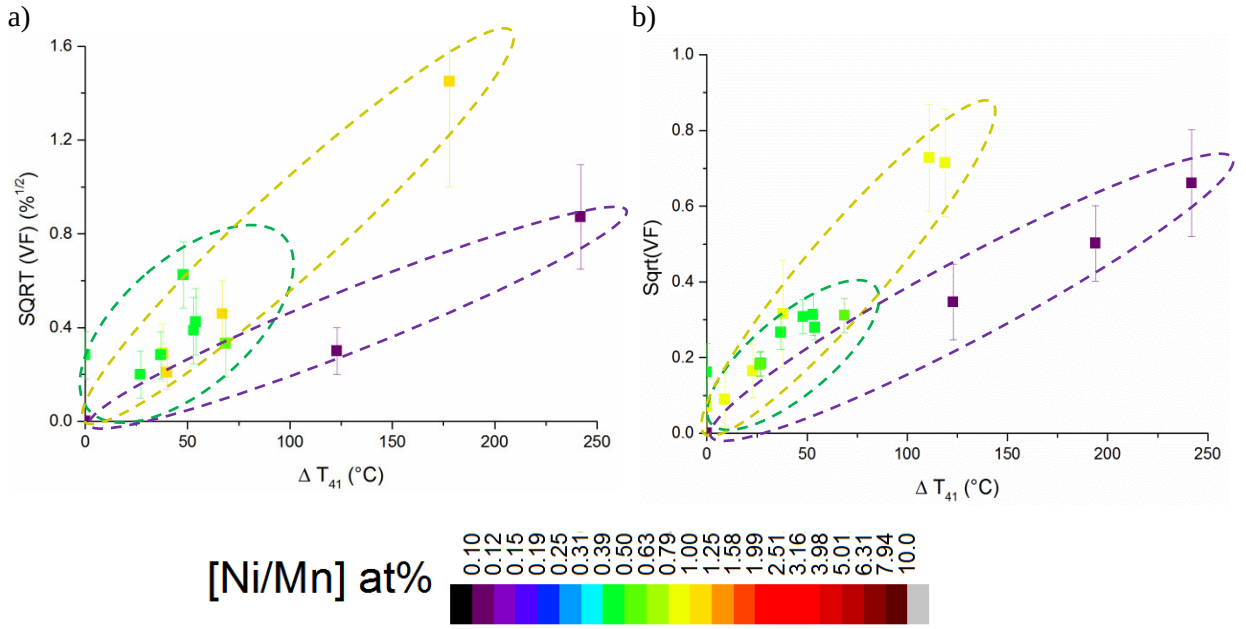


Figure xxvi: Correlation between square root of volume fraction (in %) and Charpy-V shift values for all metals analysed using (a) APT and (b) SANS. The different coloured labels represent each data point according to the ratio of Ni/Mn concentration in RPV steels before neutron irradiation.

VI. Incubation period for irradiation-induced cluster nucleation and growth

An incubation period before irradiation-induced solute clusters are detected is observed in some of these RPV steels, e.g. ANP-2, EDF-2 and NRI-1. In these steels have detected either no increase of number density and volume fraction of solute clusters during the incubation period or no change of Charpy V-notch impact test 41-J (ΔT_{41J}) transition temperature shifts (TTS) or both. The experimental results for these steels are listed in Table xxxv.

Table xxxv: RPV steels that showed potential incubation effects in either Charpy-V notch testing or APT analysis or both.

Materials	ϕt (x 10^{23} n.m^{-2})	Charpy value T_{41} (˚C)	No. Density (m^{-3})	Vol. Frac. (%)
ANP-2 (WM)	0.98	0	0	0
EDF-2 (BM)	1.71	0	7.2±0.9 x 10^{22}	0.08±0.01
NRI-1 (WM)[2]	2.00	Not Available	4.8±0.8 x 10^{22}	0

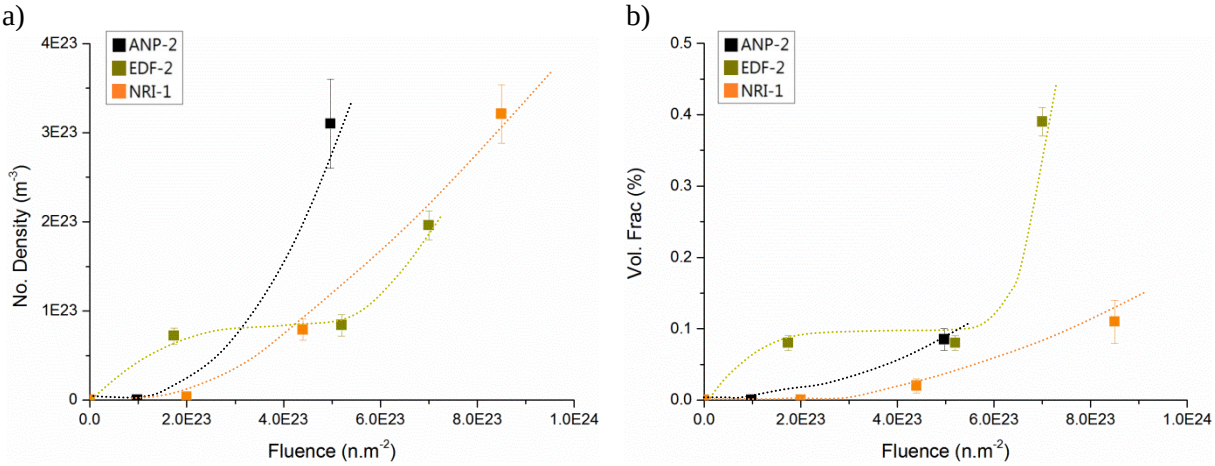


Figure xxvii: (a) Number density and (b) volume fraction of clusters against neutron fluence for ANP-2, EDF-2 & NRI-1

Although there are rather few data points, we can tentatively suggest that 2 kinds of behaviour can be seen;

[2] Experimental results & φt of NRI-1 need to be confirmed.

- ANP-2 and NRI-1 where clusters start to form at fluence, $\phi t \geq 1E23 n.m^{-2}$ (Figure xxvii and Figure xxviii), and
- EDF-2 where rapid cluster nucleation seems to occur at fluence, $\phi t \geq 5E23 n.m^{-2}$ (Figure xxvii and Figure xxix).

VI. I) Type 1 incubation period

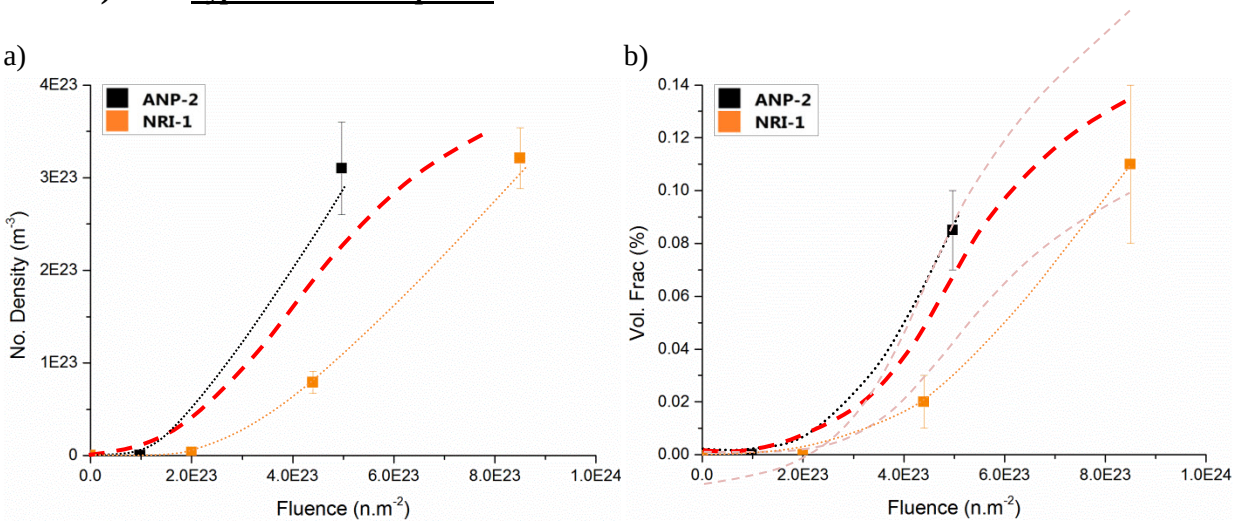


Figure xxviii: (a) Number density and (b) volume fraction of solute clusters against neutron fluence for ANP-2 and NRI-1

The behaviour of ANP-2 and NRI-1 seems very similar even though both are irradiated at different fluxes. In both materials, clusters are detected after low neutron fluence, $\phi t \geq 1E23 n.m^{-2}$. A general trend for the increase of number density and volume fraction of solute clusters with increase of neutron fluence can be suggested, as shown in Figure xxviii (a) and Figure xxviii (b), respectively, marked by the red dashed-line. Note that the general trend shown in Figure xxviii (b) is better at representing the trend of typical cluster nucleation and growth compared to Figure xxviii (a), since the volume fraction is less influenced by flux effects (see Deliverable 3.4 report).

A similar observation was reported by Odette et.al [23] in a low Cu and high Ni model alloy. They hypothesized that for low Cu and high Ni-alloyed steel an irradiation-induced phase will nucleate and grow after a significant incubation neutron fluence, resulting in severe unanticipated $\Delta T_{41}J$. They have named this as 'Late-Blooming Effect' (LBE).

Hence, in order to validate the significance of the incubation period observed in ANP-2 and NRI-1 and the resulting $\Delta T_{41}J$ that was caused by irradiation-induced clusters precipitated in ANP-2 and NRI-1, these metals will need to be irradiated to higher neutron fluence, i.e. $\phi t > 1E24$ n.m^{-2}.

VI. II) Type 2 incubation period

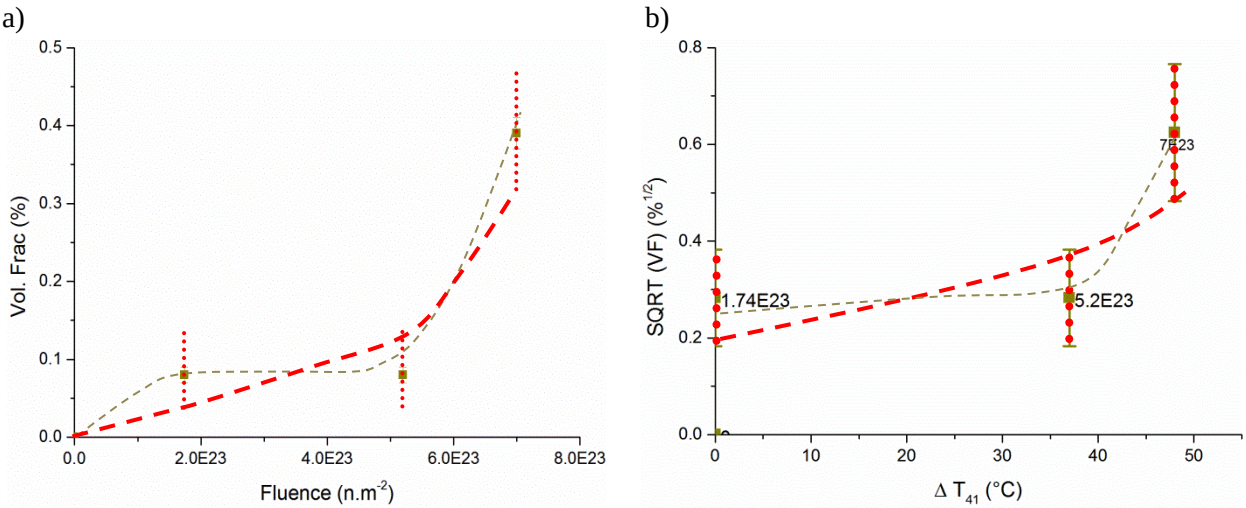


Figure xxix: Correlation between (1) volume fraction of solute clusters and neutron fluence and (2) square root of volume fraction and Charpy-V shift values for EDF-2. (Data label = Fluence)

There seems to be a clear incubation period for EDF-2 between neutron fluence, $\phi t \approx 2E23$ n.m^{-2} to $\phi t \approx 5E23$ n.m^{-2}. As mentioned earlier, the key differences between ANP-2 and NRI-1 and EDF-2 are that EDF-2 contains solute cluster at a lower fluence before the incubation period (shown by the black-dashed line in Figure xxix (a)). However, this observation may be suspect due to the fact that the APT data is highly scattered. To counter these problems, an error bar of two standard deviations is used (shown by the red-dotted lines in Figure xxix (a) and Figure xxix (b)). New trend lines are drawn and are shown as red-dashed lines in Figure xxix (a) and Figure xxix (b). With the new error bars, the incubation period observed in EDF-2 seems to have disappeared.

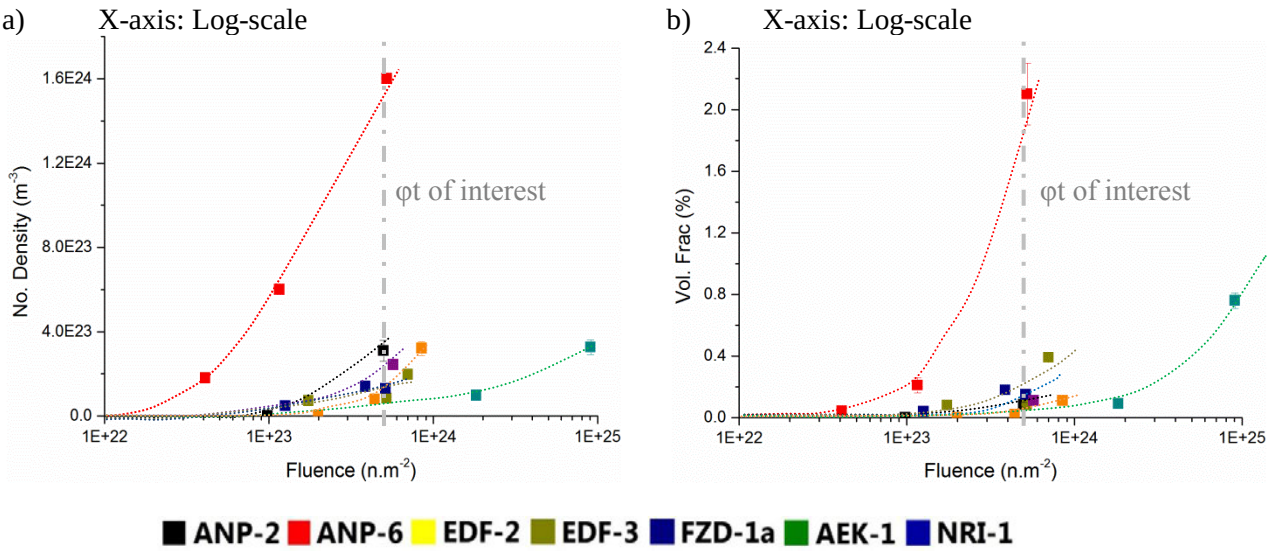


Figure xxx: (a) Number density and (b) volume fraction of clusters against ϕt for all RPV steels

It is important to note that even though ANP-2, EDF-2 & NRI-1 show a sudden increase in the number density and volume fraction of solute clusters after an incubation period, the volume fraction of solute clusters detected in these alloys at ϕt ~ $5x10^{23}$ $n.m^{-2}$ are comparable to those detected in RPV steels with similar chemical composition at similar ϕt (e.g. FZD-1a at ϕt = $5.7x10^{23}$ $n.m^{-2}$) (Figure xxx (a) and Figure xxx (b)). More research is needed into a wider range of neutron fluence in order to study the effects of incubation period in low Cu steels.

VII. References

[1] M. Serrano, S. Ortner, C. Grovenor, B. Radiguet, H. Hein, M. Hernandez-Mayoral, E. Meslin, F. Bergner, A. Ulbricht, A. Wagner, W.V. Renterghem, S. Cemmelli, F. Danoix, P. Pareige, G. Torok, F. Gillemot, R. Szekely, J. Rouden, P. Todeschini, T. Planman, Deliverable 3.9: Final report on neutron irradiation induced microstructure of RPV materials for long term operation. , FP7 LONGLIFE, 2013, pp. 93.
[2] K. Wilford, LONGLIFE Deliverable Report 3.5; Effects of P on Irradiation-Induced Cu-rich Clusters, in: J.J.H. Lim (Ed.) Rouen, France, 2013.
[3] R. Ngayam-Happy, C.S. Becquart, C. Domain, L. Malerba, Formation and evolution of MnNi Clusters in neutron irradiated dilute Fe alloys modelled by a first principle-based AKMC method, Journal of Nuclear Materials 426 (2012) 10.
[4] L. Debarberis, H. Hein, Evidence for chromium stabilisation of irradiation damage in RPV weld metals, International Journal of Pressure Vessels and Piping 83 (2006) 565-570.
[5] E.A. Little, Void-swelling in irons and ferritic steels. 1. Mechanisms of swelling suppression, Journal of Nuclear Materials 87 (1979) 11-24.
[6] E.A. Little, D.A. Stow, Void-swelling in irons and ferritic steels. 2. Experimental survey of materials irradiated in a fast-reactor, Journal of Nuclear Materials 87 (1979) 25-39.
[7] D.S. Gelles, Microstructural examination of neutron-irradiated simple ferritic alloys, Journal of Nuclear Materials 108-109 (1982) 515-526.
[8] S.H. Song, R.G. Faulkner, P.E.J. Flewitt, P. Marmy, L.Q. Weng, Small punch test evaluation of neutron-irradiation-induced embrittlement of a Cr–Mo low-alloy steel, Mater. Charact. 53 (2004) 35-41.
[9] K. Yabuuchi, R. Kasada, A. Kimura, Effect of alloying elements on irradiation hardening behavior and microstructure evolution in BCC Fe, Journal of Nuclear Materials 442 (2013) S790-S795.
[10] E.A. Little, D.A. Stow, Void-swelling in irons and ferritic steels: II. An experimental survey of materials irradiated in a fast reactor, Journal of Nuclear Materials 87 (1979) 25-39.
[11] E.A. Little, D.A. Stow, Effects of chromium additions on irradiation-induced void swelling in alpha-iron, Metal Science 14 (1980) 89-94.
[12] K. Yabuuchi, M. Saito, R. Kasada, A. Kimura, Neutron irradiation hardening and microstructure changes in Fe–Mn binary alloys, Journal of Nuclear Materials 414 (2011) 498-502.
[13] K. Yabuuchi, M. Saito, R. Kasada, A. Kimura, Neutron Irradiation Hardening of Fe-Based Binary Alloys, Materials Science Forum 654-656 (2010) 2911-2914.
[14] K. Yabuuchi, R. Kasada, A. Kimura, Effect of Mn addition on one-dimensional migration of dislocation loops in body-centered cubic Fe, Acta Mater. 61 (2013) 6517-6523.
[15] J.M. Hyde, M.G. Burke, G.D.W. Smith, P. Styman, H. Swan, K. Wilford, Uncertainties and assumptions associated with APT and SANS characteriastion of irradiation damage in RPV steels, Journal of Nuclear Materials (2013).
[16] P. Wells, N.J. Cunningham, G.R. Odette, B. Geiser, Towards understanding atom probe artifacts: Measuring and modeling the effects of trajectory aberrations and variable field evaporation potentials, IGRDM-17, UC Santa Barbara, Embiez Island, France, 2013.
[17] G.R. Odette, B.D. Wirth, A computational microscopy study of nanostructural evolution in irradiated pressure vessel steels, Journal of Nuclear Materials 251 (1997) 157-171.
[18] H. Ke, W. Xiong, L. Barnard, Krishnamurthy, P. Wells, N.J. Cunningham, D. Morgan, G.R. Odette, CALPHAD and Cluster Dynamics modeling of Ni-Mn-Si rich precipitates in RPV steels, University of Wisconsin, Madison, WI USA, Madison, 2013.

[19] B. Hu, H. Xu, S. Liu, Y. Du, C. He, C. Sha, D. Zhao, Y. Peng, Experimental investigation and thermodynamic modeling of the Mn–Ni–Si system, Calphad 35 (2011) 346-354.
[20] T. Hamaoka, A. Nomoto, K. Nishida, K. Dohi, N. Soneda, Accurate determination of the number density of G-phase precipitates in thermally aged duplex stainless steel, Philos. Mag. 92 (2012) 2716-2732.
[21] F. Danoix, P. Auger, S. Chambreland, D. Blavette, A 3D study of G-phase precipitation in spinodally decomposed alpha-ferrite by tomographic atom-probe analysis, Microsc. Microanal. Microstruct. 5 (1994) 121-132.
[22] G. Bonny, N. Castin, D. Terentyev, L. Malerba, Ageing of FeMnNiCu as simulated using an interatomic potential by Monte Carlo methods, SCK-CEN, Belgium, 2013.
[23] G.R. Odette, R.K. Nanstad, Predictive reactor pressure vessel steel irradiation embrittlement models: Issues and opportunities, Jom 61 (2009) 17-23.